

# Establishing a Design Procedure for Buried Steel-Reinforced High Density Polyethylene (SRHDPE) Pipes

Deep Kumar Khatri, M.S.  
Jie Han, Ph.D., P.E.  
Ryan Corey, M.S.  
Robert L. Parsons, Ph.D., P.E

*The University of Kansas*



A cooperative transportation research program between  
Kansas Department of Transportation,  
Kansas State University Transportation Center, and  
The University of Kansas

This page intentionally left blank.

<b>1 Report No.</b> K-TRAN: KU-11-6		<b>2 Government Accession No.</b>		<b>3 Recipient Catalog No.</b>	
<b>4 Title and Subtitle</b> Establishing a Design Procedure for Buried Steel-Reinforced High Density Polyethylene (SRHDPE) Pipes				<b>5 Report Date</b> November 2013	
				<b>6 Performing Organization Code</b>	
<b>7 Author(s)</b> Deep Kumar Khatri, M.S.; Jie Han, Ph.D., P.E.; Ryan Corey, M.S.; Robert L. Parsons, Ph.D., P.E.				<b>8 Performing Organization Report No.</b>	
<b>9 Performing Organization Name and Address</b> The University of Kansas Civil, Environmental & Architectural Engineering Department 1530 West 15 <sup>th</sup> Street Lawrence, Kansas 66045-7609				<b>10 Work Unit No. (TRAIS)</b>	
				<b>11 Contract or Grant No.</b> C1870	
<b>12 Sponsoring Agency Name and Address</b> Kansas Department of Transportation Bureau of Research 2300 SW Van Buren Street Topeka, Kansas 66611-1195				<b>13 Type of Report and Period Covered</b> Final Report July 2010–May 2013	
				<b>14 Sponsoring Agency Code</b> RE-0557-01	
<b>15 Supplementary Notes</b> For more information, write to address in block 9.					
<b>16 Abstract</b> <p>Metal and plastic pipes have been used extensively as storm sewers and buried drainage structures in transportation projects. Metal pipes have high strength and stiffness but are susceptible to corrosion from wastewaters containing acid, and from aggressive soils. Plastic pipes are resistant to corrosion, erosion, and biological attack but have certain disadvantages including lower long-term strength and stiffness (dimensional reliability), buckling, and tearing of pipe wall. To address the disadvantages of metal and plastic pipes, a new product, steel-reinforced high-density polyethylene (SRHDPE) pipe, has been developed and introduced to the market, which has high-strength steel reinforcing ribs wound helically and covered by corrosion-resistant high density polyethylene (HDPE) resin inside and outside. The steel reinforcement adds ring stiffness to the pipe to maintain the cross-section shape during installation and to support overburden stresses and traffic loading. The HDPE resin protects the steel against corrosion and provides a smooth inner wall. The combination of steel and plastic materials results in a strong and durable material with a smooth inner wall. Different methods are available for the design of metal and plastic pipes. The American Water Works Association (AWWA) Manual M11 (2004) provided the design procedure for metal pipes and the 2007 ASSHTO LRFD Bridge Design Specifications had separate design procedures for metal and plastic pipes. However, it is not clear whether any of these procedures for metal and plastic pipes can be used to design an SRHDPE pipe. Moreover, no approved installation or design specification is available specifically for the SRHDPE pipes.</p> <p>To establish a design procedure for SRHDPE pipes, various laboratory tests were conducted in this study to evaluate the stiffness, buckling resistance, and long-term creep behavior of SRHDPE pipes of 24 inches in diameter in air. In addition, large-scale plate loading tests were conducted on the pipe in a trench condition under 2 feet of shallow cover in a large geotechnical testing box (10 feet long x 6.6 feet wide x 6.6 feet high) to evaluate the performance of the SRHDPE pipe during installation and under static and cyclic loadings. In this study, Kansas River sand and crushed stone were used as bedding and backfill materials while AB-3 aggregate and Kansas River sand were used as base courses.</p> <p>Parallel plate loading test results show that the SRHDPE pipes met both the minimum pipe stiffness and buckling limit criteria according to the ASTM F2562/F2562M. The creep test conducted in air for a month demonstrated that the SRHDPE pipe deformed under a sustained load. The vertical arching factors (VAF) obtained from the measured earth pressures on the pipe crown during the installation of the pipes were compared with the analytical solutions in McGrath (1998) were used. The measured deflections of the pipes during the installation were compared with those predicted by the modified Iowa formula (1958). The measured earth pressures on the top of the pipe were compared with those estimated by Giroud and Han (2004) and the simplified distribution method in the 2007 ASSHTO LRFD Bridge Design Specifications. The measured deflections of the pipes during loading were also compared with the modified Iowa formula (1958). The strains on steel and plastic were measured at various locations during both installation and loading.</p> <p>Based on the testing and analysis, it can be concluded that (1) the pipe wall-soil interface should be designed as a fully bonded interface to be conservative, (2) the Giroud and Han (2004) method and the simplified distribution method in the 2007 AASHTO LRFD Bridge Design Specifications reasonably predicted the pressures on the top of the SRHDPE pipes induced by static and cyclic loadings, (3) the modified Iowa formula (1958) reasonably predicted the deflections of the SRHDPE pipes during the installation and over-predicted the deflections during static and cyclic loadings, (4) the pipe wall area was enough to resist the wall thrust during installation and loadings, and (5) the highest measured strains recorded in steel and plastic during the installation and loadings in all the tests were within the permissible values.</p>					
<b>17 Key Words</b> Metal Pipe, HDPE, SRHDPE, Plastic Pipe, Culvert			<b>18 Distribution Statement</b> No restrictions. This document is available to the public through the National Technical Information Service, Springfield, Virginia 22161		
<b>19 Security Classification (of this report)</b> Unclassified		<b>20 Security Classification (of this page)</b> Unclassified		<b>21 No. of pages</b> 208	
				<b>22 Price</b>	

# **Establishing a Design Procedure for Buried Steel-Reinforced High Density Polyethylene (SRHDPE) Pipes**

**Final Report**

Prepared by

**Deep Kumar Khatri, M.S.**  
**Jie Han, Ph.D., P.E.**  
**Ryan Corey, M.S.**  
**Robert L. Parsons, Ph.D., P.E.**  
The University of Kansas

A Report on Research Sponsored by

THE KANSAS DEPARTMENT OF TRANSPORTATION  
TOPEKA, KANSAS

and

THE UNIVERSITY OF KANSAS  
LAWRENCE, KANSAS

November 2013

© Copyright 2013, **Kansas Department of Transportation**

## **PREFACE**

The Kansas Department of Transportation's (KDOT) Kansas Transportation Research and New-Developments (K-TRAN) Research Program funded this research project. It is an ongoing, cooperative and comprehensive research program addressing transportation needs of the state of Kansas utilizing academic and research resources from KDOT, Kansas State University and the University of Kansas. Transportation professionals in KDOT and the universities jointly develop the projects included in the research program.

## **NOTICE**

The authors and the state of Kansas do not endorse products or manufacturers. Trade and manufacturers names appear herein solely because they are considered essential to the object of this report.

This information is available in alternative accessible formats. To obtain an alternative format, contact the Office of Transportation Information, Kansas Department of Transportation, 700 SW Harrison, Topeka, Kansas 66603-3754 or phone (785) 296-3585 (Voice) (TDD).

## **DISCLAIMER**

The contents of this report reflect the views of the authors who are responsible for the facts and accuracy of the data presented herein. The contents do not necessarily reflect the views or the policies of the state of Kansas. This report does not constitute a standard, specification or regulation.

## **Abstract**

Metal and plastic pipes have been used extensively as storm sewers and buried drainage structures in transportation projects. Metal pipes have high strength and stiffness but are susceptible to corrosion from wastewaters containing acid, and from aggressive soils. Plastic pipes are resistant to corrosion, erosion, and biological attack but have certain disadvantages including lower long-term strength and stiffness (dimensional reliability), buckling, and tearing of pipe wall. To address the disadvantages of metal and plastic pipes, a new product, steel-reinforced high-density polyethylene (SRHDPE) pipe, has been developed and introduced to the market, which has high-strength steel reinforcing ribs wound helically and covered by corrosion-resistant high density polyethylene (HDPE) resin inside and outside. The steel reinforcement adds ring stiffness to the pipe to maintain the cross-section shape during installation and to support overburden stresses and traffic loading. The HDPE resin protects the steel against corrosion and provides a smooth inner wall. The combination of steel and plastic materials results in a strong and durable material with a smooth inner wall. Different methods are available for the design of metal and plastic pipes. The American Water Works Association (AWWA) Manual M11 (2004) provided the design procedure for metal pipes and the 2007 ASSHTO LRFD Bridge Design Specifications had separate design procedures for metal and plastic pipes. However, it is not clear whether any of these procedures for metal and plastic pipes can be used to design an SRHDPE pipe. Moreover, no approved installation or design specification is available specifically for the SRHDPE pipes.

To establish a design procedure for SRHDPE pipes, various laboratory tests were conducted in this study to evaluate the stiffness, buckling resistance, and long-term creep behavior of SRHDPE pipes of 24 inches in diameter in air. In addition, large-scale plate loading tests were conducted on the pipe in a trench condition under 2 feet of shallow cover in a large geotechnical testing box (10 feet long x 6.6 feet wide x 6.6 feet high) to evaluate the performance of the SRHDPE pipe during installation and under static and cyclic loadings. In this study, Kansas River sand and crushed stone were used as bedding and backfill materials while AB-3 aggregate and Kansas River sand were used as base courses.

Parallel plate loading test results show that the SRHDPE pipes met both the minimum pipe stiffness and buckling limit criteria according to the ASTM F2562/F2562M. The creep test conducted in air for a month demonstrated that the SRHDPE pipe deformed under a sustained load. The vertical arching factors (VAF) obtained from the measured earth pressures on the pipe crown during the installation of the pipes were compared with the analytical solutions in McGrath (1998) were used. The measured deflections of the pipes during the installation were compared with those predicted by the modified Iowa formula (1958). The measured earth pressures on the top of the pipe were compared with those estimated by Giroud and Han (2004) and the simplified distribution method in the 2007 AASHTO LRFD Bridge Design Specifications. The measured deflections of the pipes during loading were also compared with the modified Iowa formula (1958). The strains on steel and plastic were measured at various locations during both installation and loading.

Based on the testing and analysis, it can be concluded that (1) the pipe wall-soil interface should be designed as a fully bonded interface to be conservative, (2) the Giroud and Han (2004) method and the simplified distribution method in the 2007 AASHTO LRFD Bridge Design Specifications reasonably predicted the pressures on the top of the SRHDPE pipes induced by static and cyclic loadings, (3) the modified Iowa formula (1958) reasonably predicted the deflections of the SRHDPE pipes during the installation and over-predicted the deflections during static and cyclic loadings, (4) the pipe wall area was enough to resist the wall thrust during installation and loadings, and (5) the highest measured strains recorded in steel and plastic during the installation and loadings in all the tests were within the permissible values.

## **Acknowledgements**

This research was financially sponsored by the Kansas Department of Transportation (KDOT) through the Kansas Transportation Research and New-Developments Program (K-TRAN) program. Mr. James J. Brennan, the Chief Geotechnical Engineer of KDOT, was the monitor for this project. Steel Reinforced High Density Polyethylene (SRHDPE) pipes were provided by Contech Construction Product Inc. The backfill and base course materials, Kansas River sand, crushed stone, and AB-3 aggregate, were provided by the Midwest Concrete Materials, Lawrence, Kansas. The former laboratory manager at the Department of Civil, Environment, and Architectural Engineering at the University of Kansas (KU), Mr. Howard J. Weaver, and the current laboratory manager, Mr. Mathew Maksimowicz, provided great assistance to the laboratory testing at KU. The graduate students, Jun Guo and Zhen Zhang, and the undergraduate students, Brandon W. Basgall and Byron Whitted, helped to construct the test sections. Dr. Jingshan Jiang and Danny Smyl provided great assistance during the construction of the test sections. The authors would like to express their appreciations to the organizations and the individuals for their help and support



# Table of Contents

Abstract .....	v
Acknowledgements .....	vii
Table of Contents .....	viii
List of Tables .....	xi
List of Figures .....	xii
Chapter 1: Introduction .....	1
1.1 Background .....	1
1.2 Problem Statement .....	3
1.3 Research Objective.....	6
1.4 Research Methodology.....	6
1.5 Organization of Report.....	7
Chapter 2: Literature Review .....	8
2.1 Loads on Pipes .....	8
2.2 Bedding and Backfill Materials.....	10
2.3 Minimum Soil Cover Requirements .....	11
2.4 Deflection .....	12
2.4.1 Estimation of the Pipe Stiffness (PS) .....	16
2.4.2 Estimation of the Modulus of Soil Reaction ( $E'$ ) .....	18
2.5 Pipe Thrust and Buckling.....	21
2.6 Profile Wall Pipes and Local Buckling.....	22
2.7 Strain .....	24
2.8 Existing Design Methods for Flexible Pipes.....	26
2.8.1 Metal Pipe.....	26
2.8.2 Plastic Pipes.....	27
2.9 Performance of Pipes under Traffic Loads .....	28
2.9.1 Field Tests.....	28
2.9.2 Laboratory Tests .....	30
2.10 Performance of Steel-Reinforced High Density Polyethylene (SRHDPE) Plastic Pipes ..	32
Chapter 3: Material Properties .....	34
3.1 Steel-Reinforced High Density Polyethylene (SRHDPE) Pipe .....	34
3.1.1 Parallel Plate Tests.....	35
3.1.2 Test Results and Discussions.....	39
3.1.3 Stub Compression Tests .....	51
3.1.4 Pipe Bending Test.....	52
3.1.5 Creep Test.....	55

3.1.6 Summary .....	60
3.2 Soil Types and Properties.....	61
3.2.1 Clayey Soil and Its Characteristics .....	61
3.2.2 Bedding and Backfill Soils and Their Characteristics.....	63
3.2.3 Base Course and Its Characteristics.....	65
Chapter 4: Large Scale Plate Loading Box Test.....	68
4.1. Large Geotechnical Testing Box and Test Sections.....	68
4.2 MTS Loading System .....	71
4.3 Instrumentation.....	73
4.3.1 Displacement Transducers and Tell-Tales .....	73
4.3.2 Strain Gages.....	76
4.3.3 Earth Pressure Cells.....	80
4.4 Data Acquisition System .....	81
4.5 Construction of Test Section .....	81
4.5.1 Construction of Test Section 1 .....	81
4.5.2 Construction of Test Section 2 .....	88
4.5.3 Construction of Test Section 3 .....	88
4.6 Quality Control.....	91
4.7 Data Collection.....	94
Chapter 5: Data Analysis and Results.....	95
5.1 Test Results from Pipe Installation .....	95
5.1.1 Earth Pressure Results .....	95
5.1.2 Deflection Results.....	102
5.1.3 Strain Data .....	107
5.2 Static Plate Loading Test Results.....	112
5.2.1 Settlement of Loading Plate .....	112
5.2.2 Earth Pressure Results .....	114
5.2.3 Pipe Deflection Results .....	123
5.2.4 Strain Results .....	130
5.3 Cyclic Plate Loading Test Result .....	143
5.3.1 Vertical Deformation of the Loading Plate .....	143
5.3.2 Maximum Earth Pressure Results.....	149
5.3.3 Pipe Deflection Results .....	154
5.3.4 Strain Results .....	161
5.4 Comparison of Static and Cyclic Test Results .....	168
5.4.1 Earth Pressure Results .....	168
5.4.2 Pipe Deflection Results .....	171
5.4.3 Strain Results .....	173
5.5 Safety against Structural Failure .....	174

5.5.1 Wall Area of Pipe .....	174
5.5.2 Global Buckling.....	175
5.5.3 Strain Limit.....	175
5.6 Handling and Installation Requirement.....	175
Chapter 6: Conclusions and Recommendations .....	176
6.1 Conclusions .....	176
6.1.1 Compression Tests in Air .....	176
6.1.2 Installation in Test Box.....	177
6.1.3 Static and Cyclic Plate Loading Tests .....	178
6.2 Recommendations .....	179
References.....	181

## List of Tables

TABLE 1.1 Comparisons of Corrugated Steel, HDPE, and SRHDPE Pipe.....	4
TABLE 2.1 Variation of Bedding Constant (k) with Bedding Angle .....	10
TABLE 2.2 Minimum Cover over the Top of the Pipe .....	12
TABLE 2.3 Parameters for the USBR Equation .....	15
TABLE 2.4 Pressure Generated by Compaction Efforts .....	16
TABLE 2.5 Typical Values of E' (psi) .....	19
TABLE 2.6 Typical Values E' (psi).....	19
TABLE 3.1 Specification of the SRHDPE Pipe.....	35
TABLE 3.2 Calculated Pipe Stiffness and Equivalent Bending Stress Values .....	45
TABLE 4.1 Loading Increment and Magnitude .....	71
TABLE 5.1 Permanent Deformations.....	148
TABLE 5.2 Comparisons of the Earth Pressures around the Pipe and the Deflections of the Pipe .....	170
TABLE 5.3 Maximum Measured Strains on the Steel and the Plastic during the Installation and Loading .....	173

## List of Figures

FIGURE 1.1 Cross Section and 3D View of an SRHDPE Pipe. ....	2
FIGURE 2.1 Pipe Deflection and Radii of Curvature of a Deflected Ellipse Shape.....	17
FIGURE 2.2 Percentage Deflection of the Unplasticized PVC Pipe in the Near Side Lane.....	29
FIGURE 2.3 Relative Variations of the Vertical Diameter to the Horizontal Diameter for Twin-Wall Pipes .....	31
FIGURE 3.1 SRHDPE Pipes .....	34
FIGURE 3.2 Test Setup and Instrumentation for the Parallel Plate Load Test .....	36
FIGURE 3.3 Symbols, Locations, and Orientations of Strain Gages on the Pipe .....	37
FIGURE 3.4 Strain Gages on the Steel and Plastic Surfaces .....	38
FIGURE 3.5 Deformed Pipe Shapes from the Photogrammetry .....	40
FIGURE 3.6 Comparison of the Load-Horizontal Deflection Curves Obtained by the Photogrammetry Method and the Displacement Transducer.....	41
FIGURE 3.7 Comparison of the Deformed Pipe Shapes from Photogrammetry with the Standard Elliptical Shapes.....	41
FIGURE 3.8 LiDAR Images.....	42
FIGURE 3.9 Deformed Pipe Shapes from the LiDAR Images .....	42
FIGURE 3.10 Load-Deflection Responses.....	44
FIGURE 3.11 Relation between the Vertical and Horizontal Deflections of the Pipes .....	44
FIGURE 3.12 Circumferential and Radial Strains against the Applied Loads on the Steel at the Springline.....	47
FIGURE 3.13 Circumferential and Radial Strains against the Applied Loads on the Steel Surface at the Crown and Invert.....	48
FIGURE 3.14 Strains against the Applied Loads on the Plastic Surface .....	49
FIGURE 3.15 Comparison of Strains Developed on the Steel Rib and Plastic Surfaces in the Radial Direction at the Springline.....	50

FIGURE 3.16 Specimen Crushing in the Stub Compression Test .....	51
FIGURE 3.17 Load-Displacement Curves of Specimens from Stub Compression Tests .....	52
FIGURE 3.18 Pipe Bending Test.....	53
FIGURE 3.19 Load-Deflection Curve of the Pipe under Bending .....	54
FIGURE 3.20 Deflection Profiles of the Pipe under Bending.....	54
FIGURE 3.21 Creep Test Set-Up .....	55
FIGURE 3.22 Symbols, Locations, and Orientations of Strain Gages on the Pipe .....	56
FIGURE 3.23 Deflection and Stiffness Factor (EI) of the Pipe with Time under the Sustained Load .....	57
FIGURE 3.24 Circumferential Strains on the Steel Surface under a Sustained Load .....	58
FIGURE 3.25 Circumferential and Radial Strains on the Plastic Surface at the Ribs under a Sustained Load.....	59
FIGURE 3.26 Circumferential and Radial Strains on the Plastic Surface at the Valley under a Sustained Load.....	59
FIGURE 3.27 Grain Size Distribution of the Clayey Soil.....	61
FIGURE 3.28 Flow Curve of the Clayey Soil .....	62
FIGURE 3.29 Densities, Vane Shear Strength, and CBR Curves .....	63
FIGURE 3.30 Grain Size Distribution of the Sand.....	64
FIGURE 3.31 Grain Size Distribution of the Crushed Stone .....	65
FIGURE 3.32 Grain Size Distribution Curve of the AB-3 Aggregate .....	66
FIGURE 3.33 Standard Proctor Compaction Curve of the AB-3 Aggregate .....	66
FIGURE 3.34 CBR Curve of the AB-3 Aggregate.....	67
FIGURE 4.2 Plate Loading Test Sections .....	69
FIGURE 4.3 Cyclic Loading Details .....	72
FIGURE 4.4 Loading Plate.....	73

FIGURE 4.5 Displacement Transducers inside the Pipe Section .....	74
FIGURE 4.6 Tell-Tales Fixed on the Pipe Specimen.....	75
FIGURE 4.7 Displacement Transducers for Deflection Measurements.....	75
FIGURE 4.8 Strain Gages Fixed outside of Pipe Specimen.....	77
FIGURE 4.9 Strain Gages Fixed inside of the Pipe Specimen.....	77
FIGURE 4.10 Symbols, Locations, and Orientations of Strain Gages on the Pipe.....	78
FIGURE 4.11 Earth Pressure Cells around the Pipe Section.....	81
FIGURE 4.12 3D Perspectives Drawing of the Box with the Wooden Shoring to Make a Trench of 6.6 ft x 4 ft x 4.5 ft.....	82
FIGURE 4.13 Compaction of Surrounding Soil Using the Vibratory Plate Compactor .....	83
FIGURE 4.14 Compaction of Surrounding Soil Using the Jackhammer .....	83
FIGURE 4.15 A Polyethylene Plastic Sheet Placed to Cover the Exposed Fat Clay .....	84
FIGURE 4.16 Bedding Material and the Earth Pressure Cell $E_{10}$ Installed at the Invert of the Pipe .....	85
FIGURE 4.17 Fully Instrumented Pipes in the Trench in Test Section 1.....	86
FIGURE 4.18 Backfill up to the Springline in Test Section 1.....	87
FIGURE 4.19 Earth Pressure Cells at the Springline in Test Section 1 .....	87
FIGURE 4.20 Compaction of Base Course Using the Vibratory Plate Compactor in Test Section 1.....	88
FIGURE 4.21 Backfilling up to the Springline in Test Section 3 .....	89
FIGURE 4.22 Earth Pressure Cells at the Springline in Test Section 3 .....	90
FIGURE 4.23 Earth Pressure Cells at the Crown in Test Section 3 .....	90
FIGURE 4.24 Cross Section of Test Section Including the Soil Lifts and Earth Pressure Cells .	91
FIGURE 4.25 Vane Shear Test on the Fat Clay .....	92
FIGURE 4.26 LWD Test on the Fat Clay.....	92

FIGURE 4.27 CBR Profiles in Test Section 1.....	93
FIGURE 4.28 Displacement Transducers Fixed to a Reference Beam .....	94
FIGURE 5.1 Measured Earth Pressures around the Pipe During Installation in Test Section 1 ..	96
FIGURE 5.2 Comparison of Measured and Calculated Pressures at the Crown During Installation in Test Section 1.....	97
FIGURE 5.3 Calculated Lateral Earth Pressure Coefficients (K) at the Springline.....	98
FIGURE 5.4 Calculated Lateral Earth Pressure Coefficients (K) at the Springline and Shoulder in Test Section 1.....	98
FIGURE 5.5 Measured Pressures around the Pipe During the Installation in Test Section 3 .....	99
FIGURE 5.6 Comparison of Measured and Calculated Pressures at the Crown During the Installation and Vertical Arching Factor (VAF).....	100
FIGURE 5.7 The Measured Lateral Pressures at the Shoulder, Springline, and Haunch with the Measured and Calculated Vertical Pressures at the Springline in Test Section 3 .....	101
FIGURE 5.8 Calculated Lateral Earth Pressure Coefficients (K) at the Shoulder, Haunch, and Springline in Test Section 3.....	102
FIGURE 5.9 Measured Deflections of the Pipe During the Installation in Test Section 1 .....	104
FIGURE 5.10 Relations between the Measured Vertical and Horizontal Deflections During the Installation in Test Section 1.....	104
FIGURE 5.11 Comparison of the Measured and Calculated Horizontal Deflections by the Iowa Formula in Test Section 1 .....	105
FIGURE 5.12 Measured Deflections of the Pipe During the Installation in Test Section 3 .....	106
FIGURE 5.13 Relations between the Measured Vertical and Horizontal Deflections During the Installation in Test Section 3.....	106
FIGURE 5.14 Comparison of the Measured and Calculated Horizontal Deflections by the Iowa Formula in Test Section 3 .....	107
FIGURE 5.15 Measured Strains on the Steel Surface During the Installation in Test Section 1	108
FIGURE 5.16 Measured Strains on the Plastic Ribs During the Installation in Test Section 1 .	108



FIGURE 5.17 Measured Strains on the Plastic at Inside and Outside Pipe Wall During the Installation in Test Section 1.....	109
FIGURE 5.18 Measured Strains on the Steel During the Installation in Test Section 3 .....	110
FIGURE 5.19 Measured Strains on the Plastic Ribs During the Installation in Test Section 3 .	111
FIGURE 5.20 Measured Strains on the Plastic at inside and Outside Pipe Wall During the Installation in Test Section 3.....	111
FIGURE 5.21 Settlement of the Loading Plate versus Applied Pressure under Static Loads....	113
FIGURE 5.22 Measured Earth Pressures around the Pipe in Test 1 .....	115
FIGURE 5.23 Measured Earth Pressures around the Pipe in Test 2 .....	116
FIGURE 5.24 Measured and Calculated Earth Pressure ( $E_{IF}$ ) at the Backfill-Base Course Interface in Test 3 .....	117
FIGURE 5.25 Measured Earth Pressures around the Pipe in Test 3 .....	118
FIGURE 5.26 Measured Earth Pressures around the Pipe in Test 1 and Test 2.....	119
FIGURE 5.27 Measured Earth Pressures around the Pipe in Test 1 and Test 3.....	120
FIGURE 5.28 Comparison of the Measured Crown Pressures with the 2007 AASHTO LRFD Bridge Design Specifications and Giroud and Han (2004) Methods .....	121
FIGURE 5.29 Calculated Lateral Earth Pressure Coefficients (K) at the Springline from the Measured Pressures in Test 3.....	122
FIGURE 5.30 Comparison of the Lateral Earth Pressure Coefficients (K) at the Shoulder, Springline, and Haunch in Test 3.....	123
FIGURE 5.31 Deflections of the Pipe under the Static Load in Test 1 .....	124
FIGURE 5.32 Deflections of the Pipe under the Static Load in Test 2 .....	125
FIGURE 5.33 Deflections of the Pipe under the Static Load in Test 3 .....	126
FIGURE 5.34 Comparison of the Deflections of the Pipe in Tests 1 and 2 .....	127
FIGURE 5.35 Comparison of the Deflection of the Pipe in Tests 1 and 3.....	128
FIGURE 5.36 Relation between the Horizontal and Vertical Deflections at the Center of the Pipe .....	129

FIGURE 5.37 Comparison of the Measured and Calculated Vertical Deflections by the Iowa Formula .....	130
FIGURE 5.38 Measured Strains on the Steel Ribs in Test 1 .....	131
FIGURE 5.39 Measured and Calculated Strains on the Steel Ribs at the Springline in the Circumferential Direction .....	132
FIGURE 5.40 Measured Strains on the Plastic at Ribs in Test 1 .....	133
FIGURE 5.41 Simplified Load Transfer Mechanism .....	133
FIGURE 5.42 Measured and Calculated Strains on the Plastic Cover at the Rib at the Pipe Crown in the Radial Direction in Test 1 .....	134
FIGURE 5.43 Measured Strains on the Inside and Outside Plastic Wall of the Pipe in Test 1..	135
FIGURE 5.44 Measured Strains on the Steel Ribs in Test 2 .....	136
FIGURE 5.45 Measured and Calculated Strains on the Steel at the Springline in the Circumferential Direction in Test 2 .....	136
FIGURE 5.46 Measured Strains on the Plastic Cover at the Ribs in Test 2 .....	137
FIGURE 5.47 Measured and Calculated Strains on the Plastic Cover at the Rib at the Pipe Crown in the Radial Direction in Test 2 .....	138
FIGURE 5.48 Measured Strains on the Inside and Outside Plastic Walls of the Pipe in Test 2	139
FIGURE 5.49 Measured Strains on the Steel Ribs in Test 3 .....	140
FIGURE 5.50 Measured and Calculated Strains on the Steel Rib at the Springline in the Circumferential Direction in Test 3 .....	140
FIGURE 5.51 Measured Strains on the Plastic Cover at the Ribs in Test 3 .....	141
FIGURE 5.52 Measured and Calculated Strains on the Plastic Cover at the Ribs at the Pipe Crown in the Radial Direction in Test 3 .....	142
FIGURE 5.53 Measured Strains on the Inside and Outside Plastic Wall of the Pipe in Test 3..	143
FIGURE 5.54 Vertical Deformation of the Loading Plate under Cyclic Loading in Test 1 .....	145
FIGURE 5.55 Vertical Deformation of the Loading Plate under Cyclic Loading in Test 1 .....	146
FIGURE 5.56 Vertical Deformation of the Loading Plate under Cyclic Loading in Test 3 .....	147

FIGURE 5.57 Vertical Deformation of the Loading Plate under Static and Cyclic Loadings...	148
FIGURE 5.58 Measured Maximum Earth Pressures around the Pipe under Cyclic Loading in Test 1.....	149
FIGURE 5.59 Measured Maximum Earth Pressures around the Pipe under Cyclic Loading in Test 2.....	150
FIGURE 5.60 Measured Maximum Earth Pressure at the Backfill-Base Course Interface in Test 3.....	151
FIGURE 5.61 Measured Maximum Earth Pressures around the Pipe under Cyclic Loading in Test 3.....	152
FIGURE 5.62 Comparison of the Maximum Earth Pressures around the Pipe under Cyclic Loading in Tests 1 and 2.....	153
FIGURE 5.63 Comparison of the Maximum Earth Pressures around the Pipe under Cyclic Loading in Tests 1 and Test 3 .....	154
FIGURE 5.64 Maximum Deflections of the Pipe under Cyclic Loading in Test 1.....	155
FIGURE 5.65 Maximum Deflections of the Pipe under Cyclic Loading in Test 2.....	156
FIGURE 5.66 Maximum Deflections of the Pipe under Cyclic Loading in Test 3.....	157
FIGURE 5.67 Comparison of the Maximum Deflections of the Pipe under Cyclic Loading in Tests 1 and 2 .....	158
FIGURE 5.68 Comparison of the Maximum Deflections of the Pipe under Cyclic Loading in Tests 1 and 3 .....	159
FIGURE 5.69 Relationship between the Maximum Horizontal and Vertical Deflections at the Center of the Pipe under Cyclic Loading.....	160
FIGURE 5.70 Measured Maximum Strains on Steel under Cyclic Loading in Test 1.....	162
FIGURE 5.71 Measured Maximum Strains on the Plastic Cover at Ribs under Cyclic Loading in Test 1.....	162
FIGURE 5.72 Measured Maximum Strains on the Inside and Outside Walls of the Pipe during Cyclic Loading in Test 1 .....	163
FIGURE 5.73 Measured Maximum Strains on the Steel under Cyclic Loading in Test 2.....	164

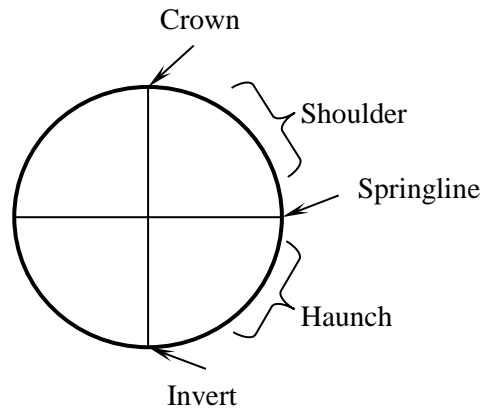
FIGURE 5.74 Measured Maximum Strains on the Plastic Cover at the Ribs under Cyclic Loading in Test 2 .....	165
FIGURE 5.75 Measured Maximum Strains on the Inside and Outside Plastic Walls of the Pipe during Cyclic Loading in Test 2 .....	165
FIGURE 5.76 Measured Maximum Strains on the Steel under Cyclic Loading in Test 3 .....	166
FIGURE 5.77 Measured Maximum Strains on the Plastic Cover at the Ribs under Cyclic Loading in Test 3 .....	167
FIGURE 5.78 Measured Maximum Strains on the Inside and Outside Pipe Walls of the Pipe under Cyclic Loading in Test 3 .....	167
FIGURE 5.79 Comparison of the Measured Earth Pressures around the Pipe under Static and Cyclic Loads in Test 1 .....	169
FIGURE 5.80 Comparison of the Earth Pressures around the Pipe under Static and Cyclic Loads in Test 2 .....	169
FIGURE 5.81 Comparison of the Earth Pressures around the Pipe under Static and Cyclic Loads in Test 3 .....	170
FIGURE 5.82 Comparison of the Deflections of the Pipe under Static and Cyclic Loads in Test 1 .....	171
FIGURE 5.83 Comparison of the Deflections of the Pipe under Static and Cyclic Loads in Test 2 .....	172
FIGURE 5.84 Comparison of the Deflections of the Pipe under Static and Cyclic Loads in Test 3 .....	172

# Chapter 1: Introduction

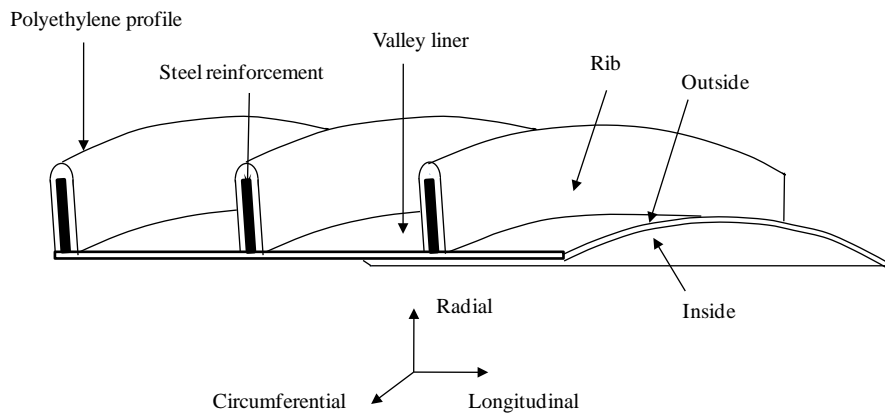
## 1.1 Background

In 1824, iron pipes were developed in England and steel pipes came in existence in 1855. From 1860 to 1900, more than 2 million feet of steel pipe was installed in the United States (Watkins 2006 as cited by Whidden 2009). Subsequently, pipe systems of different materials, ranging from rigid concrete to flexible thermal plastics, came into use as buried or underground drainage structures in civil engineering. In more recent times, metal and plastic pipes with various profile walls have been manufactured to provide higher pipe stiffness. The inherent strength, stiffness, corrosion resistance, lightness, flexibility, and ease of joining are the characteristics that are often given as reasons for using a particular material.

Metal pipes have high strength and stiffness but are susceptible to corrosion from wastewater containing acid, and from aggressive soils. Plastic pipes are resistant to corrosion, erosion, and biological attack but have certain disadvantages including lower long-term strength and stiffness (dimensional reliability), buckling, and tearing of the pipe wall. For the fiscal years 2013 to 2016, the state of Kansas has an estimated obligation of 9.8 million dollars for culvert replacement and repair (KDOT 2012). Steel-Reinforced High Density Polyethylene (SRHDPE) pipe, while not applicable to all conditions, is a new product recently used for buried pipes with the potential for expanded use. The cross section and 3D view of an SRHDPE pipe section are shown in Figure 1.1. This type of pipe has high-strength steel reinforcing ribs wound helically and covered with corrosion-resistant High Density Polyethylene (HDPE) resin inside and outside. The steel reinforcement adds ring stiffness to the pipe to maintain the cross-section shape during the installation and to support the soil overburden and traffic loading. The HDPE resin protects the steel against corrosion and provides the smooth inner wall.



a) Cross section of a pipe.



b) 3D view of an SRHDPE pipe section

**FIGURE 1.1**  
**Cross Section and 3D View of an SRHDPE Pipe.**

In pipe design, pipes are generally divided into two categories, rigid and flexible. Concrete, clay, and cast iron pipes are examples of rigid pipes while steel, aluminum, and plastic pipes are usually considered flexible. Rigid pipes are designed to be stiffer than the surrounding soil and to resist the applied loads by their inherent strength. Flexible pipes are defined as those that will deflect at least 2% without structural distress (Goddard 1994) and rely on the capacity of the surrounding soil to carry a major portion of the applied load through ring deformation to activate the lateral passive resistance of the soil. As a result, backfill quality and compaction are

the most important factors in ensuring satisfactory performance of flexible pipes. A rigid pipe requires good embedment for load distribution while a flexible pipe requires the utmost effort in backfilling and compaction, and is more prone to distresses and failures during and after installation. For all buried pipes, rigid or flexible, the structural performance is dependent on the soil-structure interaction. The type and anticipated behavior of the material around pipes must be considered for the proper design of the pipes (1990 AASHTO Standard Specification for Highway Bridges, as cited by Goddard 1994). Each type of pipe may have one or more performance limits based on type, material, and wall design.

## **1.2 Problem Statement**

There are various methods for the design of metal and plastic pipes. The 2007 AASHTO Bridge Design Specifications has separate design procedures for metal and plastic pipes. The American Water Works Association (AWWA) M11 (2004) also has a design procedure for metal pipes while Gumbel and Wilson (1981), Chambers et al. (1980), and Moser (2008) provided design procedures for plastic pipes. However, it is not clear whether any of these procedures for metal and plastic pipes can be used to design an SRHDPE pipe. Moreover, there is no approved installation or design specification for this type of pipe so far. Table 1.1 shows the comparison of corrugated steel, HDPE, and SRHDPE pipes based on the installation and design requirements.

**TABLE 1.1**  
**Comparisons of Corrugated Steel, HDPE, and SRHDPE Pipe**

<b>Material</b>	<b>Corrugated steel pipe</b>	<b>HDPE pipe</b>	<b>SRHDPE pipe</b>
<b>Applicable material specification</b>	ASTM A885, AASHTO-M36	ASTM F 2306, AASHTO M 294	ASTM F 2562
<b>Significant material requirement</b>	Dimensions and properties of pipe cross-sections (mechanical and chemical requirements and minimum seam strength) should be as per specifications.	Virgin resins must be used. Cell class 434400C  Material must have ability to withstand stress cracking	Vertically placed thin metals (helically) encapsulated by HDPE plastic
<b>Installation specification</b>	ASTM A 798, AASHTO LRFD Bridge Construction Specifications (Section 26) (1998)	ASTM D 2321, AASHTO LRFD Bridge Construction Specifications (Section 30) (2010)	Do not exist
<b>Design Specification</b>	ASTM A796, AASHTO LRFD Bridge Design Specification (Section 12.7) (2007)	ASTM A796, AASHTO LRFD Bridge Design Specification (Section 12.12) (2007)	Do not exist
<b>Trench width</b>	The ASTM C 789 standard and the 1998 AASHTO LRFD Bridge Construction Specifications (Section 26) state minimum trench width = outer diameter, plus sufficient room for compaction equipment.	The 2010 AASHTO LRFD Bridge Construction Specifications (Section 30) states minimum trench width = 1.5 times outer diameter +12 in.	No nationally approved installation or design specification. Research indicates that deflection limits will be significantly lower than conventional HDPE pipes.

(Source: <http://www.concrete-pipe.org/pdf/InstallationComparisonInspectorsContractors.pdf>)



**TABLE 1.1 (Continued)**  
**Comparisons of Corrugated Steel, HDPE, and SRHDPE Pipe**

<b>Material</b>	<b>Corrugated steel pipe</b>	<b>HDPE pipe</b>	<b>SRHDPE pipe</b>
<b>Foundation and trench wall support</b>	<p>Foundation: Moderately firm to hard in-situ soil or stabilized soil or compacted material.</p> <p>In-situ soil at foundation and trench walls should be strong enough to support pipe and compaction of embedment materials.</p>	<p>Moderately firm to hard in-situ soil or stabilized soil or stabilized soil or compacted material.</p> <p>In-situ foundation and trench wall soil should be strong enough to support pipe and compaction of embedment materials.</p> <p>Confirmation of strength of foundation at 90-95% standard Proctor compaction</p>	
<b>Bedding materials</b>	<p>Uniform support and grade.</p> <p>No compaction directly under pipe</p>	<p>Uniform support and grade.</p> <p>Coarse-grained soils</p> <p>Thickness of normal earth foundation: minimum 4 in.</p> <p>In rock, thickness: minimum 6 in.</p> <p>No compaction directly under pipe</p>	
<b>Haunch materials</b>	<p>Haunch materials provide structural strength of flexible pipe/soil system.</p> <p>Materials same as used in bedding zone.</p> <p>Place materials in by hand. 90% minimum compaction</p>	<p>Haunch materials provide majority of structural strength of flexible pipe/soil system.</p> <p>Materials same as used in bedding zone.</p> <p>Place materials in by hand Place in 6 in. lifts. 90% minimum compaction (per section 30)</p>	

(Source: <http://www.concrete-pipe.org/pdf/InstallationComparisonInspectorsContractors.pdf>)

**TABLE 1.1 (Continued)**  
**Comparisons of Corrugated Steel, HDPE, and SRHDPE Pipe**

<b>Material</b>	<b>Corrugated steel pipe</b>	<b>HDPE pipe</b>	<b>SRHDPE pipe</b>
<b>Embedment Materials</b>	<p>Compact to required density in 6 to 12 in. lifts up to a diameter of a pipe/8, or 12 in. above top of a pipe according to installation types.</p> <p>Usually requires imported/selected material.</p>	<p>Compaction to required density in 6in. lifts to 12 in. above top of a pipe.</p> <p>Removal of trench box must not allow movement of compacted material.</p> <p>Usually requires imported select material.</p>	
<b>Inspection techniques</b>	<p>The 1998 AASHTO LRFD Bridge Construction Specifications (Section 26) limits the deflection of pipe: Deflection <math>\leq 5\%</math> (acceptable)</p>	<p>The 2010 AASHTO LRFD Bridge Construction Specifications (Section 30.5.6) limits the deflection of pipe: Deflection <math>\leq 5\%</math> (acceptable)</p>	

(Source: <http://www.concrete-pipe.org/pdf/InstallationComparisonInspectorsContractors.pdf>)

### 1.3 Research Objective

The objective of this research was to evaluate short-term and long-term properties of the SRHDPE pipe. The effects of the SRHDPE properties on the load transfer mechanism were investigated during the installation and service under static and cyclic loading by large-scale plate loading tests on the buried pipe. The pipe was buried in a trench with a shallow cover. The cyclic loading was to simulate a traffic loading. The data obtained from the tests was used to establish a design procedure for the SRHDPE pipe during the installation and service.

### 1.4 Research Methodology

The research methodology adopted for this research includes: (1) a literature review on different theories and design methods from early age to current practice for predicting structural performance of both rigid and flexible buried pipes, (2) tests conducted to evaluate the short-term and long-term properties of the SRHDPE pipe in air, (3) large-scale box tests on the SRHDPE pipe to evaluate the performance during installation and service under static and cyclic

loading, and (4) establishment of a design procedure for SRHDPE pipes during the installation and service. The pipe property tests and large-scale box tests were conducted at the Department of Civil, Environmental, and Architectural Engineering in the University of Kansas (KU).

## **1.5 Organization of Report**

This report is organized in five chapters. Chapter One presents an introduction including the background, problem statement, research objective, and research methodology. Chapter Two is a detailed literature review on backfill materials, laboratory and field works, theories, and design methods from early age to current practice for predicting structural performance of buried pipes both rigid and flexible. Chapter Three describes the properties of all materials used in large-scale box tests. Chapter Four provides detailed construction procedures of the test sections and instrumentations. The data analysis and the test results are presented in Chapter Five. Chapter Six provides the summary of test results and conclusions obtained from this research and recommendations for future study.

## Chapter 2: Literature Review

This section presents a review of past studies on the structural performance of both rigid and flexible buried pipes as applicable to the research objective. It reviews important and pertinent theories and design methods, from inception to current practice, for predicting structural performance of buried pipes. A summary of both laboratory and field tests pertinent to those design theories is included. The literature review also discusses the studies that have been conducted to examine the performance of the Steel-Reinforced High Density Polyethylene (SRHDPE) pipes.

### 2.1 Loads on Pipes

Marston (1913) and Marston (1930) proposed the theory to calculate the loads on the top of rigid and flexible pipes. The Marston theory is applied to rigid pipes for both trench and embankment conditions whereas the Marston theory is applied to flexible pipes only for embankment conditions. The theoretical basis for the Marston trench load is the soil friction at the trench walls that is indifferent to the type of pipe. Therefore, there are some arguments for the use of the Marston trench load on a flexible pipe design in the United States (Schrock 1993).

For a metal pipe, the 2007 AASHTO LRFD Bridge Design Specifications considers the load on the pipe due to the weight of a soil column above the pipe. For concrete and thermoplastic pipes, the 2007 AASHTO LRFD Bridge Design Specifications expresses the load ( $W$ ) on the pipes under typical embankment conditions as the product of the soil column load ( $W_{sp} = \gamma_s H$ ) and the vertical arching factor (VAF) as follows:

$$W = \text{VAF} \times W_{sp}$$

Equation 2.1

The vertical arching factor (VAF) depends on the ratio of the stiffness of soil at the sides of a pipe to the pipe stiffness. If the soil stiffness is higher than the pipe stiffness, the VAF is less than 1.0 (i.e., the load on the pipe is decreased). If the soil stiffness is less than the pipe stiffness, the VAF is less than 1.0 (i.e., the load on the pipe is increased). The VAF for a concrete pipe is presented in the 2007 AASHTO LRFD Bridge Design Specifications. The vertical arching

factors (VAFs) for flexible pipes can be calculated using the simplified Equation 2.2 to 2.4 proposed by McGrath (1998) based on Burns and Richard (1964):

For a fully-bonded interface between pipe and soil,

$$VAF = 1.06 - 0.96 \left( \frac{S_H - 0.7}{S_H + 1.75} \right) \quad \text{Equation 2.2}$$

For a free-slip interface,

$$VAF = 0.76 - 0.71 \left( \frac{S_H - 0.7}{S_H + 1.75} \right) \quad \text{Equation 2.3}$$

$$S_H = \frac{M_s}{EA/R} \quad \text{Equation 2.4}$$

where  $S_H$  = the hoop stiffness parameter,  $M_s$  = the constrained modulus of elasticity of soil (to be discussed in **SECTION 2.4.2**),  $E$  = Young's modulus of elasticity of the pipe material,  $A$  = the wall cross-sectional area of the pipe, and  $R$  = the radius of the pipe.

The method proposed by McGrath (1998) has been incorporated into the 2000 AASHTO LRFD Bridge Design Specifications for the design of a thermoplastic pipe. The load ( $W$ ) on a pipe due to a truck wheel can be estimated using a stress distribution method. The 1992 AASHTO LRFD Bridge Design Specifications considers the wheel load as a point load on the surface and distributes it on a square area of a width of 1.5 times the fill depth. More recently, the 2007 AASHTO LRFD Bridge Design Specifications considers the wheel load to be uniformly distributed over a tire contact area, which is projected by increasing the area by either 1.15 times the fill depth in select granular backfill or the fill depth in all other cases. Giroud and Han (2004) suggested an approximate solution for the vertical stress distribution angle from a base course to a subgrade based on Burmister's theoretical solution (Burmister 1958) as follows:

$$\tan \alpha_1 = \tan \alpha_o \left[ 1 + 0.204 \left( \frac{E_1}{E_2} - 1 \right) \right] \quad \text{Equation 2.5}$$

where  $\alpha_1$  = the stress distribution angle in the base coarse,  $\alpha_o$  = the reference stress distribution angle for a uniform medium defined by  $E_1=E_2$ ,  $E_1$  = the modulus of elasticity of base coarse, and  $E_2$  = the modulus of elasticity of subgrade. The reference distribution angle for a uniform medium was taken as  $27^\circ$  (i.e., 2:1 distribution).

## 2.2 Bedding and Backfill Materials

Bedding and backfilling are critical procedures for pipe installation for the satisfactory performance of pipes. Proper bedding and backfilling lead to the transfer of loads on a pipe to the bedding and surrounding soil. Based on a bedding type, bedding constant (k) was introduced in flexible pipe design (Goddard 1992). The bedding constant (k) versus the bedding angle is shown in Table 2.1.

**TABLE 2.1**  
**Variation of Bedding Constant (k) with Bedding Angle**

Bedding Angle (degrees)	Bedding Constant (K)
0	0.11
30	0.108
45	0.105
60	0.102
90	0.096
120	0.09
180	0.083

(Source: Goddard 1992)

The 2007 KDOT Pipe and Culvert Specifications considers the bedding thickness, quality of material, and compaction of bedding materials in buried pipe design. Backfill quality and compaction are the two most important factors in ensuring satisfactory performance of flexible pipes. For flexible pipes, a wide range of non-cohesive backfill materials are strongly preferred over other soils for ease of compaction, high earth pressure response from the side (i.e., springline), and stability of the pipes when backfill materials are saturated and confined.

However, other backfill materials, such as silty sand (SM) and clayed sand (SC), are acceptable for economic purposes under conditions where there are low to moderate loads (Molin 1981) and where high levels of compaction effort at the moisture content close to the optimum level to get the required percent compaction are obtainable (Roger 1985, ASTM A798, and ASTM D2321).

The low stiffness of flexible pipe can limit compaction effort of the backfill because of possible distortion and uplift of the pipe. The 2007 AASHTO LRFD Bridge Design Specifications requires a minimum pipe stiffness to reduce the distortion, and specifically for plastic pipe, also to reduce the strain in the pipe wall which is dependent on the pipe stiffness and the compaction effort. Over-compacted soil can limit lateral deformation of the pipe during loading so that the potential for pipe buckling in the vicinity of the crown is greatly increased (Cameron 2006). Initial deformation in flexible pipes is favorable if not excessive (Webb et al. 1996). Roger et al. (1996), as cited by Cameron (2006), addressed the non-symmetric distortion of the pipe created by filling sand to one side of the pipe first before filling the other side rather than bringing up both levels simultaneously. The ratio of the profile/rib clear spacing of corrugated profile pipes or rib wall plastic pipes to the maximum size of the backfill material should be less than 0.6 or larger than 2.6 to prevent the development of loose void spaces around the pipes (Sargand et al. 1996). According to the 2007 AASHTO LRFD Bridge Design Specifications, the maximum particle size of a bedding material should be 1.25 inches.

Small trench width for pipe embedment is adequate if the in-situ soil is stiffer than the backfill material (Howard 1997), but the compaction effort is restricted by the geometry of the trench and the sensitivity of the installed flexible pipe to compaction of the backfill. According to the 2007 Kansas Department of Transportation (KDOT) specification for pipes and culverts, a trench should have a minimum width equal to 12 inches plus 1.5 times the diameter of the pipe.

## **2.3 Minimum Soil Cover Requirements**

With a thin soil cover, the pipe will experience high stress concentrations at the crown, which may cause collapse of the pipe. Therefore, precautions should be taken when designing shallow installations under roadways. Table 2.2 shows the 2007 KDOT Pipe and Culvert specifications requirement for the minimum cover over the top of a pipe. Katona (1990)

proposed an empirical relationship for the determination of the minimum soil cover thickness by ignoring the contribution of the pavement thickness under various standard AASHTO truck loadings.

**TABLE 2.2**  
**Minimum Cover over the Top of the Pipe**

PE and PVC size (inches)	Axle Load (kips)			
	18 to 50	50 to 75	75-110	110 to 150
	Soil Cover (feet)			
12 to 36	2.0	2.5	3.0	3.0
42 to 48	3.0	3.0	3.5	4.0
54 to 60	3.0	3.0	3.5	4.0

(Source: KDOT 2007)

## 2.4 Deflection

Flexible pipes are designed to transmit the load on the pipe to the soil at the sides of the pipe. As the load on the pipe increases, the vertical diameter decreases and the horizontal diameter increases. The increase in the horizontal diameter is resisted by the soil at the sides of the pipe. The cross-sectional ring and soil section deflect according to the ratio of the load on the ring to the modulus of elasticity of the pipe-soil system. The overall material modulus is complicated by the pipe, soil, and soil-structure interaction in buried systems. The material modulus becomes a combination of the structural modulus (stiffness) of the pipe and the modulus (stiffness) of the soil (Spangler 1941). Therefore,

$$deflection = \frac{soil\ load}{pipe\ stiffness + soil\ stiffness} \quad \text{Equation 2.6}$$

Spangler (1941) incorporated the effects of the surrounding soil on the pipe deflection and derived the Iowa formula (Equation 2.7) to determine the deflection of a flexible pipe:

$$\Delta X = \frac{D_L k W R^3}{E I + 0.061 e R^4} \quad \text{Equation 2.7}$$



where  $D_L$  = the deflection lag factor,  $k$  = the bedding constant (presented in Table 2.1),  $W$  = Marston's load per unit length of the pipe,  $R$  = the mean radius of the pipe,  $e$  = the modulus of passive resistance of side fill, and  $\Delta X$  = the horizontal deflection or change in diameter. Spangler (1941) developed the Iowa formula for predicting the deflection of a flexible pipe (i.e., corrugated steel pipe or CSP). The 5% vertical deflection of the pipe diameter was an early-developed limit state for a CSP.

Watkins and Spangler (1958) determined that “ $e$ ” could not possibly be a true modulus of passive resistance. A new soil parameter, the modulus of soil reaction  $E' = e \times R$ , was defined, and the Iowa formula was modified for the prediction of the horizontal deflection ( $\Delta X$ ) as follows:

$$\Delta X = \frac{D_L k W}{0.149 PS + 0.061 E'} \quad \text{Equation 2.8}$$

$$E' = \frac{\frac{P_h}{\Delta X}}{\frac{D}{D}} \quad \text{Equation 2.9}$$

where  $PS$  = the pipe stiffness (to be discussed in Section 2.4.1),  $P_h$  = the pressure at the side of a pipe caused by forcing the side of the pipe into the backfill, and  $D$  = the diameter of the pipe.

Howard (1981) proposed an empirical USBR (United States Department of the Interior: Bureau of Reclamation) equation as follows to predict the vertical deflection ( $\Delta Y$ ) of a buried flexible pipe based on back-calculated parameters from the field installations:

$$\Delta Y(\%) = T_f \left[ \frac{0.07 \gamma H}{E I / R^3 + S_f D_f} + C_f \right] + I_f \quad \text{Equation 2.10}$$

where  $T_f$  = the time-lag factor (dimensionless, 0.07 was suggested),  $\gamma$  = the backfill unit weight,  $E I / R^3$  = the pipe stiffness,  $S_f$  = the soil stiffness factor,  $C_f$  = the construction factor,

percent vertical deflection,  $I_f$  = the inspection factor, percent vertical deflection, and  $D_f$  = the design factor (dimensionless) and values were given for three cases A, B, and C. Case A was used for comparing actual deflections against calculated theoretical deflections. Case B was used when desired deflections were equal to or less than the theoretical deflection plus 0.5% deflection. Case C was used when the deflection is a critical for a pipe design.

Equation 2.10 has several features that are improved from the Iowa formula such as the prediction of the deflection immediately after backfilling, the prediction of the long-term deflection based on the initial deflection and the design factors depending on the needs of the user and the soil stiffness factor ( $S_f$ ) rather than the modulus of soil reaction. The parameters used in the USBR equation are listed in Table 2.3. This method should only be used when the depth of cover is less than 50 ft and the trench wall support is as good as or better than the pipe bedding.

**TABLE 2.3**  
**Parameters for the USBR Equation**

Bedding Soil Classification (USCS)	Degree of Compaction**			
	Dumped	Slight < 85% P <40% RD	Moderate 80- 95% P 40-70% RD	High >95% P >70% RD
<u>Highly compressible fine-grained soils</u> CH, MH, OH, OL	Soils with medium to high plasticity or with significant organic content. No data available.			
<u>Fine-grained soils</u> Soils with medium to no plasticity with less than 25% coarse-grained particles CL, ML, CL-ML	$S_f = 3$ $T_f = 1.5^*$ $C_f = 2.0$ $D_f$ for $A=1.0$ $B=0.5$ $C=0.3$	$S_f = 12$ $T_f = 2^*$ $C_f = 2.0$ $D_f$ for $A=1.0$ $B=0.5$ $C=0.3$	$S_f = 24$ $T_f = 2.5^*$ $C_f = 1.5$ $D_f$ for $A=1.0$ $B=0.67$ $C=0.5$	$S_f = 100$ $T_f = 2.5^*$ $C_f = 1.5$ $D_f$ for $A=1.0$ $B=0.75$ $C=0.67$
<u>Sandy or gravelly fine grained soils</u> soils with medium to no plasticity with more than 25% coarse-grained particles CL, ML, CL-ML <u>Coarse -grained soils with fines</u> Sands, gravels with more than 12% fines GM, GC,SM, SC	$S_f = 10$ $T_f = 1.5^*$ $C_f = 2.0$ $D_f$ for $A=1.0$ $B=0.5$ $C=0.3$	$S_f = 24$ $T_f = 2.0^*$ $C_f = 2.0$ $D_f$ for $A=1.0$ $B=0.5$ $C=0.3$	$S_f = 60$ $T_f = 2.5^*$ $C_f = 1.5$ $D_f$ for $A=1.0$ $B=0.67$ $C=0.5$	$S_f = 150$ $T_f = 2.5^*$ $C_f = 1.0$ $D_f$ for $A=1.0$ $B=0.75$ $C=0.67$
<u>Clean Coarse grained soils</u> Sands, gravels with less than 12% fines GW, GP, SW, SP or any soil beginning with one of these symbols (i.e., GP-GM)	$S_f = 12$ $T_f = 1.5$ $C_f = 2.0$ $D_f$ for $A=1.0$ $B=0.67$ $C=0.5$	$S_f = 40$ $T_f = 2.0$ $C_f = 2.0$ $D_f$ for $A=1.0$ $B=0.67$ $C=0.5$	$S_f = 120$ $T_f = 2.5$ $C_f = 1.0$ $D_f$ for $A=1.0$ $B=0.75$ $C=0.67$	$S_f = 200$ $T_f = 2.5$ $C_f = 0.5$ $D_f$ for $A=1.0$ $B=1.0$ $C=0.75$
<u>Crushed rock</u>	$S_f = 60$ $T_f = 2.0$ $C_f = 1.0$ $D_f$ for $A = 1.0$ $B = 0.67$ $C = 0.5$		$S_f = 200$ $T_f = 3.0$ $C_f = 0.5$ $D_f$ for $A=1.0$ $B=1.0$ $C=0.75$	

\*Double  $T_f$  value if bedding will become saturated.

\*\* %P = % of standard Proctor maximum dry density and %RD = % relative density.  
(Source: Howard, 1981)

During the initial backfilling, the flexible pipe deforms into a shape similar to a vertical ellipse (McGrath et al. 1998). This so called “peaking behavior” due to lateral force generated by

the compactor and the mass of the backfill placed on both sides of the pipe can be predicted by Equation 2.11 developed by Masada and Sargand (2007). The peaking behavior continues until the backfill reaches the crown of the pipe.

$$\frac{\Delta y}{D} = \frac{4.7P_c + K_o\gamma_s R}{3.874PS} \quad \text{Equation 2.11}$$

where  $P_c$  = the pressure generated by the compaction efforts (shown in Table 2.4),  $K_o = 1 - \sin\phi_s$ ,  $\phi_s$  = the internal friction angle of granular backfill soil,  $\gamma_s$  = the unit weight of the backfill soil,  $R$  = the radius of the pipe,  $D$  = the diameter of the pipe, and  $PS$  = the pipe stiffness.

**TABLE 2.4**  
**Pressure Generated by Compaction Efforts**

<b>Backfill Soil Type</b>	<b>Pressure <math>P_c</math> (psi/in.) generated by</b>	
	<b>Vibratory plate</b>	<b>Rammer</b>
Sand	0.03	0.39
Crushed stone	0.06	0.80

(Source: McGrath et al. 1999 as cited by Masada and Sargand 2007)

#### *2.4.1 Estimation of the Pipe Stiffness (PS)*

The parallel plate test (ASTM D2412-02) is a standardized test to ensure that the bending stiffness and strength of the thermoplastic pipe meet specified levels of performance. For the SRHDPE pipe, the ASTM Standard F2562/F2562M applies specifically. The parallel plate load test does not guarantee successful field performance; however, the AASHTO M294-07 specification and KDOT use this test to verify that corrugated HDPE pipes have minimum pipe stiffness at 5% deflection to pipe diameter, and no buckling or loss of load before 20% deflection. The stiffness criterion at 5% deflection to pipe diameter is important for handling and installation of pipes, while the 20% deflection criterion provides necessary ultimate load

capacity. The parallel plate load test also ensures that the pipe generally maintains its elliptical shape and that the basic design assumptions as asserted by the Iowa formula and other design methods are appropriate. The pipe stiffness can be obtained by dividing the force ( $F$ ) per unit length of a pipe specimen by the resulted deflection ( $\Delta Y$ ) at the prescribed percentage deflection (Figure 2.1a):

$$\text{Pipe stiffness (PS)} = \frac{F}{\Delta Y} \quad \text{Equation 2.12}$$

The stiffness factor ( $EI$ ) is the product of pipe stiffness (PS) and the quantity  $0.149R^3$  (Timoshenko and Gere 1961).

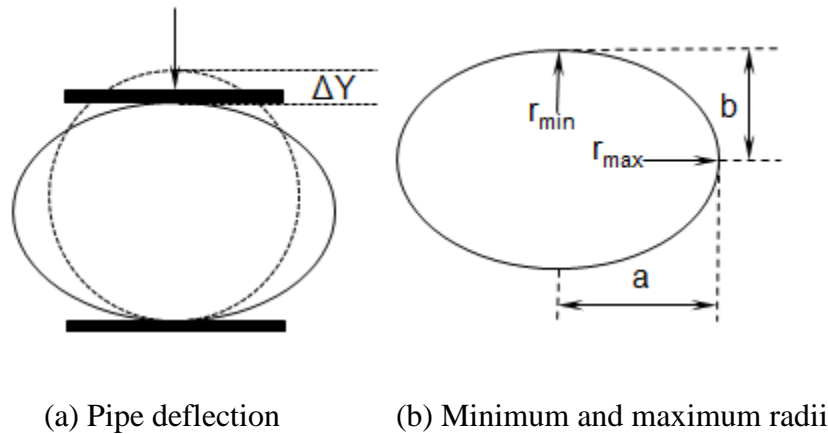


**FIGURE 2.1**  
**Pipe Deflection and Radii of Curvature of a Deflected**  
**Ellipse Shape**

Equation 2.13 can be used to calculate the moment at any point along the cross-section in a deformed pipe based on its elastic behavior:

$$M = EI \left( \frac{1}{R_i} - \frac{1}{R_0} \right) \quad \text{Equation 2.13}$$

where  $R_o$  = the original radius of the pipe section before loading and  $R_i$  = the radius of the pipe cross-section at the point where the moment is to be determined after deformation under a load. The moments at the crown and the springline of the pipe are calculated using the maximum and minimum radii of the pipe cross-section,  $R_{max} = a^2/b$  and  $R_{min} = b^2/a$ , respectively in which 'a' is the major semi diameter and 'b' is the minor semi diameter of the elliptical section (Figure 2.1b). The bending stress ( $\sigma_b$ ) is calculated using the bending equation,  $\sigma_b = M/S$ , where S= is the section modulus at the location where the moment (M) is applied.

#### *2.4.2 Estimation of the Modulus of Soil Reaction (E')*

Since the pipe stiffness (PS) for flexible pipes is 0.8 to 4.25 percent of the soil modulus (E') in most cases, the ring stiffness factor has little influence on the deflection of pipes in comparison with the soil stiffness factor (Watkins et al. 1973). E' is a pipe-soil interaction modulus, which is a semi-empirical constant, rather than a soil modulus alone. A table of E' values as shown in Table 2.5 was developed by Howard (1977) to predict initial deflections of buried flexible pipes at a depth of up to 50 ft. Hartley and Duncan (1987) calculated E' based on empirical deflection equations using the field data, the elastic solution based on the constrained soil modulus ( $M_s$ ), and a finite element computer program. Based on these three approaches, Hartley and Duncan (1987) found that E' was also a function of depth and recommended sets of E' values in Table 2.6 for use in the Iowa Formula. Selig (1990) further presented E' values using a hyperbolic finite element technique. Moore (2001) reported on the research in the USA, which leads to a revised outlook on E' and its replacement with Young's modulus  $E_s$  (recognized to vary with the level of vertical stress).

**TABLE 2.5**  
**Typical Values of E' (psi)**

Unified Soil Classification System (USCS)	Degree of Compaction	Dumped	Slight	Moderate	High
	Level of Standard Compaction		<sup>1</sup> R <sub>D</sub> <85 %	R <sub>D</sub> = 85-95%	R <sub>D</sub> > 95%
	Density Index		<sup>2</sup> I <sub>D</sub> < 40%	I <sub>D</sub> = 40 - 70%	I <sub>D</sub> > 70%
	Coarse\Fines				
CH, MH or CH-MH (Liquid limit> 50%)	< 25% coarse	43.5	203.0	406.0	1000.5
CL, ML or CL-ML (Liquid limit< 50%)	>25% coarse	101.5	406.0	1000.5	2001.0
GM, GC, SM, SC	>12% fines	101.5	406.0	1000.5	2001.0
GW, GP,SW,SP	<12% fines	203.0	1000.5	2001.0	3001.5
Crushed Stone		1000.5	3001.5	3001.5	3000.5
Accuracy in terms of percent deflection <sup>3</sup>		±2%	±2%	±1%	±0.5%

<sup>1</sup>R<sub>D</sub> = dry density ratio (i.e., the ratio of target dry density to maximum dry density for the compactive effort)

<sup>2</sup>I<sub>D</sub> = density index (%) for a clean granular (coarse) material

<sup>3</sup> for ±1% accuracy and predicted deflection of 3%, actual deflection would be between 2 and 4%.

(Source: Howard 1977)

**TABLE 2.6**  
**Typical Values E' (psi)**

Type of soil	Depth of Cover (ft)	Standard ASSHTO Relative Compaction			
		85%	90%	95%	100%
Fine-grained soils with less than 25% sand content (CL, ML, CL-ML)	0-5	500	700	1000	1500
	5-10	600	1000	1400	2000
	10-15	700	1200	1600	2300
	15-20	800	1300	1800	2600
Coarse-grained soils with fines (SM, SC)	0-5	600	1000	1200	1900
	5-10	900	1400	1800	2700
	10-15	1000	1500	2100	3200
	15-20	1100	1600	2400	3700
Coarse-grained soils with little or no fines (SP, SW, GP, GW)	0-5	700	1000	1600	2500
	5-10	1000	1500	2200	3300
	10-15	1050	1600	2400	3600
	15-20	1100	1700	2500	3800

(Source: Hartley and Duncan 1978)

The above  $E'$  values were obtained by back calculations. Krizek (1971) suggested replacing  $E'$  in the Iowa formula with the constrained modulus ( $M_s$ ), which is a more basic soil property and define soil-structure response. Neilson (1967) simplified the Burns and Richard (1964) elastic solutions with the following approximation:

$$E' = 1.5 M_s \quad \text{Equation 2.14}$$

$$M_s = \frac{E_s (1 - \nu_s)}{(1 + \nu_s) (1 - 2\nu_s)} \quad \text{Equation 2.15}$$

where  $M_s$  = the constrained modulus of elasticity,  $E_s$  = the soil modulus of elasticity, and  $\nu_s$  = the Poisson's ratio of soil.

For trench conditions, the backfill takes the applied load at the springline and transfers the load to the natural soil through the trench walls. The performance of the backfill material is also influenced by the resistance from the natural soil. The influence of the natural soil forming the trench walls on the lateral soil support has been addressed by Leonhardt, as cited by Cameron et al. (2006), who introduced the Leonhardt correction factor,  $\Omega$  (Equation 2.16) based on the modulus of soil reaction,  $E'$  as defined in the Iowa formula (Equation 2.8). The effective side-fill stiffness is given by the product of the modulus of soil reaction  $E'$  and the correction factor  $\Omega$ .

$$\Omega = \frac{1.662 + 0.639 (B/D - 1)}{(B/D - 1) + [1.662 - 0.361 (B/D - 1)] E' / E_N} \quad \text{Equation 2.16}$$

where  $E_N$  = the Young's modulus of the natural soil forming the trench wall,  $B$  = the width of the trench, and  $D$  = the pipe diameter.

When  $E'$  is much less than  $E_N$ , the trench walls are considered rigid. If the ratio of the trench width to the pipe diameter is 2, the effective modulus for the pipe support is 2.3 times  $E'$ . As  $E'$  approaches the value of  $E_N$ ,  $\Omega$  is reduced. Less influence is apparent for a wider trench and the correlation factor may be ignored for a trench width to pipe diameter ratio of 5 or greater (Cameron et al. 2006).



## 2.5 Pipe Thrust and Buckling

White and Layer (1960) proposed the compression ring theory, in which corrugated steel pipes could be designed by checking the wall strength for the possible yielding of the wall material against the weight of the soil prism above the pipe, given that standard pipe wall profiles and a uniform compacted backfill were used in the design of the pipe-soil system. Arching action was not considered by this design method. In addition, the deflection of the pipe was to be well within the standard limit of 5%.

Watkins (1960) indicated that during experiments and under some soil and pipe conditions, the pipes did buckle before a 5% vertical deflection was reached. Watkins (1960) investigated the buckling condition for the flexible pipes by running a series of tests and modifying the backfill density and stiffness, and the pipe flexibility. From his investigation, he determined that the tendency of a pipe to buckle or yield due to thrust was a function of the pipe flexibility and the soil stiffness. Meyerhof and Baikie (1963) conducted tests on curved plates in contact with sand backfill. They found similarly that buckling was a function of the pipe flexibility and the soil stiffness, which was quantified by the parameter  $k_b$ , the coefficient of soil reaction. Based on the pipe flexibility and the soil stiffness, Watkins (1966) and (1971) showed that the pipe had a wall yielding zone and a buckling zone, with a “difficult to define” transition zone between these two zones. This result confirmed White and Layer’s compression ring theory for conditions with adequate pipe and soil stiffness (1960). The transition zone between the buckling and yielding zones is complex because of the variations in the pipe sections, the pipe materials, and the soil backfill.

The ASTM A796 standard and the 2007 AASHTO LRFD Bridge Design Specifications (Section 12.7) suggest the critical buckling stress ( $f_{cr}$ ) for corrugated steel pipes as follows:

$$\text{If } D < \frac{r}{k} \sqrt{\frac{24E}{f_u}}, f_{cr} = f_u - \frac{f_u^2}{48E} \left( \frac{\psi_s D}{r} \right)^2 \quad \text{Equation 2.17}$$

$$\text{If } D > \frac{r}{k} \sqrt{\frac{24E}{f_u}}, f_{cr} = \frac{12E}{\left( \frac{\psi_s D}{r} \right)^2} \quad \text{Equation 2.18}$$

where  $D$  = the pipe diameter,  $r$  = the radius of gyration of corrugation,  $E$  = the modulus of elasticity of the pipe material,  $\psi_s$  = the soil stiffness factor, and  $f_u$  = the specified minimum tensile strength

Moser (2008) recommended either of two Equations 2.19 and 2.20 for the critical buckling stresses of circular pipes. These two equations work well for metal pipes but they are conservative for plastic pipes. The 2007 AASHTO LRFD Bridge Design Specifications also specifies the critical buckling stress ( $f_{cr}$ ) for an HDPE pipe, which is determined by Equation 2.21:

$$f_{cr} = 2 \times \sqrt{\frac{E'}{1-\nu^2} \times \frac{EI}{R^3}} \quad \text{Equation 2.19}$$

$$f_{cr} = 1.15 \times \sqrt{\frac{2EE'}{1-\nu^2} \times \left(\frac{t}{D}\right)^3} \quad \text{Equation 2.20}$$

$$f_{cr} = 9.24 \frac{R}{A_{eff}} \sqrt{B' R_w \psi_s M_s \frac{EI}{0.149 R^3}} \quad \text{Equation 2.21}$$

where  $R$  = the radius to centroid of a pipe wall,  $A_{eff}$  = the effective wall area,  $\psi_s$  = the factor for soil stiffness (0.9), and  $E$  = the modulus of elasticity.

## 2.6 Profile Wall Pipes and Local Buckling

The corrugated or profile walls are formed by decentralizing the material from the pipe wall to provide higher pipe stiffness. The structural efficiency of the profile wall pipe is obtained by making wall sections deep enough with as little area as possible (i.e., the pipe wall elements are thinned as much as possible). Since a properly installed flexible pipe carries stresses largely in compression, the thin pipe wall elements are susceptible to instability in compression, or local buckling. High compressive strains developing across pipe sections may cause local buckling on various components of the profile at a stress lower than the full yield strength of the pipe wall

material. Local buckling can compromise the integrity of a pipe. Bryan (1891) introduced the critical buckling stress equation of plates:

$$\sigma_{cr} = \frac{k_b \pi^2 E}{12(1-\nu^2) \left(\frac{w}{t}\right)^2} \quad \text{Equation 2.22}$$

where  $k_b$  = buckling coefficient,  $E$  = modulus of elasticity,  $w$  = plate width,  $t$  = plate thickness, and  $\nu$  = Poisson's ratio.

The strength of a plate or a plate element in a built-up section can be limited by its critical buckling stress like the Euler column buckling, which is not a function of the material strength but the plate's dimensions and boundary conditions. The buckling coefficient  $k_b$  is a function of the boundary conditions of the plate, the width to thickness ratio of the plate, and the length of the plate. For most applications, the length of element is assumed relatively long, and the coefficient  $k_b$  becomes a function of the boundary conditions only. The coefficient  $k_b$  is then presented as a numeric value for the boundary conditions. If the critical buckling stress is reached before the yield strength, the plate will buckle.

It is recognized that although an individual element of a section may buckle, the structural section does not fail, but continues performing with a post-buckled strength. Von Karman (1932) and Winter (1947) investigated the post-buckling strength of steel elements and introduced the concept of effective area. The effective area  $A_{eff}$  of a section can be determined by subtracting the ineffective area of each element from the gross section area using Equation 2.23. The effective width,  $b_e$ , of an element is obtained using an effective width factor  $\rho$  for Equations 2.24, 2.25, and 2.26. The effective area  $A_{eff}$  of the structural section is used to determine the limit states of the structural member, such as yielding due to thrust and or bending, or column buckling.

$$A_{eff} = A_g - \frac{\sum (w - b_e)t}{w} \quad \text{Equation 2.23}$$

$$b_e = \rho w \quad \text{Equation 2.24}$$

$$\rho = \frac{1 - \frac{0.22}{\lambda}}{\lambda} \quad \text{Equation 2.25}$$

$$\lambda = \left( \frac{w}{t} \right) \sqrt{\frac{\varepsilon_{yc}}{k_b}} \geq 0.673 \quad \text{Equation 2.26}$$

where  $\rho$  = effective width factor,  $\lambda$  = slenderness factor,  $w$  = plate width,  $t$  = thickness, and  $\varepsilon_{yc}$  = compressive strain limit

The potential for local buckling of the profile elements in the lined corrugated pipe has received attention since 1990s. Hashash and Selig (1990) and DiFrancesco (1993) observed ripples in the liner when they conducted field and laboratory tests on thin-wall HDPE pipes. Moore and Hu (1995) observed the three-dimensional response of a lined corrugated HDPE pipe in the hoop compression test. Moser (1998) concluded that local buckling was a critical performance limit in the tests conducted on profile-wall pipes. McGrath and Sagan (2001) proposed the stub compression test to assess local buckling capacity of profiled wall plastic pipes by modifying the American Iron and Steel Institute method used in cold-form steel design. The localized deformations were investigated for four commonly used pipe profiles (lined, corrugated, boxed, and tubular profiles) using the three-dimensional finite-element analysis (Dhar and Moore 2006). Among these profile pipes, local bending had the greatest effect on the stresses developed in the lined, corrugated profile.

## 2.7 Strain

Plastic materials offer a corrosive resistant, light weight, and moldable pipe material for pipe fabrication. The plastic material can also be easily molded into a variety of shapes improving strength with respect to area of the pipe wall. With the visco-elastic properties of the plastic, new limit states were incorporated into the pipe design. Because the modulus of the

plastic material changes with time, design methods may limit the allowable strain based on the short term and long term modulus of elasticity of the plastic, depending on load duration applied to the pipe. Strain developed in the pipe is calculated as the summation of the bending strains, ring compression strains, and strains due to the Poisson's effect. Carlstrom and Molin (1966) introduced a method to determine the bending strain in the extreme fiber of a pipe based on an elastic solution of strain as a function of pipe deflection and modified by the empirical placing factor  $D_f$ . The placing factor  $D_f$  was improved by Leonhardt (1978), Bishop and Lang (1984), and Turkopp et al. (1985) which accounts for variations in strain due to pipe/soil stiffness ratio, compaction effort, and non-uniform soil stiffness.

$$\varepsilon_b = D_f \left( \frac{t}{D} \right) \left( \frac{\Delta Y}{D} \right) \quad \text{Equation 2.27}$$

The strain due to thrust can be calculated based on the weight of the soil prism or the internal pressure on the pipe.

$$\varepsilon_r = \frac{P D}{2 A E} \quad \text{Equation 2.28}$$

where  $D_f$  = the shape factor,  $t$  = the minimum wall thickness,  $\Delta Y$  = the vertical decrease in diameter,  $D$  = the mean diameter,  $D_o$  = the outside diameter,  $P$  = the pressure on pipe,  $A$  = the area of the pipe wall, and  $E$  = the modulus of elasticity of the pipe material.

Moser (2008) presented a total combined circumferential strain of the non-pressure pipe as the sum of bending strain ( $\varepsilon_b$ ), ring compression strain ( $\varepsilon_r$ ), and Poisson's effect strain ( $\varepsilon_p$ ). The strain induced by the Poisson's effect is determined by:

$$\varepsilon_p = -\nu \times (\text{longitudinal strain}) \quad \text{Equation 2.29}$$

The 2007 AASHTO LRFD Bridge Design Specifications suggested the total factored combined compressive strain due to thrust ( $T_L$ ) and bending in the pipe wall,  $\varepsilon_c$ , as follows:

$$\varepsilon_c = \varepsilon_b + \frac{T_L}{A_{eff} E_{50}} \times \frac{\gamma_B}{\gamma_p} \leq \frac{1.5 F_u}{E_{50}} \quad \text{Equation 2.30}$$

This combined compressive strain should be less than the limiting combined compressive strain, which is given as follows:

$$\varepsilon_{b(max)} = \frac{1.5 F_u}{E_{50}} - \frac{T_L}{A_{eff} E_{50}} \times \frac{\gamma_B}{\gamma_p} \quad \text{Equation 2.31}$$

where  $\gamma_B$  = the modified factor applied to the combined factor (1.5),  $F_u$  = the long-term tensile strength of the pipe wall material,  $A_{eff}$  = the effective wall area,  $E_{50}$  = the long-term modulus of the pipe wall material, and  $\gamma_p$  = the maximum load factor. The total factored combined tensile strain in the pipe wall should also be less than the limiting combined tensile strain.

## 2.8 Existing Design Methods for Flexible Pipes

### 2.8.1 Metal Pipe

#### 2.8.1.1 AASHTO Method

In the 2007 AASHTO LRFD Bridge Design Specifications, metal pipes are evaluated for thrust and buckling in pipe wall. The thrust per unit length of wall of the pipe,  $T_L$ , is specified in Equation 2.32. Equation 2.17 and 2.18 are used to calculate the critical buckling stress ( $f_{cr}$ ) for metal pipes. The seam resistance of the longitudinal seams should resist the thrust in corrugated steel pipes.

$$T_L = p_f \frac{D_o}{2} \quad \text{Equation 2.32}$$

where  $D_o$  = the outside diameter and  $P_f$  = the factored vertical crown pressure.

## 2.8.2 Plastic Pipes

The design of plastic pipes includes:

1. Pipe deflection
2. Local buckling
3. Pipe wall strain

### 2.8.2.1 AASHTO Method

In the 2007 AASHTO LRFD Bridge Design Specifications, plastic pipes are evaluated for deflection, local buckling, and strain in the pipe wall. The deflection is evaluated using the modified Iowa formula (Equation 2.8). The thrust per unit length of wall of the pipe,  $T_L$ , is specified in Equation 2.32. The area of a profile wall is reduced to an effective area  $A_{eff}$  (see Equation 2.23) for buckling effects to evaluate the resistance to axial thrust. The result of the stub compression test, AASHTO T 341, is also used to evaluate the effective area. The critical buckling stress ( $f_{cr}$ ) for a plastic pipe is calculated using Equation 2.21. The strains developed on plastic pipes are evaluated using Equation 2.30.

### 2.8.2.2 Chambers et al. (1980)

Chambers et al. (1980) investigated buried plastic pipes and proposed a design procedure based on pipe deflection, critical strain level, and critical buckling pressure. A modified Iowa formula (Equation 2.8) is used to determine the deflection due to the soil load, traffic load, and installation. The critical wall buckling is obtained using the following equation:

$$f_{cr} = C_B C_D \sqrt{E'(PS_v)} \quad \text{Equation 2.33}$$

where  $C_B$  = the coefficient of buckling (0.5 for earth load and 0.07 for wheel load),  $C_D$  = the correction factor to account for deflection 1.5, and  $PS_v = PS_o$  (short-term pipe stiffness for a wheel load) or  $PS_v = PS_{10}$  (10-year pipe stiffness for earth load).

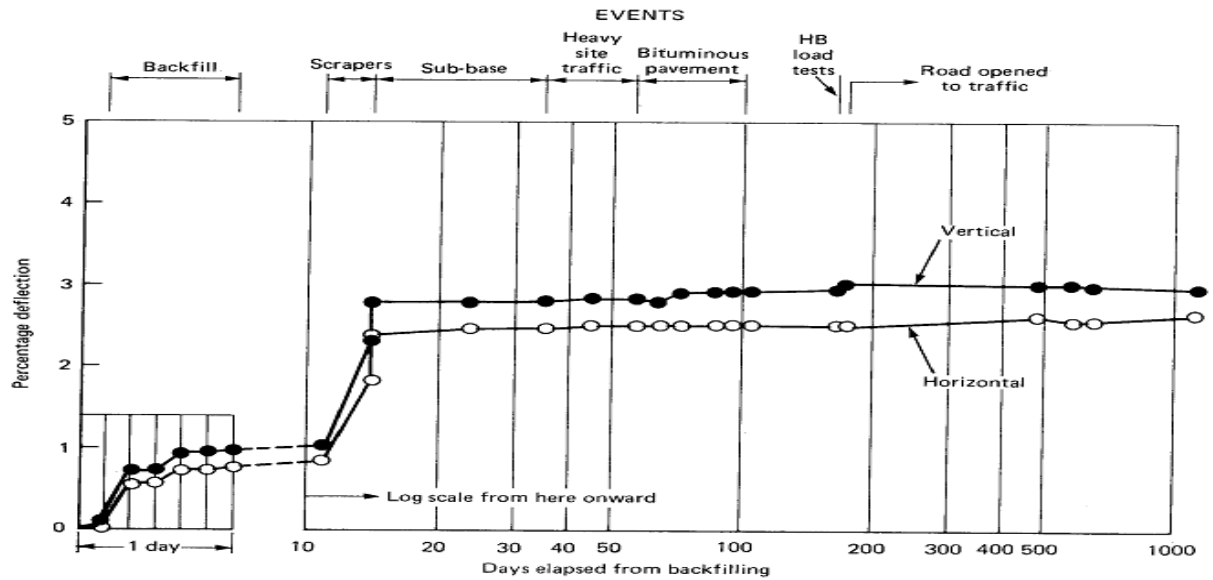
## 2.9 Performance of Pipes under Traffic Loads

The existing design methods for flexible pipes described in Section 2.8, no matter whether they were developed from empirical or theoretical bases, deal with the loads on buried flexible pipes as a result of static loading. This condition often exists for pipes buried in field (or under embankments), where the applied load is the dead weight of the trench fill (or embankment) above the pipe. However, these methods are not valid for flexible pipes installed at shallower depths under temporary or permanent pavement structures used by heavy vehicles. To date there has been very little investigation of the performance of buried flexible pipes under repeated loading.

### *2.9.1 Field Tests*

A field study was undertaken in the United Kingdom (Trott and Gaunt 1976) to monitor the deformations of flexible pipes laid in a trench beneath a highway. Performance of the pipes was monitored during installation and highway construction under pre-service load testing and followed with the opening of the highway. This research team confirmed that the greater part of the pipe deflections occurred within the first few heavy axle loads during the construction period, after which (when the road was opened to traffic) deflections rapidly stabilized as shown in **FIGURE 2.2**. In other words, the pipes approached a state of ring compression as opposed to the earlier “ring bending” during backfilling and passage of the scrapers. This finding was further supported by other field tests, for example, Faragher et al. (2000) and McGrath et al. (2002), and by laboratory tests, for example, Rogers et al. (1995), Faragher (1997), and Moghaddas Tafreshi and Khalaj (2008).





(Source: Trott and Gaunt 1976)

**FIGURE 2.2**  
**Percentage Deflection of the Unplasticized PVC Pipe in the Near Side Lane**

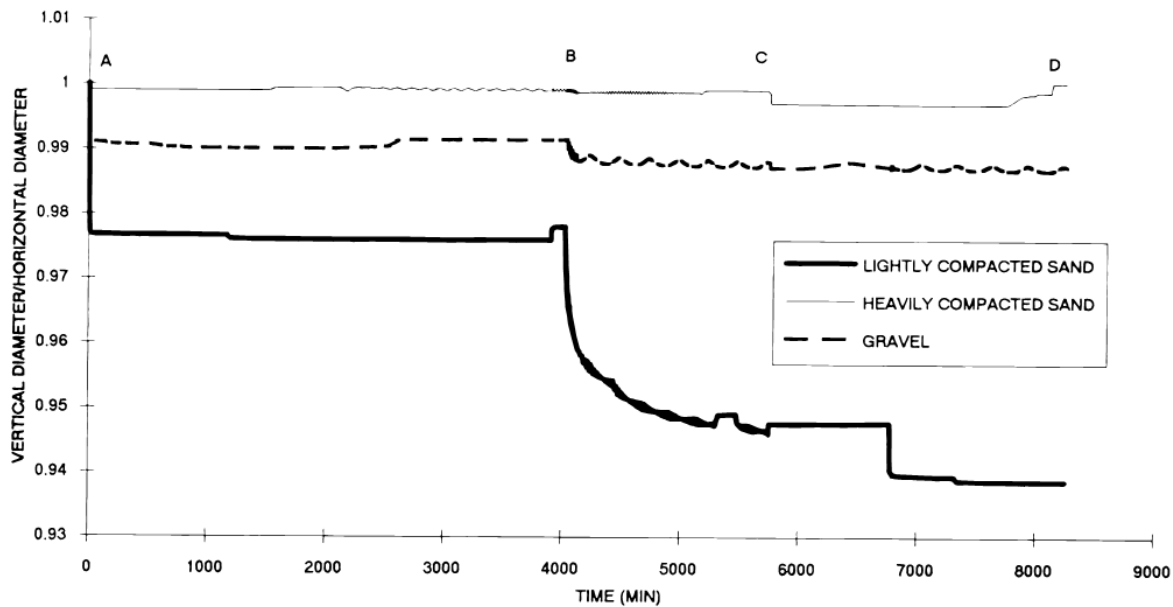
Faragher et al. (2000) carried out full-scale tests under real installation conditions to investigate the behavior of five flexible pipes of 24 inches in diameter and one flexible pipe of 42 inches in diameter buried in trenches under repeated loading. To predict the long-term pipe deformation (vertical deflection) from the initial loading cycles, power law curves were developed from the vertical deflection field data.

Arockiasamy et al. (2006) carried out totally thirty-six (36) field tests on large polyethylene, metal, and PVC pipes of 36 inches and 48 inches in diameters subjected to highway truck loading. Numerical simulations using a finite element method were also performed to determine pipe-soil interaction under live load applications. The field test results showed that the buried flexible pipes, embedded with highly compacted sand with silt, demonstrated good performance without exhibiting any visible joint opening or structural distress. A vertical deflection limit of 2% was suggested for HDPE pipes during the construction phase for highway applications.

### *2.9.2 Laboratory Tests*

Rogers et al.(1995) investigated twin-wall annular corrugated HDPE pipes with inside diameters, ranging from 4 to 14 inches, subjected to three different loads: (1) a uniform static vertical stress of 10 psi, to simulate a stationary heavy vehicle or a burial depth of approximately 13ft, (2) 1,000 cycles of 10 psi stress with 0.01 Hz frequency in a sinusoidal waveform, to simulate the heavy vehicle over a shallow buried pipe, and (3) a static stress of 20 psi, to simulate a burial depth of approximately 26ft. The applied pressure taken to simulate the heavy truck was the calculated pressure on the top of the pipe due to the stationary heavy vehicle on a pavement surface. The results showed that good performance could be achieved with plastic pipes when buried with care in a wide variety of pipe surrounding materials. In addition, the strain profiles indicated that the maximum tensile strains occurred at the pipe crown, whereas the distribution of strains around the circumference depended on the type of surrounding material and loadings.

Faragher (1997) conducted laboratory tests on 24 inch diameter plastic pipes. The pipes were buried to a cover depth of 3 ft 3 inches in lightly compacted sand, heavily compacted sand, and gravel backfills. The pipe was first subjected to 10 psi surcharge (static) stress and then to the repeated application of a surface stress of 10 psi, with a frequency of 0.01 Hz in a truncated sinusoidal waveform and plateaus at the maximum and minimum points. As a result, more rapid loading was achieved than that of a pure sine wave. This loading procedure was relatively severe due to the large impact. In addition, the pipe was subjected to 20 psi surcharge (static) stress. The effect of surrounding conditions on the pipe deformation is demonstrated in Figure 2.3 for complete loading. The pipe surrounded with the gravel and heavily compacted sand deformed much less throughout the loading than the pipe with lightly compacted sand.



(Source: Faragher 1997)

**FIGURE 2.3**  
**Relative Variations of the Vertical Diameter to the Horizontal Diameter for Twin-Wall Pipes**

Mir Mohammad Hosseini and Moghaddas Tafreshi (2002) conducted tests on 4 inch diameter thin steel pipes buried in a test tank with a dimension of 32 inches x 32 inches x 32 inches to evaluate the behavior of the pipes under different loading conditions. Both cyclic and monotonic loads were applied using a loading plate. Soil density and pipe burial depth were varied. It was found that the soil density and the pipe burial depth are the two most important factors affecting the soil-pipe interaction. The pipe under the cyclic load with low amplitude might have the same deformation under a cyclic load with high amplitude, provided the cycles of the load continued for a long period. Moghaddas Tafreshi and Khalaj (2008) conducted similar tests with various repeated loads at the magnitudes of 36, 60, and 80psi under plate loading and their results supported the findings of Mir Mohammad Hosseini and Moghaddas Tafreshi (2002).

## **2.10 Performance of Steel-Reinforced High Density Polyethylene (SRHDPE) Plastic Pipes**

Steel-Reinforced or Steel-Ribbed High Density Polyethylene (SRHDPE) plastic pipes are a new product recently used for buried systems. Moser (2008) performed research on SRHDPE pipes with different pipe diameters embedded into the soil compacted at 87% of standard Proctor density. The test results showed that the SRHDPE pipe behaved the same as a low stiffness corrugated metal flexible pipe. Moore (2009) conducted a comprehensive study on SRHDPE pipes of 24 and 60 inches in diameter. Stub compression tests and hoop compression tests carried out on various diameter pipes demonstrated that the helically-wound steel ribs maintained wall stability (local buckling) at the required burial depth to a sufficient factor of safety. To evaluate the performance of a deeply buried pipe system, large-scale buried pipe tests were conducted on 24 and 60 inch diameter pipes. The tests showed that the pipe deflections were under the permissible limit (5%) and the pipe deformed like a conventional flexible metal culvert. Moore (2009) concluded that the conventional AASHTO design method for the deflection of a flexible steel pipe can be used to design the SRHDPE pipe with respect to pipe deformation.

Steel-reinforced and conventional HDPE pipes were installed with crushed stone backfill on the Manhead road, north of Randolph, Utah, by the Utah Department of Transportation (UDOT) (Folkman 2011). They were monitored to evaluate the relative performance of these two pipes. The method of the installation for both pipes was identical. The pipes were 24 inches in diameter. Two pipes of each type were installed in parallel at a distance of 5 inch spacing. The soil cover over the pipes was approximately 3 feet. The deflections of the pipes were measured immediately after the installation and during the service life to determine the changes in horizontal and vertical diameters. Both the steel-reinforced and conventional HDPE pipes have performed adequately to date. The conventional HDPE pipe had larger deflections than the steel reinforced HDPE pipe, which was less sensitive to the installation. The maximum vertical and horizontal deflections were -2.86 % and 3.01 %, respectively for the steel reinforced HDPE pipe, while the conventional HDPE pipe had -6.77 % vertical deflection and 6.90 % horizontal deflection right after the construction of the test sections. In addition, the maximum vertical and horizontal deflections were -2.35 % and 2.50 %, respectively for the steel-reinforced HDPE pipe, while the HDPE pipe had -6.53 % vertical deflections and 6.40 % horizontal deflections after

one year of installation. The reason for the reduction of the deflections of the pipes after one year was not determined at that time (Folkman 2011).

Three steel-reinforced HDPE pipes, which had a diameter of 48 inches and a length of 100 ft, were tested by installing them beneath the Sunshine Road in Fort Benning, Georgia (Hardert 2011). A 28 ft thick fill was placed over the pipes with a two-lane road across the fill. The deflected cross-sections of the pipes were determined using a laser device measuring the distance to the wall of the pipe from a center point every  $20^{\circ}$  around the pipe. The deflections of the pipes measured in September, 2010 and 2011 were reported. Based on the deflected shape measurements, the pipes underwent some minor movements but maintained relatively uniform round and symmetrical shapes. In one year, the greatest increases in the vertical and horizontal diameters were 0.13 and 0.10 ft, and the greatest decrease in the vertical and horizontal diameters were 0.12 and 0.09 ft.

## Chapter 3: Material Properties

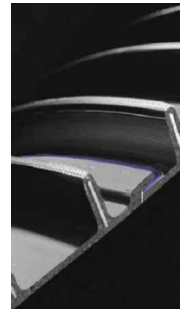
This chapter reports the types of materials and test methods used and properties obtained in this study. Various test methods were conducted to evaluate the stiffness, buckling resistance, and long-term creep behavior of the SRHDPE pipe sections under vertical compression in air. In addition, tests were performed to obtain the physical and mechanical properties of soils, which were used in large-scale box tests.

### 3.1 Steel-Reinforced High Density Polyethylene (SRHDPE) Pipe

SRHDPE pipes of 24 inches in diameter, manufactured and provided by Contech Construction Products Inc., were used in this research. This type of pipe has high-strength steel reinforcing ribs wound helically and covered by corrosion-resistant High Density Polyethylene (HDPE) resin inside and outside. Figure 3.1 shows pictures of SRHDPE pipes. The pipe profile is manufactured using a high-quality stress-rated thermoplastic that meets the requirement of ASTM F2562/F2562M. The specifications of the SRHDPE pipes are provided in Table 3.1 based on the manufacturer's data:



a) SRHDPE pipes



b) Section of the rib wall

(Source: Contech Construction Products Inc.)

**FIGURE 3.1**  
**SRHDPE Pipes**

**TABLE 3.1**  
**Specification of the SRHDPE Pipe**

Cell classification	345464C (as per ASTM D3350)
Materials	Steel and HDPE
Structure type	Helical pipe
Pipe diameter (in.)	24
Rib height (in.)	0.51
Rib thickness (in.)	0.058
Rib spacing (in.)	1
Pipe wall area (A) (in. <sup>2</sup> /ft) (neglecting plastic)	0.35496
Moment of inertia (I) (in. <sup>4</sup> /in.) of pipe wall(neglecting plastic)	0.000641
Modulus of elasticity of Steel(E) (ksi)	29,000
Yield strength of steel( $F_y$ ) (ksi)	80
Tensile strength of steel( $F_u$ ) (ksi)	85
Radius of gyration(r) (in.) (neglecting plastic)	0.147

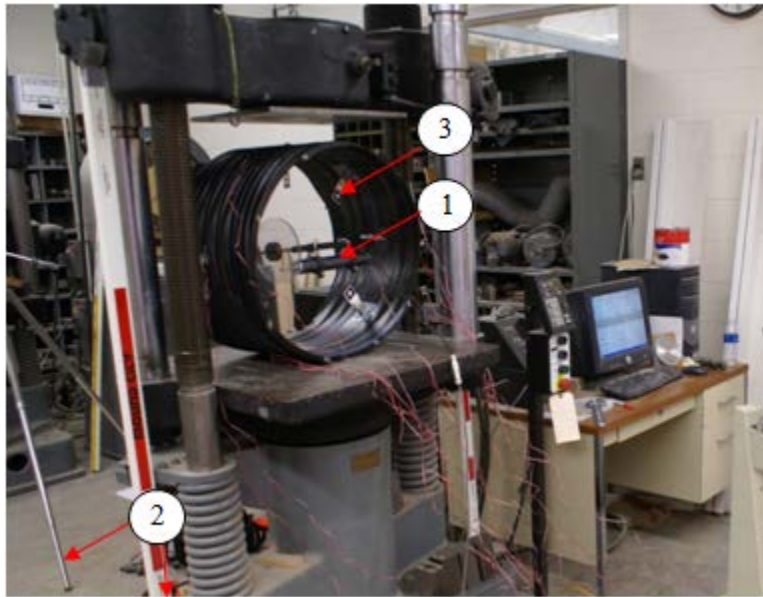
The tests used to evaluate the properties of the SRHDPE pipe sections are discussed in Sections 3.1.1 to 3.1.4.

### *3.1.1 Parallel Plate Tests*

Three parallel plate tests were carried out (a) to obtain the load and deformation characteristics of the SRHDPE pipe, (b) to determine the maximum load capacity of the pipe, (c) to observe the failure modes of the pipe per ASTM F2562/F2562M, and (d) to check the specification compliance of pipe stiffness. A universal testing machine was used to apply the compression load on a pipe sample of 24 inches in diameter and 14 inches in length. The pipe was compressed at the rate of  $0.5 \pm 0.01$  inches/min. up to a vertical deflection equal to 5 % pipe diameter. The rate was then increased to 3 inches/min. up to a vertical deflection equal to 20 % pipe diameter for flattening. This test procedure followed ASTM F2562/F2562M.

#### **3.1.1.1 Instrumentation**

Extensive instrumentation with three technologies: displacement transducers, photogrammetry, and LiDAR were used to monitor the changes in shape of the pipe during loading as shown in Figure 3.2.



- 1: Displacement transducer on a specially designed frame
- 2: Camera and stadia rod for the photogrammetry
- 3: Photogrammetry targets

**FIGURE 3.2**  
**Test Setup and Instrumentation for the Parallel Plate Load Test**

The displacement transducer in the compression machine measured the vertical deflection of the pipe during loading. The horizontal displacement of the pipe was measured by another displacement transducer installed horizontally on a specially designed frame in the center of the pipe. The installation of the displacement transducers was challenging to get the deflected shape during loading because any point on the pipe moves both vertically and horizontally at the same time. This is why other non-contact technologies, such as Photogrammetry and LiDAR, were used. For the photogrammetry method, targets were fixed on the inside wall of the pipe at  $90^\circ$  intervals. Photos of the deformed pipe during the test were taken at a time interval of 10 seconds. 3D images were also scanned at the start of the test, during the test, and at the end of the test using Riegl LMS-Z620 LiDAR. The major advantage of LiDAR is that it can generate a 3D image of the pipe.

Fourteen uniaxial, foil-type electrical resistance strain gages (labeled as G1 to G14) were used to measure the circumferential, radial, and longitudinal strains of the pipe at various locations (Figure 3.3). Eight strain gages were affixed at the center of the specimens on the steel surface at the crown, invert, and springline to determine both radial and circumferential strains. The plastic cover was removed at the desired locations to place the strain gages on the steel surface. Since the steel rib height was too small to attach the strain gages on the top of the rib,



they were fixed at the neutral axis of the steel rib. In addition, six strain gages were placed on the plastic surfaces at ribs, inside and outside between the ribs (i.e., valley) to measure the strains in the plastic. For example, G10 and G13 were outside while G11 and G14 were inside. These four strain gages were used to measure the strains in the plastic in the longitudinal direction. Figure 3.4 shows the strain gages fixed on both steel and plastic.

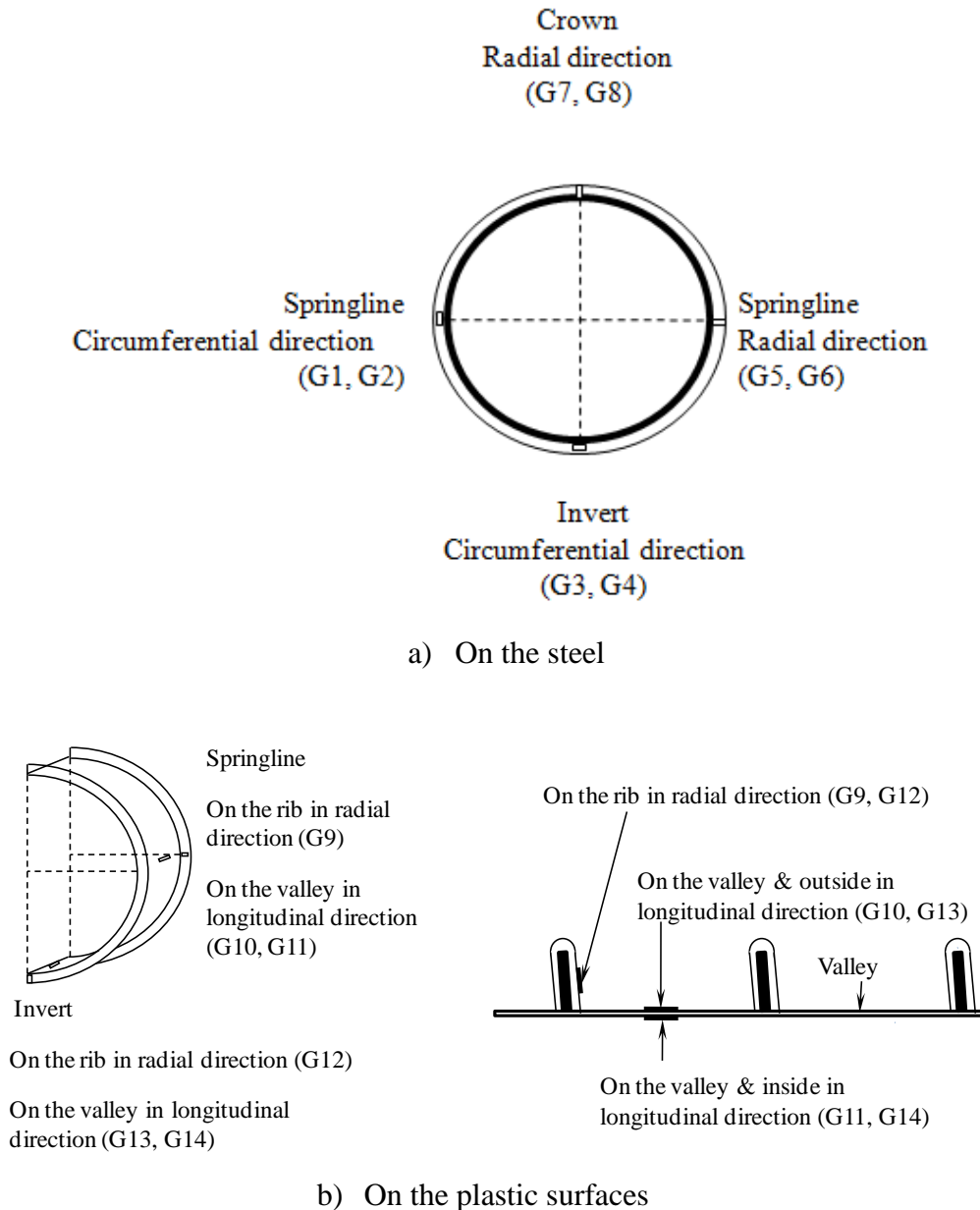
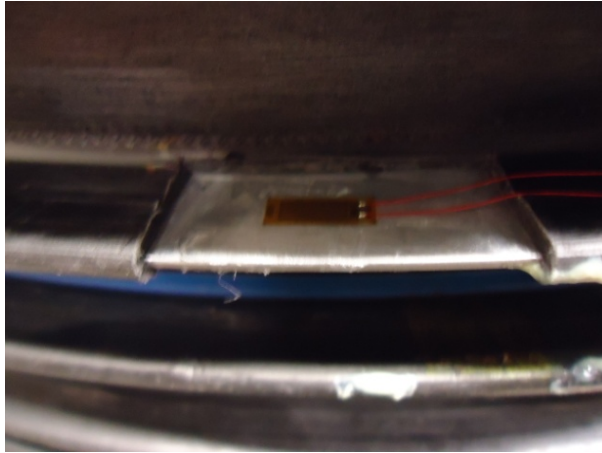
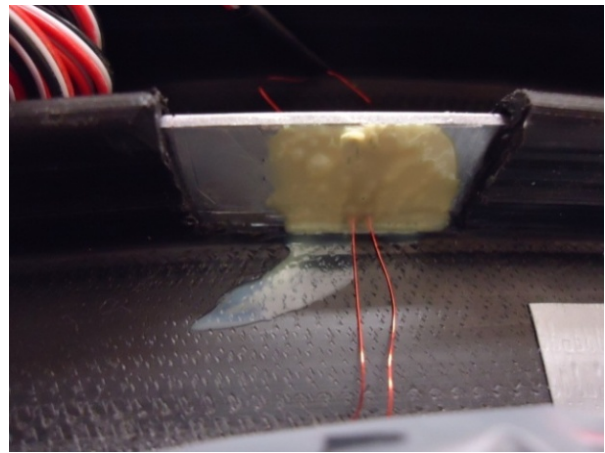


**FIGURE 3.3**  
**Symbols, Locations, and Orientations of Strain Gages on the Pipe**



a) On steel (circumferential direction)



b) On the steel (radial direction)  
with coating material



c) On plastic (circumferential direction)

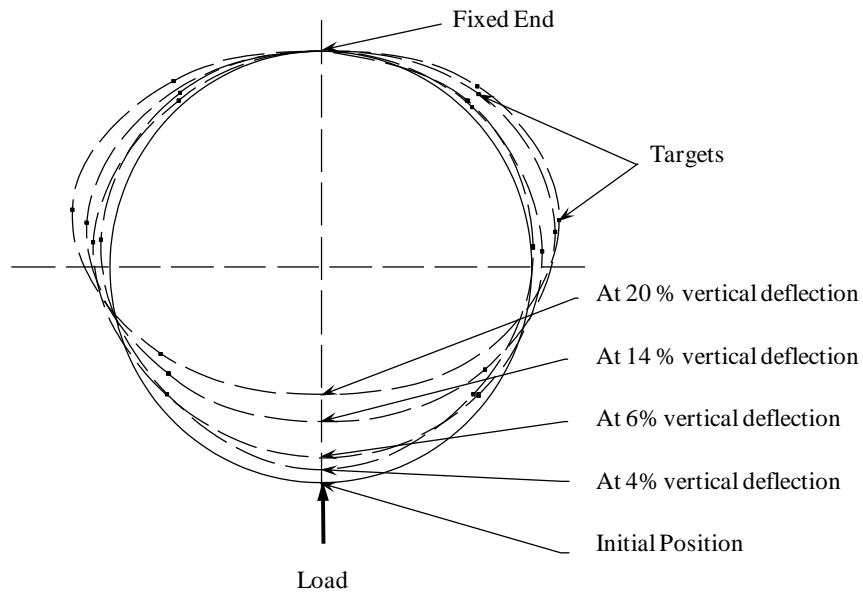
**FIGURE 3.4**  
**Strain Gages on the Steel and Plastic**  
**Surfaces**

### *3.1.2 Test Results and Discussions*

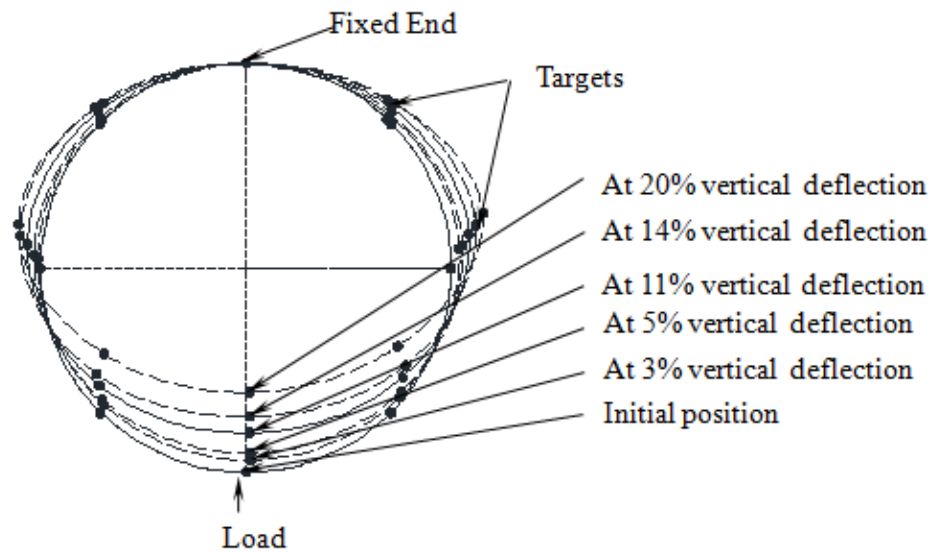
#### *3.1.2.1 Deformed Pipe Shape*

The displacement transducers could only measure the deflections of the pipes in the vertical and horizontal directions. Photogrammetry was used to generate the deformed shapes (Figure 3.5) of the pipe in Test 2 and 3. The load-horizontal deflection curves of the pipes from the photogrammetry method compared well with those from the displacement transducer measurement as shown in Figure 3.6. Therefore, the photogrammetry was able to capture the deformation of the pipe during the loading. In addition, the deformed shapes of the pipe in Test 2 at 6 % and 14 % vertical deflections to the pipe diameter under the load in air were compared with the standard elliptical shapes (Figure 3.7) and it was confirmed that the deformed shapes of the pipes resembled closely with the elliptical shapes.

The 3D scanned images of the pipe in Test 2 obtained by the LiDAR scanner before and at the end of the test are shown in Figure 3.8. These images clearly show the change of the pipe shape. They were exported to the AutoCAD software for further analysis. Using the AutoCAD, the deformed shapes of the SRHDPE pipe were drawn as shown in Figure 3.9. The deflection profile during loading shows that the left side had less deflection than the right side because it took some time to scan the pipe starting from the left side to the right side and the test was continuing during the scan.



a) Test 2



b) Test 3

**FIGURE 3.5**  
**Deformed Pipe Shapes from the Photogrammetry**

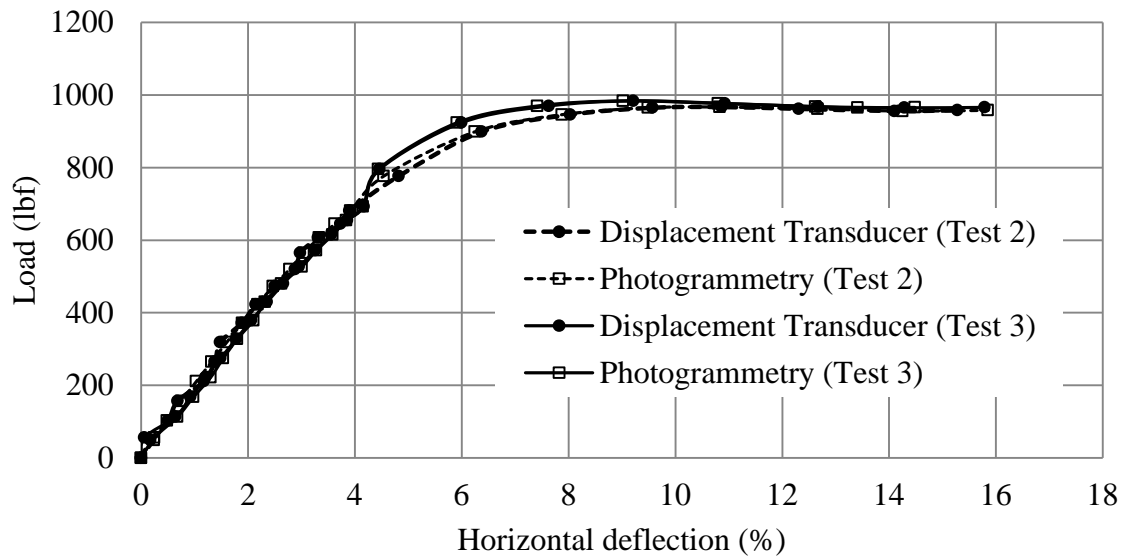


**FIGURE 3.6**  
**Comparison of the Load-Horizontal Deflection Curves Obtained by the**  
**Photogrammetry Method and the Displacement Transducer**

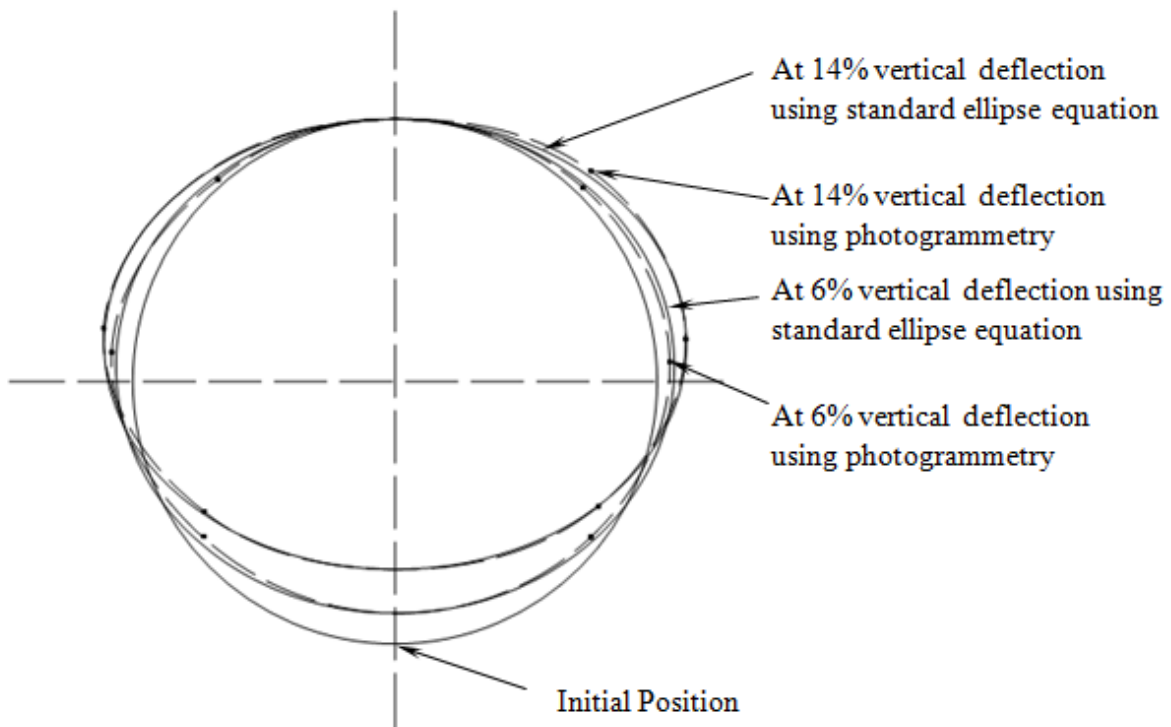
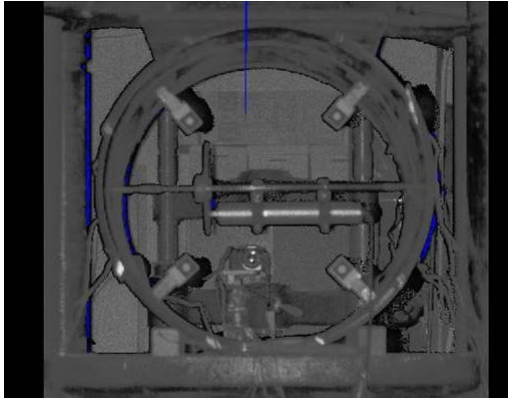
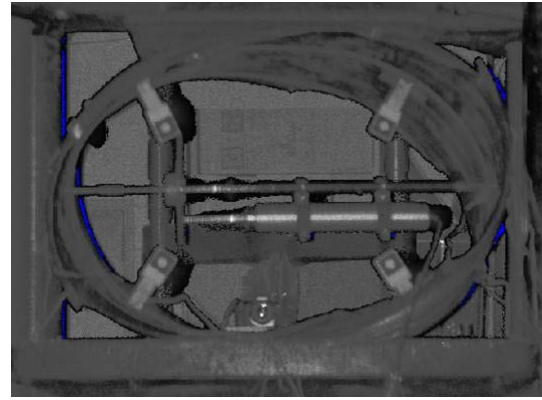


**FIGURE 3.7**  
**Comparison of the Deformed Pipe Shapes from Photogrammetry with the Standard**  
**Elliptical Shapes**



a) Before test



b) At the end of test

**FIGURE 3.8**  
**LiDAR Images**

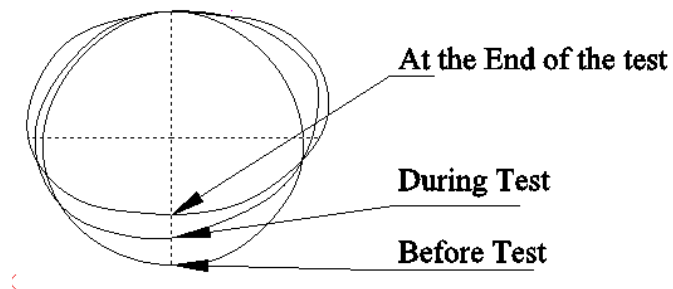


**FIGURE 3.9**  
**Deformed Pipe Shapes from the LiDAR Images**

### 3.1.2.2 Load-Deflection Responses

Figure 3.10 shows the load-deflection responses of these pipes from the displacement transducer measurements. It is shown that the pipe started yielding at approximately 6% vertical deflection to pipe diameter. The average ultimate load capacity of 960 lbf was reached at approximately 10 % vertical deflection due to the out of plane buckling (will be discussed in the strain measurement section later) occurring on the ribs at the springline of the pipes. Neither valley liner nor wall crack was observed on the plastic. Based on visual observation, no reverse

curve developed at the crown of the pipe during the test until 20% vertical deflection to pipe diameter was reached. Figure 3.11 shows the vertical deflection was approximately 1.25 times the horizontal deflection.

The pipe stiffness was calculated using Equation 2.12 at 5% vertical deflection to pipe diameter. The bending stresses ( $\sigma_b$ ) on the steel ribs were calculated using the bending equation ( $\sigma_b=M/S$ , where  $S$  = the section modulus of the pipe wall) in which the moments calculated by Equation 2.13. The bending stresses ( $\sigma_b$ ) were calculated at the springline and crown and corresponded to the yield load at approximately 6% vertical deflection to pipe diameter, assuming an axisymmetric (2D) geometry and isotropic material for simplicity. The calculated pipe stiffness and bending stresses in the extreme fiber of the steel reinforcement at 6% deflection are shown in Table 3.2. The extreme fiber bending stresses obtained are close to the steel yield values provided by the manufacturer. In addition, the calculated stiffness is more than the specified value (34 psi) per ASTM F2562/F2562M for Class 1 pipe of 24 inches in diameter at 5% vertical deflection to pipe diameter. Furthermore, the load at 20 % deflection is greater than 75 % of the peak load, although the peak load was reached before 20 % deflection. This satisfies the buckling limit criterion per ASTM F2562/F2562M.

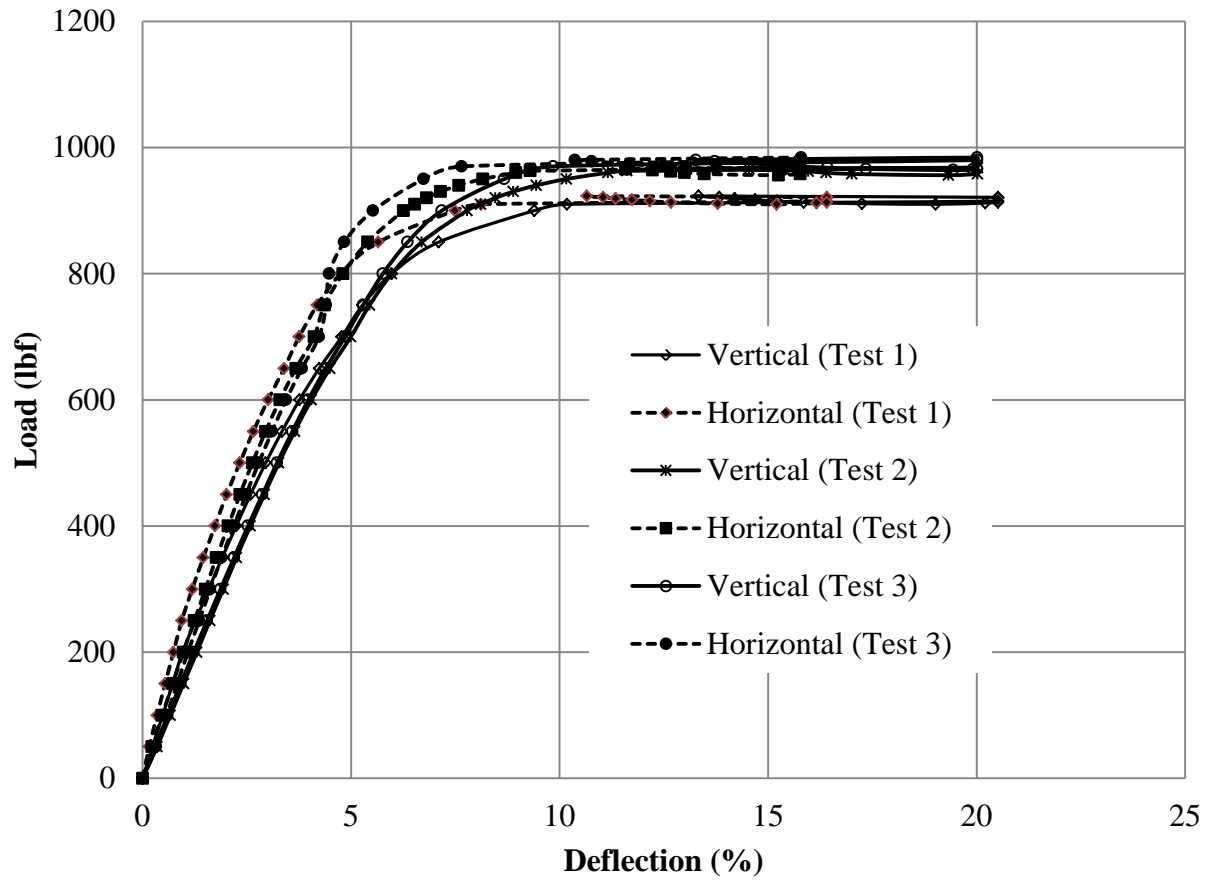


**FIGURE 3.10**  
Load-Deflection Responses

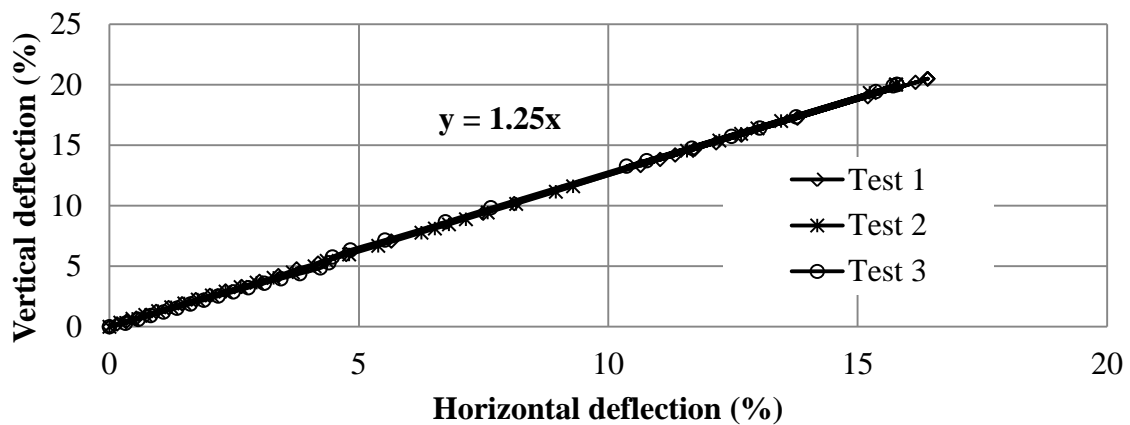


**FIGURE 3.11**  
Relation between the Vertical and Horizontal Deflections of the Pipes



**TABLE 3.2**  
**Calculated Pipe Stiffness and Equivalent Bending Stress Values**

Test No.	Load (at 5% vertical deflection) (lbf)	Pipe stiffness (at 5% vertical deflection) (psi)	Initial pipe stiffness (based on the initial slope of the curve) (psi)	Equivalent Bending stress, $\sigma_b$	
				At springline (ksi)	At crown (ksi)
1	727	43	56	78	71
2	701	42	51	85	78
3	715	43	48	81	68
Average	<b>714</b>	<b>43</b>	<b>52</b>	<b>81</b>	<b>72</b>

### 3.1.2.3 Strain

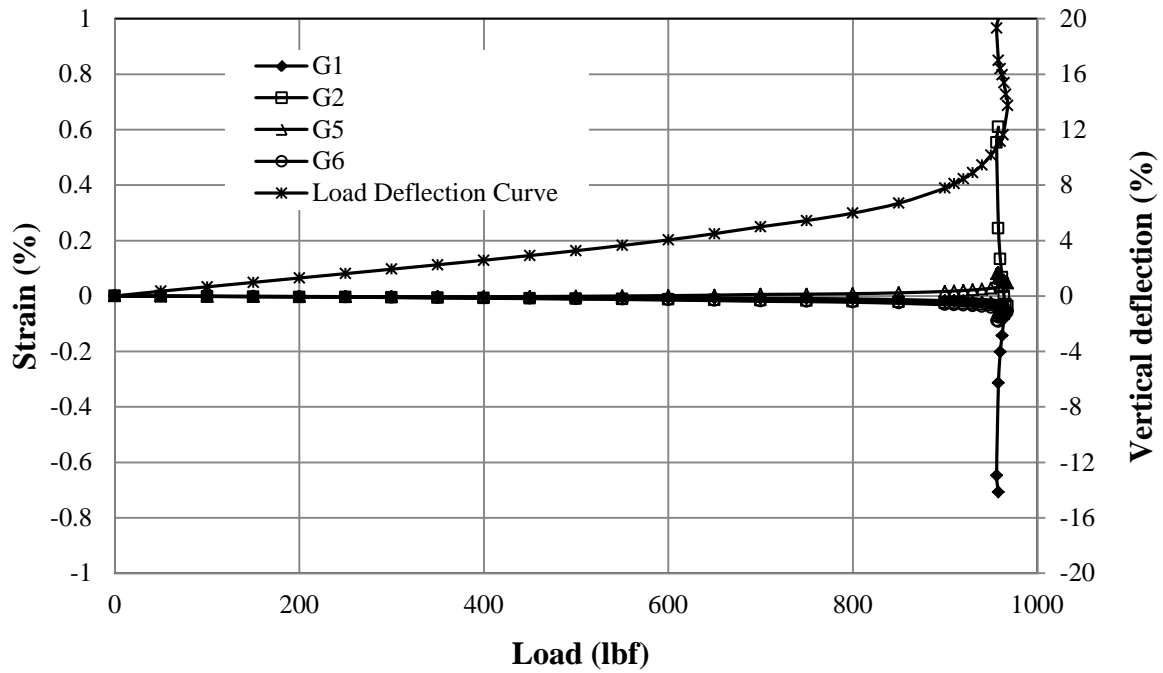
The above test results reflected the overall behavior of the SRHDPE pipes; however, local behavior of the pipes is important for the failure mechanisms of the pipes. Strain gages were attached on both steel and plastic surfaces in last two parallel plate load tests (Tests 2 and 3) to measure the strain developments in the pipes and to facilitate understanding of the possible failure mechanisms of the pipes. The symbols, locations, and orientations of the fourteen strain gages are presented in Figure 3.3. The strains measured on the HDPE surfaces were adjusted by multiplying a factor of 1.29 to account for the stiffness difference between strain gage and glue as suggested by Brachman et al. (2008). All the strain data are plotted against applied compressive loads in Figure 3.12 to 3.14. Positive values imply tensile strains while negative values are compressive strains.

Figure 3.12 shows the circumferential and radial strains developed on the steel surface of the pipe at the springline. The maximum circumferential strain of 0.7% (G1, compressive strain) developed in Test 2 while the maximum radial strain of 0.28% (G5, tensile strain) developed in Test 3. Figure 3.12 shows that the circumferential and radial strains were small (less than 0.1%) before the yielding of the pipes. The strains suddenly increased when the loads were close to the ultimate load capacity of the pipes. Both strain gages (G1 and G2 in Test 2 or Test 3) in the circumferential direction at the springline had compressive strains before the failure of the pipes.

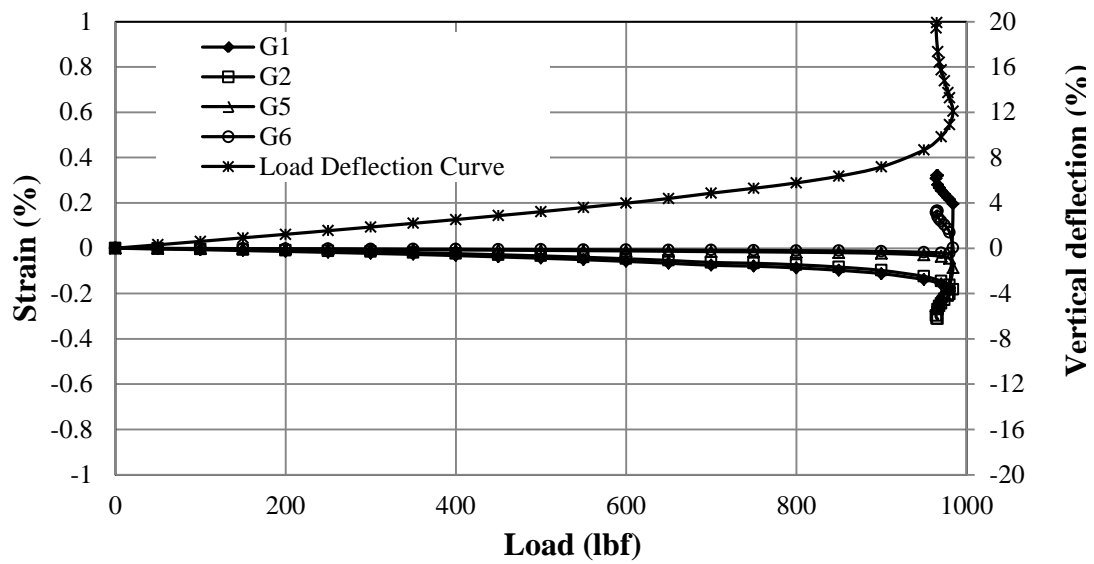
At the failure of the pipes, the two strain gages (one on each side of the steel rib) in the circumferential or radial direction showed one positive and one negative strain, which indicate the out of plane buckling of the steel ribs.

Figure 3.13 shows the circumferential and radial strains versus the applied loads on the steel surface at the crown and invert. At the crown, both strain gages (G7 and G8) in the radial directions showed small tensile strains while at the invert, both strain gages (G3 and G4) in the circumferential direction had small compressive strains. In Test 2, G4 suddenly changed from the compressive to tensile strain when the applied load was close to the ultimate load capacity of the pipe. This sudden change indicated the out of plane buckling of the steel rib. It is important to observe that the buckling occurred after the steel reinforcing began to yield.

Figure 3.14 shows that the strain developments on the plastic were similar in Tests 2 and 3; however, the magnitudes of the strains in Test 3 were larger than those in Test 2. The maximum strains (G10 and G11) developed on the plastic were approximately 2.5% in the valley inside and outside of the pipes in the longitudinal direction at the springline in Test 3, but they had opposite signs (i.e., tensile versus compressive strain). From Figure 3.12 to 3.14, it is also clear that the plastic cover had much larger strains than the steel ribs. In other words, the strains at the steel ribs and the plastic cover are not compatible.

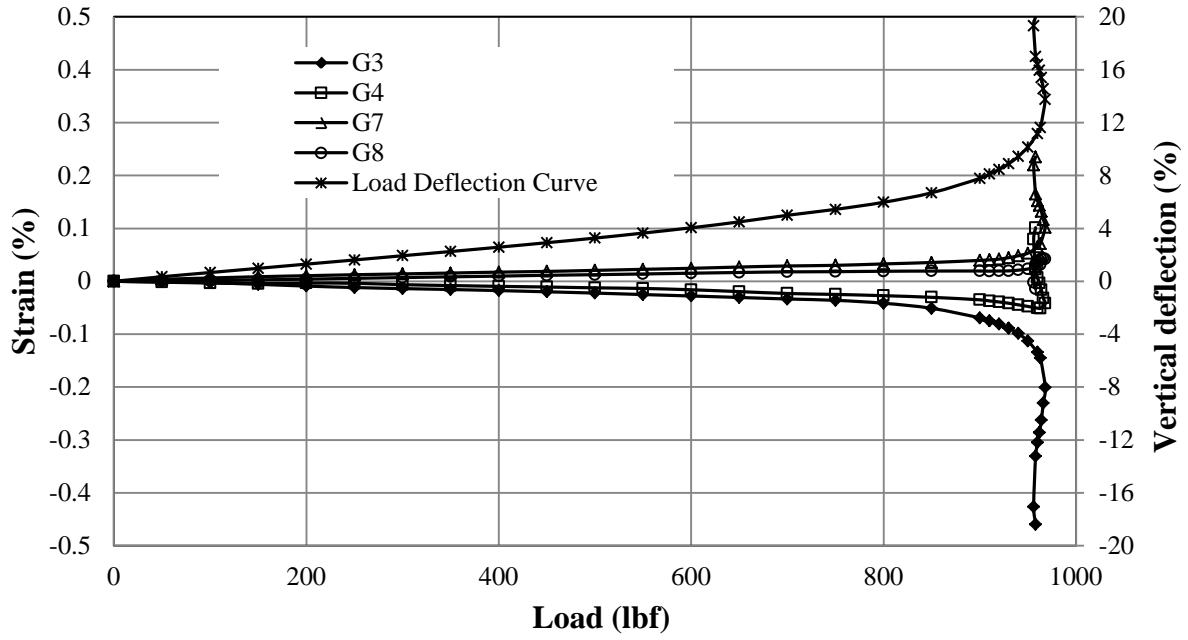


(a) Test 2

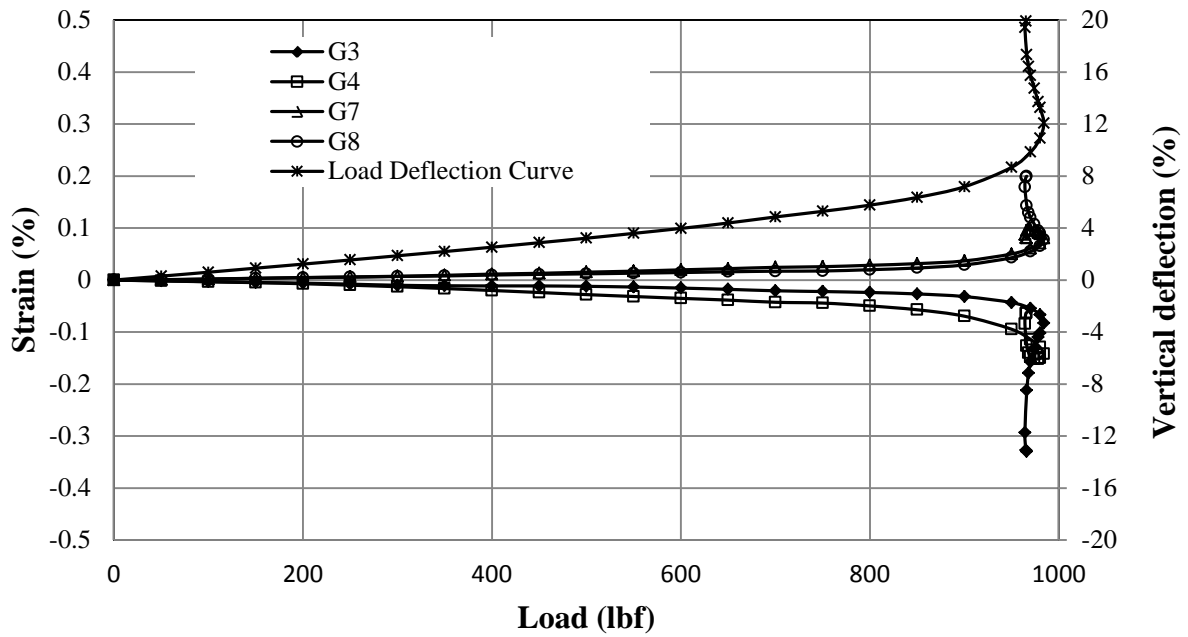


(b) Test 3

**FIGURE 3.12**  
Circumferential and Radial Strains against the Applied Loads on the Steel at the Springline

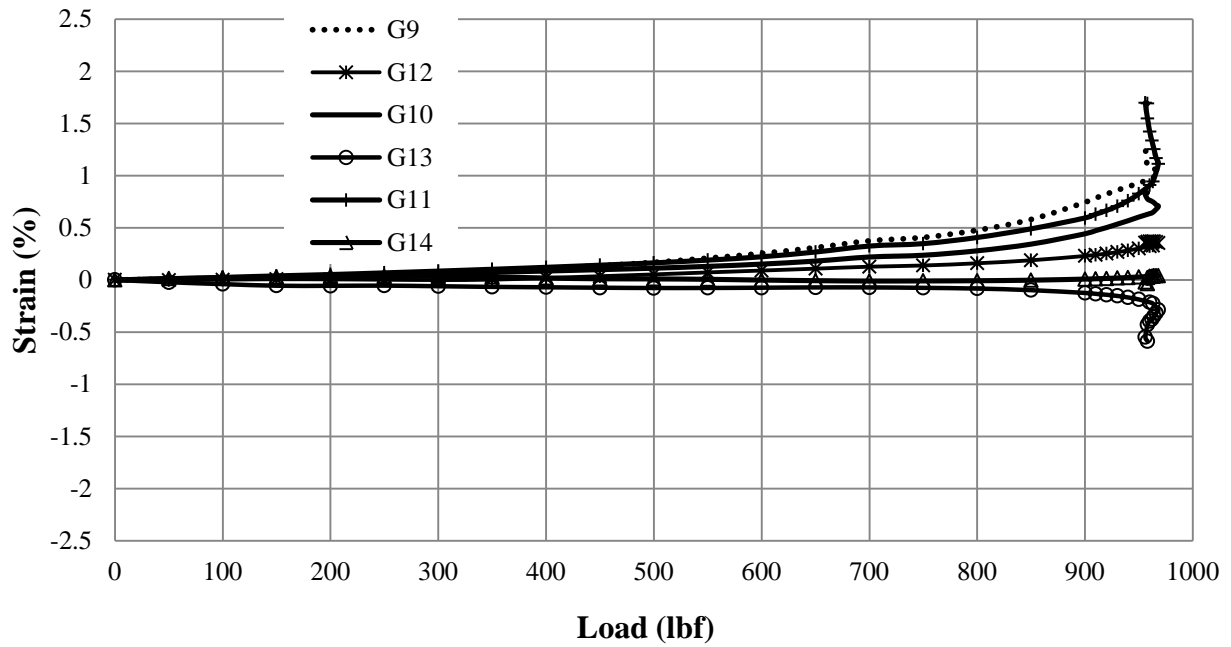


(a) Test 2

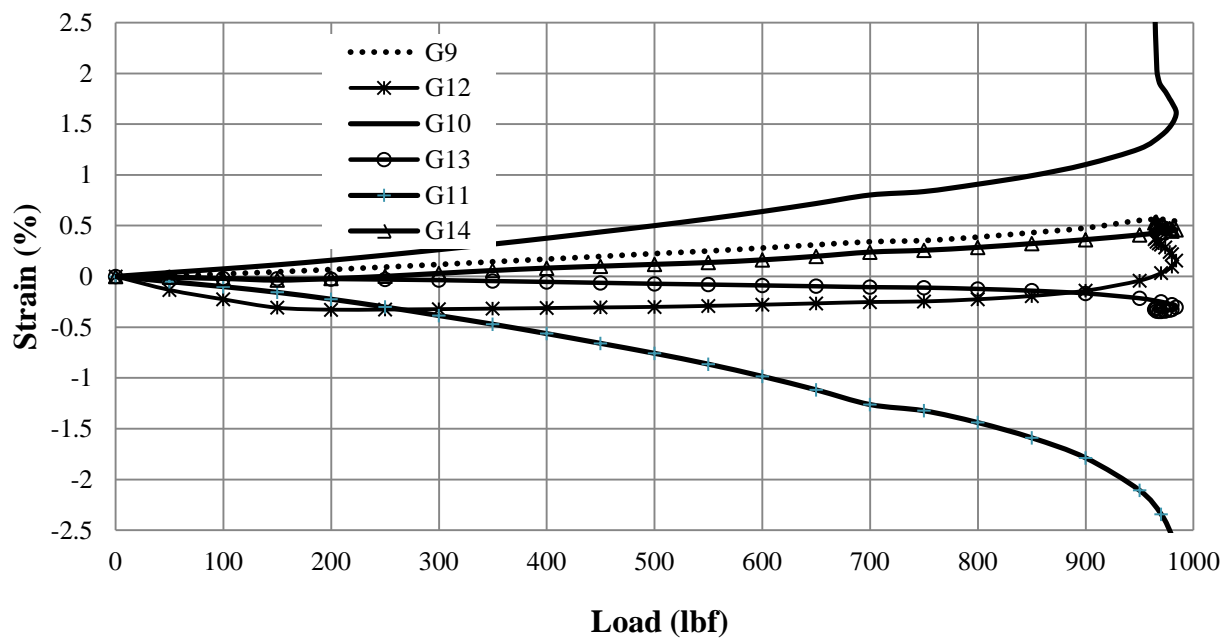


(b) Test 3

**FIGURE 3.13**  
Circumferential and Radial Strains against the Applied Loads on the Steel Surface at the Crown and Invert

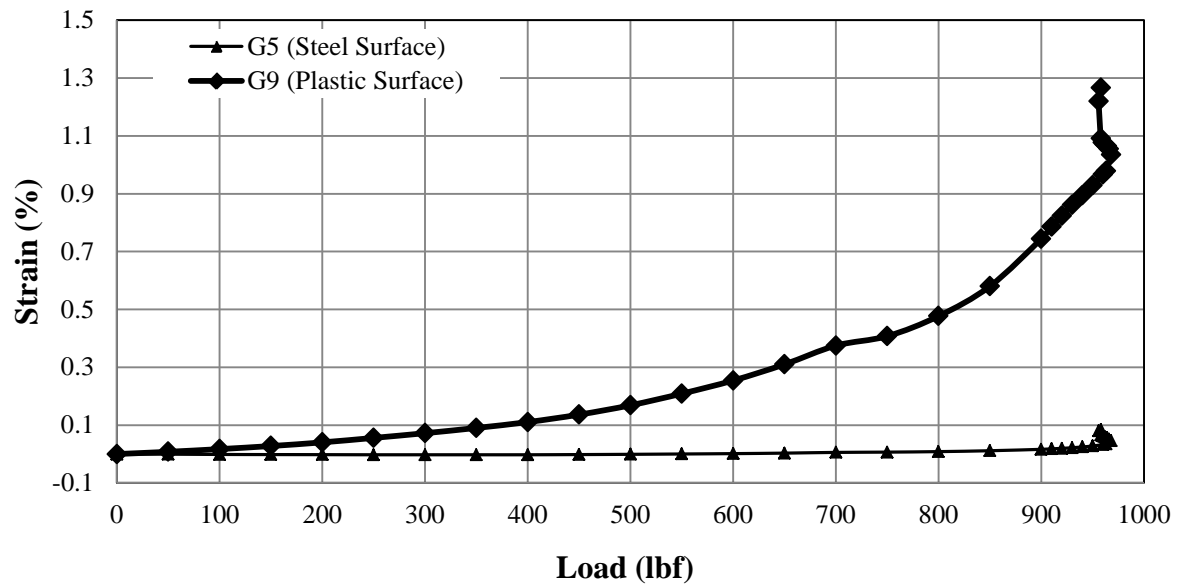


(a) Test 2

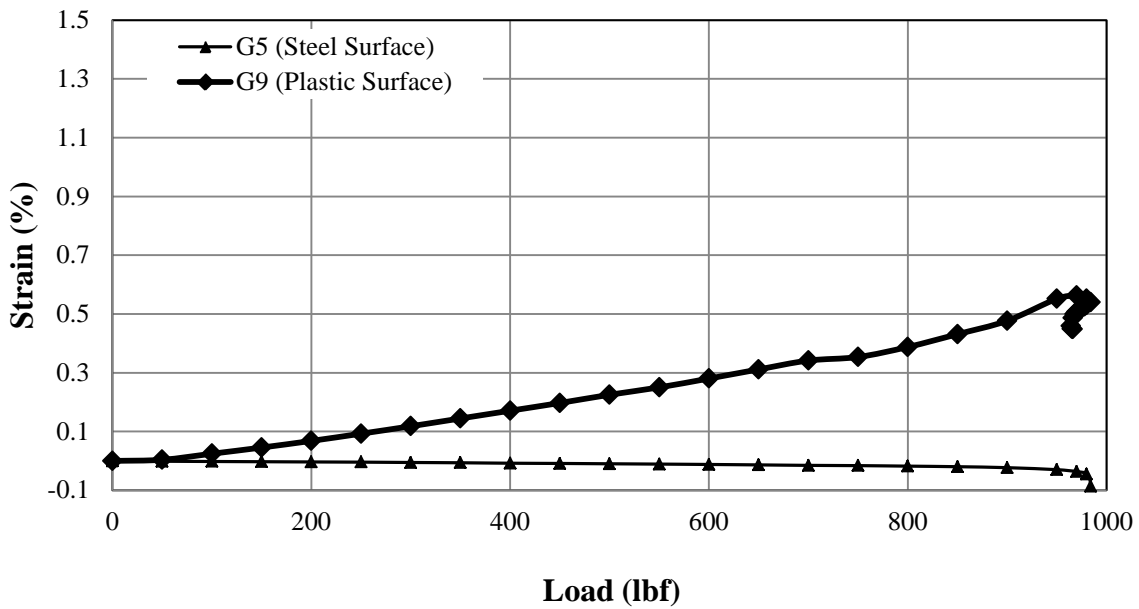


(b) Test 3

**FIGURE 3.14**  
**Strains against the Applied Loads on the Plastic Surface**



(a) Test 2



(b) Test 3

**FIGURE 3.15**  
**Comparison of Strains Developed on the Steel Rib and Plastic Surfaces in the**  
**Radial Direction at the Springline**

### 3.1.3 Stub Compression Tests

Stub compression tests were carried out on four specimens, as per NCHRP report 631 (McGrath et al. 2009), to evaluate the resistance to local buckling due to the compressive circumferential strain in the pipe. Each specimen was compressed in a universal test machine between two rigid plates at the rate of  $0.05 \pm 0.01$  inches/min until the failure of the specimen. The specimens were carefully cut from a 24 inches diameter pipe to make the ends parallel to each other and to the radial line through the center of the specimen. The test specimens had a longitudinal length of 3 inches (i.e., three periods) and circumferential length of 2 inches Figure 3.16 shows a picture of the specimen taken during the test.



**FIGURE 3.16**  
**Specimen Crushing in the Stub**  
**Compression Test**

The load-deflection curves are shown in Figure 3.17. The ultimate axial forces ranged from 2,904 to 3,758 lbf with an average value of 3,231 lbf with a total variation between the samples of 29.4 %. Moore (2009) found an ultimate axial load of 4,200 lbf with a variation of 68%. These high variations were due to lack of precision to cut the specimen ends so that each rib was loaded uniformly. Moore (2009) later prepared the specimens with a machine shop mill to provide the precise specimen ends. The similar technique was used by the independent testing laboratory, TRI on the SRHDPE pipe of 24 inches in diameter and an ultimate axial load of 5,986 lbf was found with a variation of 3.8%. Based on the load-deflection curve, the average

equivalent modulus of elasticity of the profile wall ( $E_{wall}$ ) under compression was calculated using Equation 3.1 and found to be 3,000 ksi.

$$E_{wall} = \frac{P L}{\Delta A} \quad \text{Equation 3.1}$$

where  $P$  = the axial force,  $\Delta$  = the deflection of the specimen at load  $P$ ,  $L$  = the circumferential length of the specimen, and  $A$  = the equivalent profile wall area.

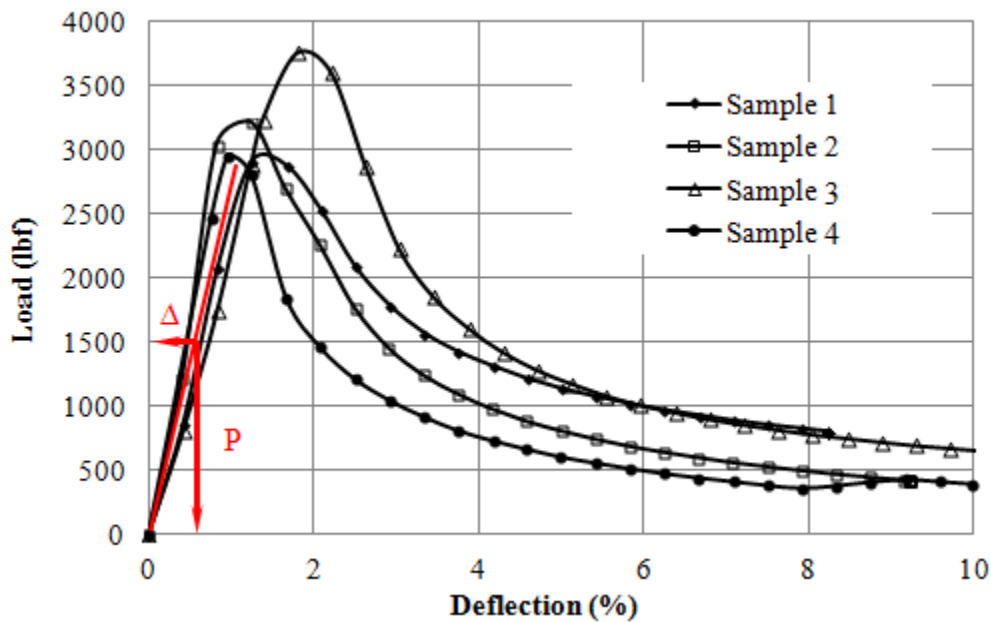


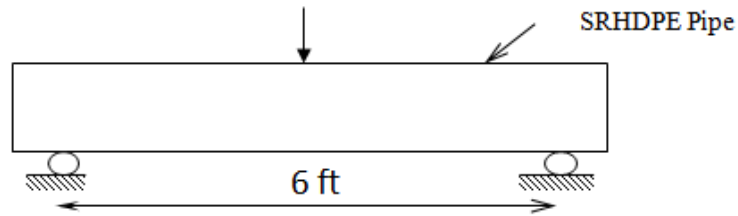
**FIGURE 3.17**  
**Load-Displacement Curves of Specimens from Stub Compression Tests**

#### 3.1.4 Pipe Bending Test

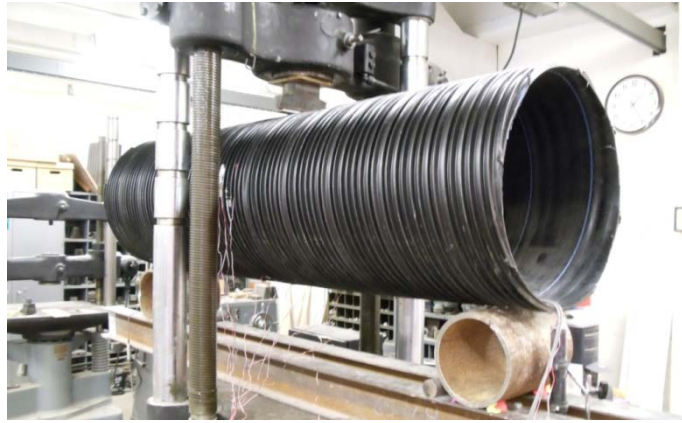
A three-point bending test was carried out on the SRHDPE pipe to evaluate the bending stiffness of the pipe. The pipe specimen of 7 ft long and 24 inches in diameter was placed on two roller supports, which were spaced 6 ft apart center to center as shown in Figure 3.18. To make the contact surfaces smooth at the both ends of the pipe, the space between the ribs was filled with the hydrocarbon and then covered by the polyethylene. The load was applied at the rate of



0.5 ± 0.02 inches/min. Three displacement transducers, one at the center and two at the ends of the testing pipe, were used to determine the deflection shape of the pipe. During the test, the specimen was failed due to high concentration of the applied load at the point of application of the load on the pipe.



(a)



(b)

**FIGURE 3.18**  
**Pipe Bending Test**

Based on the load-deflection curve shown in Figure 3.19, the average equivalent bending stiffness ( $EI_c$ ) of the pipe section was calculated using Equation 3.2 and found to be  $2.6 \times 10^8$  lb·inches<sup>2</sup>. The deflection shapes of the pipe are shown in Figure 3.20.

$$EI_c = \frac{PL^3}{48\Delta}$$

**Equation 3.2**

where  $P$  = the applied force at the center of the pipe span,  $\Delta$  = the deflection when the applied load is  $P$ ,  $L$  = the circumferential length of the specimen,  $I_c$  = the moment of inertia of the pipe section, and  $E$  = the equivalent modulus of the pipe.

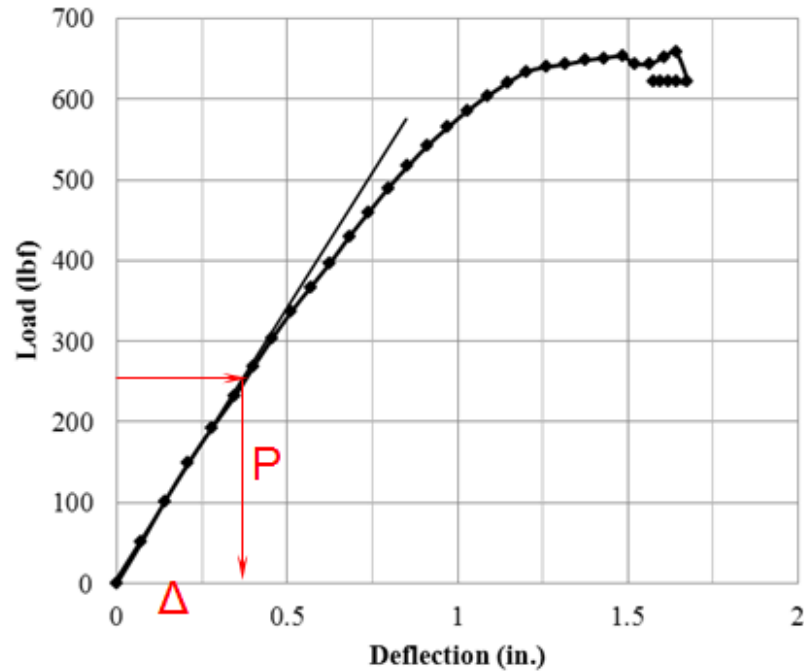


**FIGURE 3.19**  
Load-Deflection Curve of the Pipe under Bending

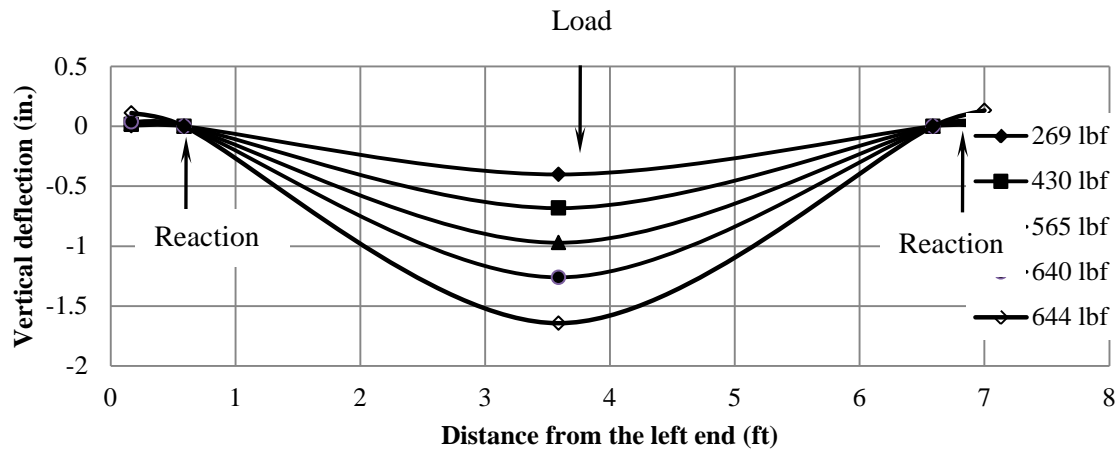


**FIGURE 3.20**  
Deflection Profiles of the Pipe under Bending

### 3.1.5 Creep Test

A creep test was carried out by placing the pipe specimen between two rigid plates and applying a constant line load to evaluate long-term creep behavior of the SRHDPE pipe. The pipe specimen was 24 inches in diameter and 14 inches in length. Figure 3.21 shows the creep test set-up. The applied load of 480 lbf was selected as half of the average ultimate load capacity (i.e., 960 lbf, presented in Section 3.1.1) obtained from the parallel plate tests. The vertical and horizontal deflections of the pipe were measured with time by digital dial gages with an accuracy of 0.001mm. The test was carried out at approximately 27°C room temperature for one month.



**FIGURE 3.21**  
**Creep Test Set-Up**

Twelve strain gages (labeled as G1 to G12) were fixed to measure the strains of the pipe on the steel and plastic at various locations and orientations as shown in Figure 3.22. Four strain gages, from G1 to G4, were affixed at the center of the specimen on the steel at the crown and springline to determine circumferential strains. Strain gages were not fixed in the radial direction because the expected strains in that direction were observed to be low during the parallel plate load tests. Eight strain gages from G5 to G12 were placed on the plastic at ribs, and inside and outside between the ribs (i.e., valley). For example, G9 and G11 were outside while G10 and G12 were inside in valley.

The vertical and horizontal deflection curves with time under the sustained load are shown in Figure 3.23a. Most of the deflections occurred immediately after the application of the load and increased with time at a slow rate. The vertical deflection is approximately 1.25 times the horizontal deflection, which is the same ratio as obtained in the parallel plate load tests discussed in Section 3.1.1.

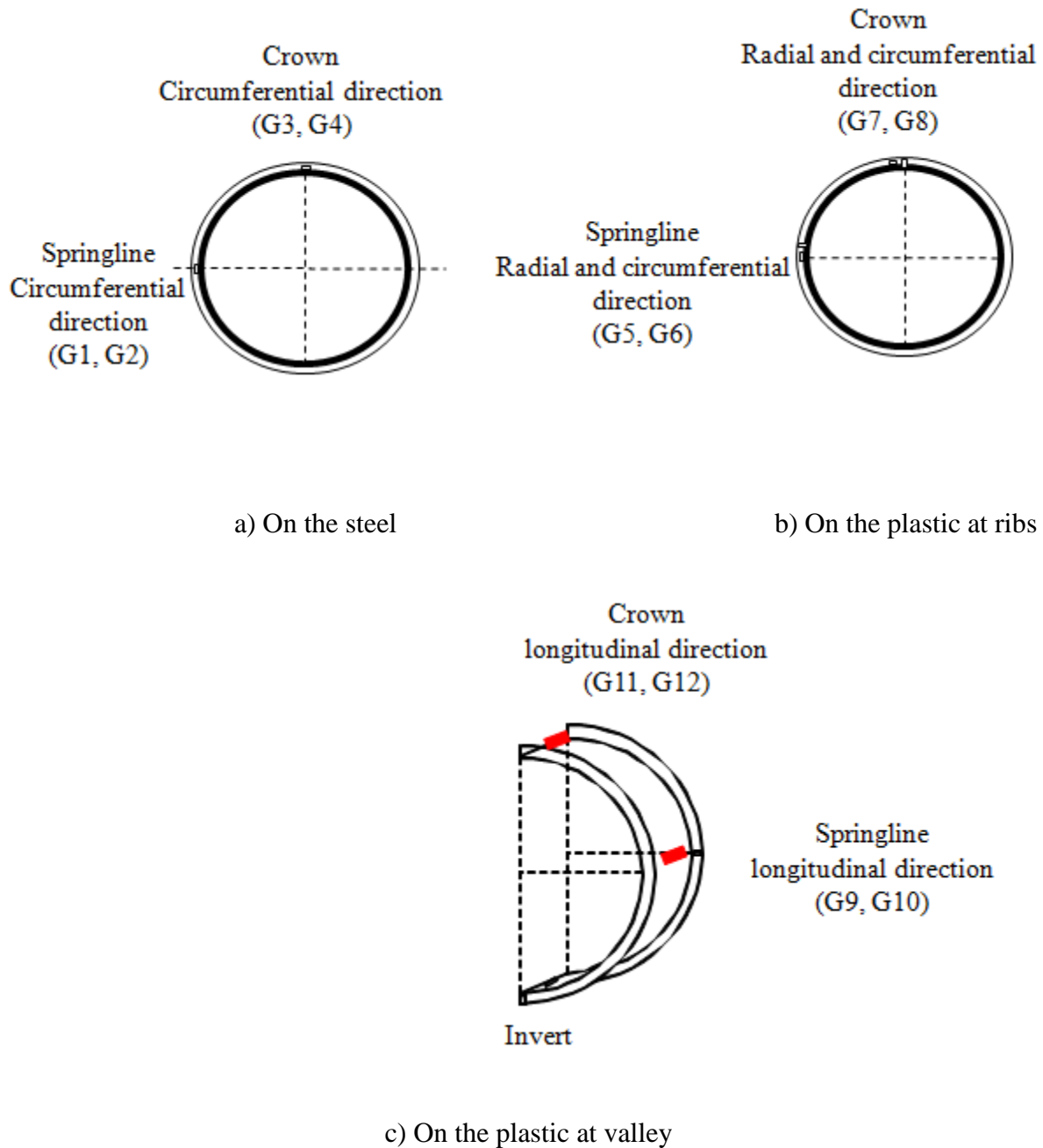
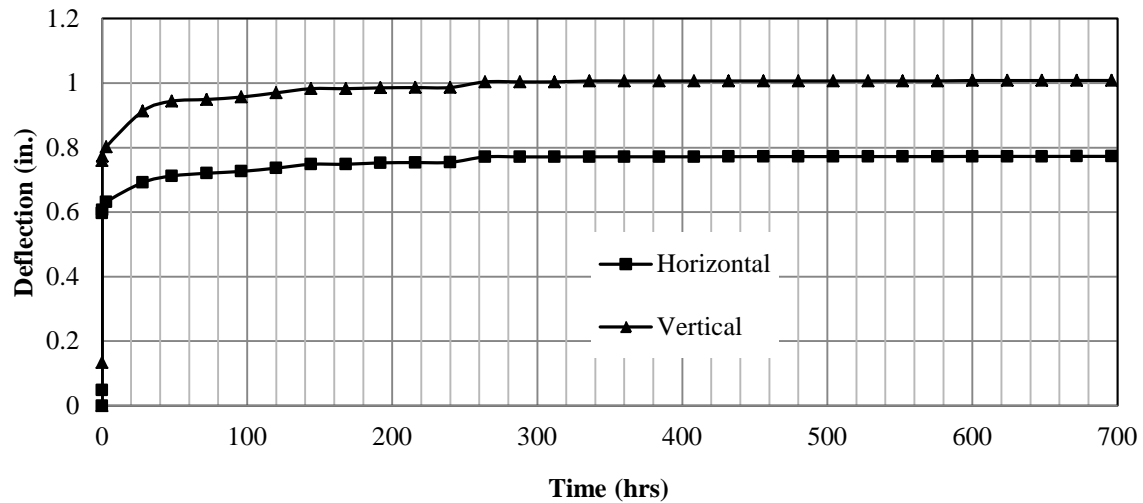
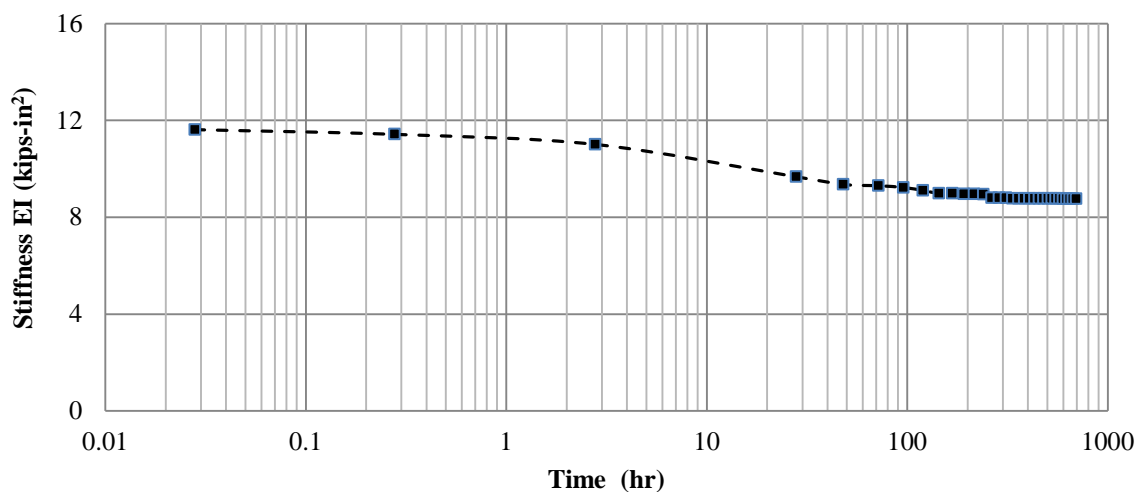


**FIGURE 3.22**  
Symbols, Locations, and Orientations of Strain Gages on the Pipe

The relation,  $EI = 0.149 R^3 PS$ , was used to calculate the time-dependent stiffness factor (EI) of the pipe from the test results. The stiffness factor (EI) is plotted against time in Figure 3.23b, which shows a 75% reduction in the stiffness factor (EI) from the initial value in one month (i.e., at the end of the test). It should be pointed out that this creep test was conducted in air. Further research is needed to investigate the creep behavior of SRHDPE pipes in a buried condition.



(a) Deflections



(b) Stiffness factor (EI)

**FIGURE 3.23**  
**Deflection and Stiffness Factor (EI) of the Pipe with Time under the Sustained Load**

All the strain data are plotted against time (in log scale) in Figures 3.24 to 3.26. Figure 3.24 shows the circumferential strains developed on the steel of the pipe. The maximum circumferential strain of 0.02% (G2, compressive strain) was developed at the springline immediately after the application of the sustained load and increased to 0.045% in one month. All strain gages (G1 to G4) show compressive strains on the steel in the circumferential direction, both at the springline and the crown.

Figure 3.25 shows the radial (G5 and G7) and circumferential (G6 and G8) strains developed on the plastic. The strains and their changes over the time on the plastic were higher than those on the steel. The strain gages in the radial direction, G5 at the springline and G7 at the crown, had more changes in the strain values over the time than the strain gages, G6 at the springline and G8 at the crown, in the circumferential direction. The maximum radial tensile strain of 0.12%, at G2 developed on the plastic on the rib at the springline immediately after the application of the sustained load and then increased to the maximum value of 0.25% over one month. Figure 3.26 shows the strains on the plastic inside and outside the wall at valley between the ribs. The changes in strains from the two strain gages (G9 to G12) were small. These changes depended on whether or not the valley plastic wall was affected by the movement of the steel ribs under a sustained load.

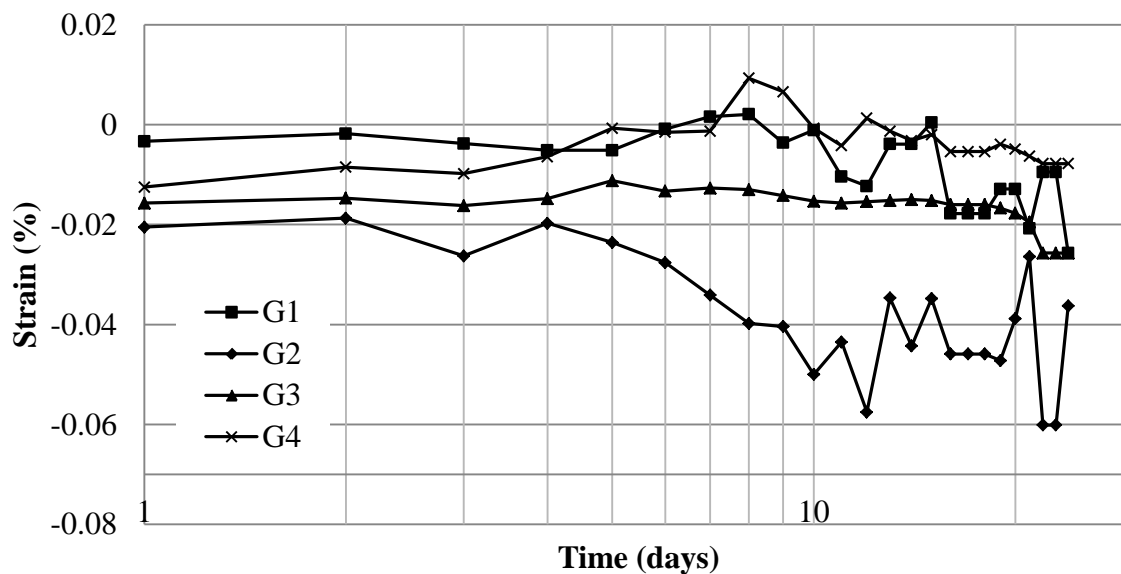


**FIGURE 3.24**  
**Circumferential Strains on the Steel Surface under a Sustained Load**

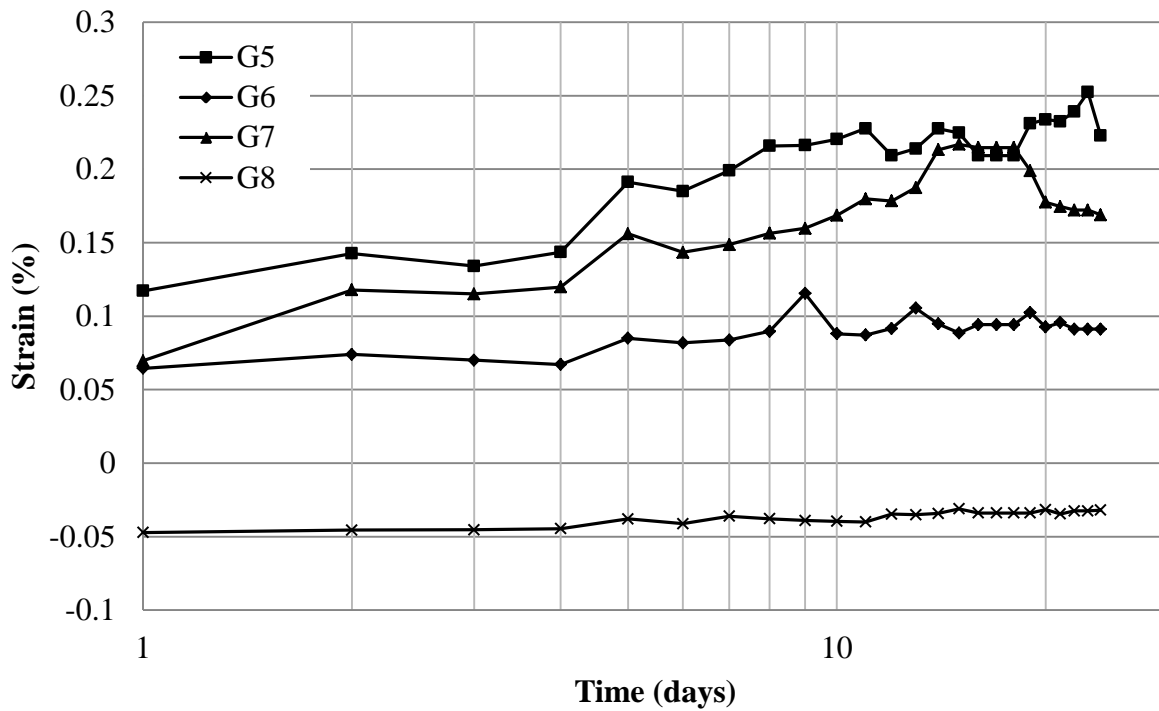


**FIGURE 3.25**  
Circumferential and Radial Strains on the Plastic Surface at the Ribs under a Sustained Load

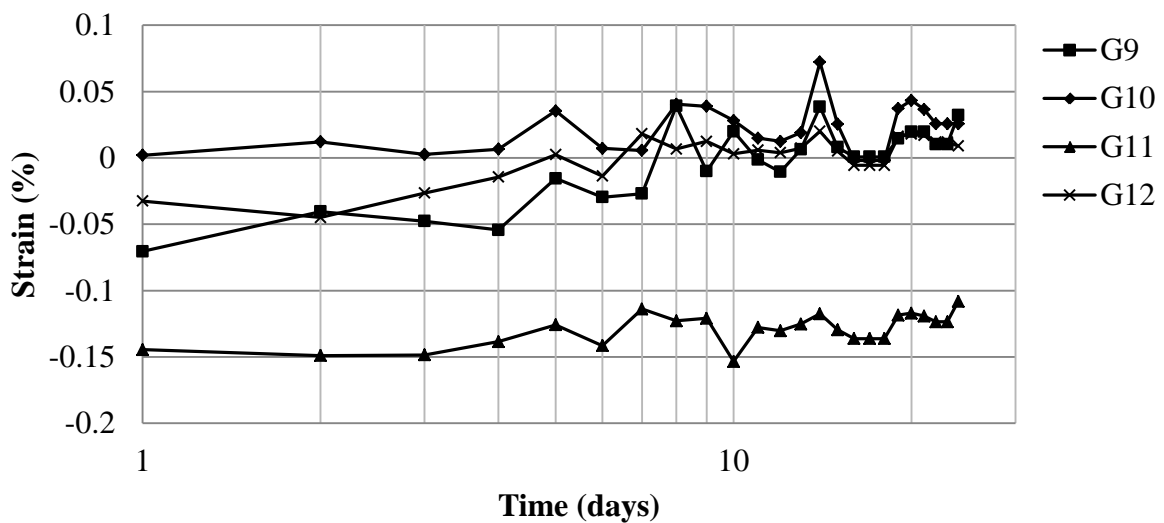


**FIGURE 3.26**  
Circumferential and Radial Strains on the Plastic Surface at the Valley under a Sustained Load

### 3.1.6 Summary

The various tests were conducted in air on the SRHDPE pipes in this study to evaluate properties of the pipes. The following conclusions can be drawn from this study:

#### 3.1.6.1 Parallel Plate Tests

1. Parallel plate test results show that the SRHDPE pipes investigated meet both minimum pipe stiffness and buckling limit criteria according to ASTM F2562/F2562M. The average bending stresses in the steel ribs were determined as 81 and 72 ksi at the springline and crown, respectively.
2. The pipes started yielding at approximately 6% vertical deflection to pipe diameter and reached the ultimate load capacity at approximately 10% vertical deflection. These numbers are close to those obtained by Schluter and Shade (1999) for the flexible metal pipes.
3. The vertical deflection of the SRHDPE pipe tested in the parallel plate load tests was approximately 1.25 times the horizontal deflection.
4. The photogrammetry method became effective to obtain the deflected shapes of the pipe under loading. The deflected shape of the SRHDPE pipe was found to be elliptical. The LiDAR Scanner can also be used to obtain the deflected shapes of pipe only if the point of interest is not rapidly changing.
5. The strains measured on the steel showed that the pipe had out of plane buckling on the ribs of the pipe wall at high level of load. The measured strains on plastic ribs were higher than strains of the steel during loading, indicating the strain incompatibility of steel ribs and plastic during the loading.

#### 3.1.6.2 Stub Compression, Beam, and Creep Tests

1. Based on the stub compression test data, the profile wall of the pipe could resist a load of 1,077 lbf/in and the average equivalent modulus of elasticity of the profile wall ( $E_{wall}$ ) under compression was found to be 3,000 ksi.
2. In the three point bending test, the equivalent bending stiffness of the pipe section was found to be  $2.6 \times 10^8 \text{ lb} \cdot \text{inches}^2$ .



3. The SRHDPE pipe deformed with time under a sustained load in air. As a result, the stiffness factor (EI) of the pipe decreased with time. The pipe deformation and strain data showed that the rate of stiffness factor (EI) reduction decreased with time within one month.

### 3.2 Soil Types and Properties

#### 3.2.1 Clayey Soil and Its Characteristics

The clayey soil used for the surrounding soil of the trench in the test box was fat clay. The properties of the clayey soil were evaluated through various laboratory tests conducted at KU, including hydrometer, Atterberg limits, specific gravity, compaction, and unconfined compression tests. The grain-size distribution of the soil was determined using the hydrometer test performed in accordance with ASTM D422-63 and is shown in Figure 3.27. The liquid limit of 54 % (Figure 3.28) and the plastic limit of 26% were obtained from the Atterberg limits tests following ASTM D4318-05. Based on the Atterberg limits and the grain size distribution, the clayey soil was classified as a fat clay (CH) according to the Unified Soil Classification System (USCS). The soil specific gravity of 2.71 was obtained following ASTM D854-10.

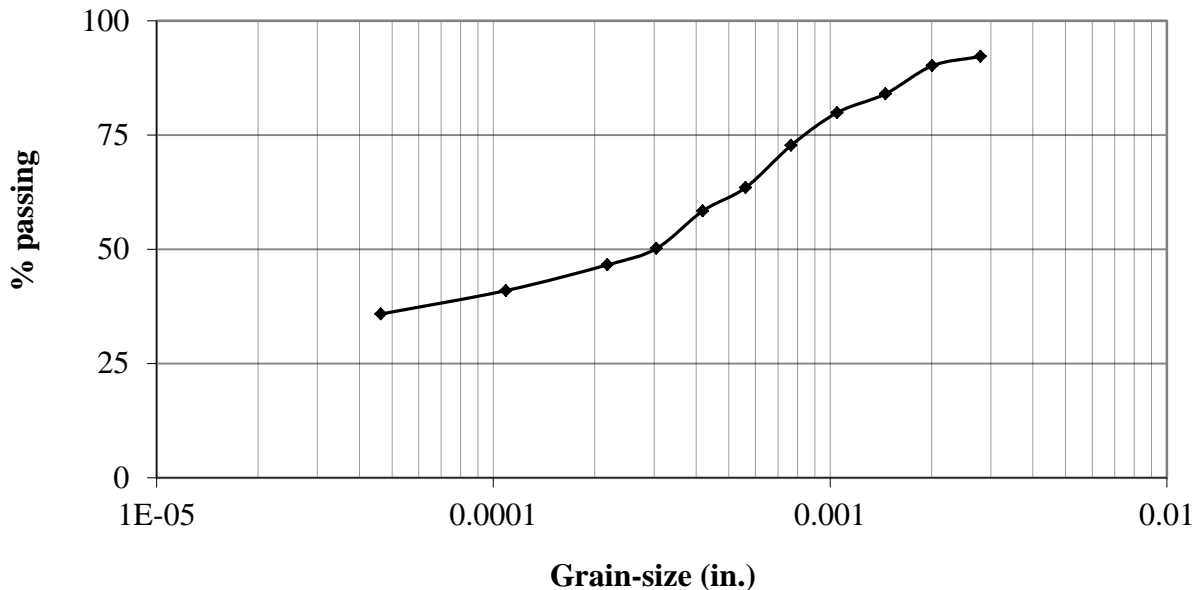


**FIGURE 3.27**  
**Grain Size Distribution of the Clayey Soil**

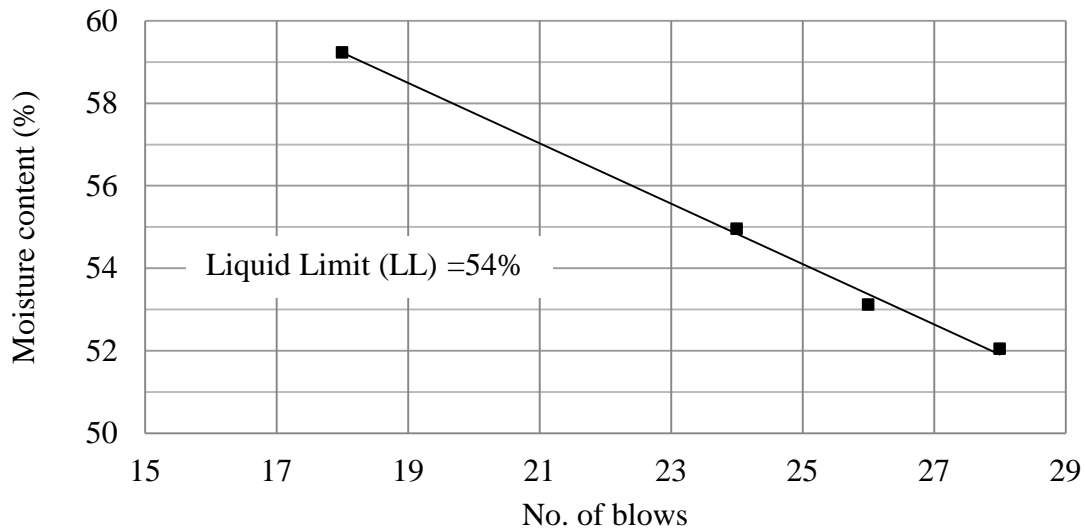


**FIGURE 3.28**  
**Flow Curve of the Clayey Soil**

The standard Proctor test was conducted on the soil in accordance with ASTM D698-07. The maximum dry density was determined to be  $97.8 \text{ lb/ft}^3$  and its corresponding optimum moisture content (OMC) was 24%. Modified compaction tests were also conducted. The maximum dry density was determined to be  $104 \text{ lb/ft}^3$  and the optimum moisture content was 21%. Unconfined compression tests (ASTM D 2166), CBR tests, and vane shear tests were also carried out. A correlation between the CBR value and the vane shear strength ( $c_u$ ) was established ( $c_u = 298 \text{ CBR}$ , where  $c_u$  is in psf and CBR in percentage). The compaction curves, vane shear strengths, and CBR values are shown in Figure 3.29.

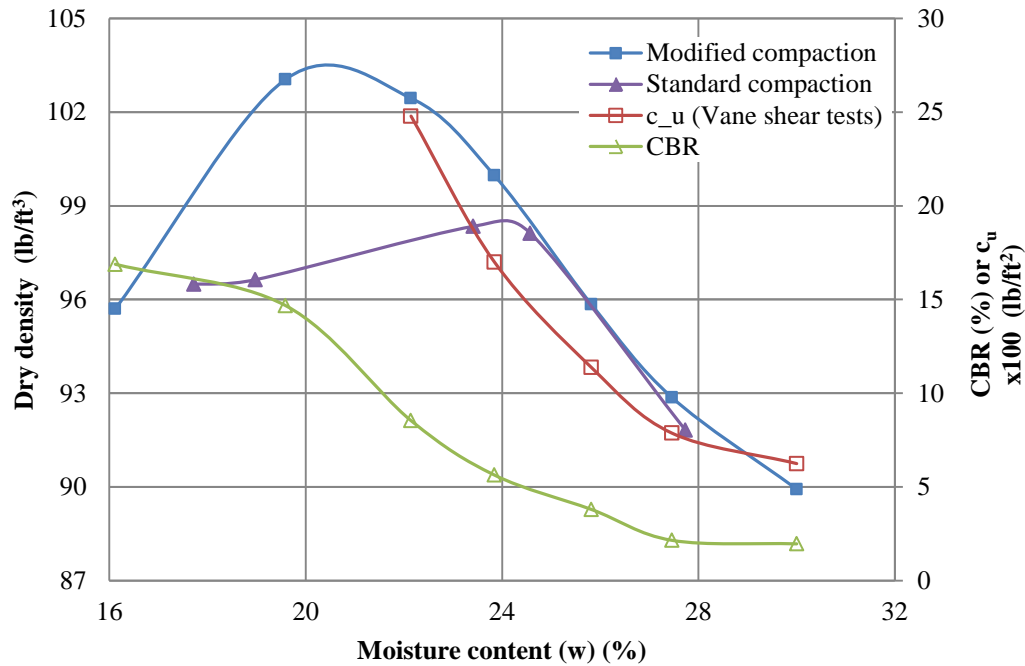


**FIGURE 3.29**  
Densities, Vane Shear Strength, and CBR Curves

### 3.2.2 Bedding and Backfill Soils and Their Characteristics

#### 3.2.2.1 Sand

Kansas River sand is a poorly-graded sand based on the USCS, which was used as the backfill and bedding materials in two box tests. Figure 3.30 shows the grain size distribution of this sand, which had a mean size of 0.022 inches, a uniformity coefficient  $C_u$  of 3.18, and a curvature coefficient  $C_c$  of 0.93. The minimum and maximum unit weights were 102 and 120 lb/ft<sup>3</sup> based on the minimum and maximum density tests conducted in accordance with ASTM D4254-00 and ASTM D4253-00, respectively. The minimum and maximum density values were used to evaluate the relative density of the sand. The relative compaction of the sand was correlated to the relative density using the relation,  $R = 80 + 0.2D_r$ , suggested by Lee and Singh (1971). The peak frictional angle of 37° was obtained by the direct shear tests on the sand compacted at 70% relative density (ASTM D3080). A small box plate-loading test was carried out to estimate the modulus of the Kansas River sand compacted at 70 % relative density as 2,027 psi.

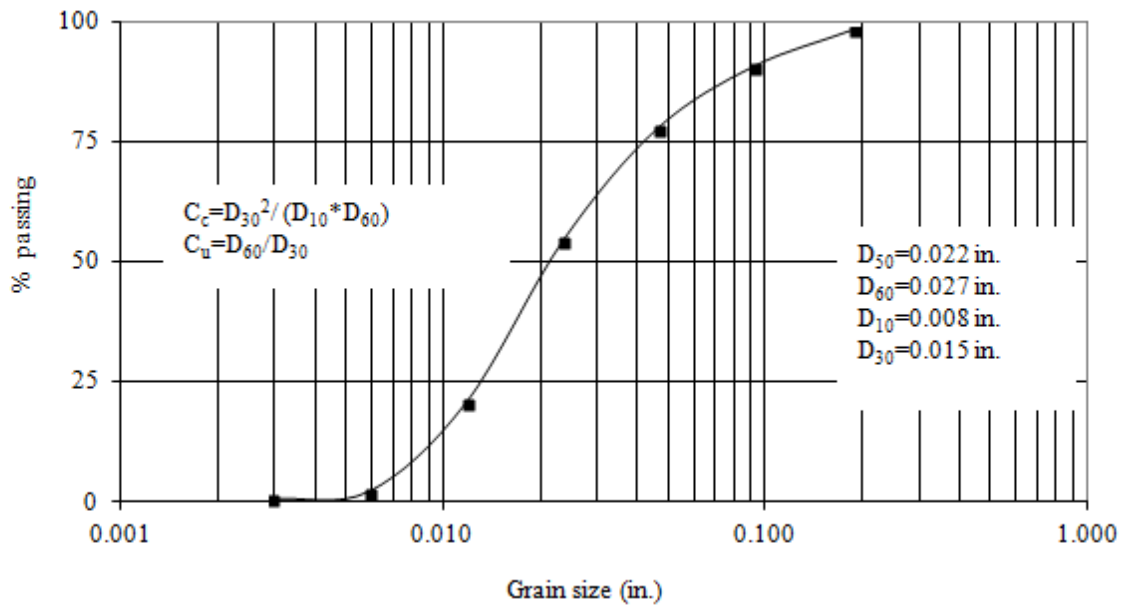


**FIGURE 3.30**  
**Grain Size Distribution of the Sand**

#### 3.2.2.2 Crushed Stone

Crushed stone, used as backfill and bedding materials in one box test, was well graded based on the USCS. Figure 3.31 shows the grain size distribution of the crushed stone. It had a mean size of 0.44 inches, a uniformity coefficient  $C_u$  of 2.3, and a curvature coefficient  $C_c$  of 1.01. The minimum and maximum unit weights of the sand were 86 and 103 lb/ft<sup>3</sup> based on the minimum and maximum density tests. The peak frictional angle of the crushed stone was 53°, obtained by direct shear tests (ASTM D3080), in which the crushed stone was placed by raining particles into the box from a height of approximately 2 ft. A small box plate-loading test was carried out to estimate the modulus of the crushed stone, which was determined to be 1,125 psi (the crushed stone was rained into the box from the height of approximately 2 ft). The raining of the crushed stone into the box from a two foot height resulted in the relative density of 50%.

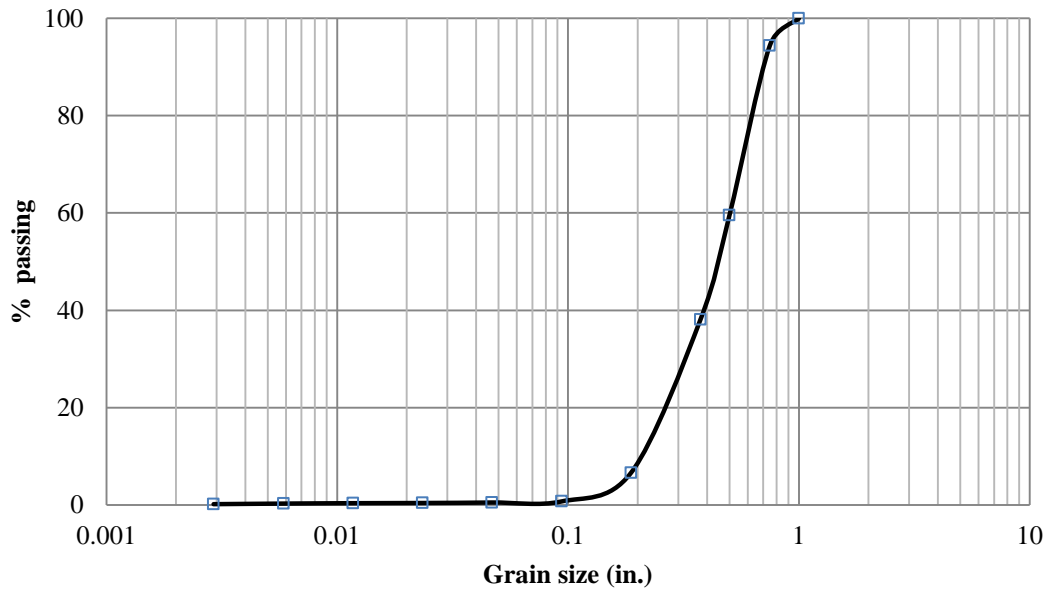
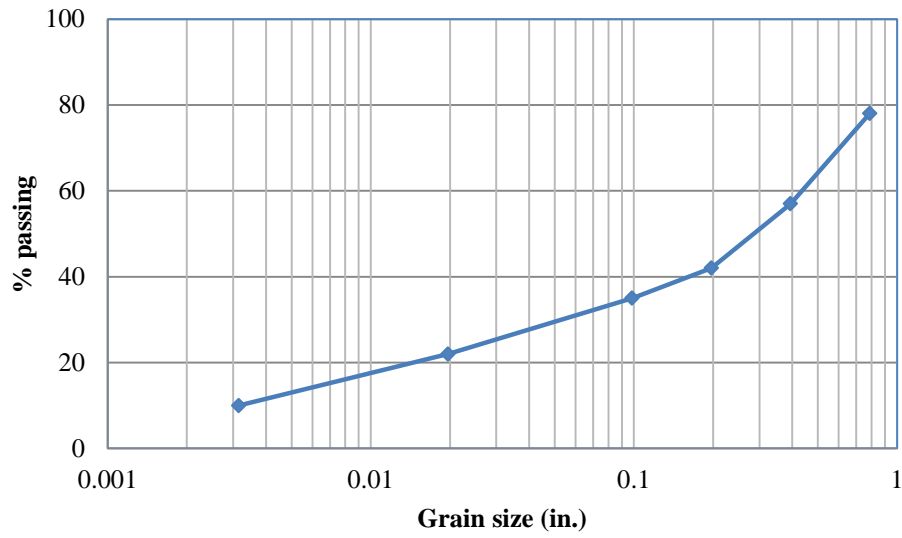


**FIGURE 3.31**  
**Grain Size Distribution of the Crushed Stone**

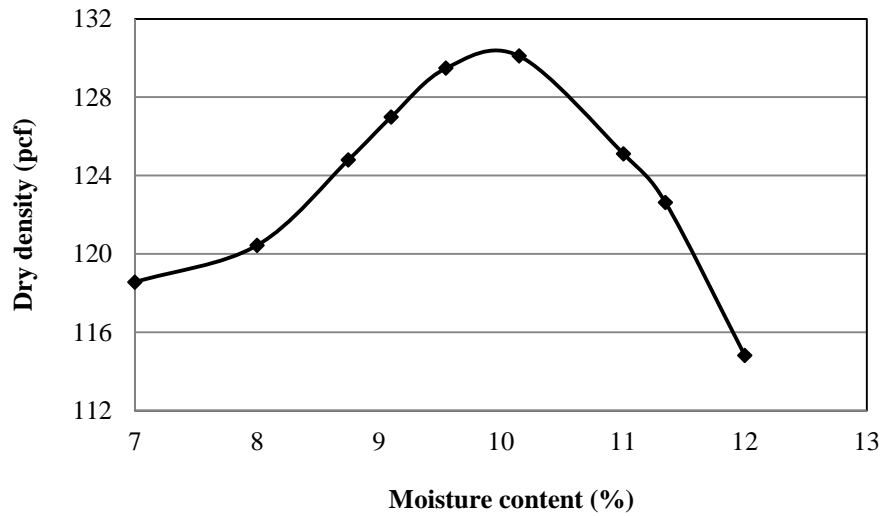
### *3.2.3 Base Course and Its Characteristics*

Kansas River sand and AB-3 aggregate were used as base courses in the box tests. The same sand used as a backfill material was also used as the base course for two box tests. The grain size distribution of the AB-3 aggregate is shown in Figure 3.32. The AB-3 aggregate was well-graded with a specific gravity of 2.69, a mean size of 0.27 inches, a uniformity coefficient  $C_u$  of 13.3, and a curvature coefficient  $C_c$  of 2.25. The fine particles of the AB-3 aggregate had a liquid limit of 20 and a plastic limit of 13. Figure 3.33 shows the compaction curve of the AB-3 aggregate by the standard Proctor compaction tests, which resulted in a maximum dry density of 130pcf at the optimum moisture content of 10%. Figure 3.34 shows the CBR results of the AB-3 aggregate. A small box plate-loading test was carried out to estimate the modulus of the AB-3 aggregate compacted at the 95 % maximum unit weight as 5,279 psi.



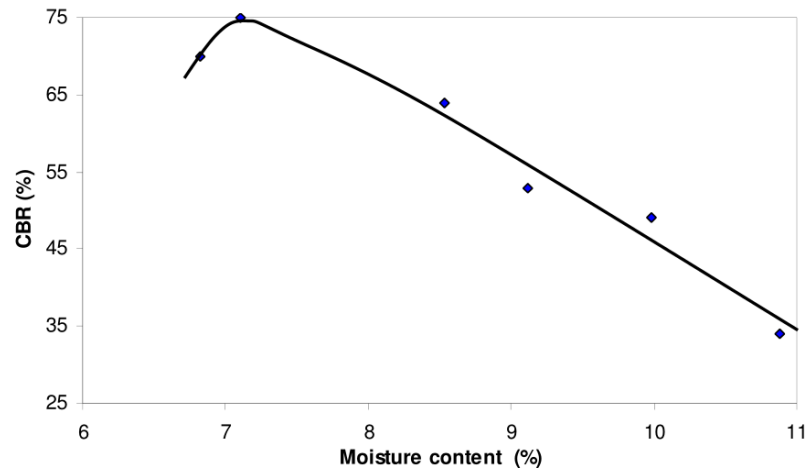
(Source: Pokharel 2010)

**FIGURE 3.32**  
**Grain Size Distribution Curve of the AB-3 Aggregate**



(Source: Pokharel 2010)

**FIGURE 3.33**  
**Standard Proctor Compaction Curve of the AB-3 Aggregate**



(Source: Pokharel 2010)

**FIGURE 3.34**  
**CBR Curve of the AB-3 Aggregate**

## **Chapter 4: Large Scale Plate Loading Box Test**

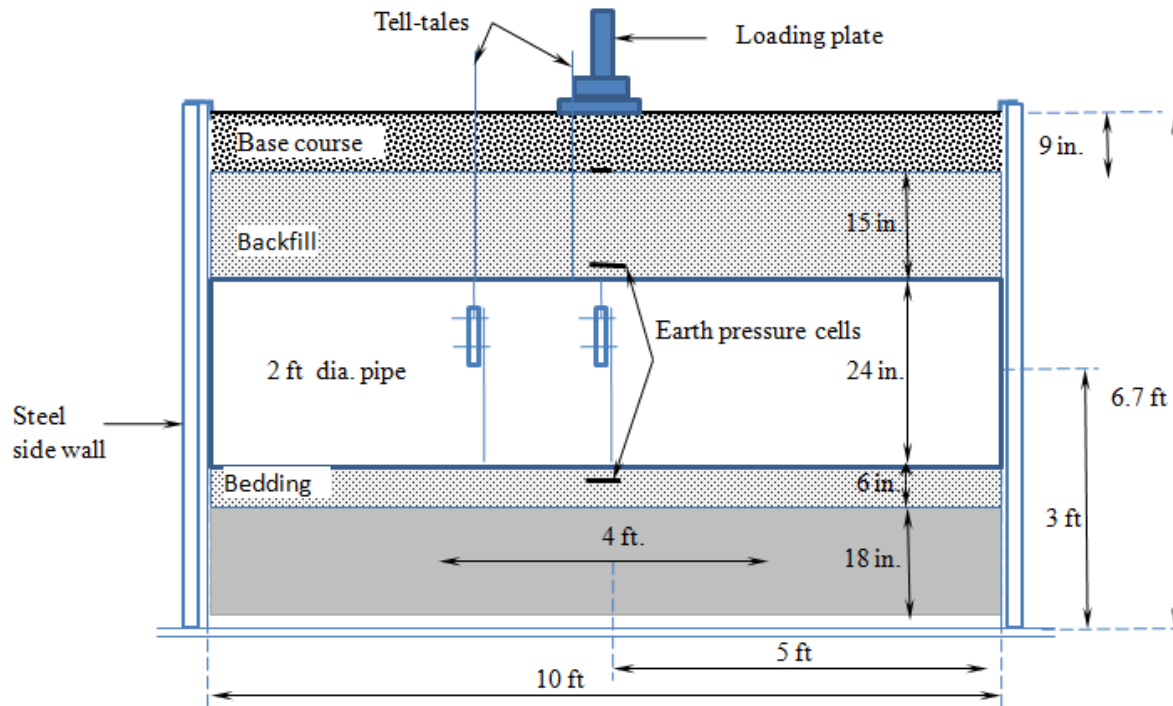
Large-scale plate loading box tests were conducted in a large geotechnical testing box to evaluate the performance of the SRHDPE pipes under a shallow cover during the installation and loading (static and cyclic) conditions. To acquire the data from the experiment, extensive instrumentation including strain gages, displacement transducers, pressure cells, and tell-tales were installed. The preparation of the trench, bedding, backfilling, and soil cover followed the 2007 Kansas Department of Transportation Culvert and Pipe Specifications and the 1998 AASHTO LRFD Bridge Construction Specifications. Several tests, such as moisture content measurements, vane shear tests, light weight deflectometer (LWD) tests, and dynamic cone penetrometer (DCP) tests were conducted to ensure the consistency of the test sections.

### **4.1. Large Geotechnical Testing Box and Test Sections**

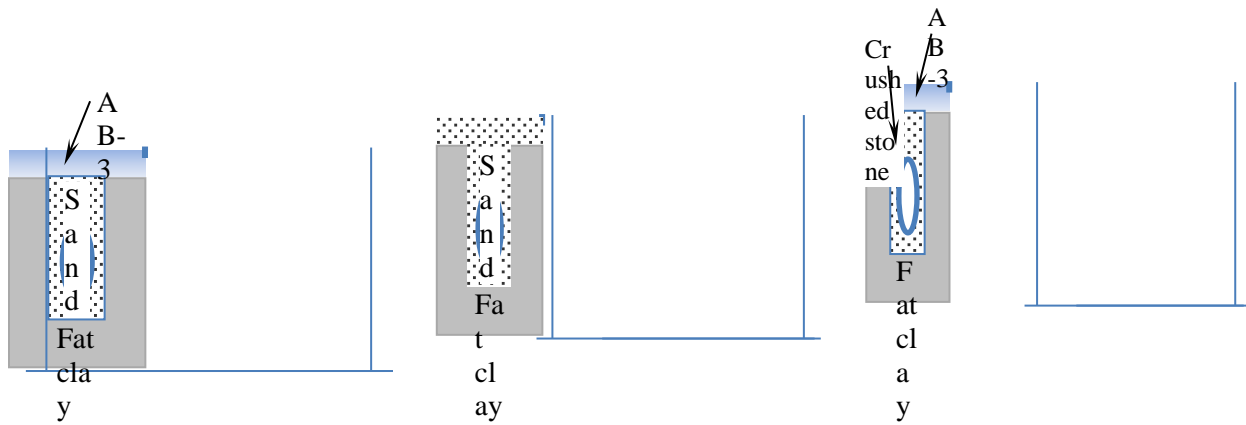
Figure 4.1 shows the large geotechnical steel box used in this research, which was extended in length to 10 ft from the existing steel box (7ft long, 6.6 ft wide, and 6.6 ft high) to minimize the boundary effect on test results. Three side walls and the base of the box were fixed. The front wall was detachable with several 6 inch high steel channel sections fixed by nuts and bolts. The height of the front wall was increased with each fill lift during the preparation of the test section by adding the detachable channel sections. Figure 4.2 shows the cross-section and longitudinal test sections of the box with extensive instrumentation. The test sections had a trench of 6.3 ft long, 4 ft wide, and 4.5 ft deep in the fat clay. The trench consisted of 6 inch thick bedding material, 2 ft backfill, and 2 ft soil cover including a 9 inch thick base course. Sections of twenty-four inch diameter SRHDPE pipes were inspected and selected based on their glossy appearance, no chalking, no sticky or tacky materials, and no blisters, voids, or other defects. The pipes were then cut into a length of 6 ft 4 inches by a hand-held reciprocating saw. Three box tests were conducted; including the first test with sand as the backfill and the AB-3 as the base course, the second test with the sand as both the backfill and the base course, and third test with the crushed stone as the backfill and the AB-3 as the base course.







b) Longitudinal section



c) Test 1

d) Test 2

e) Test 3

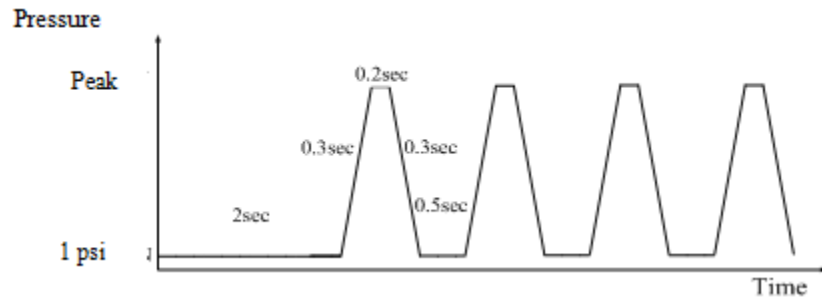
**FIGURE 4.2 Continued**  
**Plate Loading Test Sections**

## 4.2 MTS Loading System

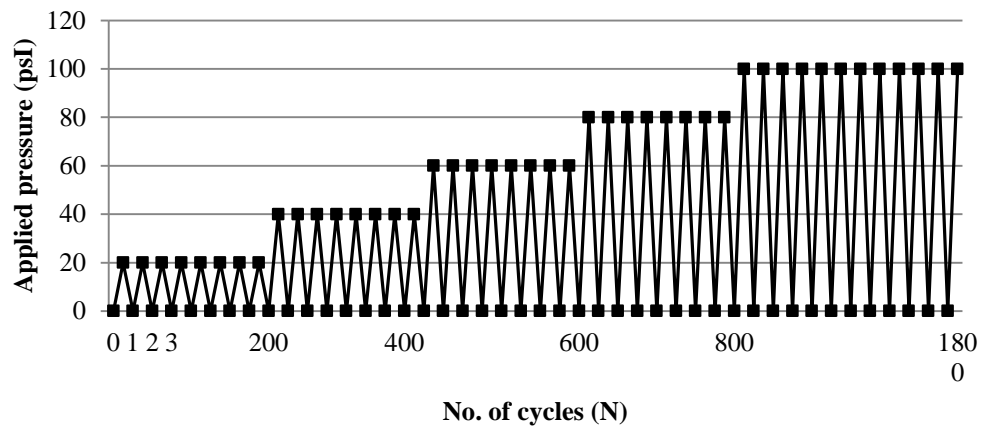
A servo hydraulic MTS loading system consisting of a steel loading frame, a hydraulic actuator, and a servo-control unit connected to a data acquisition system and a hydraulic control valve, was used to apply static and cycle loads on test sections prepared in the large geotechnical testing box. The load actuator has a 55 kip capacity. The static and cyclic loads were applied as shown in Table 4.1. Figures 4.3 shows the details of the cyclic loading applied to simulate the traffic loading with increasing intensities. Each cyclic load had a trough value of 1 psi, which was applied to keep the plate in contact with the surface and to prevent impact loading on the surface. The loading wave frequency was 0.77 Hz. A 1 ft diameter loading plate was connected to the actuator to apply the load. The loading plate had a 1.18 inch thick steel plate with a 0.4 inch thick rubber base attached at the bottom to simulate a rubber tire contact. Figure 4.4 shows the loading plate used in this research.

**TABLE 4.1**  
**Loading Increment and Magnitude**

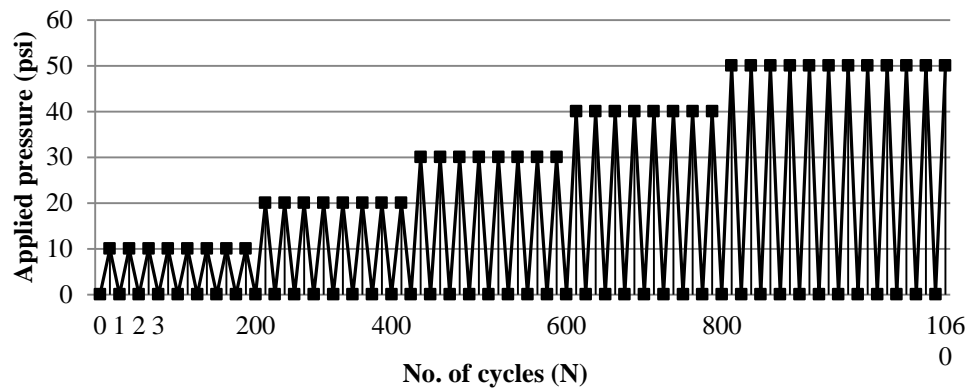
Test no	Description	Static loading (psi)		Cyclic loading (psi)	
		Increment	Max.	Increment peak ( each 200 cycles)	Max. Peak (cycles)
Test 1	Sand as bedding, backfill, and AB-3 as a base coarse	10	80	20	100 (1000 cycles)
Test 2	Sand as bedding and backfill, and base course	5	50	10	50 (260 cycles)
Test 3	Crushed stone as bedding and backfill and AB-3 as a base course	10	100	20	100 (1000 cycles)



(a) Cyclic loading wave form



(b) Cycle loading for Test 1 and 3



(c) Cycle loading for Test 2

**FIGURE 4.3**  
**Cyclic Loading Details**



**FIGURE 4.4**  
**Loading Plate**

### **4.3 Instrumentation**

The instrumentation used in the box tests included displacement transducers, strain gages, earth pressure cells, and tell-tales to capture the response of the pipes during the installation and loading as described in Sections 4.3.1 through 4.3.3.

#### ***4.3.1 Displacement Transducers and Tell-Tales***

Five displacement transducers, manufactured by Tokyo Sokki Kenkyujo, Co., Ltd, Japan, were used to measure the changes in vertical and horizontal diameters during the installation and loading. The transducers were fixed at a center of the pipe section and 1 ft away from the center as shown in Figure 4.5. The transducers were fixed to the pipe wall by replacing original caps of the transducers with M2.5 flat head machine screws which had a diameter of 0.1 inches, a length of 0.47 inch, and a thread size of 0.018 inches. Small holes of approximately 0.079 inches were drilled to fasten the displacement transducers to the pipe wall.



**FIGURE 4.5**  
**Displacement Transducers inside the Pipe Section**

Two string pots were used to measure the vertical displacements of the crown of the pipe, at the center and 1 ft away from the center, through the two tell-tales as shown in Figure 4.6. Each tell-tale had a hollow metal tube of 0.25 inches in diameter with 0.016 inches wall thickness. A steel rod of 0.12 inches in diameter was inside the tube. The bottom of the steel rod was fixed to the pipe crown through the nut-bolt arrangement by drilling a small hole of approximately 0.16 inches in diameter on the pipe wall. The top of the rod was then tied to the string of a string pot, fixed on a rigid support. Figure 4.7 shows a schematic diagram of the displacement transducers and tell-tales. One displacement transducer was used to measure the settlement of the loading plate during the loading. In addition, one more displacement transducer was added for Test 3 to measure the settlement of the base course 1 ft away from the center in the direction of the pipe run.





**FIGURE 4.6**  
Tell-Tales Fixed on the Pipe Specimen

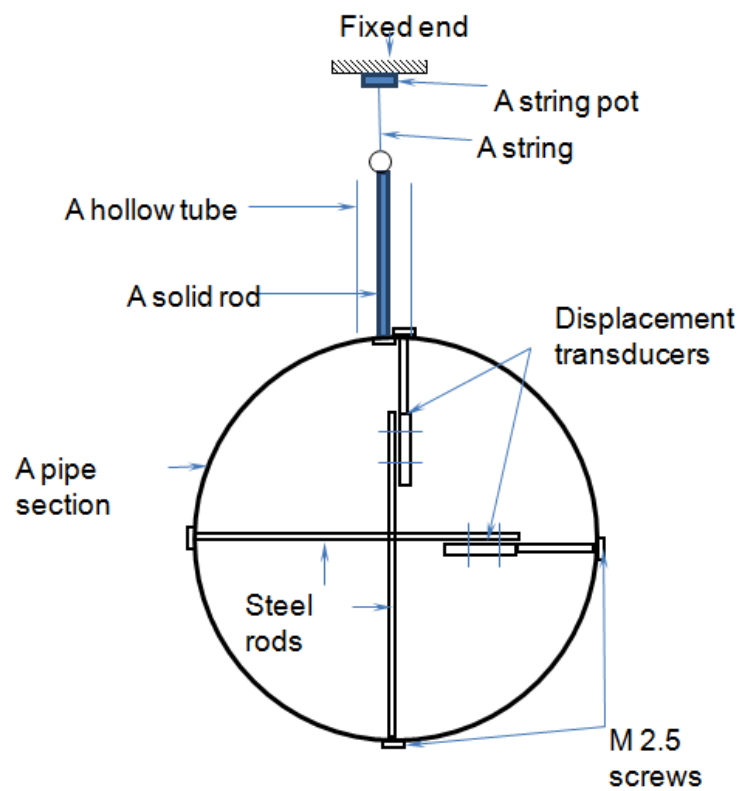


**FIGURE 4.7**  
Displacement Transducers for Deflection Measurements

### 4.3.2 Strain Gages

Uniaxial foil-type electrical resistance (C2A-13-250 LW -120) strain gages, manufactured by Vishay Precision Group, were used to measure the circumferential, radial, and longitudinal strains of the pipe at various locations. Figures 4.8 and 4.9 show strain gages installed outside and inside of the pipe section, respectively. The symbols, locations, and orientations of the strain gages fixed on the pipe are shown in Figure 4.10. Eight strain gages labeled without a prime (') sign were affixed on the steel at the center of the specimens at the crown, invert, and springline to determine both radial and circumferential strains. The plastic cover was removed at the desired locations to place the strain gages on the steel. Since the steel rib height was too small to attach the strain gages on the top of the rib, they were fixed at the neutral axis of the steel rib. Another set of eight strain gages labeled with single prime (') symbol were placed on the plastic at ribs. In addition, eight more strain gages labeled with a double prime (") symbol were placed on the plastic, inside and outside of the pipe, between the ribs (i.e., valley) to measure the strains in the plastic. For example, the strain gages notations ( $G_{SC1}$  and  $G_{SC2}$ ) without a prime symbol represent the strains on the steel. The first subscript letter of the notation represents the location of the strain gage (for example, "S" stands for springline, "I" for Invert, and "C" for crown). The second subscript letter represents the direction of strain measurement (for example, "C" and "R" stand for the circumferential and radial direction, respectively). Moreover, the third subscript letters, "1" and "2", represent the strain gages on the left and right sides of the rib or outside and inside of the valley, respectively. For example,  $G'_{SC2}$  represents the strain gage fixed on the plastic, at the left side of the rib, at the springline to measure the strain in the circumferential direction.

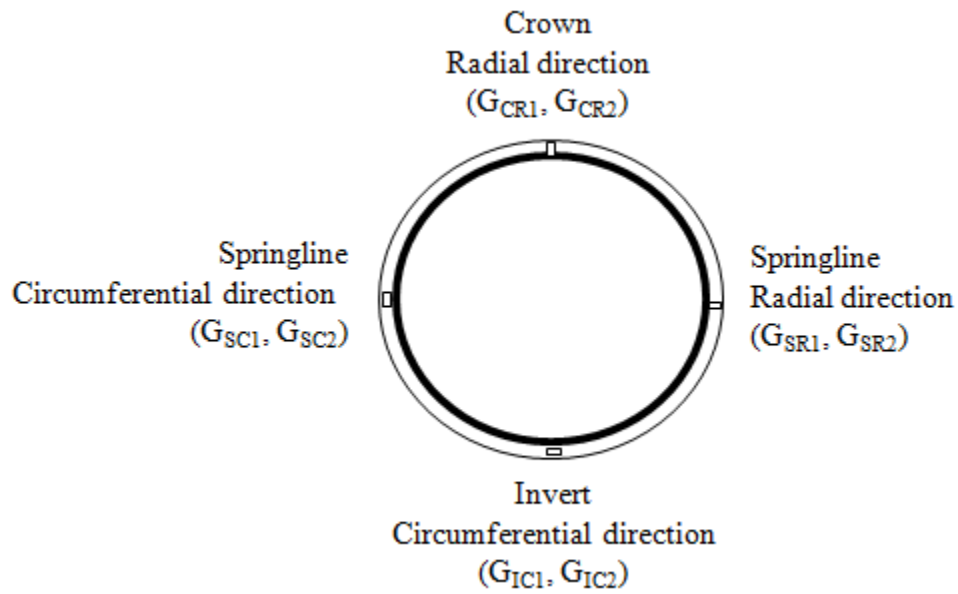




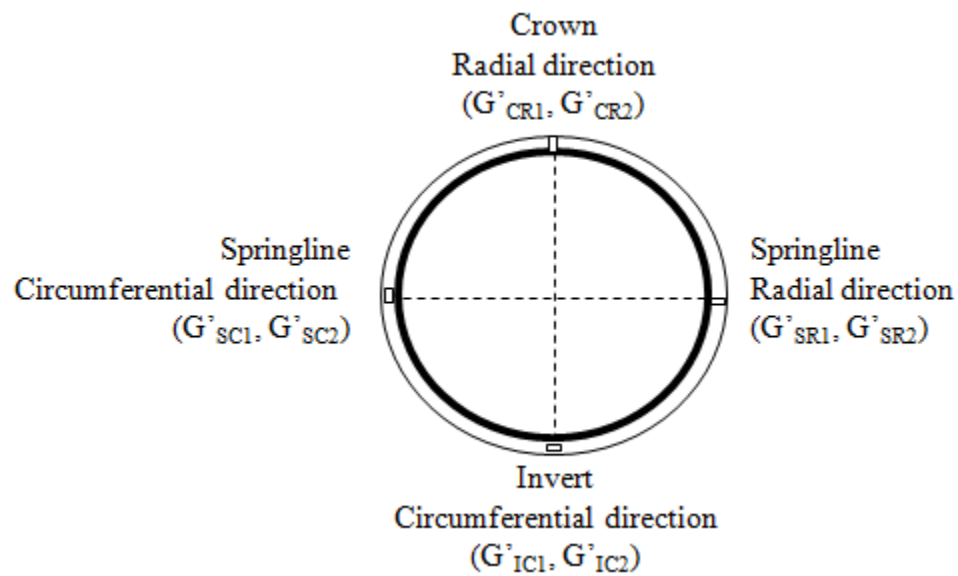
**FIGURE 4.8**  
**Strain Gages Fixed outside of Pipe Specimen**



**FIGURE 4.9**  
**Strain Gages Fixed inside of the Pipe Specimen**

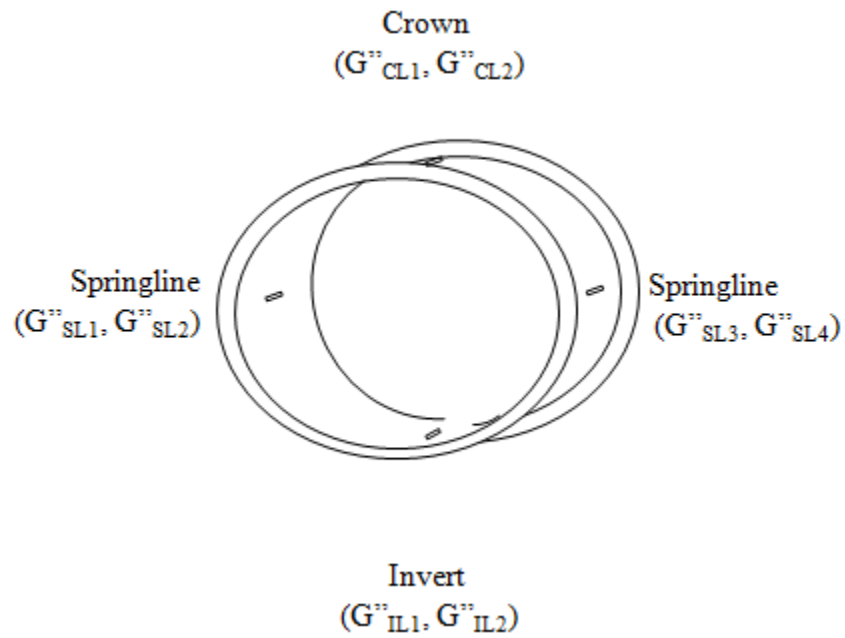


a) On the steel at ribs

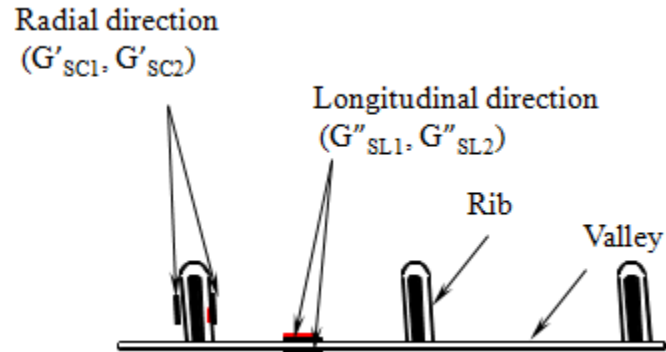


b) On the plastic at ribs

**FIGURE 4.10**  
**Symbols, Locations, and Orientations of Strain Gages on the Pipe**



c) In the longitudinal direction on the plastic at valley



d) Strain gages on the plastic surface

**FIGURE 4.10 Continued**  
**Symbols, Locations, and Orientations of Strain Gages on the Pipe X**

### 4.3.3 Earth Pressure Cells

Ten earth pressure cells with two capacities of 29 psi and 72 psi were installed at a central vertical plane around the pipe beneath the loading plate to measure pressures developed during the installation and loading. The notations, locations, and orientations of the earth pressure cells are shown in Figure 4.11. The subscripts of the notations represent the positions at which the earth pressure cells were placed. The subscript letters I, H, S, SH, and C stand for invert, haunch, springline, shoulder, and crown of the pipe, respectively whereas the numerical value gives the horizontal distance from the position defined by the subscript letter. For example, the notations,  $E_{C0}$  and  $E_{C6}$ , represent earth pressure cells placed at the crown along the central plane and along the plane 6 inch horizontal distance from the crown, respectively. Four pressure cells ( $E'_{H0}$ ,  $E'_{S0}$ ,  $E'_{SH0}$ , and  $E'_{S10}$ ) labeled with the prime (') symbol were installed for the horizontal earth pressure measurement whereas the remaining pressure cells without the prime (') symbol were installed for the vertical earth pressure measurement. Five pressure cells ( $E'_{I0}$ ,  $E'_{S0}$ ,  $E'_{SH0}$ ,  $E_{C0}$ , and  $E_{C6}$ ) shown in rectangular shapes with solid fill were used for Test 1 and 2. After analyzing Test 1 and 2 data, the decision was made to add more pressure cells, which were shown in rectangular shapes without solid fill, to capture the additional information of the pressure distribution around the pipe.

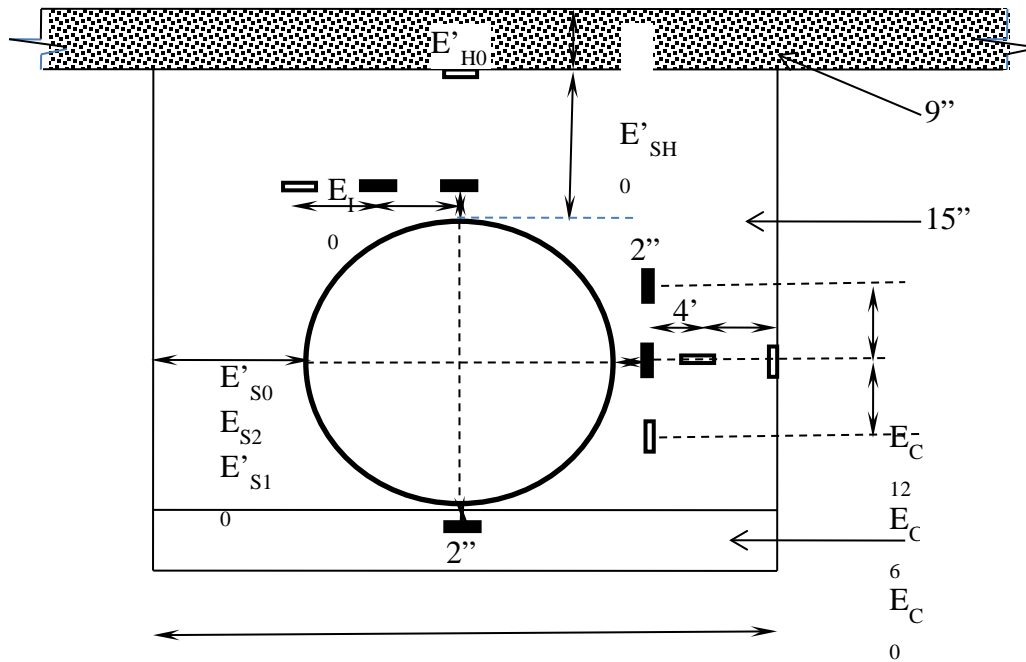


**FIGURE 4.11**  
**Earth Pressure Cells around the Pipe Section**

#### 4.4 Data Acquisition System

Four smart dynamic DC-204R data recorders with a manual channel selector were used to record the earth pressures around the pipe, strains at various locations on the steel and plastic, and deflections of the pipe.

#### 4.5 Construction of Test Section

The test sections were constructed in the large geotechnical testing box following the test conditions proposed by Brachman et al. (2008). The detail construction procedure was described in Sections 4.5.1 to 4.5.3.

##### 4.5.1 Construction of Test Section 1

###### 4.5.1.1 Surrounding Soil

Prior to the placement of the fat clay in the box, the walls of the box were covered with a polyethylene plastic sheet to reduce the possible friction at the soil-steel interface. The reduction of the friction at the soil-steel interface may reduce the boundary effects on the test results.

Moreover, the plastic-covered walls also helped to keep the moisture content of the soil constant during the construction and testing of the test sections. The walls of the box were then marked to assist the compaction of the soil in every 6 inch lift. The detachable channel sections from the front side of the box were removed for the access to the box. Then, wooden shoring as shown in Figure 4.12 was constructed to form the trench because excavation of the trench was not possible by a backhoe in the laboratory. Manual excavation of the stiff in-situ soil using only shovels would have been very difficult and taken a prohibitively long time. Loss of moisture from the wall of the trench during the trench construction would have made the trench wall stiffer. The clear width of the wooded shoring was maintained in such a way that the trench was 4 ft wide. The trench width was selected according to the 2007 KDOT Pipe and Culvert Specifications.

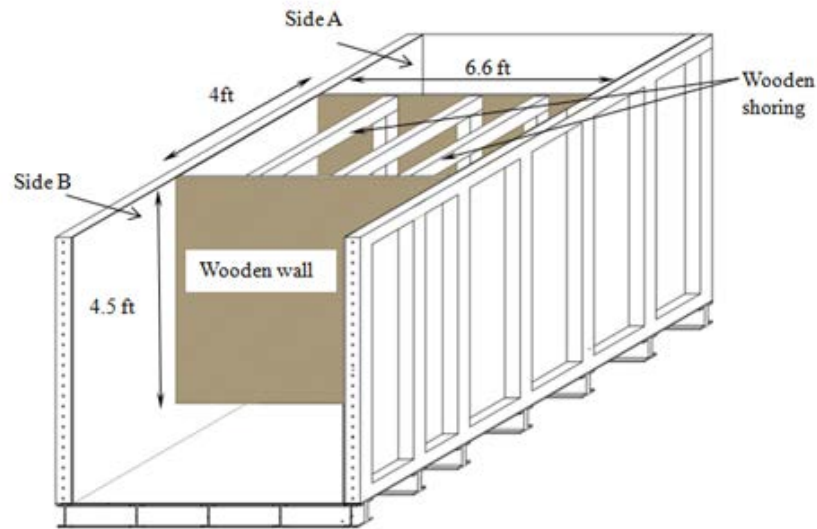


**FIGURE 4.12**  
**3D Perspectives Drawing of the Box with the Wooden**  
**Shoring to Make a Trench of 6.6 ft x 4 ft x 4.5 ft**

The fat clay was kept at the moisture content of approximately 26% and was placed in compacted lifts of 6 inch and compacted by the vibratory plate compactor TPE 1830 to achieve the desired CBR value between 2 and 3%. A Bosch electric jackhammer was also used to compact the soil near the sides and corners of the box because the vibratory compactor did not work around these areas. Figures 4.13 and 4.14 show VIBCO vibratory plate compactor and Bosch jackhammer, respectively. The fat clay was placed and compacted until the compacted fat

clay reached the height of 5 ft 3 inch on both sides the shored area and the height of 1.5 ft inside the shored area. The shoring was then removed, leaving a completed 6 ft long, 4 ft wide, and 3 ft 9 in deep trench. The compacted soil was covered carefully during the construction to keep the moisture content at 26% using the plastic sheet as shown in Figure 4.15.



**FIGURE 4.13**  
**Compaction of Surrounding Soil Using the Vibratory Plate Compactor**



**FIGURE 4.14**  
**Compaction of Surrounding Soil Using the Jackhammer**





**FIGURE 4.15**  
**A Polyethylene Plastic Sheet Placed to Cover the**  
**Exposed Fat Clay**

#### 4.5.1.2 Bedding

Kansas River sand was compacted to achieve a relative density of approximately 70% using the vibratory plate compactor and controlled by the volume weight approach. The soils required for the compacted 6 inch bedding layer were weighed by using the crane and weighing scale of 2,000 lb capacity. In each test the middle 33% of the bedding material in the direction of the pipe run was not compacted following the 2007 KDOT Pipe and Culvert Specifications. The bedding material was leveled and the earth pressure cell  $E_{10}$  was installed in the bedding material below the loading plate before the placement of the pipe in the trench as shown in Figure 4.16.



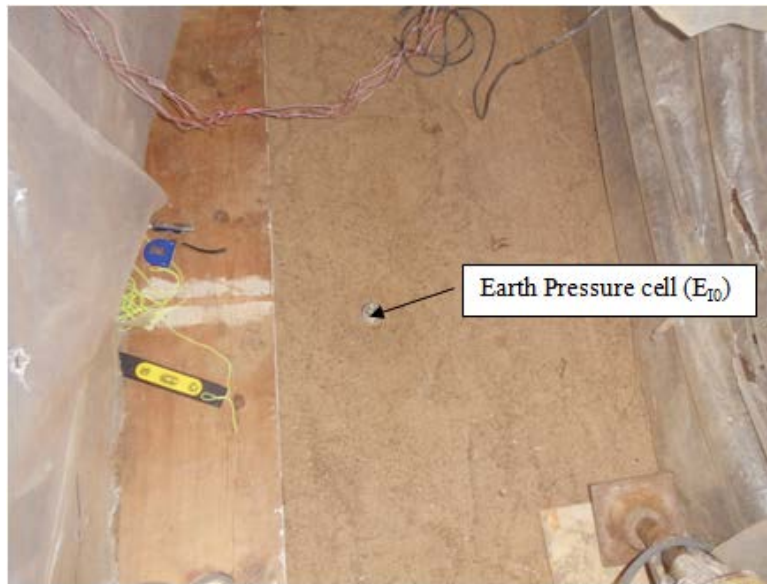


**FIGURE 4.16**  
**Bedding Material and the Earth Pressure Cell  $E_{10}$**   
**Installed at the Invert of the Pipe**

#### 4.5.1.3 Placement of Pipe

After the bedding was prepared, a pipe section instrumented with displacement transducers and strain gages was carefully installed, leveled, and aligned in the trench shown in Figure 4.17. The ends of the pipes were plugged by thin foam sheets to prevent the flow of the backfill into the pipe during the installation and loading as shown in Figure 4.17. All of the sensors were connected to the four separate DC-204R data recorders. The recorders were then adjusted and balanced to set all the initial values to zero. The measurements of the tell-tales were taken manually using the reference fixed point during the backfilling because the string pots described under the instrumentation section could not be placed during the construction of the test section.



**FIGURE 4.17**  
**Fully Instrumented Pipes in the Trench in Test**  
**Section 1**

#### 4.5.1.4 Backfilling

Kansas River sand was used as a backfill material and the backfilling was performed in 6 inch compacted lifts to get a relative density of approximately 70 %. The vibratory plate compactor and jackhammer were used for the compaction of the sand up to a height of 15 inches above the crown of the pipe. The compaction directly above the pipe surface was avoided to prevent possible damage of the pipe due to the compaction equipment. For each test, the haunch area was monitored to avoid a void in the haunch area. The backfilling was done in equal lifts on both sides of the pipe so as not to disturb the pipe alignment. Figure 4.17 shows the backfill placed up to the springline. During the backfilling, the earth pressure cells were installed around the pipe for each test as described in Section 4.3.3. Figure 4.19 shows the installation of the earth pressure cells at the springline during the backfilling. At the springline and shoulder, the earth pressure cells were placed vertically with a piece of plywood (2.5 inches x 3.5 inches) on the back of each earth pressure cell. The piece of plywood was attached to keep the earth pressure cell vertical during the construction of the test section. The readings of the strain gages, displacement transducers, and earth pressure cells were taken using the DC-204R recorders after completion of each lift during the backfilling. Tell-tale readings were taken manually.



**FIGURE 4.18**  
**Backfill up to the Springline in Test Section 1**

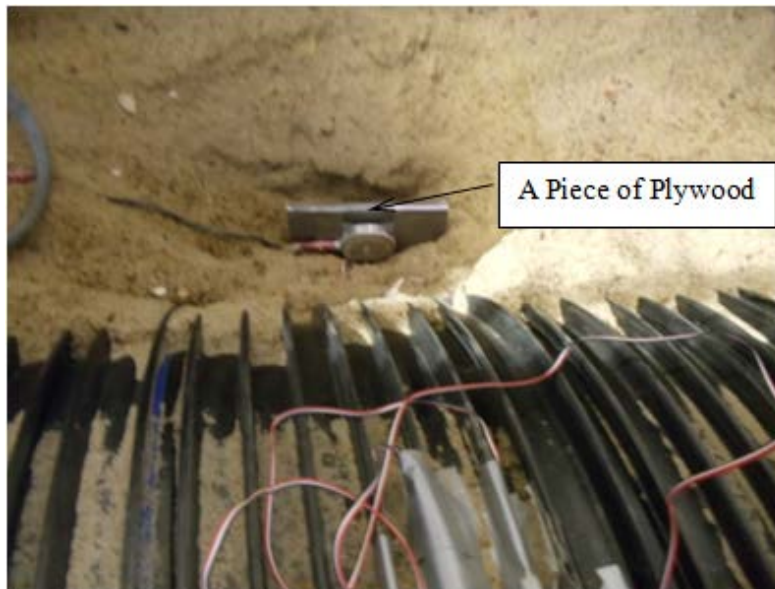


**FIGURE 4.19**  
**Earth Pressure Cells at the Springline in Test Section 1**

#### 4.5.1.5 Base Course Preparation

After the compaction of the backfill to the same height of the fat clay, A 9 inch thick base course (described in Section 3.2.3) was prepared. AB-3 aggregate was used as the base course in this test and was placed and compacted uniformly in two layers by the vibratory plate compactor and the jackhammer for several passes until desired densities were achieved. The AB-3 base

course was compacted at 95 % of the maximum density at a moisture content of around 9%. The quantity of soil required for the each compacted lift was controlled by the volume weight approach and weighed by the crane and weighing scale of 2,000 lb capacity. Figure 4.20 shows the compaction of the base course.



**FIGURE 4.20**  
**Compaction of Base Course Using the Vibratory**  
**Plate Compactor in Test Section 1**

#### *4.5.2 Construction of Test Section 2*

The surrounding soil, bedding, and backfill material were placed and compacted following the same procedures adopted in Test Section 1. Instead of the AB-3 base course, the Kansas River sand was used as the base course in this test. A 9 inch thick base course was compacted uniformly in two layers by the vibratory plate compactor and the jackhammer for several passes until the desired relative density of 70 % was achieved. The quantity of soil required for the each compacted lift was controlled by the volume-weight approach and weighed by the crane and weighing scale of 2,000 lb capacity.

#### *4.5.3 Construction of Test Section 3*

The surrounding soil and bedding were placed and compacted following the same procedures adopted in Test Section 1. However, instead of AB-3 aggregate, crushed stone was



used for the bedding and backfill material. Backfilling was performed by dumping the crushed stone (no compaction) in 6 inch lift. Figure 4.21 shows the backfill material placed up to the springline. The instrumentation was done as described in Section 4.3 with the additional earth pressure cells. Figure 4.22 and 4.23 show the earth pressure cells installed at the springline and at the crown with the piece of plywood and sand bag during the placement of the backfill. Each earth pressure cell placed vertically was attached with a piece of plywood (2.5 inches x 3.5 inches) on the back. The piece of plywood was attached to keep the earth pressure cell vertical during the construction of the test section. In addition, each earth pressure cell was covered with a sand bag. The sand bag was placed to avoid the uneven distribution of the aggregate contact on the sensor surface because the sensor area of the earth pressure cell with a 1.8 inch diameter would have few contact points for crushed stone with a  $\frac{3}{4}$  inch maximum particle size.



**FIGURE 4.21**  
**Backfilling up to the Springline in Test Section 3**



**FIGURE 4.22**  
**Earth Pressure Cells at the Springline in Test Section 3**



**FIGURE 4.23**  
**Earth Pressure Cells at the Crown in Test Section 3**

AB-3 aggregate was used as a base course for this test section. A 9 inch thick base course was compacted in two layers with the vibratory plate compactor and the jackhammer for several passes until the desired densities were achieved. The AB-3 base course was compacted at 95 % of the maximum density at a moisture content of around 9%.

A sketch of the cross section of the test sections is shown in Figure 4.24, which presents the compaction schedule of the backfill and the base course, and also includes the locations of the earth pressure cells.

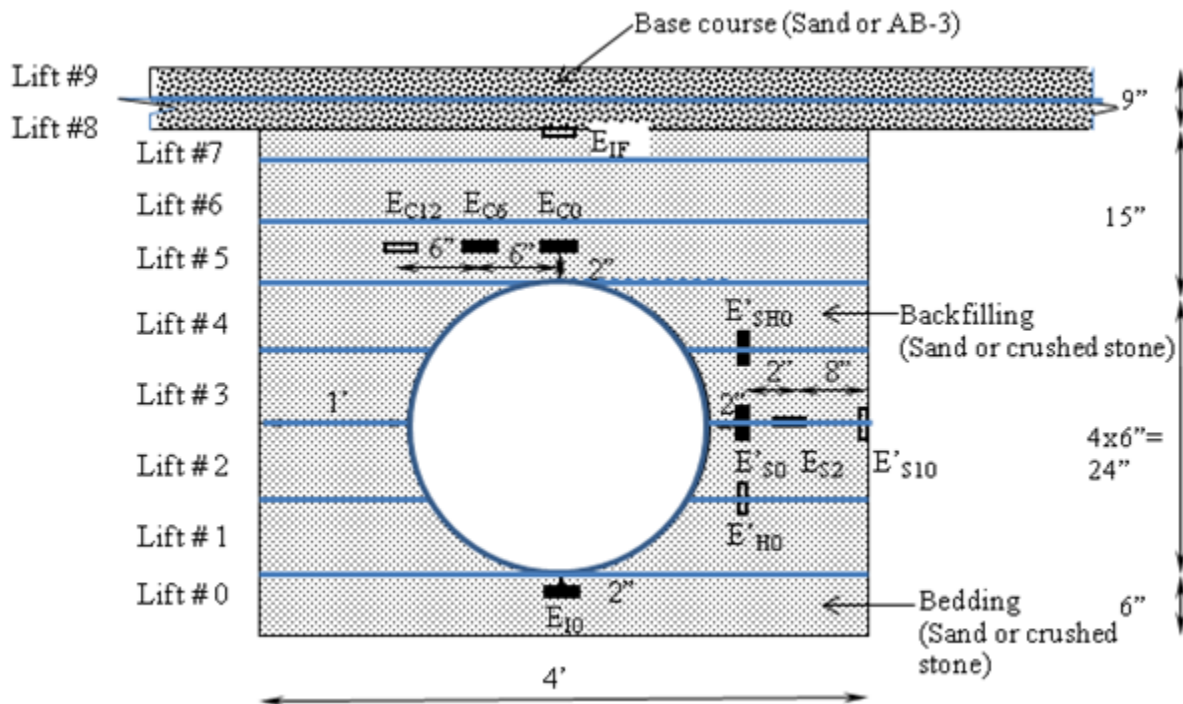


**FIGURE 4.24**  
**Cross Section of Test Section Including the Soil Lifts and Earth Pressure Cells**

## 4.6 Quality Control

The vane shear tests (ASTM D2573-08) were carried out on each compacted lift of the fat clay to keep the CBR value between 2 and 3 %. The relation,  $c_u = 298 \text{ CBR}$ , established in Section 3.2.1, was used to determine the CBR values from the undrained shear strength values measured from the vane shear tests. Figure 4.25 shows a picture taken during the vane shear test.

Non-destructive Light Weight deflectometer (LWD) tests were conducted over the compacted fat clay, the Kansas River sand, and the AB-3 aggregate at various locations during the preparation of the test sections as shown in Figure 4.26. The dynamic deformation moduli ( $E_{vd}$ ) obtained from LWD tests (using a 1 ft diameter plate) were in a range of 1,200 and 1,550



psi for the fat clay, 2,200 and 3,050 psi for the sand, and 4,700 and 7,050 psi for the AB-3 aggregate.



**FIGURE 4.25**  
**Vane Shear Test on the Fat Clay**



**FIGURE 4.26**  
**LWD Test on the Fat Clay**

After the preparation of the test sections, Dynamic Cone Penetration (DCP) tests were carried out from the top of the base courses to the depth at four different locations following ASTM D6591-03. The relationship between the CBR value at the depth of penetration and the penetration index in inches per blow of DCP is given in Equation 4.1 (Webster et al. 1992). The CBR profiles of the test sections obtained from the DCP tests are shown in Figure 4.27. The



average CBR value of the fat clay and the AB-3 aggregate, resulting from the DCP tests, were approximately 2.5 % and 20%, respectively.

$$CBR(\%) = \frac{292}{(PI \times 25.4)^{1.12}}$$

**Equation 4.1**

where PI= the penetration index

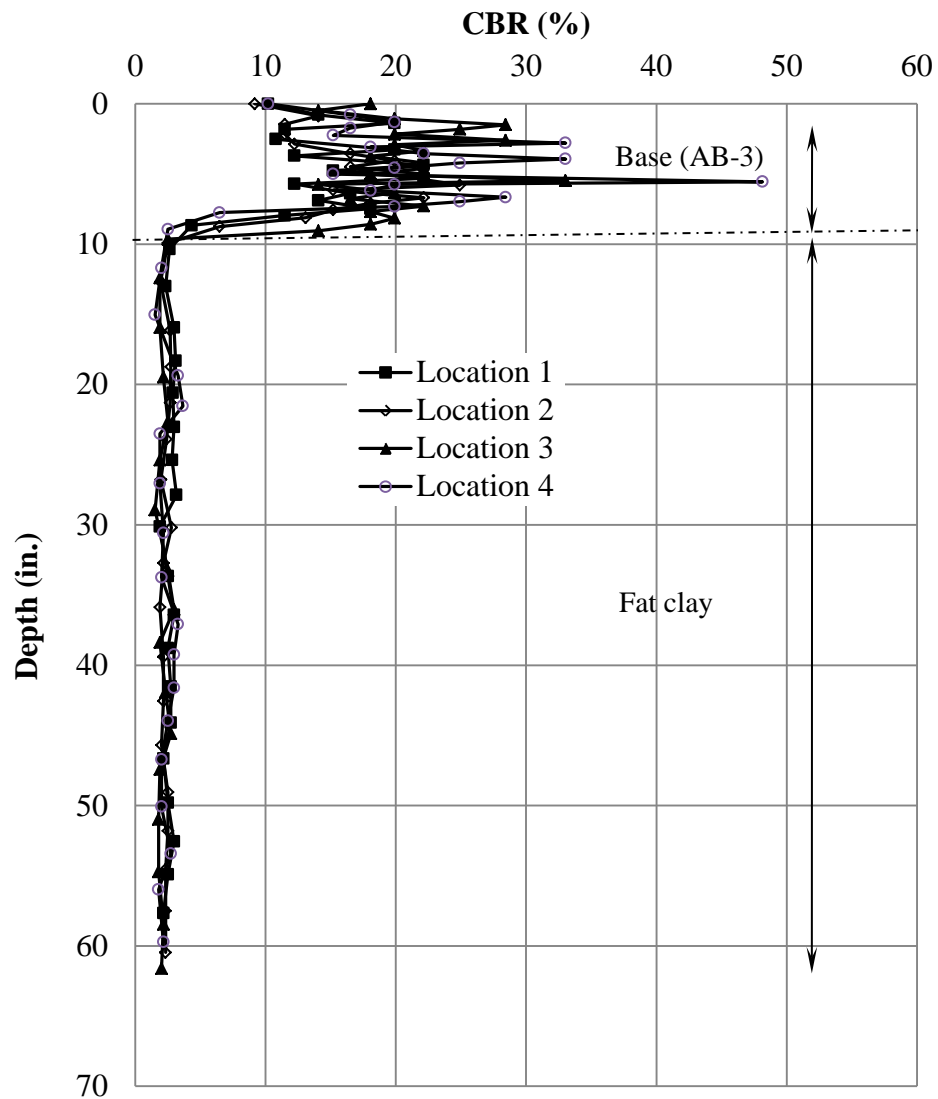


**FIGURE 4.27**  
**CBR Profiles in Test Section 1**

## 4.7 Data Collection

Figure 4.28 shows a test section ready for a plate loading test. All sensors were connected to the data acquisition system. The Multi Purpose Test (MPT) software was used to apply both static and cyclic loads as mentioned in Section 4.2. For each test of the pipe, the following data were collected:

- a) The applied load and displacement of the actuator
- b) The settlement of the loading plate from the displacement transducer
- c) The displacement of the pipe crown from the tell-tale
- d) The deflection (or change of diameter) at the center and 12 inches from the center of the testing pipe from the displacement transducers
- e) The pressure distribution around the pipe using the earth pressure cells
- f) The circumferential and longitudinal strains developed on the steel and plastic at the center of the pipe under the loading plate from the strain gages



**FIGURE 4.28**  
**Displacement Transducers Fixed to a Reference Beam**

## Chapter 5: Data Analysis and Results

This chapter contains a summary and analyses of the test results obtained from the three large-scale box tests. The test results include those obtained during the installation, static plate loading tests, and cyclic plate loading tests. The test results from static and cyclic plate loading tests were compared and they were also compared with available theories and results by others.

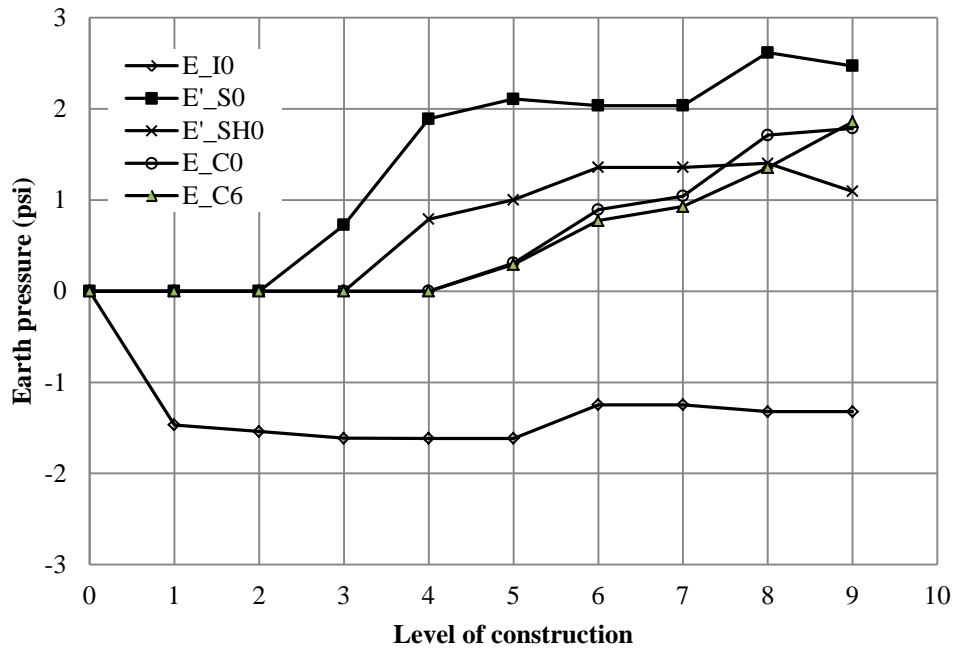
### 5.1 Test Results from Pipe Installation

This section discusses the experimental data collected through the instrumentation and monitoring of earth pressure cells, displacement transducers, strain gages, and tell-tales during the installation of the pipes. Since Test 2 used the same trench and the same backfill material as Test 1 and was prepared after removing the base course, the backfill material, and the pipe used in Test 1, no monitoring of sensors was taken during the re-construction of the section for Test 2. Therefore, only the installation results from Test 1 and Test 3 are presented herein. The Kansas River sand and the crushed stone were used as the backfill materials in Test 1 and 3, respectively. Both tests used the 9 inch AB-3 aggregate as the base course.

#### *5.1.1 Earth Pressure Results*

##### *5.1.1.1 Test 1*

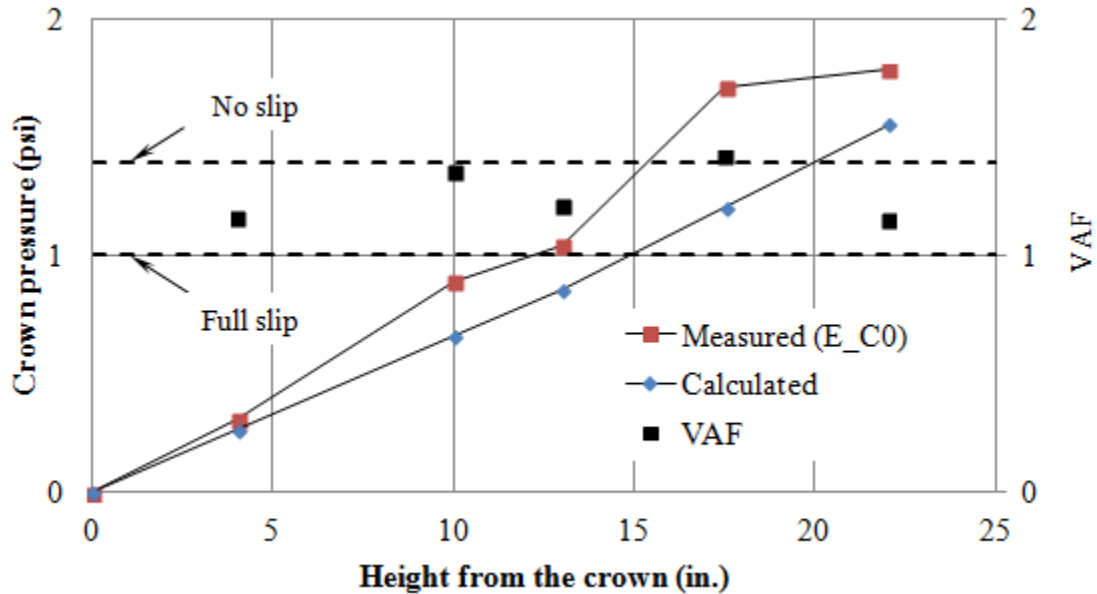
Figure 5.1 shows the pressures developed around the pipes against the levels of construction (labeled as 1 to 9 as shown in Figure 4.23). The earth pressure cells,  $E_{C0}$  and  $E_{C6}$ , fixed at the crown and 6 inches away from the crown measured similar earth pressures during the installation. The vertical pressure recorded by the pressure cell fixed at the invert ( $E_{I0}$ ) was negative. The negative pressure measured by  $E_{I0}$  continued decreasing slightly until the fill height reached 6 inches over the pipe crown (i.e., Level 5 of the construction) and then increased as the construction proceeded. This result is because all of the sensors were set to zero for initial readings after the placement of the pipe inside the trench. Therefore, the initial reading recorded by the earth pressure cell ( $E_{I0}$ ) due to the weight of the pipe was not considered. As the level of construction increased, the invert of the pipe moved upward and released the vertical pressure on the pressure cell ( $E_{I0}$ ).



**FIGURE 5.1**  
**Measured Earth Pressures around the Pipe During Installation in**  
**Test Section 1**

The overburden pressure  $E_{C0, cal}$  (i.e., the unit weight of the soil ( $\gamma_s$ ) x the thickness of the soil from the crown (H)) was calculated at the crown of the pipe. The pressure measured at the crown by the earth pressure cell ( $E_{C0}$ ) was then compared with the calculated overburden vertical pressure and are shown in Figure 5.2. The vertical arching factors (VAFs), calculated as the ratio of the measured pressure to the calculated pressure at the crown, are shown in Figure 5.2. The VAFs varied from 1.15 to 1.41 with average value of 1.26. As described by McGrath (1998), the SRHDPE pipe behaved similarly to a corrugated steel pipe based on the vertical arching factor and the hoop stiffness. In addition, the vertical arching factors calculated using the Burns and Richard no-slip and full-slip solutions (Equation 2.2 and 2.3) resulted in VAFs of 1.40 and 1.01, respectively. In this calculation, the hoop stiffness needed for the Burns and Richard solutions was estimated using Equation 2.4 based on the constrained modulus ( $M_s = 4,500$  psi), of the backfill (i.e., the Kansas River sand), the radius of the pipe, and the area and modulus of elasticity of the steel reinforcement. The constrained modulus,  $M_s$ , of the sand was back-calculated from the modulus of elasticity of the sand determined from the small plate loading test as described in Section 4.7. The vertical arching factors (VAF) from the measurement of the

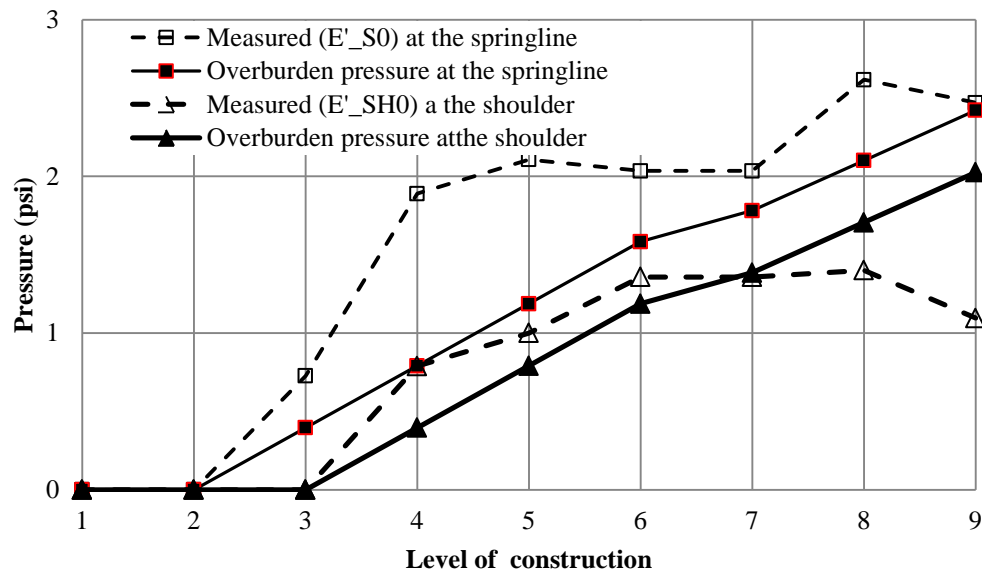
earth pressures on the crown were close to the vertical arching factor obtained from the Burns and Richard solutions for the no-slip case as shown in Figure 5.2. Therefore, the SRHDPE pipe should be designed based on a no-slip condition for the VAF value.



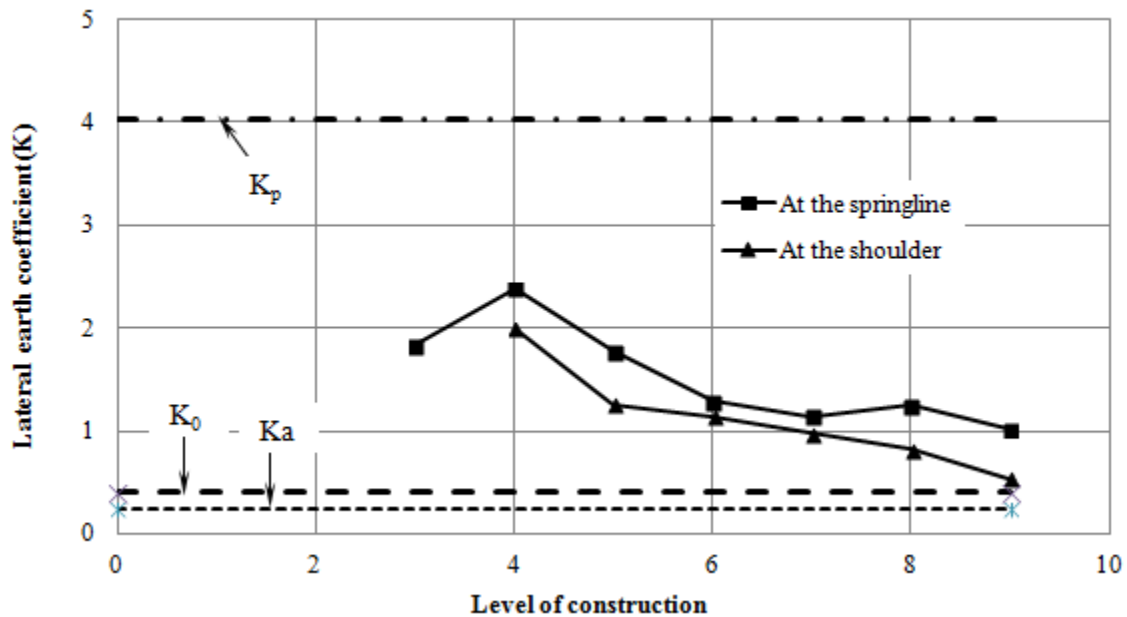
**FIGURE 5.2**  
**Comparison of Measured and Calculated Pressures at the Crown During Installation in Test Section 1**

Figure 5.3 shows the measured lateral pressures ( $E'_{s0}$  and  $E'_{sh0}$ ) and the calculated overburden pressures at the springline and shoulder. Figure 5.4 shows the coefficients of lateral earth pressure ( $K$ ) at the springline and the shoulder calculated as the ratio of the measured lateral pressures to the overburden pressures. Figure 5.4 compares the measured coefficients at the springline and shoulder with the lateral earth pressure coefficients,  $K_a$ ,  $K_o$ , and  $K_p$ , calculated using the friction angle of the sand of  $37^\circ$ . The measured coefficients ( $K$ ) were found to be between  $K_o$  and  $K_p$ . The coefficient ( $K$ ) was the highest at level 4 (i.e., when the fill height reached the crown of the pipe) and then decreased to a value of close the coefficient  $K_o$ . The higher values of the coefficients ( $K$ ), when the construction levels were close to the pipe, may be due to the higher effect of the compaction on the pipe. It can be concluded from Figure 5.4 that the lateral pressure generated by the backfill soil should be represented by the combination of

lateral earth force due to the backfill and a force generated by the compaction effort during the backfilling.



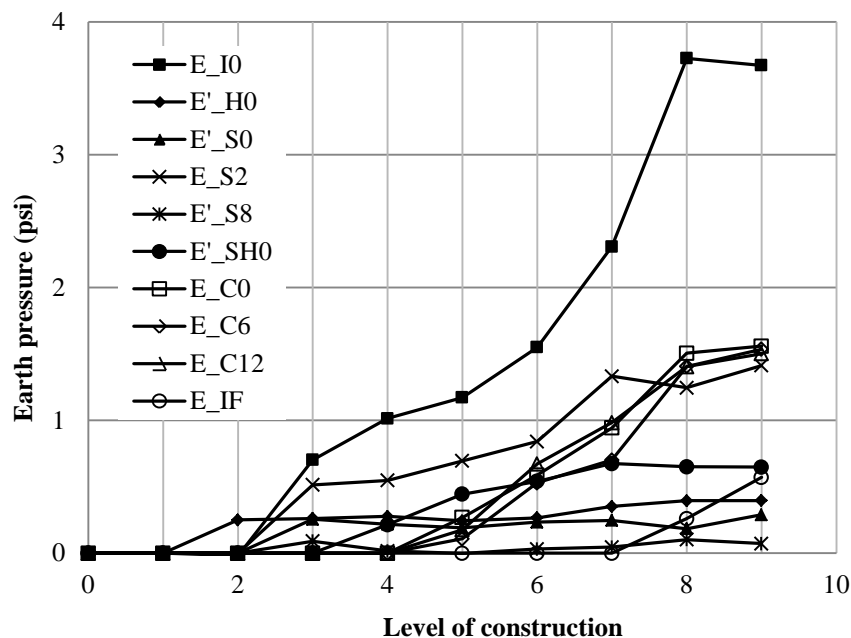
**FIGURE 5.3**  
Calculated Lateral Earth Pressure Coefficients (K) at the Springline



**FIGURE 5.4**  
Calculated Lateral Earth Pressure Coefficients (K) at the Springline and Shoulder in Test Section 1

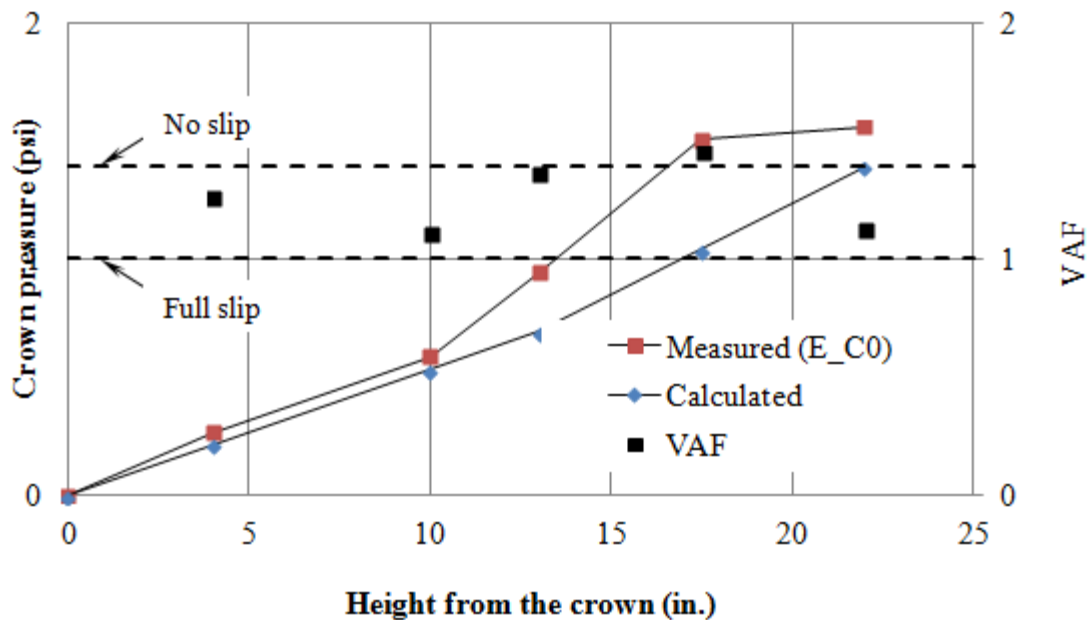
### 5.1.1.2 Test 3

Figure 5.5 shows the pressures developed around the pipes against the levels of construction (labeled as 1 to 9 as shown in Figure 4.23). The earth pressure cell  $E_{I0}$  fixed at the invert showed the highest pressures during the entire installation process. The earth pressure  $E_{I0}$  at the invert in Test Section 1 was very different from that pressure in Test Section 3. This is because the invert of the pipe moved upward in Test Section 1 due to the compaction of the sand at the sides of the pipe and reduced the vertical pressure on the pressure cell ( $E_{I0}$ ) as the level of construction increased. However, the invert of the pipe did not move up in Test Section 3 since the crushed stone (i.e., the backfill material) was placed by dumping with no compaction during the backfilling. The earth pressure cells,  $E_{C0}$ ,  $E_{C6}$ , and  $E_{C12}$ , fixed at the crown, 6 inches, and 12 inches away from the crown had the similar pressures during the installation. The pressures measured at the crown by the earth pressure cell  $E_{C0}$  were higher than the pressures at the springline measured by the earth pressure cell  $E'_{S0}$  as the backfilling increased. The earth pressure cell  $E'_{S8}$  placed at the trench wall at the springline level showed only small changes in pressure values during the pipe installation.



**FIGURE 5.5**  
Measured Pressures around the Pipe During the Installation  
in Test Section 3

The vertical earth pressure measured at the crown by the earth pressure cell ( $E_{C0}$ ) was compared with the calculated overburden vertical pressure in Figure 5.6. Figure 5.6 also shows the calculated vertical arching factors (VAFs) at the crown. The VAFs varied from 1.10 to 1.44 with an average value of 1.26. The VAFs calculated using the Burns and Richard solutions for no-slip and full-slip conditions (Equations 2.2 and 2.3) were 1.42 and 1.03, respectively. The hoop stiffness needed for the Burns and Richard solutions was calculated using Equation 2.4 based on the constrained modulus ( $M_s = 2500$  psi) of the backfill (i.e., the crushed stone), the radius of the pipe, and the area and modulus of elasticity of the steel reinforcement. The constrained modulus  $M_s$  was back-calculated from the modulus of elasticity of the crushed stone determined from the small plate loading test as described in Section 4.7. The calculated VAFs from the measurement of earth pressures are close to those obtained from the Burns and Richard solutions for the no-slip case as shown in Figure 5.6. The SRHDPE pipe should be designed for the VAF value based on the no-slip condition.



**FIGURE 5.6**  
**Comparison of Measured and Calculated Pressures at the Crown During the Installation and Vertical Arching Factor (VAF)**

Figure 5.7 shows the calculated overburden pressures at the springline were close to the vertical pressures measured by the earth pressure cell  $E_{S2}$ . Therefore, the calculated overburden



pressure was used to calculate the lateral earth coefficient ( $K$ ). For example, the coefficients of lateral earth pressure at the springline were calculated by dividing the lateral pressures ( $E'_{s0}$ ) measured at the springline by the overburden pressures calculated at the springline. The calculated coefficients of lateral earth pressure at the springline are shown in Figure 5.8. The average lateral earth pressure ( $K$ ) was found to be 0.21, which was close to the lateral earth pressure coefficient at rest ( $K_0$ ). The lateral earth pressure coefficient at rest ( $K_0$ ) calculated as 0.19 using the friction angle of the crushed stone of  $54^\circ$ . Similarly, the lateral earth pressure coefficients ( $K$ ) were calculated at the shoulder and the haunch using the pressures recorded by  $E'_{SH0}$  and  $E'_{H0}$ , respectively and are shown in Figure 5.8. Figure 5.8 clearly shows that the coefficient of the lateral earth pressure  $K$  was close to the lateral earth pressure coefficient at rest ( $K_0$ ) during the installation of the SRHDPE pipe.

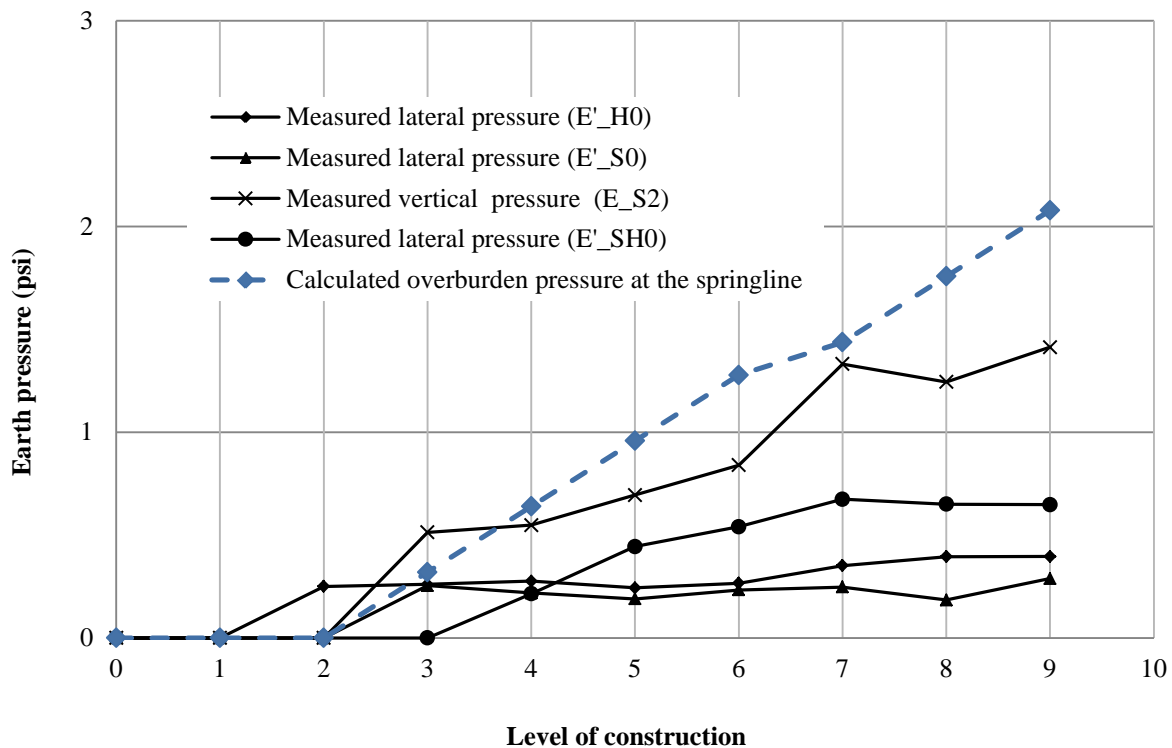


**FIGURE 5.7**  
The Measured Lateral Pressures at the Shoulder, Springline, and Haunch with the Measured and Calculated Vertical Pressures at the Springline in Test Section 3

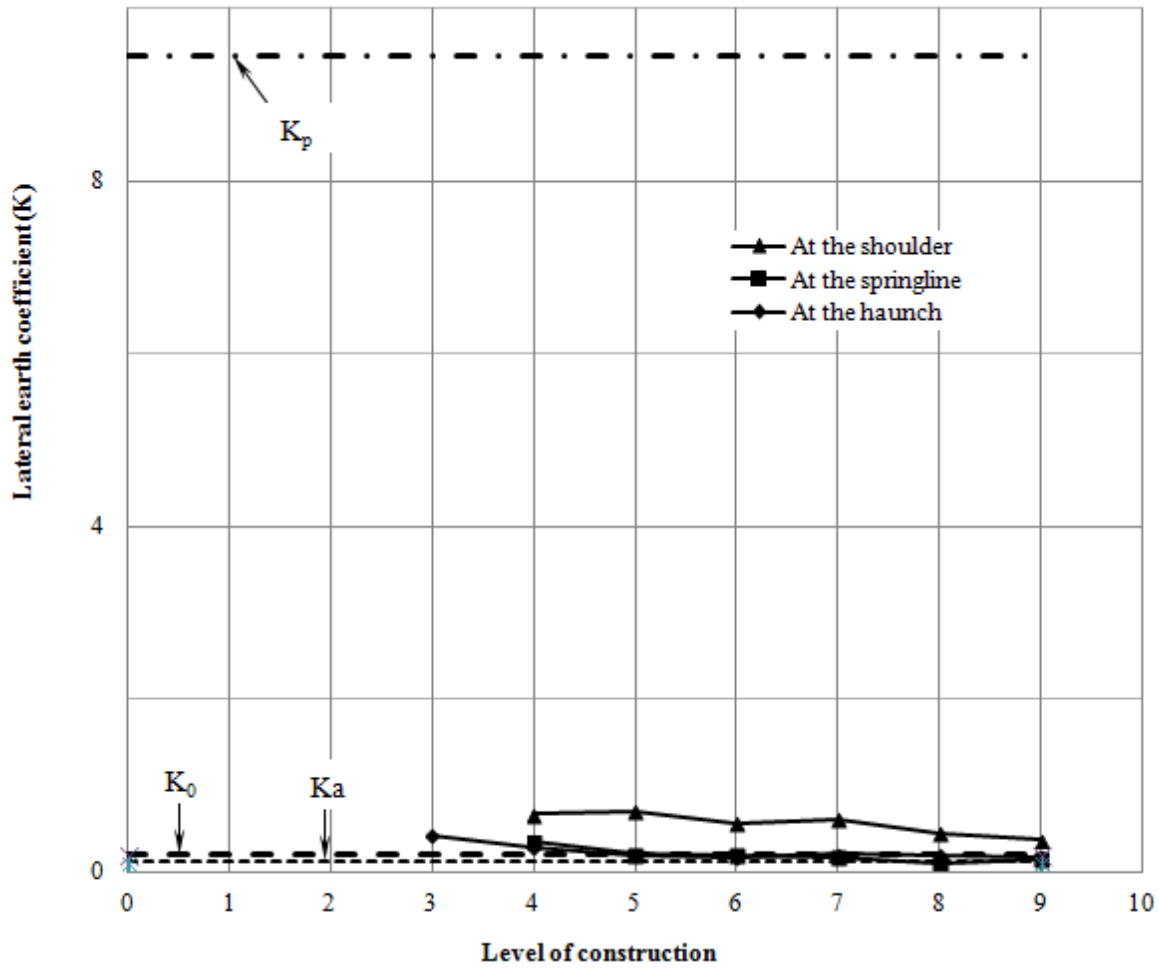


**FIGURE 5.8**  
**Calculated Lateral Earth Pressure Coefficients (K) at the Shoulder, Haunch, and Springline in Test Section 3**

### 5.1.2 Deflection Results

#### 5.1.2.1 Test 1

The deflections of the pipe (or the changes in the inside diameters) against the levels of construction are shown in Figure 5.9. The pipe exhibited peak deflections during the backfilling. When the backfill height was at the same elevation with the pipe crown, the vertical diameter was increased by an average of 0.27 inches (1.14%) while the horizontal diameter was reduced by an average of 0.26 inches (-1.10%). When the compaction of the lifts was above the pipe crown, the vertical diameter started decreasing and the horizontal diameter started increasing as the compaction commenced further. At the end of the construction of the test section, the net

increase in the vertical diameter and the decrease in the horizontal diameter were 0.20 inches (0.86%) and 0.21 inches (0.89%), respectively. The vertical deflection of the pipe was approximately equal to horizontal deflection during the installation of the pipe as shown in Figure 5.10. During the initial backfilling, the pipe started being lifted upward until the backfilling reached the crown and then started moving downward as the compaction continued. The pipe was lifted by a maximum of 1.23 inches during the initial backfilling.

The peak deflection calculated using Equation 2.10 proposed by Masada and Sargand (2007) was 1.28 %, which was close to the measured peak deflection (1.14%). The lateral pressure ( $P_c$ ) generated by the rammer for the sand backfill as 0.39 psi/inch was selected from Table 2.4 to calculate the peak deflection. The lateral earth pressure coefficient at rest ( $K_o$ ) was calculated as  $K_o = 1 - \sin \phi$ , where  $\phi$  is the friction angle of  $37^\circ$ . The horizontal deflection of the pipe measured during the backfilling was also compared with the Iowa formula using Equation 2.8 as shown in Figure 5.11. The bedding constant ( $k$ ) of 0.1, the VAF of 1.26 (calculated in Section 5.1.1), the unit weight of the sand, and the modulus of elasticity of 2,027 psi were used to calculate the horizontal deflection. In the vertical deflection calculation, the effect of the compaction effort on the pipe during the installation was ignored because of the unknown pressure increase caused by the compaction equipment during the installation of the pipe. The measured horizontal deflections were higher than predicted by calculation. The higher horizontal deflections may be not including the effect of the compaction effort during the installation in the vertical deflection calculation.

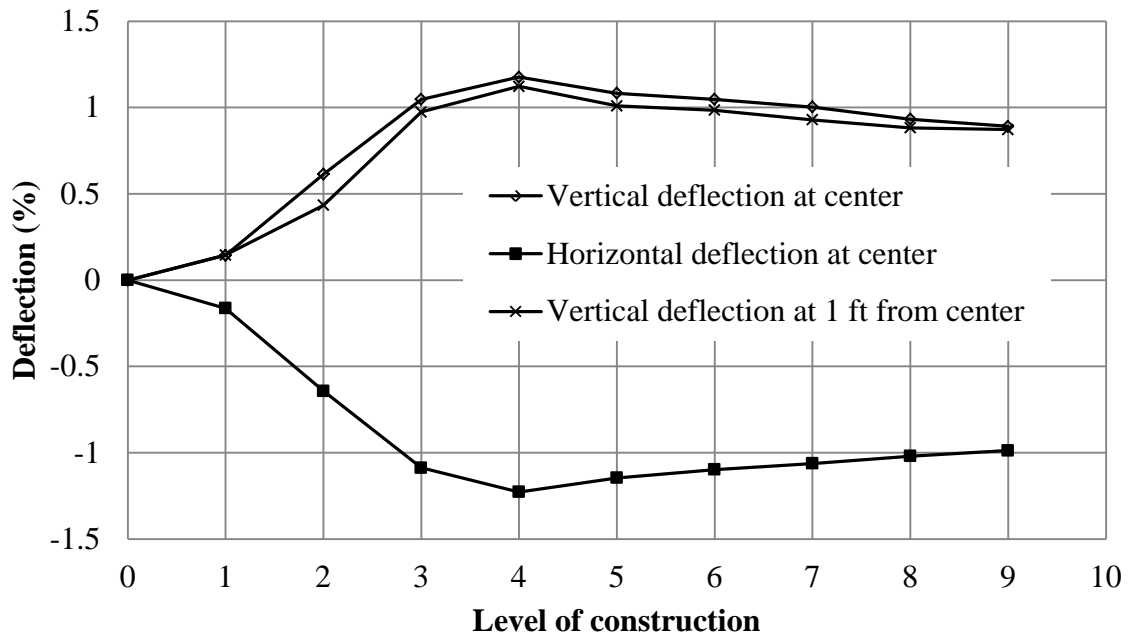


**FIGURE 5.9**  
Measured Deflections of the Pipe During the Installation in Test Section 1

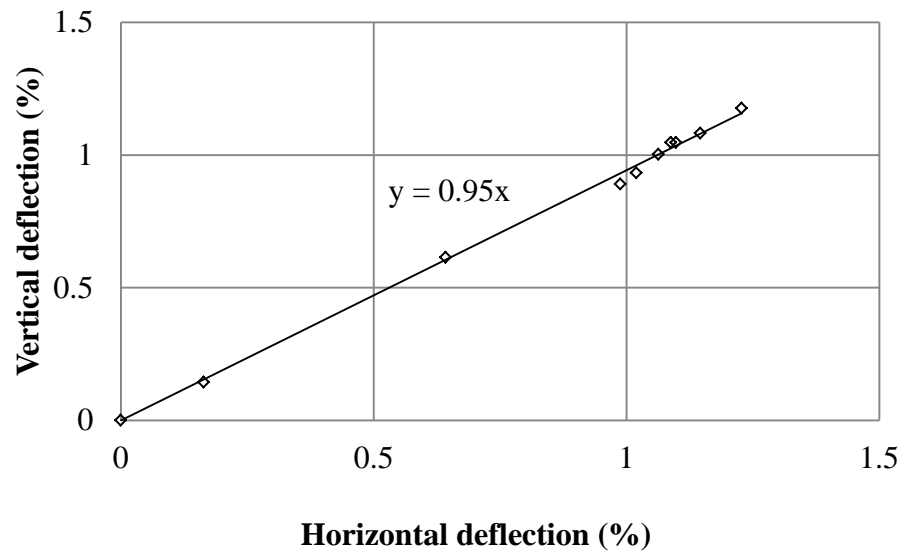


**FIGURE 5.10**  
Relations between the Measured Vertical and Horizontal Deflections During the Installation in Test Section 1

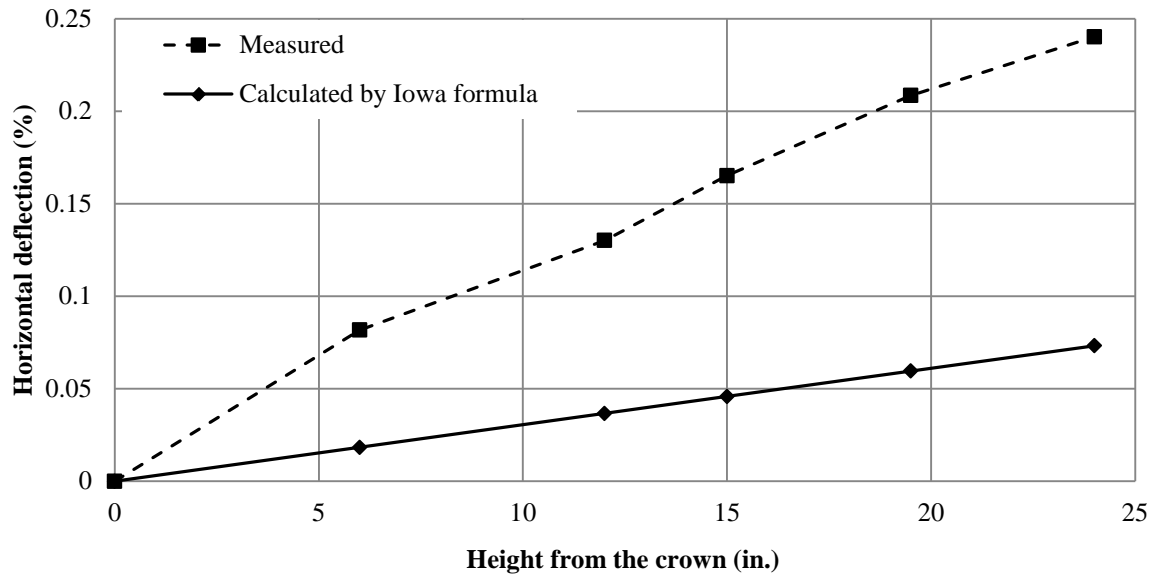


**FIGURE 5.11**  
**Comparison of the Measured and Calculated Horizontal Deflections by the Iowa Formula in Test Section 1**

#### 5.1.2.2 Test 3

The deflections of the pipe (or the changes in the inside diameters) against the levels of construction are shown in Figure 5.12. Similar to the pipe installed with the sand as the backfill, the pipe exhibited peak deflections during backfilling. When the backfill height was at the same elevation with the pipe crown, the vertical diameter was increased by an average of 0.050 inches (0.21%) while the horizontal diameter was reduced by an average of 0.057 inches (-0.24%). When the backfilling was above the pipe crown, the vertical diameter started decreasing and the horizontal diameter started increasing as the backfilling commenced further. At the end of the construction of the test section, the net decrease in the vertical diameter and the increase in the horizontal diameter were 0.007 inches (-0.03%) and 0.014 inches (0.06%), respectively. The ratio of the vertical deflection of the pipe to the horizontal deflection was equal to 0.85 on average during the installation of the pipe as shown in Figure 5.13. The pipe was not lifted up during the initial backfilling by dumping the crushed stone.

The peak deflection calculated using Equation 2.10 proposed by Masada and Sargand (2007) was 0.08 %, which was lower to the measured peak deflection of 0.21%. The Masada and Sargand (2007) equation underestimated the peak deflection. The lateral earth pressure coefficient at rest ( $K_o$ ) calculated as  $K_o = 1 - \sin \phi$ , where  $\phi$  is the friction angle with the value of

54°, was used to calculate the peak deflection. The horizontal deflection measured during the backfilling was also compared with Iowa formula using Equation 2.8 as shown in Figure 5.14. The bedding constant (K) of 0.1, a VAF of 1.26 (calculated in Section 5.1.1), the unit weight of the crushed stone, and the modulus of elasticity (1,125 psi) were used to calculate the horizontal deflection. The calculated horizontal deflections were close to the measured deflections.

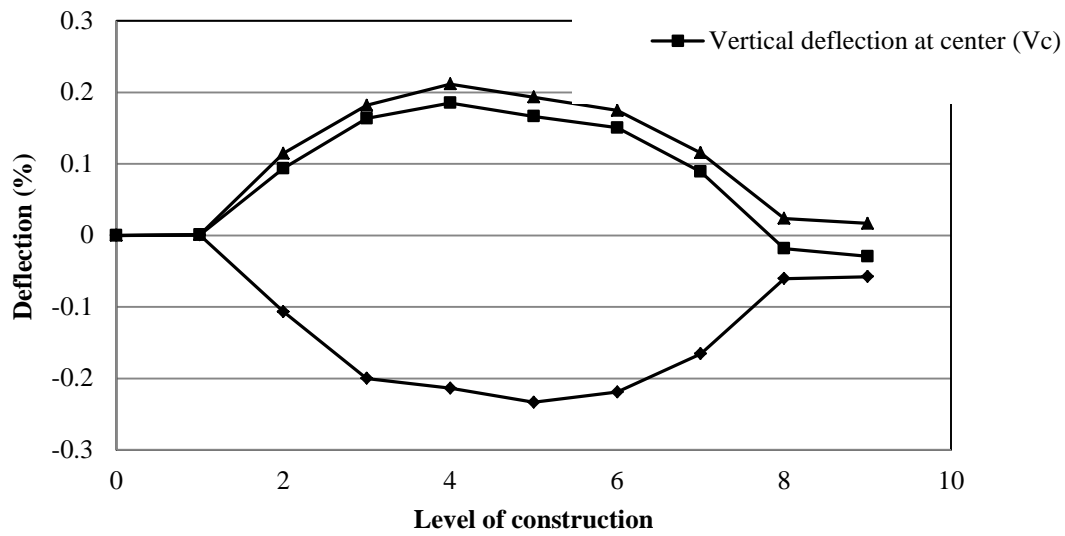


**FIGURE 5.12**  
Measured Deflections of the Pipe During the Installation in Test Section 3

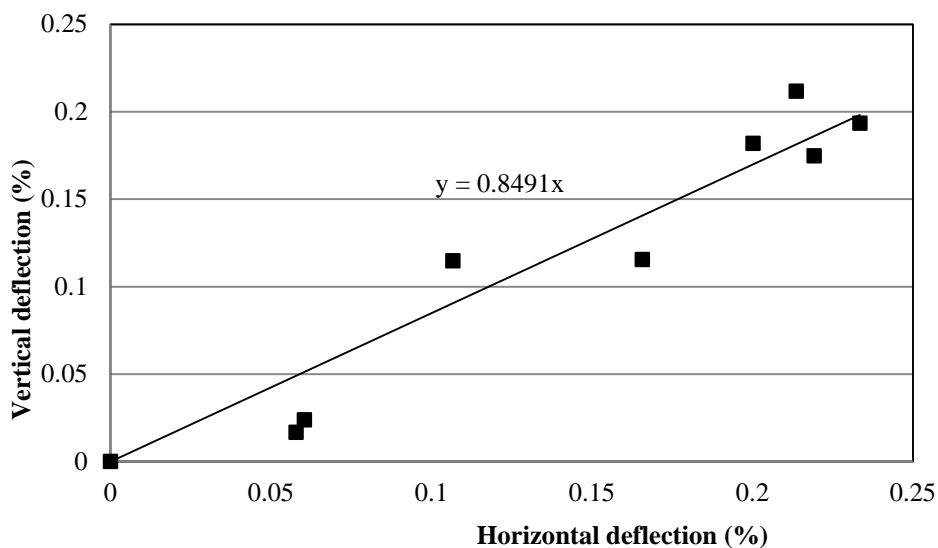


**FIGURE 5.13**  
Relations between the Measured Vertical and Horizontal Deflections During the Installation in Test Section 3

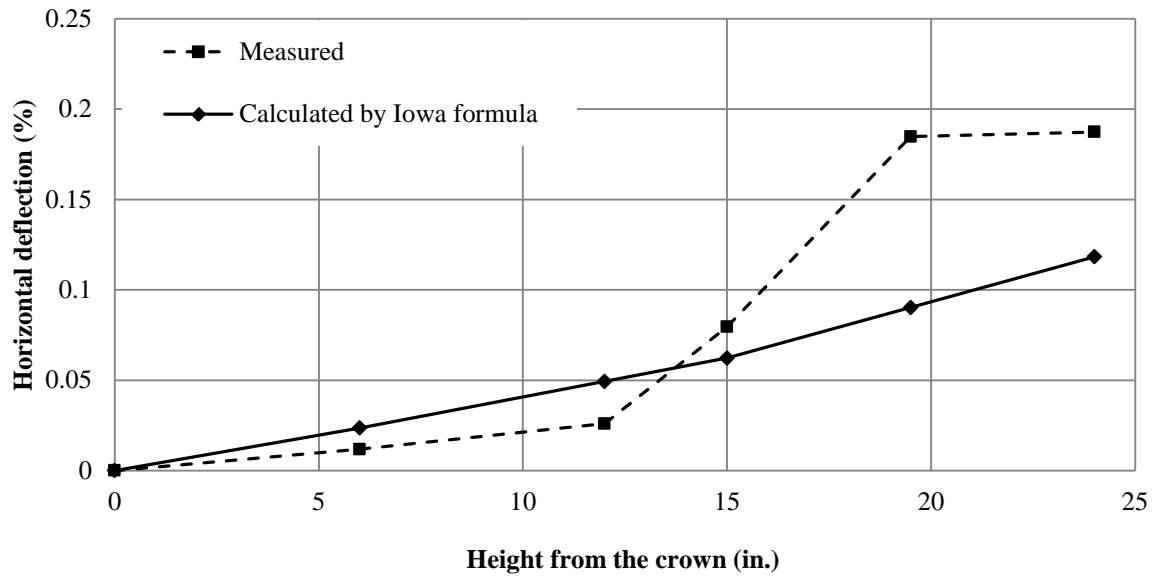


**FIGURE 5.14**  
**Comparison of the Measured and Calculated Horizontal Deflections by the Iowa Formula in Test Section 3**

### 5.1.3 Strain Data

#### 5.1.3.1 Test 1

Most of the strain gages used in this test performed well during the installation of the pipe except the strain gage ( $G'_{SR1}$ ) attached on the plastic rib at the springline in the radial direction. All the strain values on the plastic material were adjusted according to Brachman et al. (2008) as described earlier in Section 3.1.1. The measured strains are plotted against the levels of construction in Figures 5.15 to 5.17. Positive values are tensile strains while negative values are compressive strains.

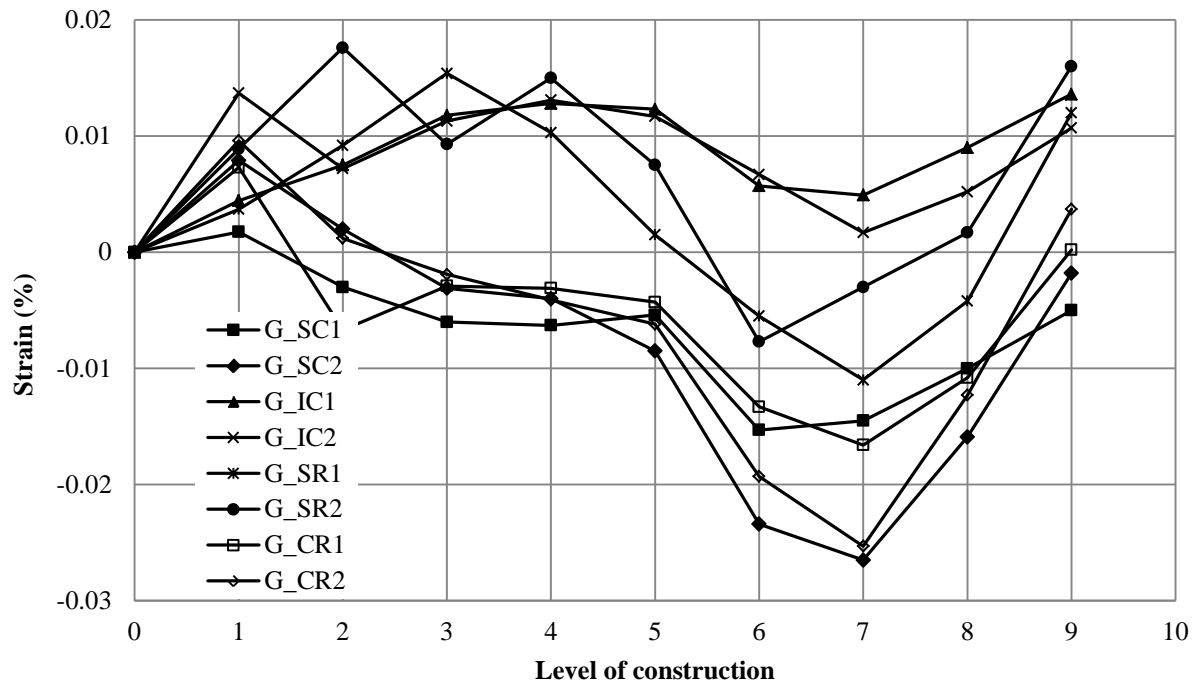


**FIGURE 5.15**  
Measured Strains on the Steel Surface During the Installation in Test Section 1

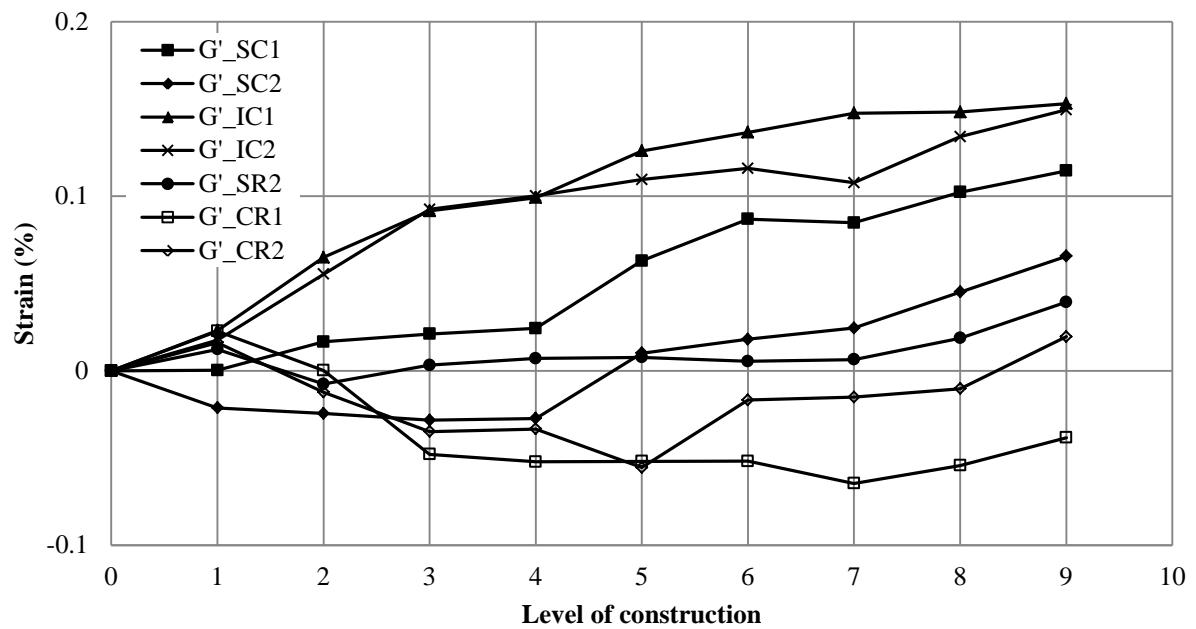


**FIGURE 5.16**  
Measured Strains on the Plastic Ribs During the Installation in Test Section 1



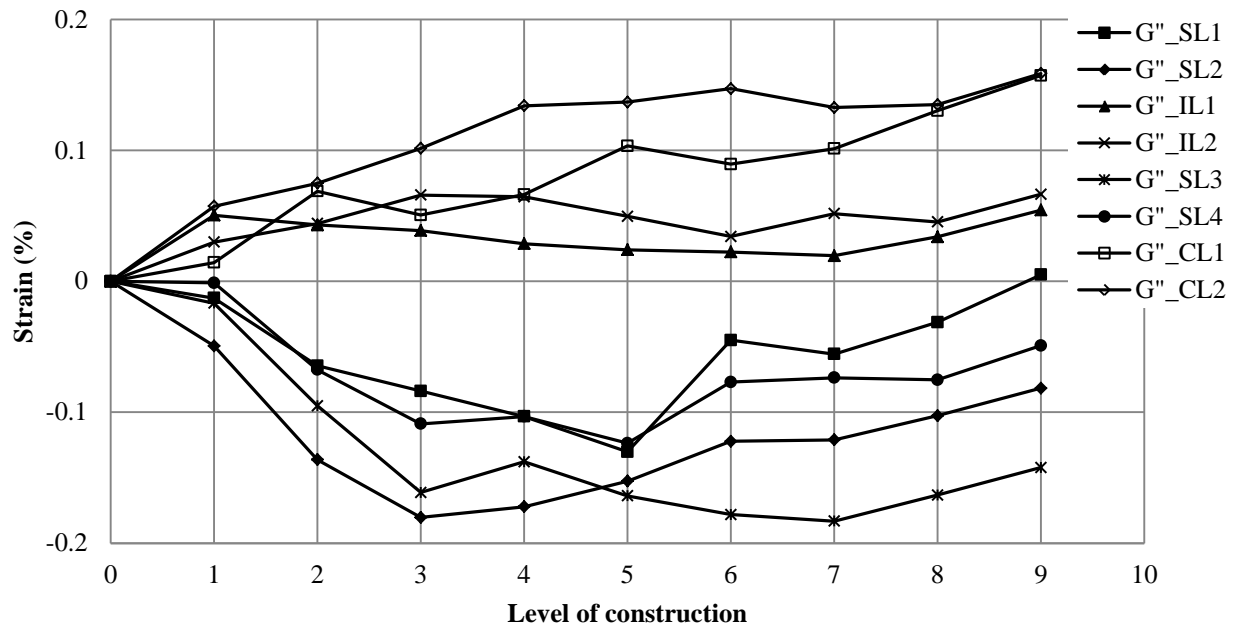


**FIGURE 5.17**  
**Measured Strains on the Plastic at Inside and Outside Pipe Wall During the Installation in Test Section 1**

The circumferential and radial strains developed on the steel of the pipe are shown in Figure 5.15. The strain gages,  $G_{SC1}$  and  $G_{SC2}$  at the springline and  $G_{CR1}$  and  $G_{CR2}$  at the crown, showed an increase in compressive strains, while the strain gages  $G_{IC1}$  and  $G_{IC2}$  at the invert and  $G_{SR1}$  and  $G_{SR2}$  at the springline showed increasing strain values until the backfill reached the pipe crown (i.e., Level 4 of construction). All strain gages then showed an increase in compressive strains up to three more layers of compaction (i.e., up to Level 7 of compaction). After that, all strain gages measured increasing tensile strains. The maximum radial strain of 0.0026% ( $G_{CR1}$ , compressive strain) and the maximum circumferential strain of 0.0027% ( $G_{SC2}$ , compressive strain) were developed during the installation. The strain gages fixed on both sides of a steel rib at any particular location (for example,  $G_{SC1}$  and  $G_{SC2}$  at the springline at the rib), gave similar values (i.e., there were no sudden changes in strain values). This result indicates that the out-of-plane buckling of the steel ribs observed during the parallel plate load tests at a high level of load did not occur during the installation of the pipe.

Figure 5.16 shows the circumferential and radial strains on the plastic at the ribs against the levels of construction. The strains developing on the plastic were higher in magnitude than

the strains on the steel. Most of the strain gages showed increases in tensile strains with the level of construction, but the strain gages  $G'_{CR1}$  and  $G'_{CR2}$  had an increase in the compressive strains until the backfill was even with the pipe crown. A maximum tensile strain of 0.15% was recorded during the installation.

The strains measured by the strain gages on the plastic wall inside and outside are shown in Figure 5.17. All strain gages showed an increase in tensile strains after compaction up to the springline (i.e., Level 2 of construction). The strain gages affixed on the pipe inside walls experienced more tensile strains than those on the outside walls. The magnitudes of the strains on the pipe walls were higher than the strains on the steel and the plastic at the ribs. The maximum tensile strain of 0.17% ( $G'_{CL2}$ ) was recorded on the pipe wall during the installation.

### 5.1.3.2 Test 3

Most of the strain gages used in this test performed well during the installation of the pipe except the strain gages  $G_{CR1}$ ,  $G_{SR2}$ ,  $G'_{SR1}$ , which were attached to the steel at the crown in the radial direction. All the strain values on the plastic material were adjusted according to Brachman et al. (2008) as described earlier in Section 3.1.1. The measured strains are plotted against the levels of construction in Figures 5.18 to 5.20.

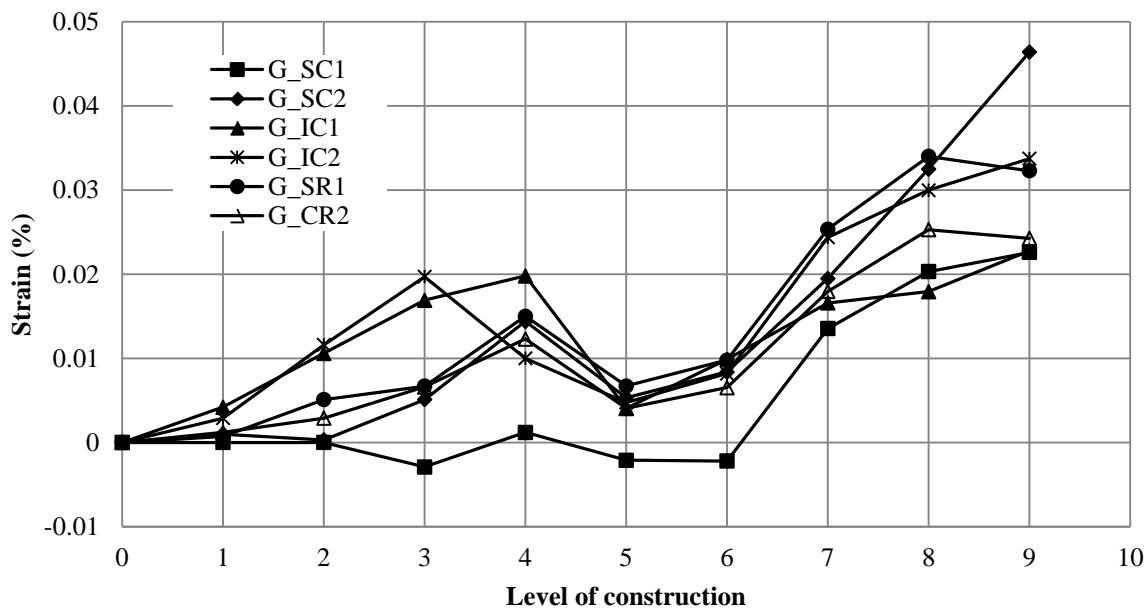


**FIGURE 5.18**  
**Measured Strains on the Steel During the Installation in Test Section 3**

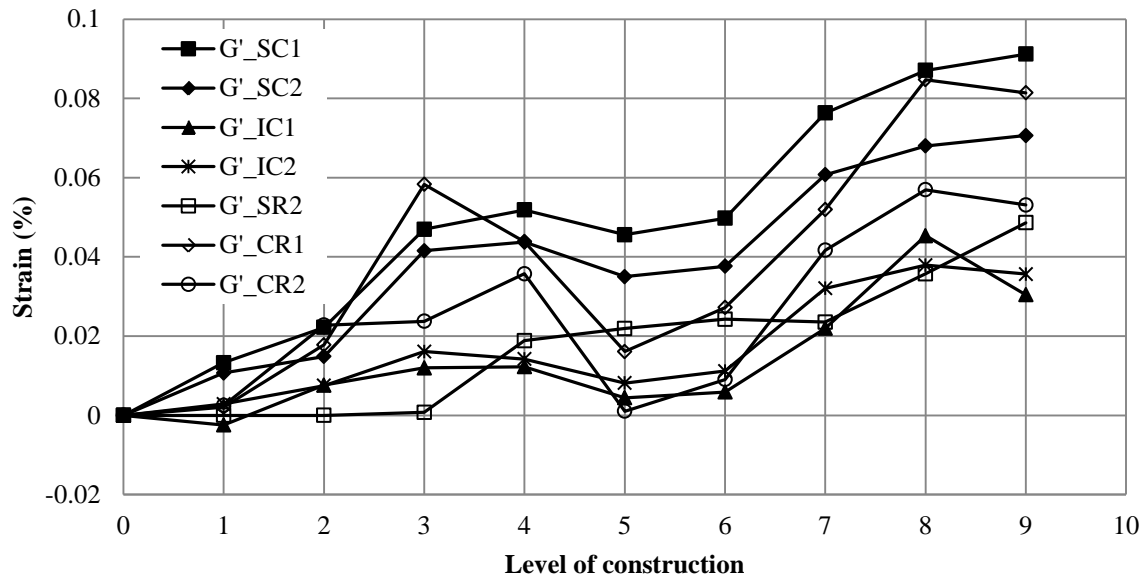


**FIGURE 5.19**  
Measured Strains on the Plastic Ribs During the Installation in Test Section 3

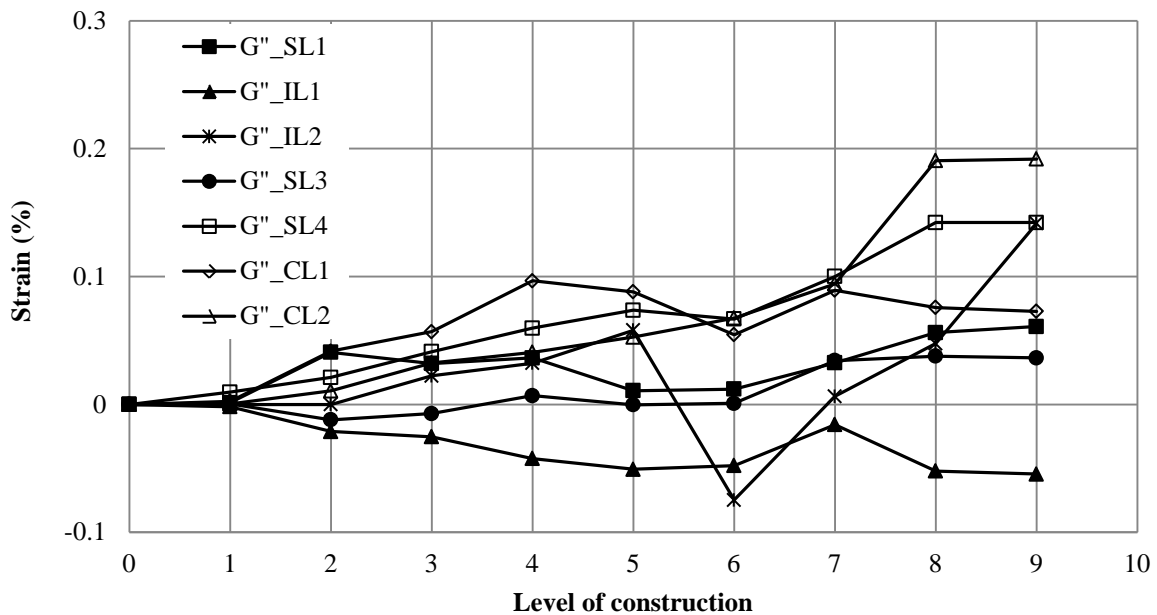


**FIGURE 5.20**  
Measured Strains on the Plastic at inside and Outside Pipe Wall During the Installation in Test Section 3

The circumferential and radial strains developed on the steel of the pipe are shown in Figure 5.18. Most of the strain gages showed increasing strains until the backfill reached the pipe

crown (i.e., Level 4 of construction). There were some decreases in the strains from Levels 4 to 6 of construction. After Level 6, all the strain gages had an increasing trend in the measured strains. The maximum circumferential strain of 0.043% ( $G_{SC2}$ , tensile strain) developed during the installation. The strain gages fixed on both sides of a steel rib at any particular location (for example,  $G_{SC1}$  and  $G_{SC2}$  at the springline at the rib), gave similar strain values (i.e., there were no sudden changes in the strain values). This result indicates that the out-of-plane buckling of the steel ribs observed during the parallel plate load tests at a high level of load did not occur during the installation of the pipe.

Figure 5.19 shows the circumferential and radial strains on the plastic at the ribs against the levels of construction. The strains developing on the plastic were higher in the magnitude than the strains on the steel. Most of the strain gages showed an increase in the tensile strains with the level of construction. The maximum tensile strain of 0.063% was recorded during the installation.

The strains measured by the strain gages on the plastic wall inside and outside the pipe are shown in Figure 5.20. All the strain gages showed an increase in the tensile strains. The strain gages affixed on the pipe inside walls experienced more tensile strains than those on the outside walls. The magnitudes of the strains on the pipe walls were higher than the strains on the steel and the plastic cover at the ribs. The maximum tensile strain of 0.19% ( $G''_{CL2}$ ) was recorded on the pipe wall during the installation.

## **5.2 Static Plate Loading Test Results**

During the static plate loading tests, the settlements of the loading plate, the earth pressures around the pipe, the deflections of the pipe, and the strains on the pipe were measured and they are presented in the subsequent sections.

### ***5.2.1 Settlement of Loading Plate***

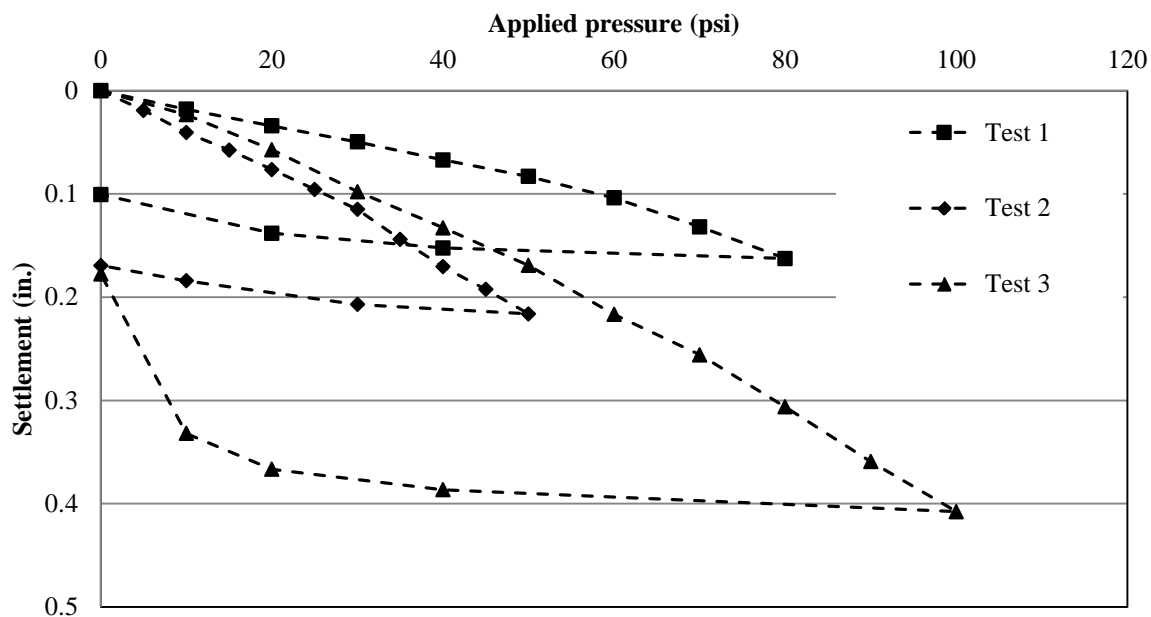
#### **5.2.1.1 Test 1**

Figure 5.21 shows the settlements of the loading plate against the applied pressures during loading and unloading. The total settlement of the loading plate was 0.163 inches at the applied pressure of 80 psi, which is the typical tire pressure of a highway truck. This total

settlement consisted of an elastic deformation of 0.063 inches and a permanent deformation of 0.1 inches based on the unloading curve. Using the initial slope of the pressure-settlement curve, the elastic modulus of the test section ( $E_s$ ) was calculated using Equation 5.1 as 5,068 psi.

$$E_s = 0.79 d (1 - \nu^2) \frac{p}{\delta} \quad \text{Equation 5.1}$$

where  $E_s$  = the elastic modulus of the test section,  $\nu$  = the Poisson's ratio (a typical value of 0.33 was used),  $p$  = the applied pressure on the elastic range, and  $\delta$  = the settlement of the loading plate at  $p$ .



**FIGURE 5.21**  
**Settlement of the Loading Plate versus Applied Pressure under Static Loads**

#### 5.2.1.2 Test 2

The total settlement of the loading plate in Test 1 was 0.215 inches at the applied pressure of 50 psi, as shown in Figure 5.21. This total settlement consisted of an elastic deformation of 0.045 inches and a permanent deformation of 0.17 inches. Based on the initial slope of the pressure-settlement curve, the elastic modulus of the test section ( $E_s$ ) was calculated using Equation 5.1 as 2,214 psi.

### 5.2.1.3 Test 3

The total settlement of the loading plate in Test 3 was 0.40 inches at the applied pressure of 100 psi, as shown in Figure 5.21. This total settlement consisted of an elastic deformation of 0.18 inches and a permanent deformation of 0.22 inches. Based on the initial slope of the pressure-settlement curve, the elastic modulus of the test section ( $E_s$ ) was calculated using Equation 5.1 as 2,500 psi.

Figure 5.21 shows that Test 1 had the smallest settlement while the Test 2 had the largest settlement among all three tests. The reason Test 1 had the smallest settlement is that the section in Test 1 had a well-compacted sand and a stiff AB-3 aggregate as the base course. In Test 2, Kansas River sand was used as the base course and was weaker or less stiff than the AB-3 aggregate. In Test 3, however, the crushed stone in the trench was not compacted; therefore, it deformed more than the compacted sand.

## 5.2.2 Earth Pressure Results

The distribution of earth pressures around the pipe due to the applied static load was measured using the earth pressure cells. The earth pressures discussed in this section are those induced by the applied load on the loading plate only. In other words, the measured earth pressures during the pipe installation were excluded.

### 5.2.2.1 Test 1

Figure 5.22 shows the measured earth pressures around the pipe against the pressures applied on the loading plate. The earth pressure cell placed at the pipe crown ( $E_{C0}$ ) showed the highest earth pressure on the pipe. The earth pressure at the crown under the applied pressure of 80 psi was approximately 11 psi. The vertical earth pressure at 6 inches away from the center ( $E_{C6}$ ) was 0.43 to 0.5 times that at the pipe crown ( $E_{C0}$ ). The horizontal pressure at the pipe springline ( $E_{S0}$ ) was 0.32 times the vertical earth pressure at the crown ( $E_{C0}$ ). The ratio of the horizontal pressure at the springline ( $E'_{S0}$ ) to that at the shoulder ( $E'_{SH0}$ ) was 1.3 to 1.5. The higher horizontal pressure at the springline ( $E'_{S0}$ ) as compare with that at the shoulder ( $E'_{SH0}$ ) is

attributed to the additional lateral pressure applied by the pipe at the springline level due to more outward deflection of the pipe.

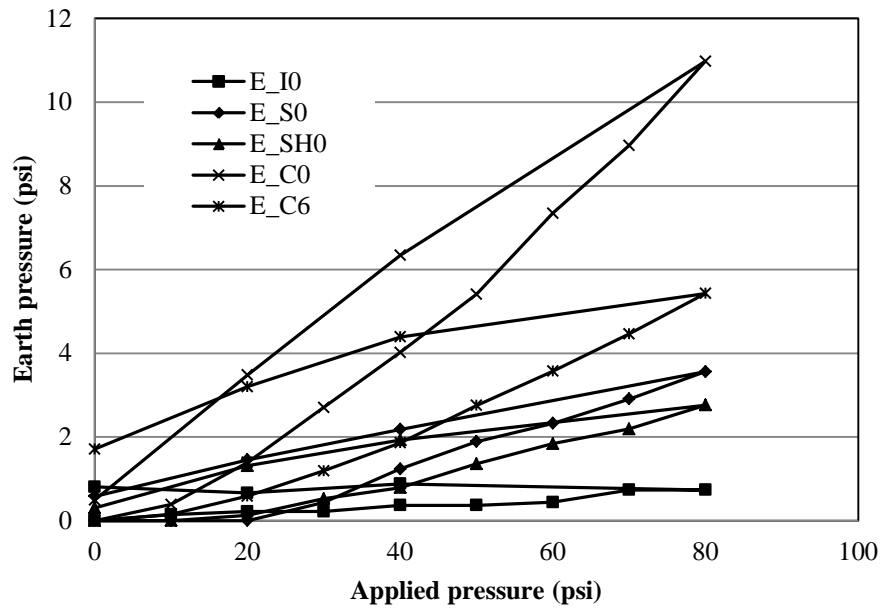


**FIGURE 5.22**  
**Measured Earth Pressures around the Pipe in Test 1**

#### 5.2.2.2 Test 2

Figure 5.23 shows the measured earth pressures versus the applied pressures. The earth pressure cell at the pipe crown ( $E_{C6}$ ) showed the highest earth pressure on the pipe. The earth pressure at the crown under the applied pressure of 50 psi was approximately 7.3 psi. The vertical earth pressure 6 inches away from the center ( $E_{C6}$ ) was 0.62 to 0.67 times that at the pipe crown ( $E_{C0}$ ). The horizontal pressure at the pipe springline ( $E'_{S0}$ ) was 0.32 times the vertical earth pressure at the crown ( $E_{C0}$ ). The ratio of the horizontal pressure at the springline ( $E'_{S0}$ ) to the pressure at the shoulder ( $E'_{SH0}$ ) was 1.16 to 1.30. This result is attributed to the additional lateral pressure applied by the pipe at the springline level due to more outward deflection of the pipe.

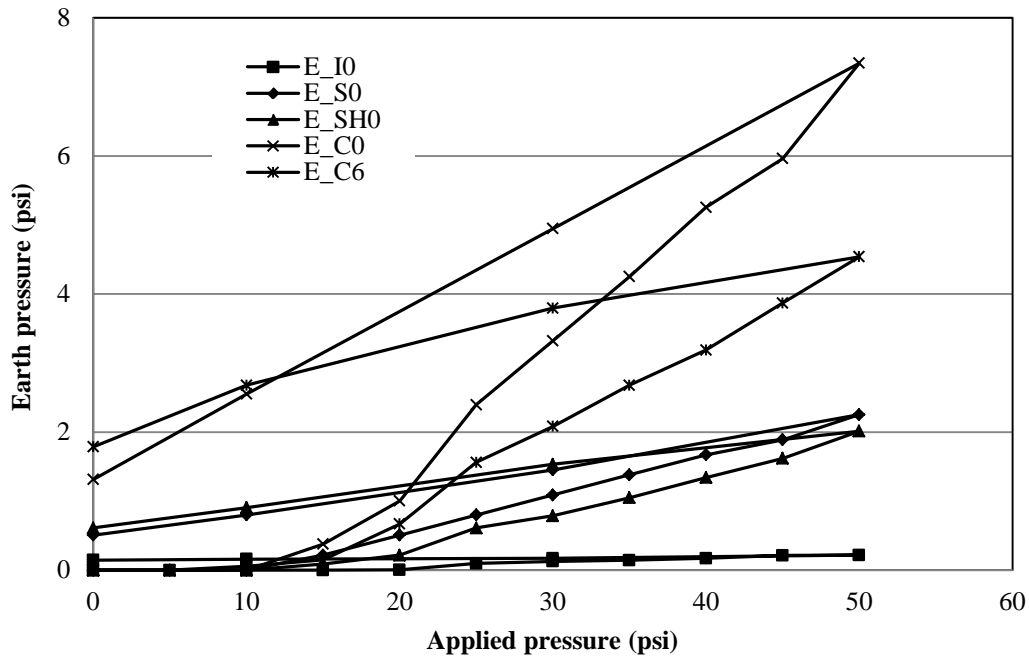


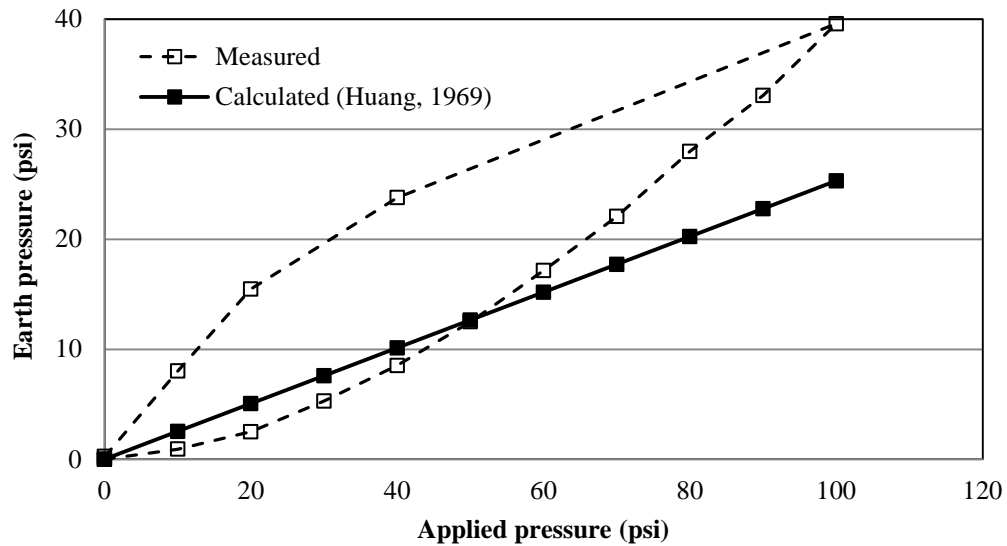
**FIGURE 5.23**  
**Measured Earth Pressures around the Pipe in Test 2**

### 5.2.2.3 Test 3

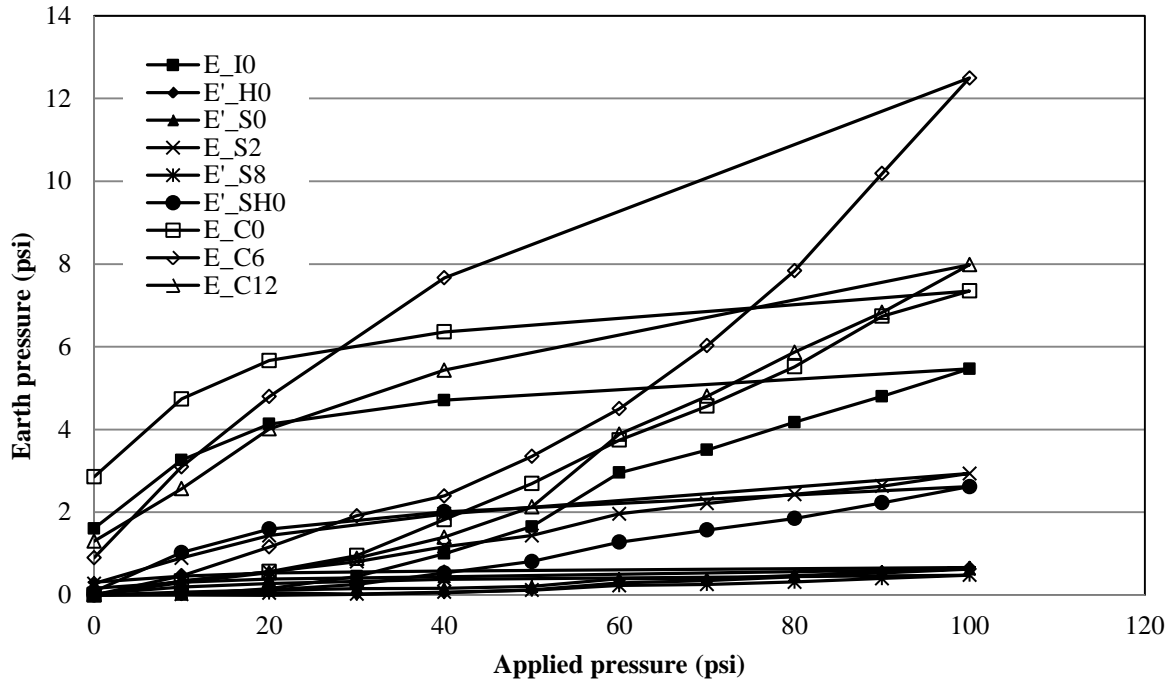
Figures 5.24 and 5.25 show the measured earth pressures by the earth pressure cell ( $E_{IF}$ ) at the base course and backfill interface and nine other earth pressure cells around the pipe at different applied pressures, respectively. Figure 5.26 shows the measured interface pressures were close to those calculated using the chart developed by Huang (1969) when the applied pressure was less than 60 psi. However, for pressures higher than 60 psi, the measured earth pressures were higher than those calculated pressures because of the stress concentration on the pipe crown in the test. In the calculation, the elastic moduli of 1,125 and 5,280 psi (determined in Sections 3.2.2 and 3.2.3) were used for the crushed stone backfill and the AB-3 base course, respectively. Figure 3.25 shows that the pressures recorded by the earth pressure cell ( $E_{C6}$ ) placed 6 inches away from the pipe crown were the highest during loading. The earth pressure at the crown ( $E_{C0}$ ) under the applied pressure of 100 psi was approximately 7.35 psi. The earth pressure cells at the crown and 1ft away from the crown (i.e.,  $E_{C0}$  and  $E_{C12}$ ) showed approximately the similar earth pressures during loading. The vertical earth pressure at 6 inches away from the center ( $E_{C6}$ ) was 1.2 to 1.5 times that at the pipe crown ( $E_{C0}$ ). During loading, the



highest lateral earth pressure was at the shoulder of the pipe. The highest pressures may be due to the relatively higher outward deflection of the pipe at the shoulder than the deflection at the springline and at the haunch. The horizontal earth pressure at the shoulder ( $E'_{SH0}$ ) was 0.33 to 0.36 times that at the pipe crown ( $E_{C0}$ ). The ratio of the horizontal pressure at the springline ( $E'_{S0}$ ) to that at the shoulder ( $E'_{SH0}$ ) was 3.23 to 4.2.



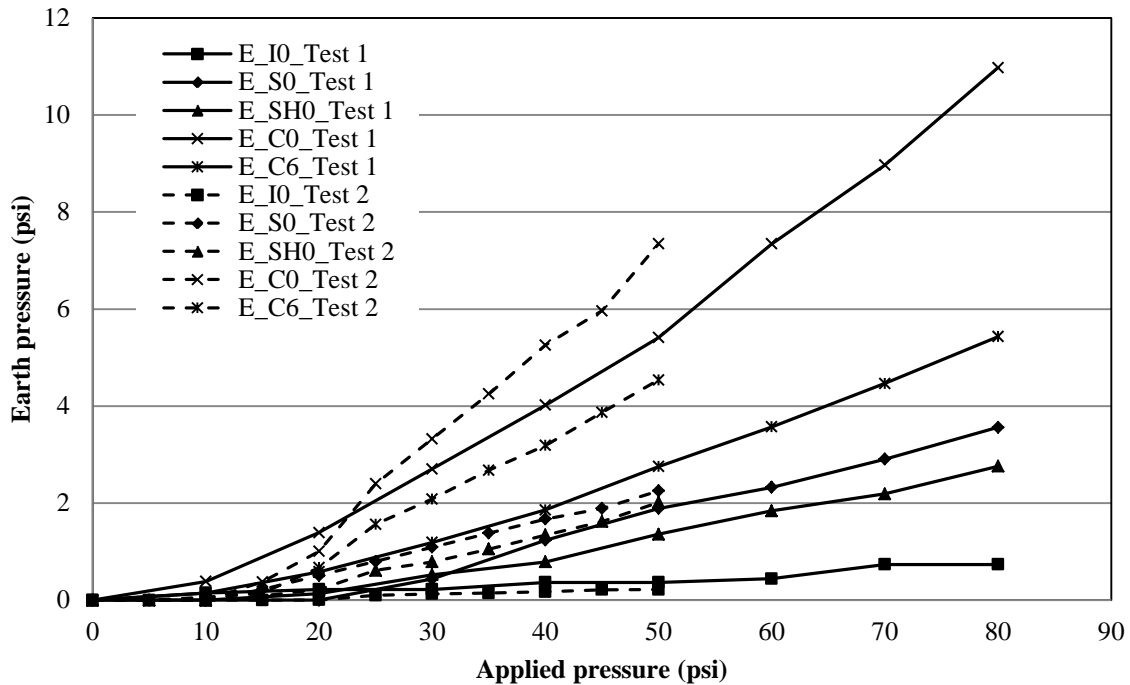
**FIGURE 5.24**  
**Measured and Calculated Earth Pressure ( $E_{IF}$ ) at the Backfill-Base**  
**Course Interface in Test 3**



**FIGURE 5.25**  
**Measured Earth Pressures around the Pipe in Test 3**

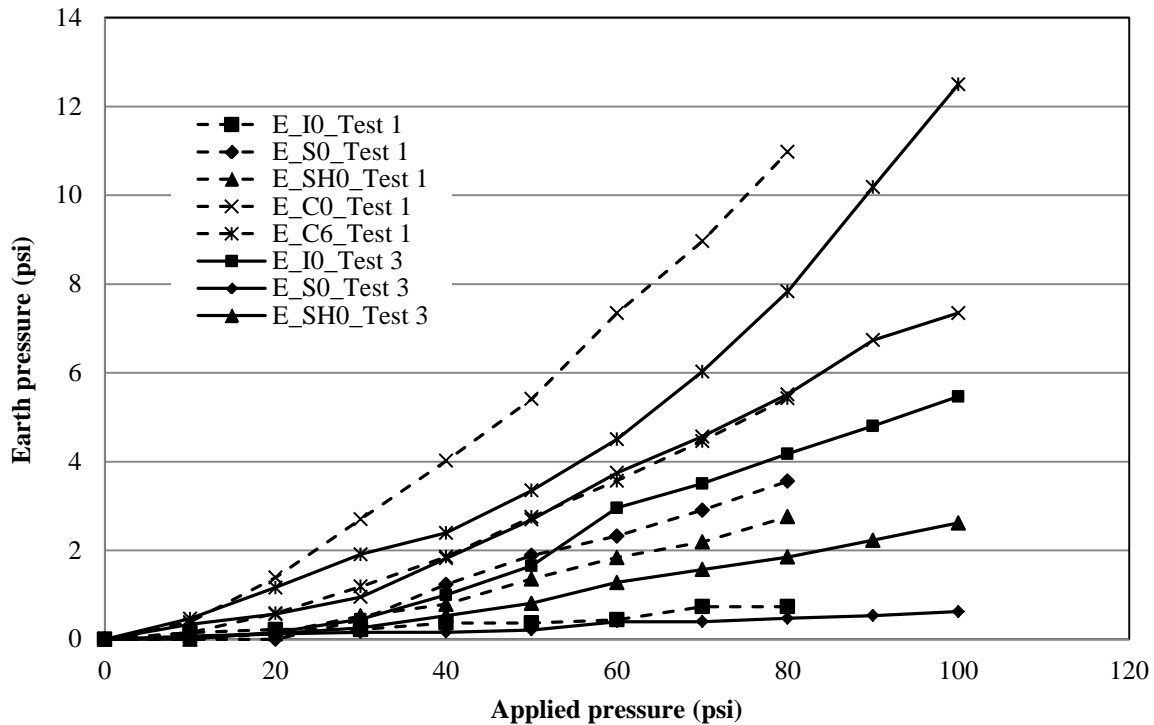
#### 5.2.2.4 Comparison of Test Results

Figure 5.26 shows the comparison of the earth pressure distributions around the pipe in Test 1 (with the AB-3 base course and the sand backfill) and Test 2 (with the sand as the base course and the backfill). The measured earth pressures in Test 1 were less than those earth pressures in Test 2, with the exception of the earth pressures measured at the invert ( $E_{I0}$ ). The differences were even more pronounced at the higher applied pressure. The lower earth pressures around the pipe in Test 1 were due to the higher distribution of the pressures by the stiff AB-3 base course than the sand base course.



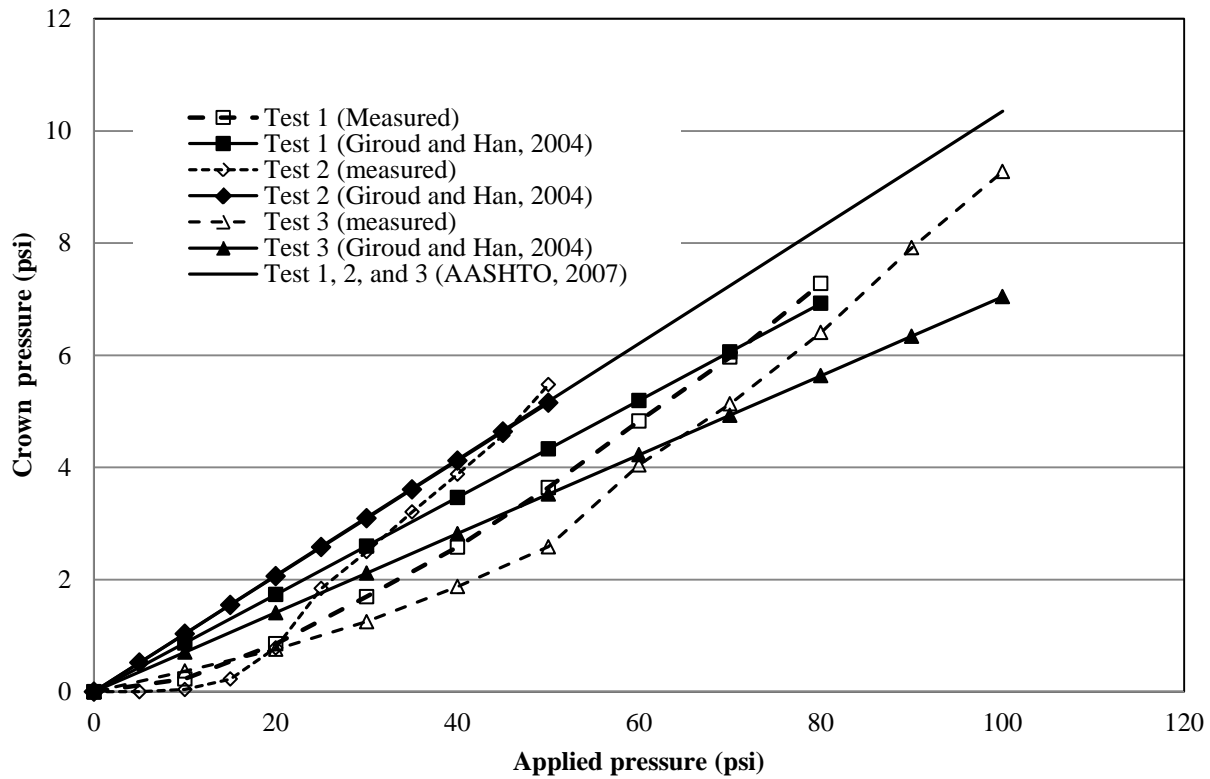
**FIGURE 5.26**  
**Measured Earth Pressures around the Pipe in Test 1 and Test 2**

Figure 5.27 shows the comparison of the measured earth pressures around the pipe for two different backfills: the Kansas River sand in Test 1 and the crushed stone in Test 3. The vertical earth pressures at the crown ( $E_{C0}$ ) were higher than those ( $E_{C6}$ ) at 6 inches away from the crown in Test 1 whereas the earth pressures at the crown ( $E_{C0}$ ) were lower than those ( $E_{C6}$ ) in Test 3. Similarly, the horizontal earth pressures at the springline ( $E_{S0}$ ) were lower than those ( $E_{SH0}$ ) at the shoulder in Test 3 while the horizontal earth pressures at the springline ( $E_{S0}$ ) were higher than those ( $E_{SH0}$ ) at the shoulder in Test 1. The earth pressure cell at the invert ( $E_{I0}$ ) showed a higher earth pressure in Test 3 than that in Test 1 because the pipe was lifted up in Test 1 as discussed in Section 5.1.1 but there was little or no lift-up of the pipe in Test 3 during backfilling.



**FIGURE 5.27**  
**Measured Earth Pressures around the Pipe in Test 1 and Test 3**

The vertical earth pressures on the top of the pipe under the applied static load in each test were calculated using the simplified distribution method (AASHTO 2007) and the approach proposed by Giroud and Han (2004) (as discussed in Section 2.1). The moduli of elasticity of the Kansas River sand, the crushed stone, and the AB-3 aggregate needed for the calculation of the earth pressures were determined from the small plate loading tests (see Sections 3.2.2 and 3.2.3). The calculated earth pressures are then compared with the average pressures of EC0, EC6, and EC12 measured on the top of the pipe in Figure 5.28. The measured pressures at the crown of the pipe were close to those calculated using the Giroud and Han (2004) method as compare with the simplified distribution method (AASHTO 2007).



**FIGURE 5.28**  
**Comparison of the Measured Crown Pressures with the 2007 AASHTO LRFD Bridge Design Specifications and Giroud and Han (2004) Methods**

In Tests 1 and 2, the pressure cell  $E_{S2}$  was not placed to measure the vertical pressure at that location. The pressure cell  $E_{S2}$  at the springline was added in Test 3 and the measured earth pressure was used to calculate the coefficient of lateral earth pressure ( $K$ ). Figure 5.29 shows the coefficient of lateral earth pressure at the springline ( $K$ ), which was calculated from the measured horizontal pressure at the springline ( $E'_{S0}$ ) divided by the measured vertical pressure measured at the springline ( $E_{S2}$ ). The average coefficient of lateral earth pressure at the springline ( $K$ ) was approximately 0.2. Similarly, the coefficients of lateral earth pressure at the shoulder and the haunch were calculated by the measured horizontal pressures  $E'_{SH0}$  and  $E'_{H0}$  divided by the measured vertical pressures by  $E_{S2}$ . Figure 5.30 shows the calculated coefficients at the shoulder, the springline, and the haunch as compared with the theoretical coefficients of lateral earth pressure,  $K_a$ ,  $K_o$ , and  $K_p$ , calculated using the friction angle of the crushed stone of  $54^\circ$ . The calculated coefficients ( $K$ ) at the springline and the haunch from the measured pressures were close to the lateral earth coefficient at rest  $K_o$ . However, the calculated coefficient at the

shoulder (K) from the measured pressures was 0.70, which was higher than the lateral earth coefficient at rest  $K_0$ .

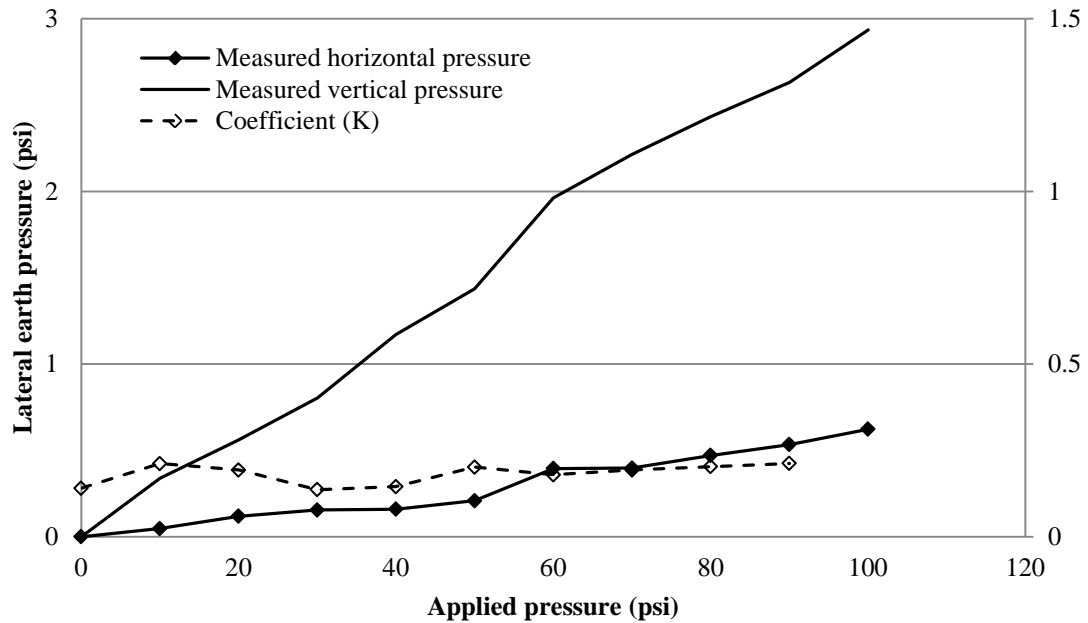


**FIGURE 5.29**  
Calculated Lateral Earth Pressure Coefficients (K) at the Springline from the Measured Pressures in Test 3

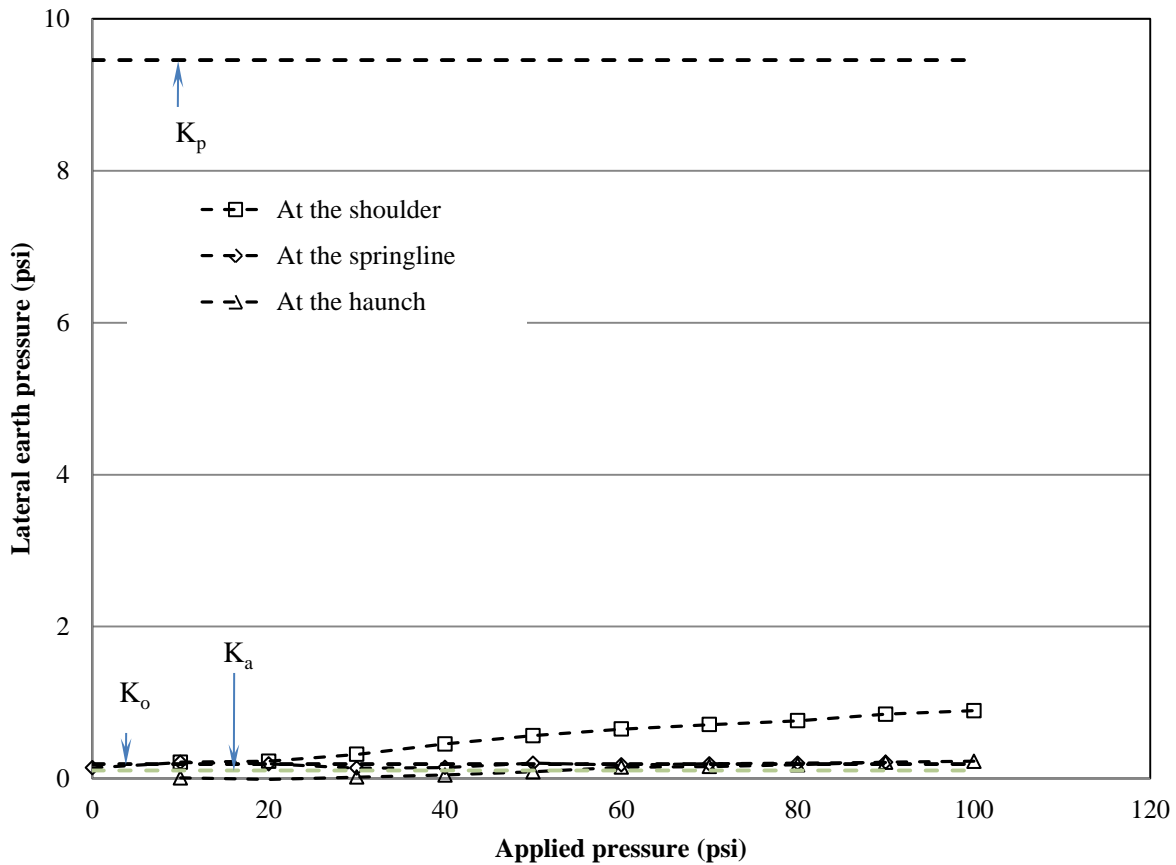


**FIGURE 5.30**  
**Comparison of the Lateral Earth Pressure Coefficients (K) at the Shoulder, Springline, and Haunch in Test 3**

### 5.2.3 Pipe Deflection Results

#### 5.2.3.1 Test 1

The deflections of the pipe (or the changes of the inside diameters) against the applied pressures from Test 1 are shown in Figure 5.31. As the load increased, the vertical diameter of the pipe ( $\Delta D_V$ ) decreased while the horizontal diameter of the pipe ( $\Delta D_H$ ) increased. Figure 5.32 also shows that the horizontal deflection of the pipe ( $\Delta D_H$ ) was less than the vertical deflection ( $\Delta D_V$ ). When the applied pressure was 80 psi, the decrease in the vertical diameter and the increase in the horizontal diameter at the center of the pipe section ( $\Delta D_{VC}$  and  $\Delta D_{HC}$ ) were 0.035 inches (0.147% of the initial diameter) and 0.021 inches (0.89% of the initial diameter), respectively. The vertical deflections at the center of the pipe ( $\Delta D_{VC}$ ) were 1.60 to 1.67 times the

horizontal deflections at the center of the pipe ( $\Delta D_{HC}$ ), and 2.00 to 2.55 times the vertical deflections at 1 ft from the center of the test pipe ( $\Delta D_{V1}$ ).

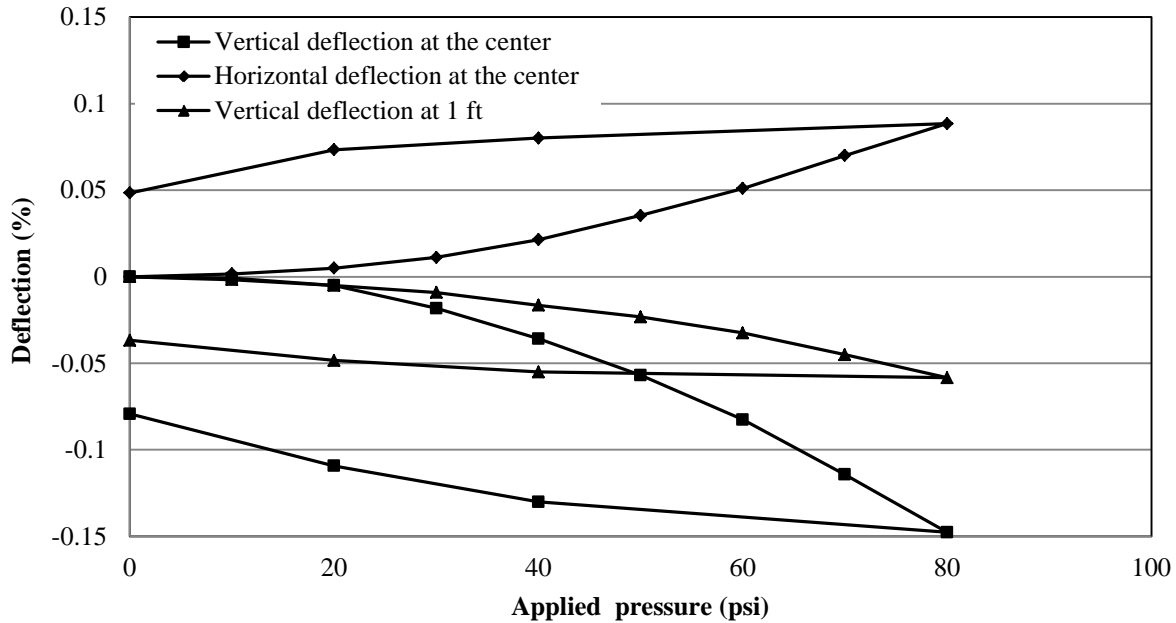
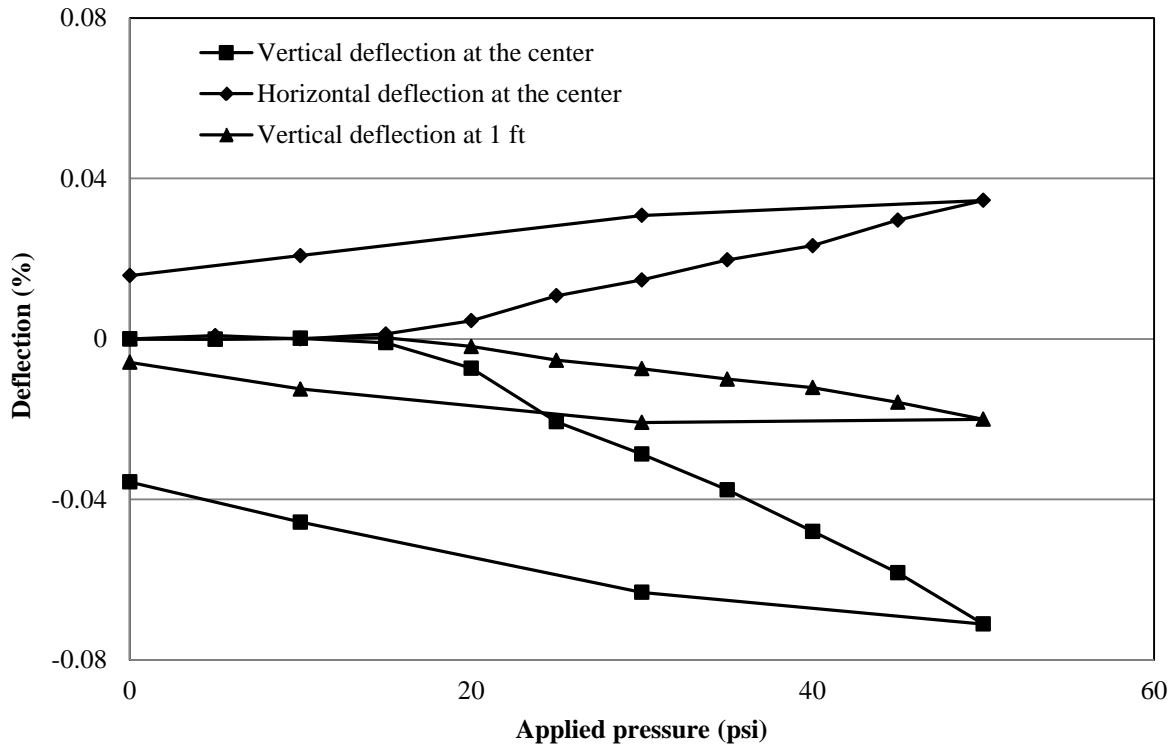


**FIGURE 5.31**  
**Deflections of the Pipe under the Static Load in Test 1**

#### 5.2.3.2 Test 2

Figure 5.32 shows the deflections of the pipe against the applied pressures from Test 2. When the applied pressure was 50 psi, the decrease in the vertical diameter and the increase in the horizontal diameter at the center of the pipe section ( $\Delta D_{VC}$  and  $\Delta D_{HC}$ ) were 0.017 inches (0.07% of the initial diameter) and 0.008 inches (0.035% of the initial diameter), respectively. The vertical deflections at the center of the pipe ( $\Delta D_{VC}$ ) were 1.60 to 1.67 times the horizontal deflections at the center of the pipe ( $\Delta D_{HC}$ ), and 3.5 to 3.9 times the vertical deflections at 1 ft from the center of the test pipe ( $\Delta D_{V1}$ ).

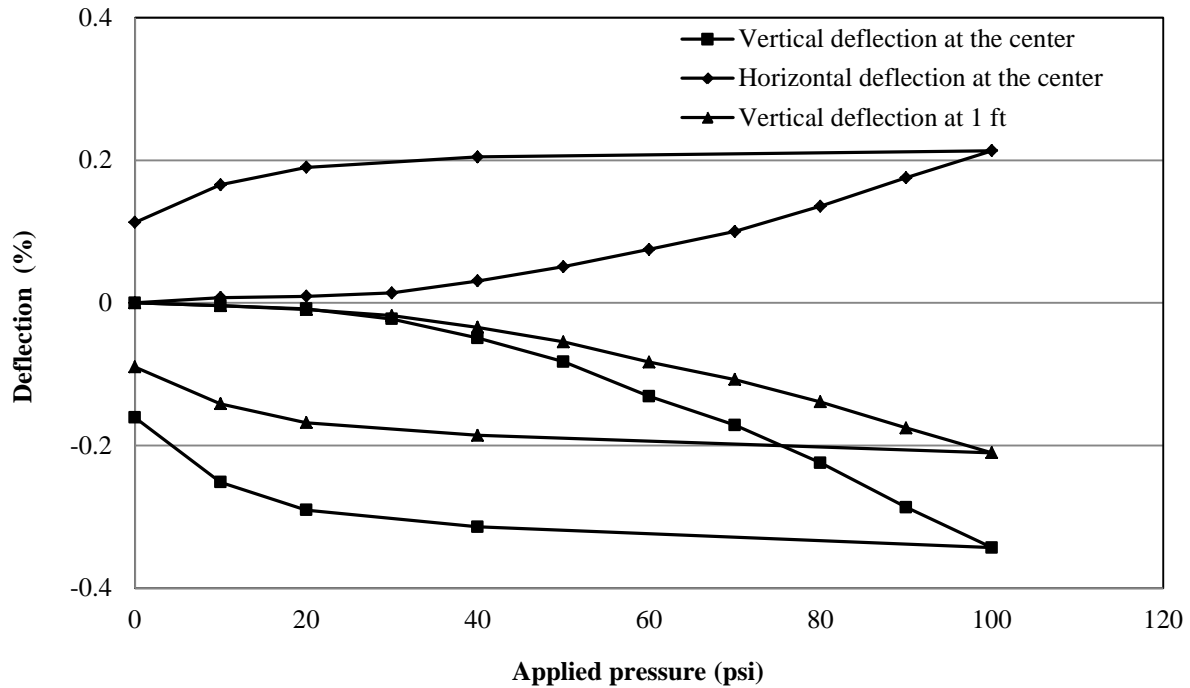




**FIGURE 5.32**  
Deflections of the Pipe under the Static Load in Test 2

#### 5.2.3.3 Test 3

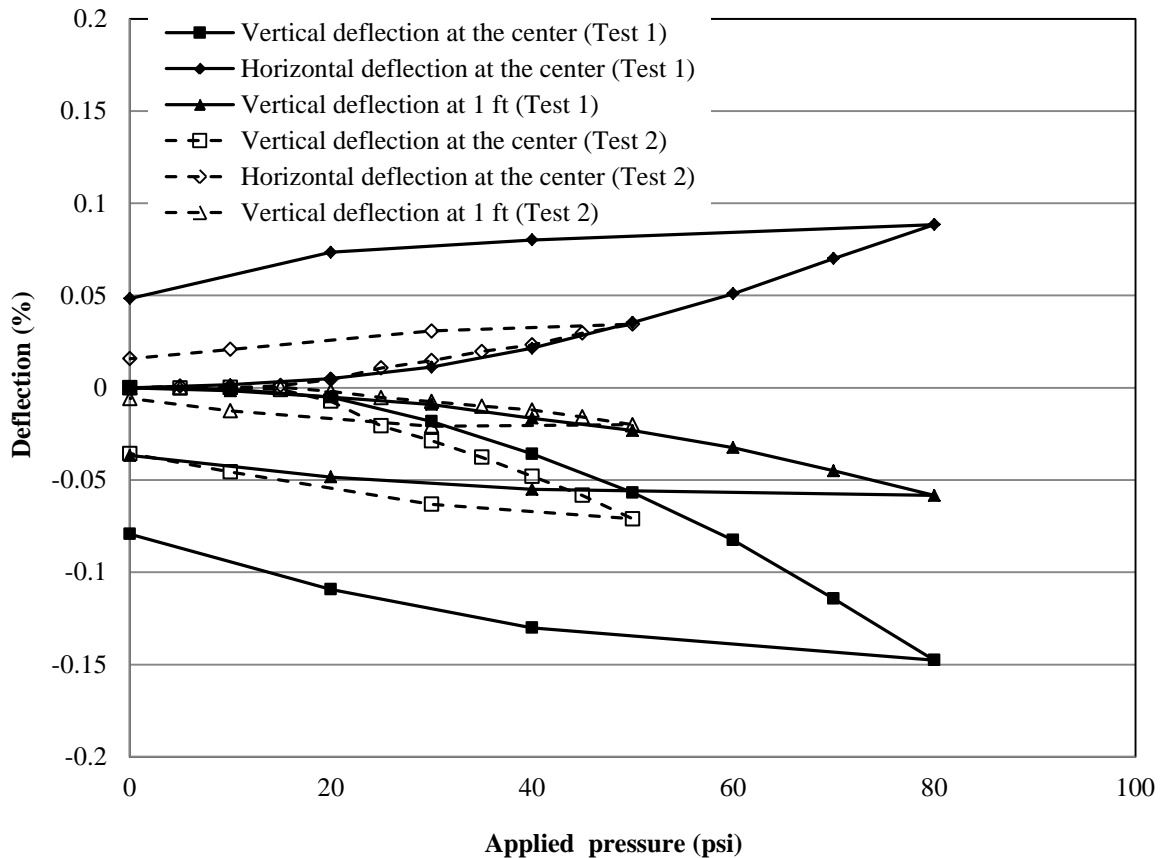
Figure 5.33 shows the deflections of the pipe against the applied pressures from Test 3. When the applied pressure was 100 psi, the decrease in the vertical diameter and the increase in the horizontal diameter at the center of the pipe section ( $\Delta D_{VC}$  and  $\Delta D_{HC}$ ) were 0.081 inches (0.34% of the initial diameter) and 0.050 inches (0.21% of the initial diameter), respectively. The vertical deflections at the center of the pipe ( $\Delta D_{VC}$ ) were approximately 1.64 times the horizontal deflections at the center of the pipe ( $\Delta D_{HC}$ ), and 1.53 times the vertical deflections at 1 ft from the center of the test pipe ( $\Delta D_{V1}$ ).



**FIGURE 5.33**  
Deflections of the Pipe under the Static Load in Test 3

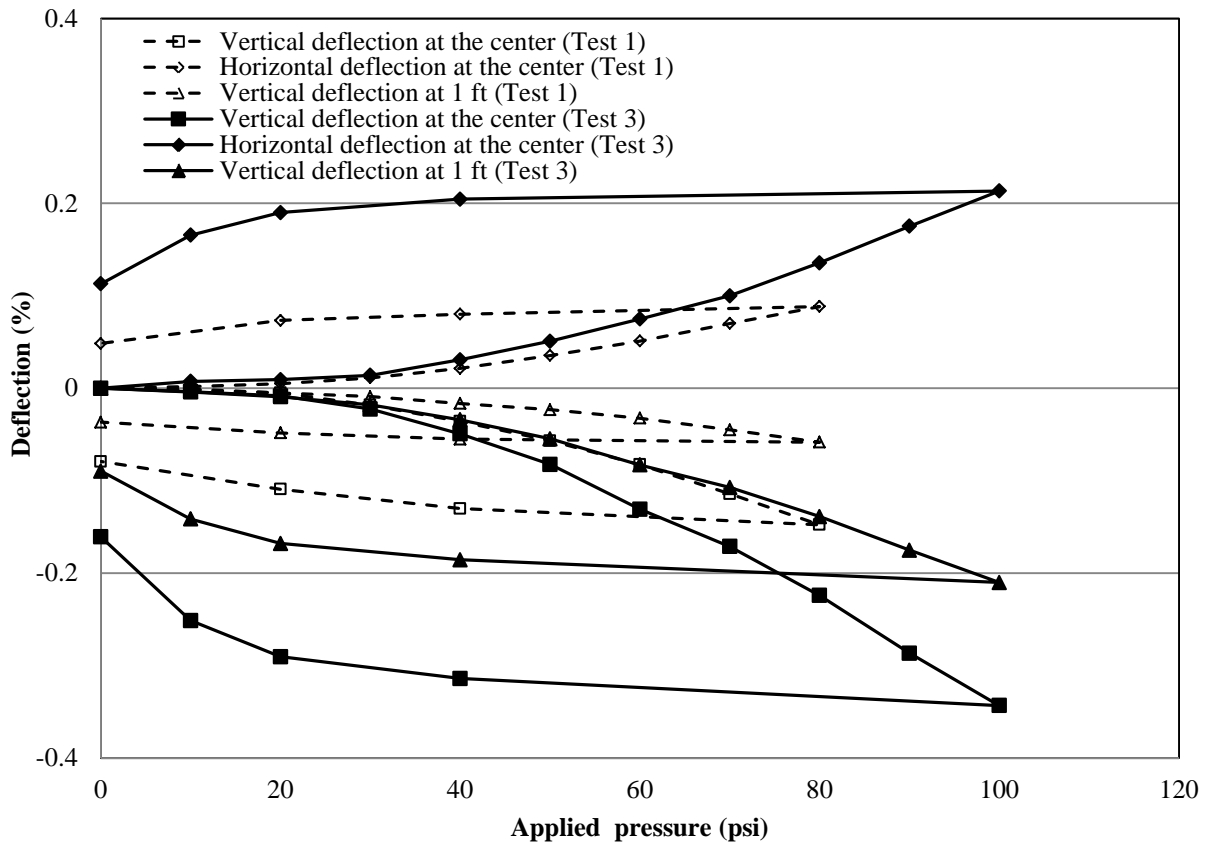
#### 5.2.3.4 Comparison of test results

Figure 5.34 shows the comparison of the deflection of the pipe in Test 1 (with the AB-3 base course and the sand backfill) and Test 2 (with the sand as the base course and the backfill). The measured vertical deflections at the center of the pipe ( $\Delta D_{VC}$ ) in Test 1 were smaller than those deflections in Test 2. However, the measured horizontal deflections at the center ( $\Delta D_{HC}$ ) and the vertical deflections measured at 1 ft longitudinally away from the center of the pipe ( $\Delta D_{V1}$ ) were nearly the same in both tests. The differences in the vertical deflections in Tests 1 and 2 resulted from the wider distribution of the load by the stiffer AB-3 base course in Test 1 than that in Test 2.



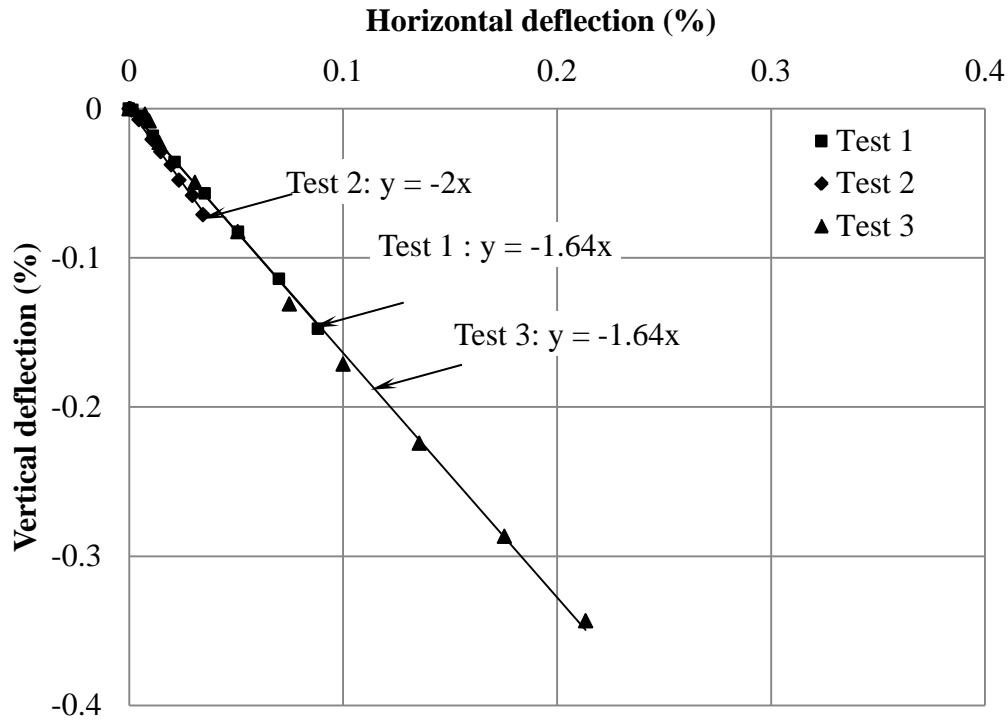
**FIGURE 5.34**  
**Comparison of the Deflections of the Pipe in Tests 1 and 2**

Figure 5.35 shows the comparison of the measured deflections of the pipe in Test 1 (with the sand backfill) and Test 3 (with the crushed stone backfill). The measured deflections of the pipe in Test 1 were smaller than those deflections in Test 3. The reason for Test 3 to have larger deflections is that the crushed stone (dumped) had a lower modulus of elasticity than the Kansas River sand (well compacted). The lower modulus of the crushed aggregate caused more load concentrated on the pipe.



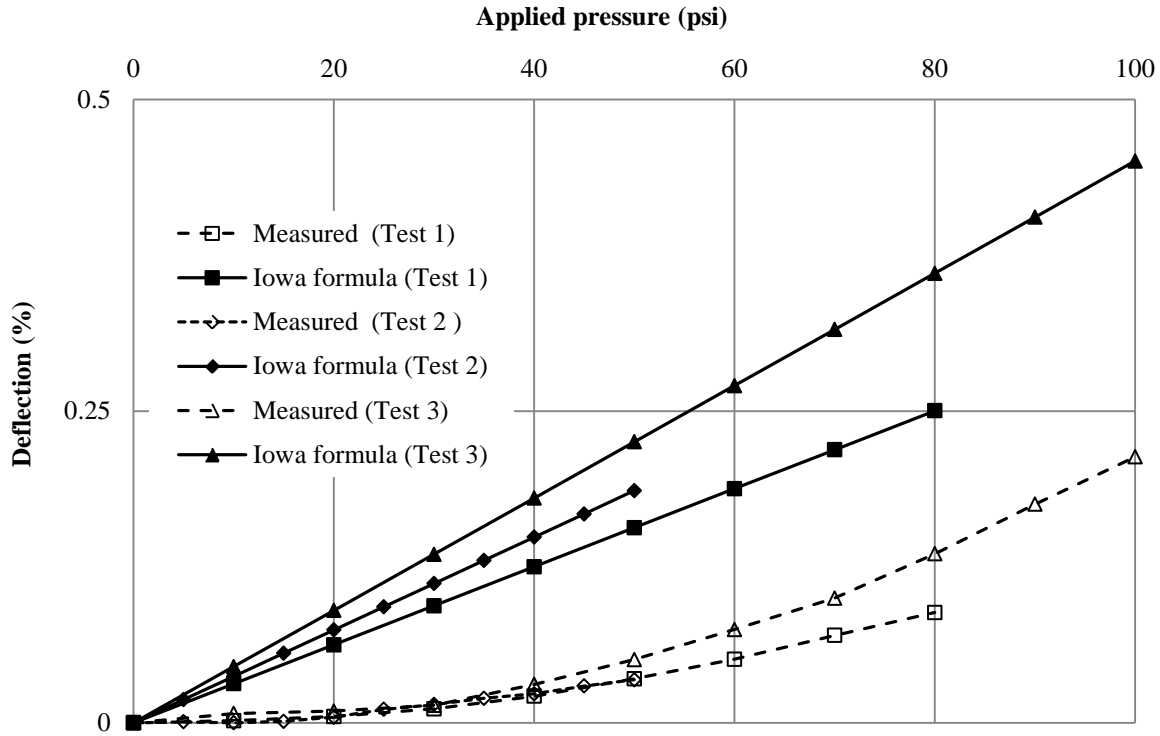
**FIGURE 5.35**  
**Comparison of the Deflection of the Pipe in Tests 1 and 3**

Figure 5.36 shows the relationship between the vertical and horizontal deflections at the center of the pipe during loading. The ratio of the vertical to horizontal deflection ( $\Delta D_{VC}/\Delta D_{HC}$ ) was approximately 1.64 in Test 1 and 3 whereas the ratio was approximately 2.0 in Test 2. The ratios of the vertical to horizontal deflection ( $\Delta D_{VC}/\Delta D_{HC}$ ) at the center of the pipe under the buried conditions were higher than those ratios for the pipe tested in air (i.e., 1.25). The higher ratios under the buried conditions were due to the resistance of the backfill against the horizontal deflections of the pipe.



**FIGURE 5.36**  
**Relation between the Horizontal and Vertical Deflections at the Center of the Pipe**

Figure 5.37 shows the measured horizontal deflections during loading compared with the calculated horizontal deflections using the Iowa formula (i.e., Equation 2.8). The calculation of the horizontal deflections at the center of the pipe were based on the bedding constant ( $k$ ) of 0.1, the earth pressure at the crown (i.e., live load), the moduli of subgrade reaction of 4,500 psi for the Kansas River sand and 2,500 psi for the crushed stone. The moduli of the subgrade reaction for the Kansas River sand and the crushed stone were determined using Equations 2.14 and 2.15 from the modulus of elasticity described in Section 3.2.2. The earth pressures at the crown were calculated using the Giroud and Han (2004) method (see Figure 5.28). It is shown that the Iowa formula over-predicted the deflections of the pipe during loading in all tests.



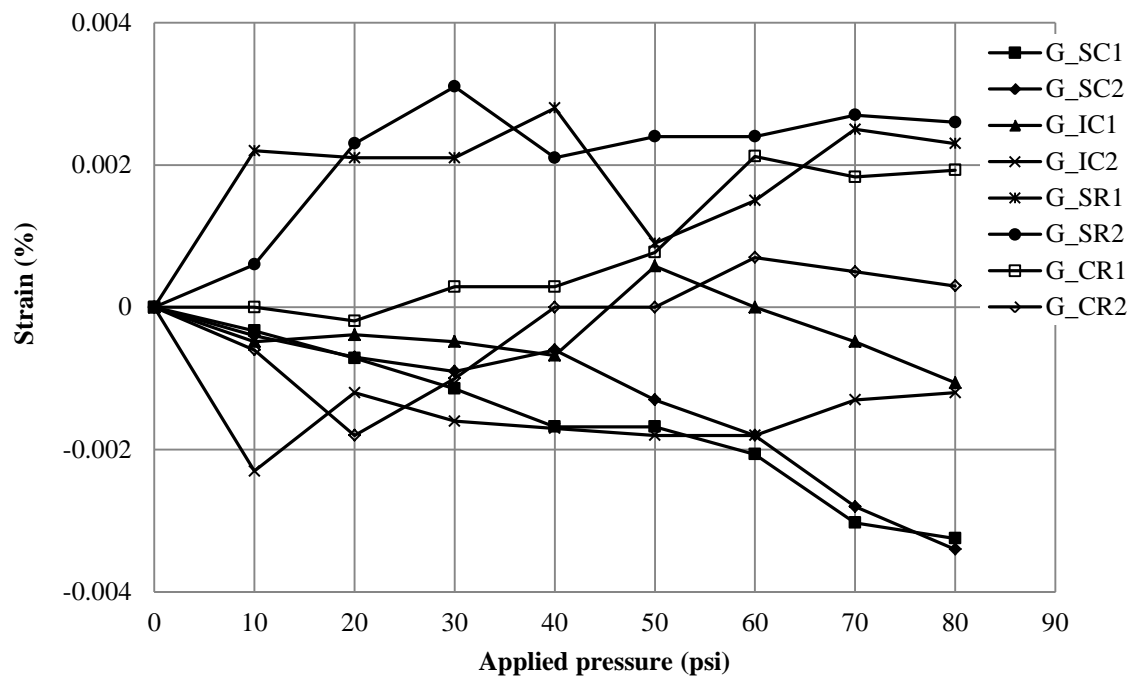
**FIGURE 5.37**  
**Comparison of the Measured and Calculated Vertical Deflections by the Iowa Formula**

## 5.2.4 Strain Results

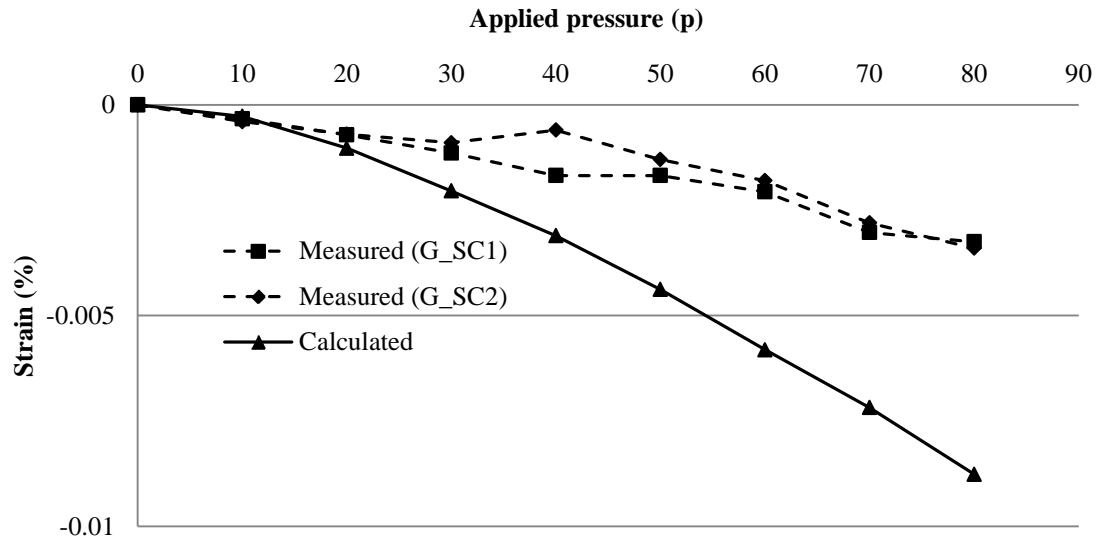
### 5.2.4.1 Test 1

The circumferential and radial strains on the steel of the pipe are shown in Figure 5.38. The strain gages,  $G_{SC1}$  and  $G_{SC2}$  at the springline and  $G_{IC1}$  and  $G_{IC2}$  at the invert in the circumferential direction, showed an increase in the compression strains, while  $G_{SR1}$  and  $G_{SR2}$  at the springline and  $G_{CR1}$  and  $G_{CR2}$  at the crown in the radial direction showed an increase in the tensile strains under the applied pressures. The maximum circumferential strain of 0.0034% ( $G_{SC1}$ , compressive strain) and the maximum radial strain of 0.0031% ( $G_{SR2}$ , tensile strain) developed at the maximum plate load. The strain gages fixed on both sides of the steel rib at any particular location gave similar values (i.e., there were no sudden changes in the strain values). This result indicates that the out-of-plane buckling of the steel ribs observed during the parallel plate load tests at a high level of load did not occur during the static loading. The maximum

strains, which were observed at the springline in the circumferential direction, are compared with the calculated values in Figure 5.39. The strains on the steel were calculated assuming the pipe carries all the applied loads on the top of the pipe (i.e., neglecting the side resistance from the fill at the springline). The calculated strains were higher than the measured strains.



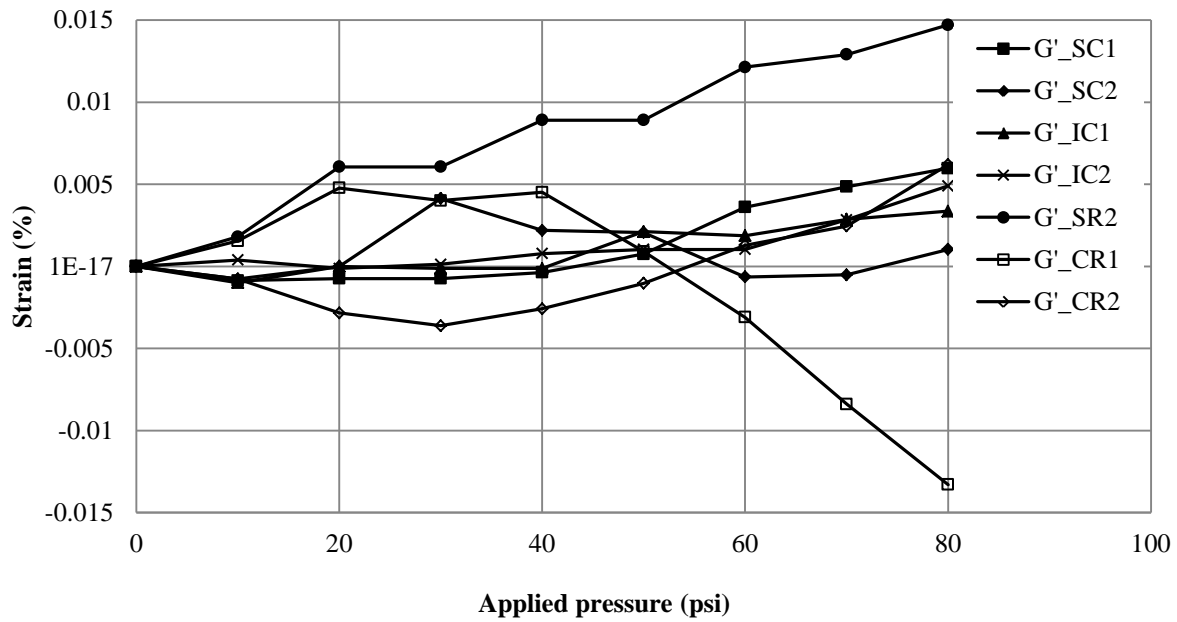
**FIGURE 5.38**  
**Measured Strains on the Steel Ribs in Test 1**



**FIGURE 5.39**  
**Measured and Calculated Strains on the Steel Ribs at the Springline in the Circumferential Direction**

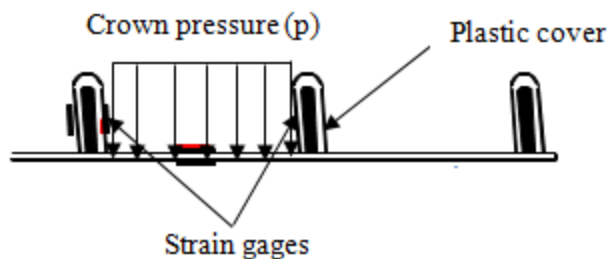
Figure 5.40 shows the circumferential and radial strains on the plastic at ribs against the applied static pressures. The strains developing in most locations on the plastic were higher in magnitude than those strains on the steel. Most of the strain gages showed an increase in tensile strains with an increase of the pressures except the strain gage  $G'_{CR1}$  which had an increase in compressive strains. During the static loading test, strain gages  $G'_{SR2}$  and  $G'_{CR1}$  on the plastic rib in the radial direction at the springline and the crown showed the maximum tensile strain of 0.014% and the maximum compressive strain of 0.013%, respectively.



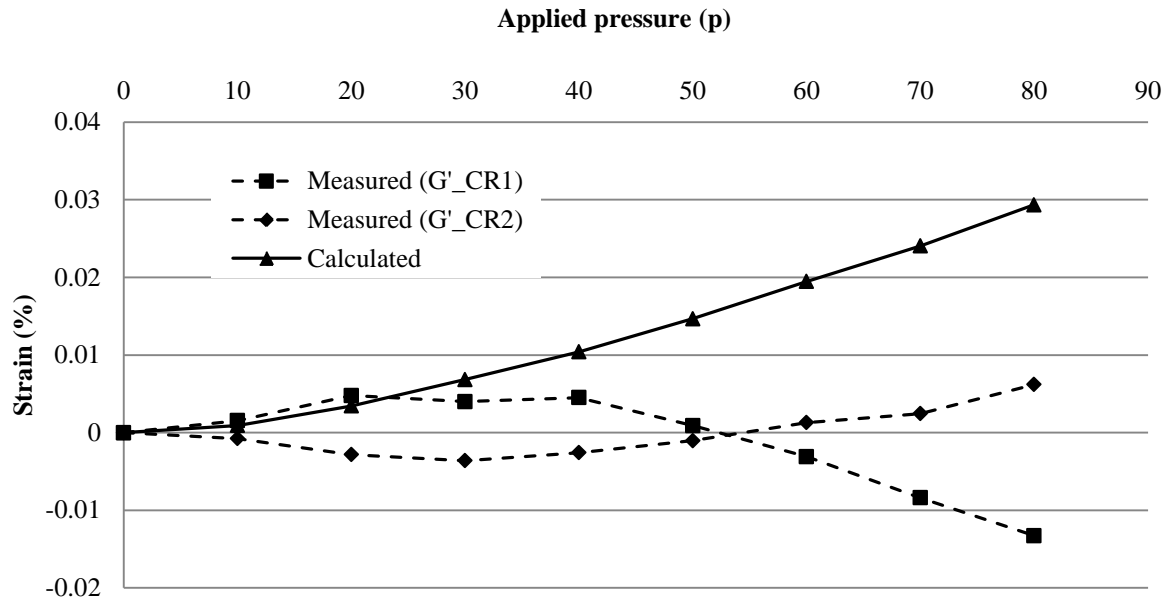


**FIGURE 5.40**  
**Measured Strains on the Plastic at Ribs in Test 1**

To calculate the strain in the plastic cover on the steel rib, we simplified the problem by assuming the load transfer mechanism as shown in Figure 5.41. Neglecting the arching effect and the friction between the plastic cover and the steel rib, all the load applied on an area between two ribs have to be carried by the plastic cover on the two ribs based on the vertical equilibrium. Since the maximum earth pressures and the strains (on the plastic) during static loading was observed on the top of the pipe at the crown, the strains on the plastic cover at the ribs in the radial direction at the pipe crown were calculated and were compared with the measured strains. Figure 5.42 shows the comparison between the measured and calculated strains in the plastic cover on the rib at the pipe crown. The calculated strains were higher than the measured strains.

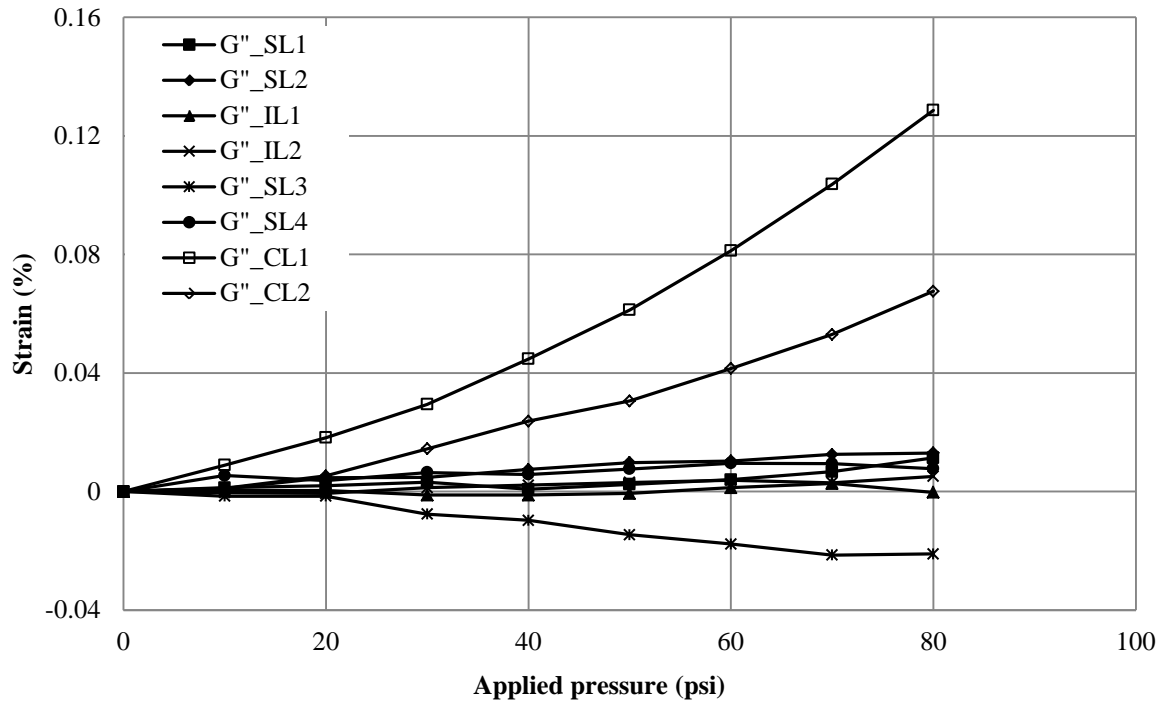


**FIGURE 5.41**  
**Simplified Load Transfer Mechanism**



**FIGURE 5.42**  
**Measured and Calculated Strains on the Plastic Cover at the Rib at the Pipe Crown**  
**in the Radial Direction in Test 1**

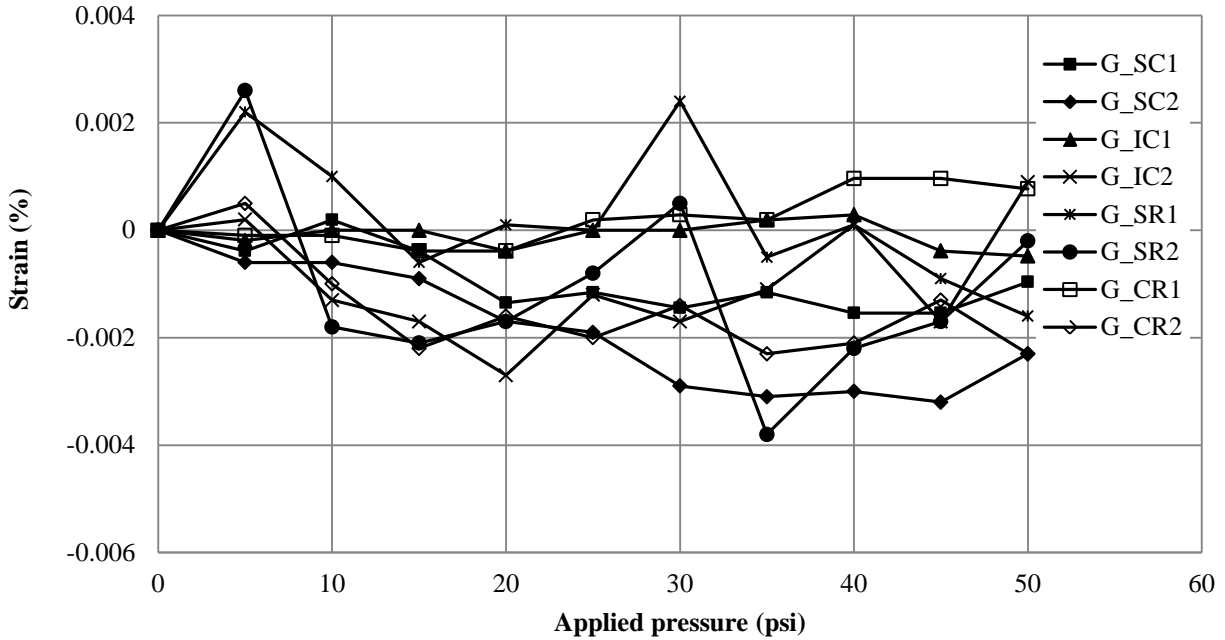
Figure 5.43 shows the strains measured by the strain gages on the plastic wall inside and outside the pipe. The magnitudes of the strains on the pipe walls were higher than the strains on the steel and plastic at the ribs. Most strain gages showed an increase in the tensile strains with an increase of the applied pressures except the strain gage  $G''_{SL3}$ , which had an increase in the compressive strains under the applied pressures. The maximum tensile strain of 0.13% was recorded by the strain gage  $G''_{CL1}$  while the maximum compressive strain of 0.023% was recorded by the strain gage  $G''_{SL3}$  under the applied static pressure of 80 psi. The strain gages on the pipe valley experienced the tensile strains and those on the inside wall had more tensile strains than those on the outside wall. This behavior of the valley wall on strain values indicates that the valley wall may have the combined bending and membrane effects. A numerical model is needed to investigate the load transfer mechanism of the plastic wall (i.e., the valley) further.



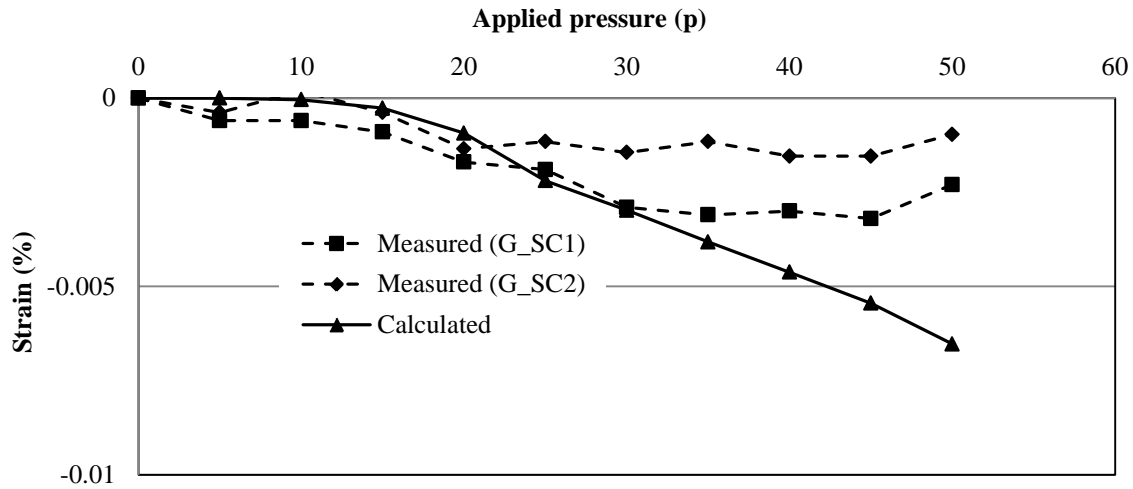
**FIGURE 5.43**  
**Measured Strains on the Inside and Outside Plastic Wall of the Pipe in Test 1**

#### 5.2.4.2 Test 2

The circumferential and radial strains on the steel of the pipe are shown in Figure 5.44. Most strain gauges showed an increase in the compressive strains with an increase of the static pressures except the strain gage  $G_{CR1}$  at the crown in the radial direction. The maximum circumferential strain of 0.0032% ( $G_{SC2}$ , compressive strain) and the maximum radial strain of 0.0007% ( $G_{CR1}$ , tensile strain) developed at the maximum applied static pressure. The strain gauges on both sides of the steel rib at any particular location gave similar strain values (i.e., there was no sudden change in the strain values). This result indicates that the out-of-plane buckling of the steel ribs observed during the parallel plate load tests at a high level of load did not occur during static loading. Figure 5.45 shows the comparison of the measured and calculated strains on the steel at the springline in the circumferential direction using the simplified load transfer mode proposed for Test 1.



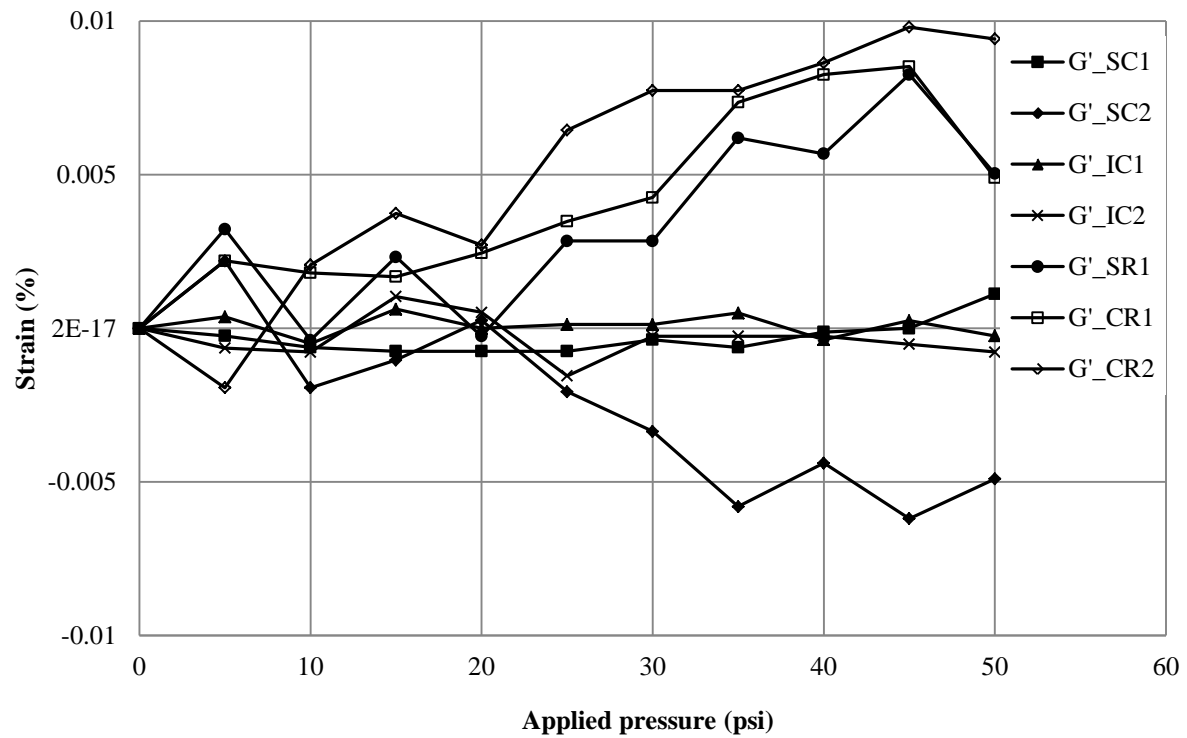
**FIGURE 5.44**  
**Measured Strains on the Steel Ribs in Test 2**



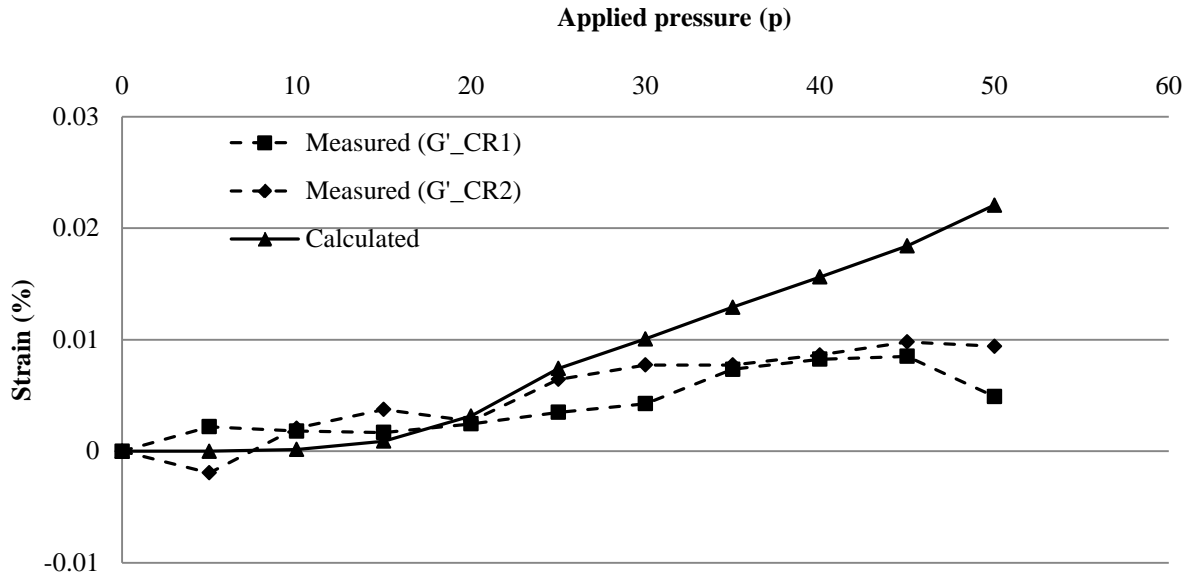
**FIGURE 5.45**  
**Measured and Calculated Strains on the Steel at the Springline in the Circumferential Direction in Test 2**

Figure 5.46 shows the circumferential and radial strains on the plastic cover on the ribs against the applied static pressures. The strains measured at most locations on the plastic cover were higher than those strains on the steel. The maximum circumferential strain of 0.0061%

( $G'_{SC2}$ , compressive strain) and the maximum radial strain of 0.0098% ( $G'_{CR2}$ , tensile strain) developed during loading. Figure 5.47 shows the comparison of the measured and calculated strains in the plastic cover on the ribs at the pipe crown.

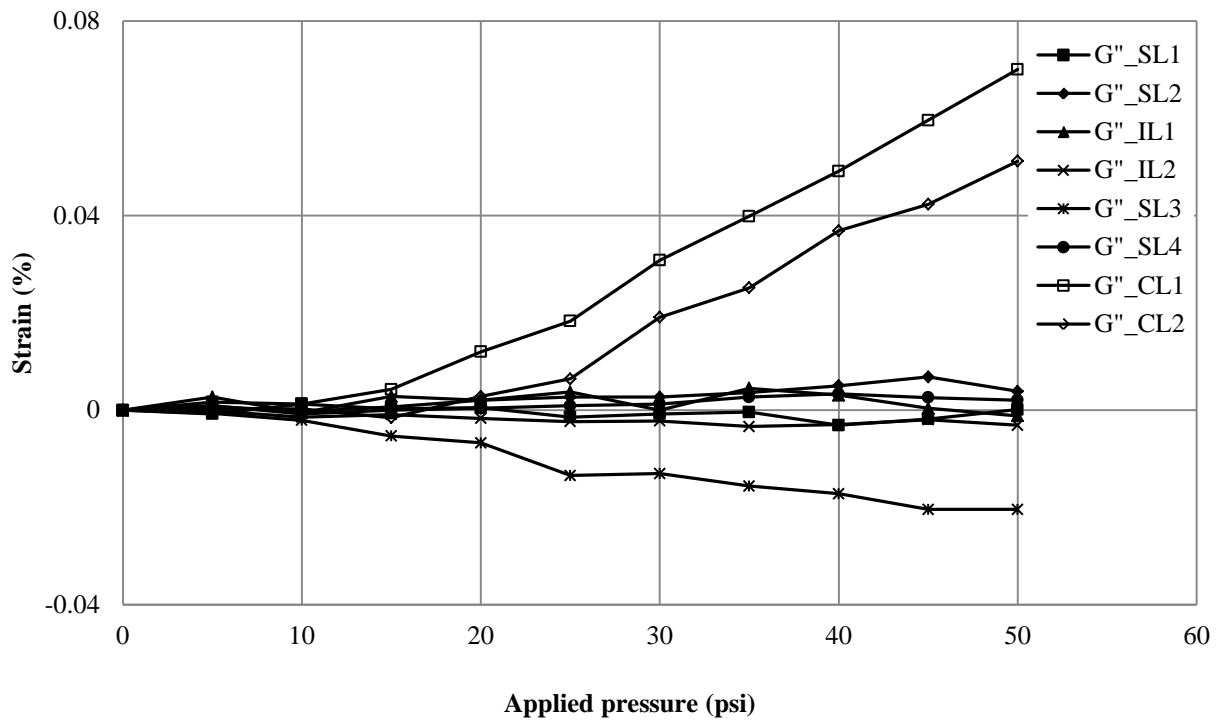


**FIGURE 5.46**  
Measured Strains on the Plastic Cover at the Ribs in Test 2



**FIGURE 5.47**  
**Measured and Calculated Strains on the Plastic Cover at the Rib at the Pipe Crown in the Radial Direction in Test 2**

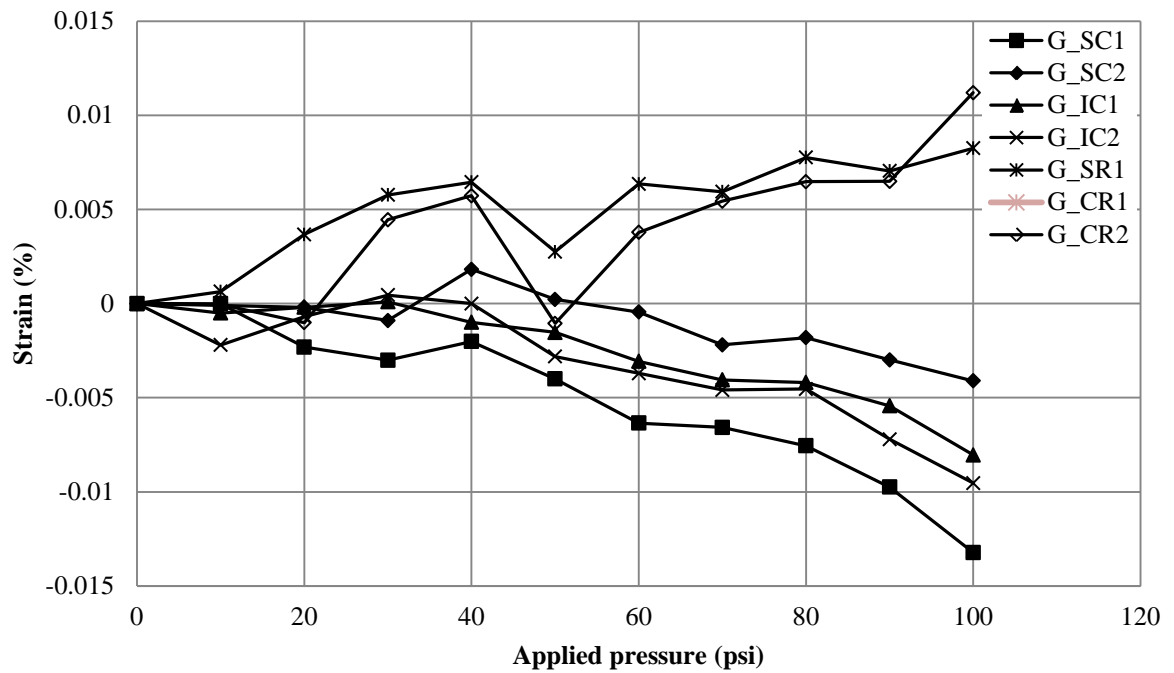
The strains measured by the strain gages on the inside and outside plastic walls are shown in Figure 5.48, which indicates that the magnitudes of the strains on the pipe walls were higher than those strains on the steel rib and plastic cover. The strain gages on the inside wall of the pipe experienced more tensile strains than those strains on the outside wall. Most strain gages showed an increase in the tensile strains with an increase of the applied pressures except the strain gage  $G''_{SL3}$ , which had an increase in the compressive strains under the applied static pressures. The strain gage  $G''_{CL1}$  at the crown measured the maximum tensile strain of 0.07% while the strain gage  $G''_{SL3}$  at the springline measured the maximum compressive strain of 0.019% during static loading.



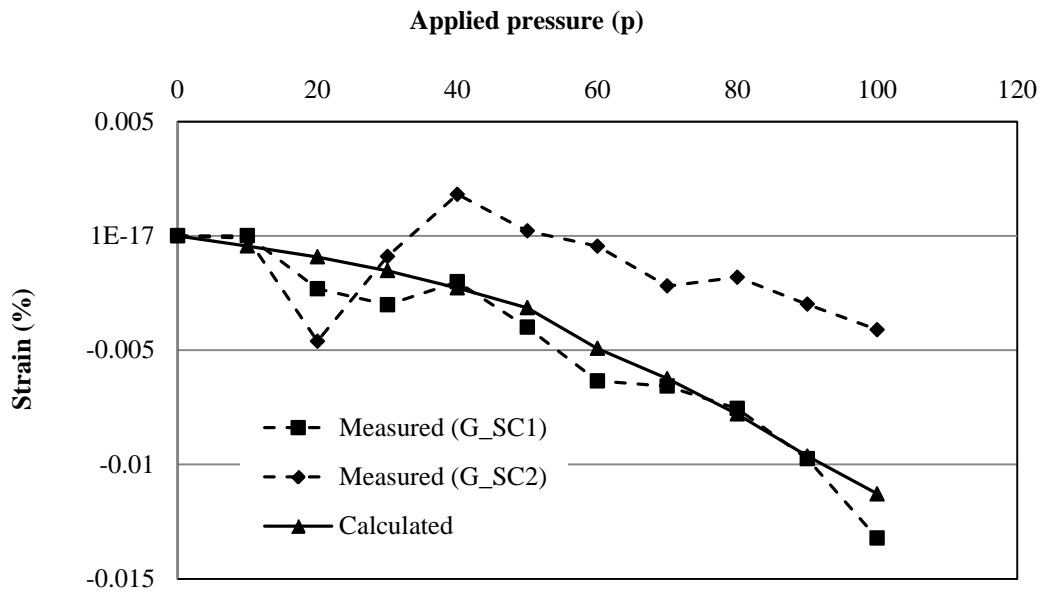
**FIGURE 5.48**  
**Measured Strains on the Inside and Outside Plastic Walls of the Pipe in Test 2**

#### 5.2.4.3 Test 3

The circumferential and radial strains on the steel of the pipe are shown in Figure 5.49. The strain gages,  $G_{SC1}$  and  $G_{SC2}$  at the springline and  $G_{IC1}$  and  $G_{IC2}$  at the invert in the circumferential direction, showed an increase in the compression strains while  $G_{SR1}$  at the springline and  $G_{CR2}$  at the crown in the radial direction showed an increase in the tensile strains under the applied static pressures. The maximum circumferential strain of 0.020% ( $G_{SC1}$ , compressive strain) and the maximum radial strain of 0.011% ( $G_{CR2}$ , tensile strain) developed during static loading. The strain gages on both sides of the steel rib at any particular location gave similar values (i.e., there was no sudden change in the strain values). This result indicates that the out-of-plane buckling of the steel ribs observed during the parallel plate load tests at a high level of load did not occur during static loading. Figure 5.50 shows the comparison of the measured and calculated strains in the steel rib at the pipe crown.



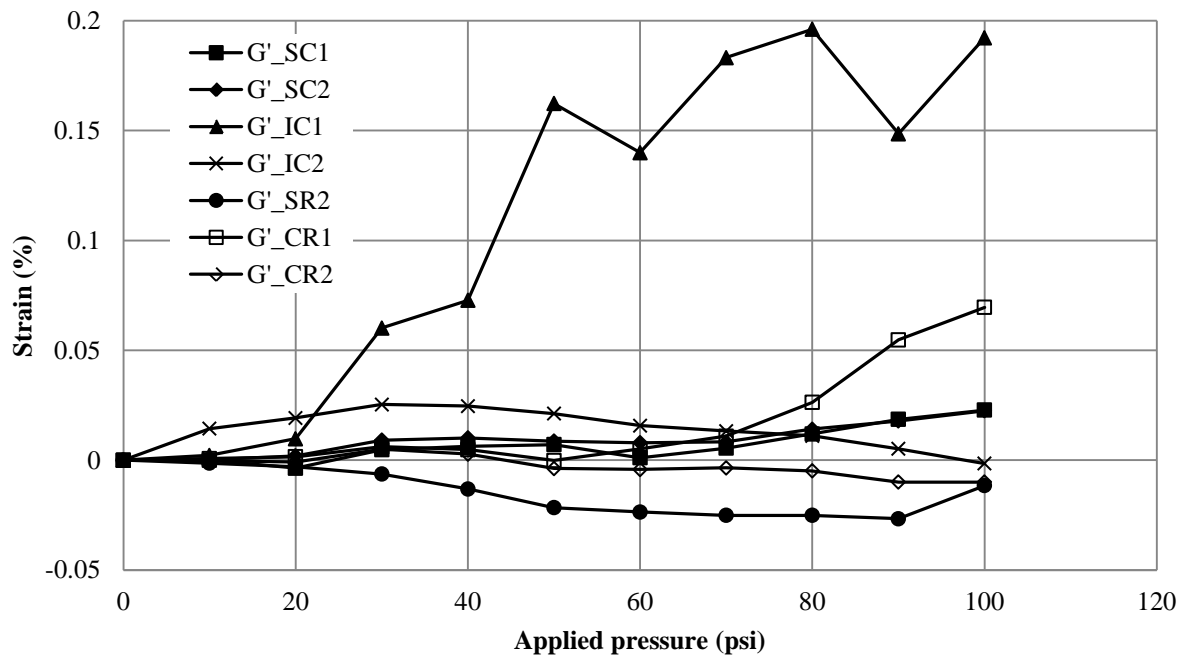
**FIGURE 5.49**  
Measured Strains on the Steel Ribs in Test 3



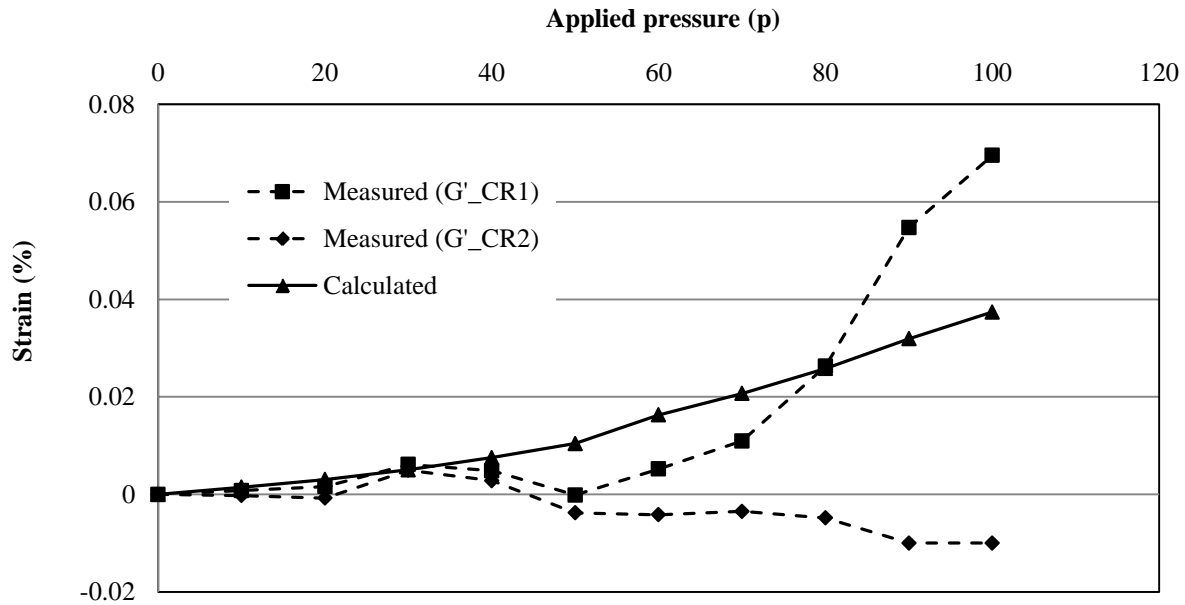
**FIGURE 5.50**  
Measured and Calculated Strains on the Steel Rib at the Springline in the Circumferential Direction in Test 3



Figure 5.51 shows the circumferential and radial strains on the plastic cover at the ribs against the applied static pressures. The strains measured at most locations on the plastic cover were higher in magnitude than those strains on the steel. The maximum circumferential strain of 0.19% ( $G'_{IC1}$ , tensile strain) and the maximum radial strain of 0.07% ( $G'_{CR1}$ , tensile strain) developed during static loading. Figure 5.52 shows the comparison of the measured and calculated strains in the plastic cover on the ribs at the pipe crown.



**FIGURE 5.51**  
**Measured Strains on the Plastic Cover at the Ribs in Test 3**



**FIGURE 5.52**  
**Measured and Calculated Strains on the Plastic Cover at the Ribs at the Pipe Crown in the Radial Direction in Test 3**

The strains measured by the strain gages on the inside and outside plastic walls are shown in Figure 5.53, and indicate that the magnitudes of the strains on the pipe walls were higher than those strains on the steel and plastic cover at the ribs. The strain gages on the pipe inside walls experienced more tensile strains than those on the outside walls. Most strain gages showed an increase in the tensile strains with an increase of the applied static pressures except the strain gages  $G''_{SL2}$  and  $G''_{SL4}$ , which had an increase in the compressive strains under the applied pressures. The maximum tensile strain of 0.360% was recorded by the strain gage  $G''_{CL1}$  at the crown while the maximum compressive strain of 0.054% was recorded by the strain gage  $G''_{SL4}$  at the springline during static loading.

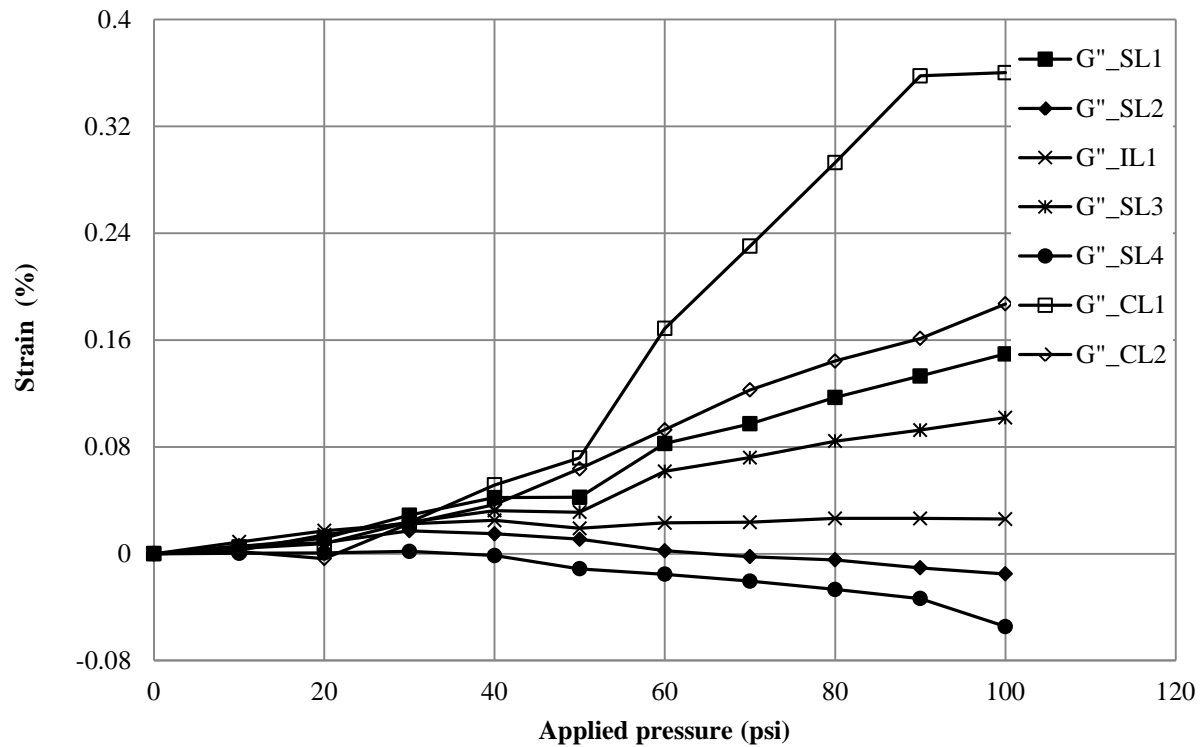


**FIGURE 5.53**  
Measured Strains on the Inside and Outside Plastic Wall of the Pipe in Test 3

### 5.3 Cyclic Plate Loading Test Result

After the static plate loading tests, cyclic loads, as described in Section 4.1.2, were applied on each test section. The vertical deformation of the loading plate, the earth pressures around the pipe, the deflections of the pipe, and the strains experienced in the pipe were monitored and are presented in the subsequent sections.

#### 5.3.1 Vertical Deformation of the Loading Plate

The vertical deformations of the loading plate against the applied cyclic pressures in Tests 1, 2, and 3 are shown in Figures 5.54, 5.55, and 5.56, respectively. It is shown that the test sections with the AB-3 base course in Tests 1 and 3 had more elastic rebound than that with the sand base course in Test 2. The settlement of the loading plate under cyclic loading is the permanent deformation of the plate after unloading in the load cycle. Figure 5.57 shows the comparison of the settlements of the loading plate for all the tests under both static and cyclic

loadings. Table 5.1 shows the load step, the number of load cycles, and the permanent deformation of the loading plate for each load step in Tests 1, 2, and 3. The permanent deformation was higher in Test 2 because the Kansas River sand was used as the base course instead of the AB-3 aggregate. Even though Tests 1 and 3 had the same base course (i.e., 9 inches thick AB-3 aggregate), the permanent deformation was higher in Test 3 than in Test 1 because the crushed stone in Test 3 was dumped in place without any compaction.

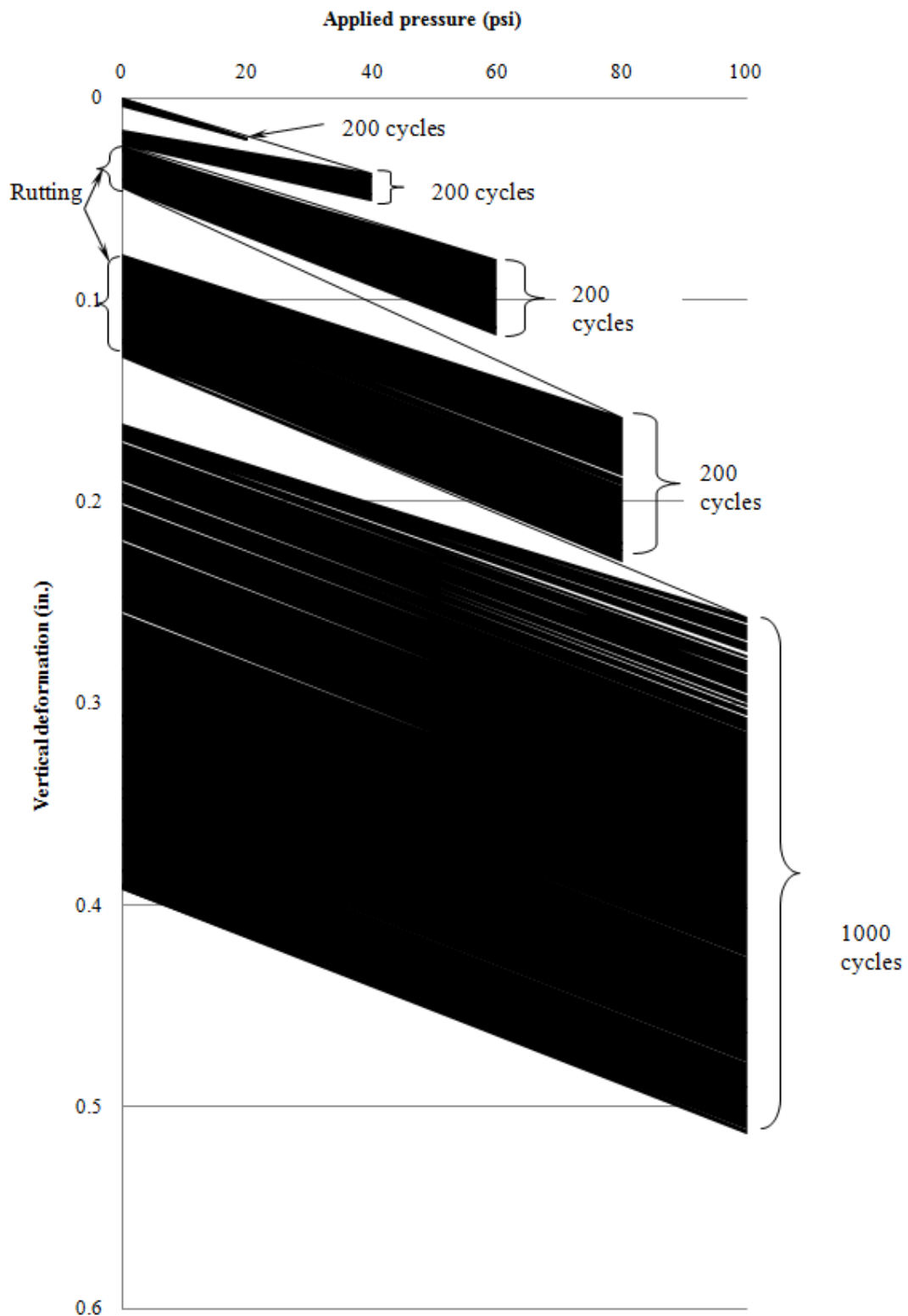


**FIGURE 5.54**  
**Vertical Deformation of the Loading Plate under Cyclic Loading in Test 1**

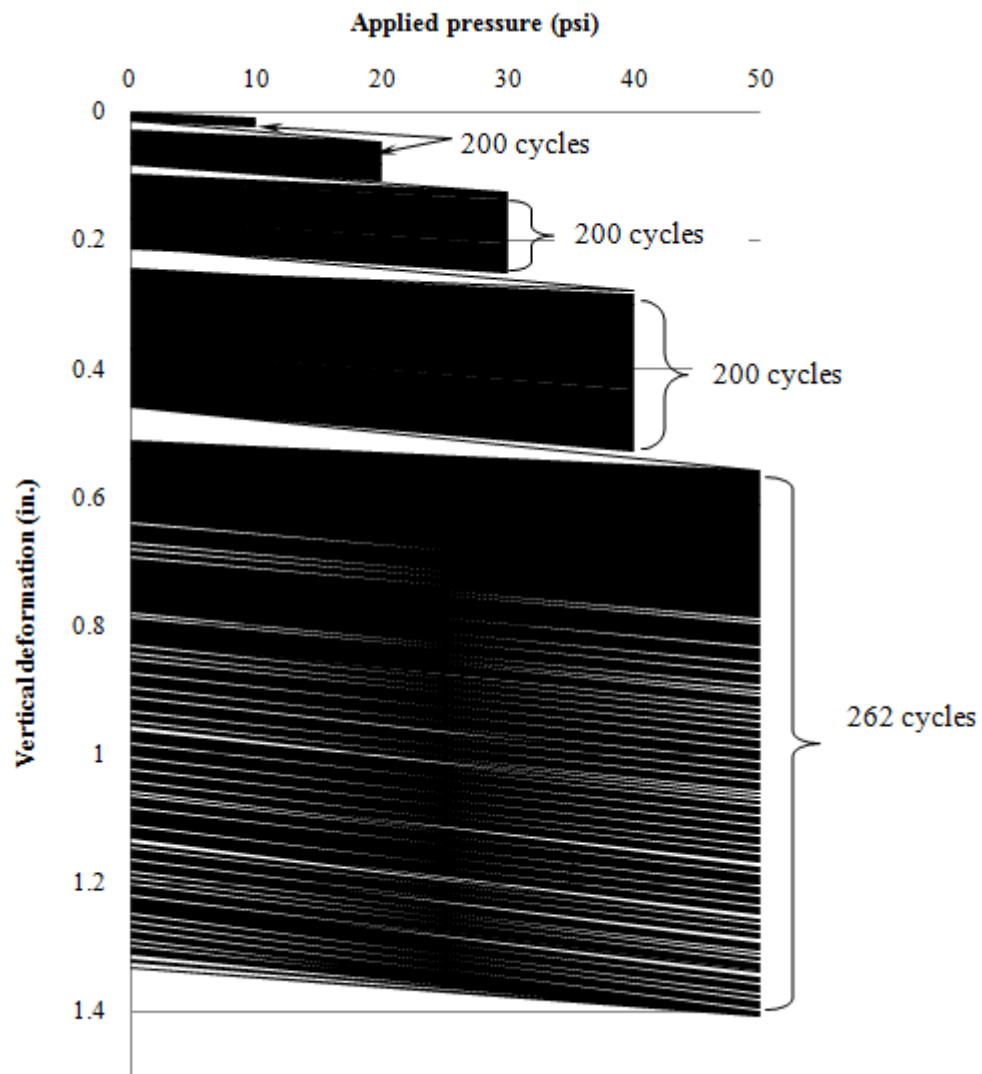


**FIGURE 5.55**  
**Vertical Deformation of the Loading Plate under Cyclic Loading in Test 1**

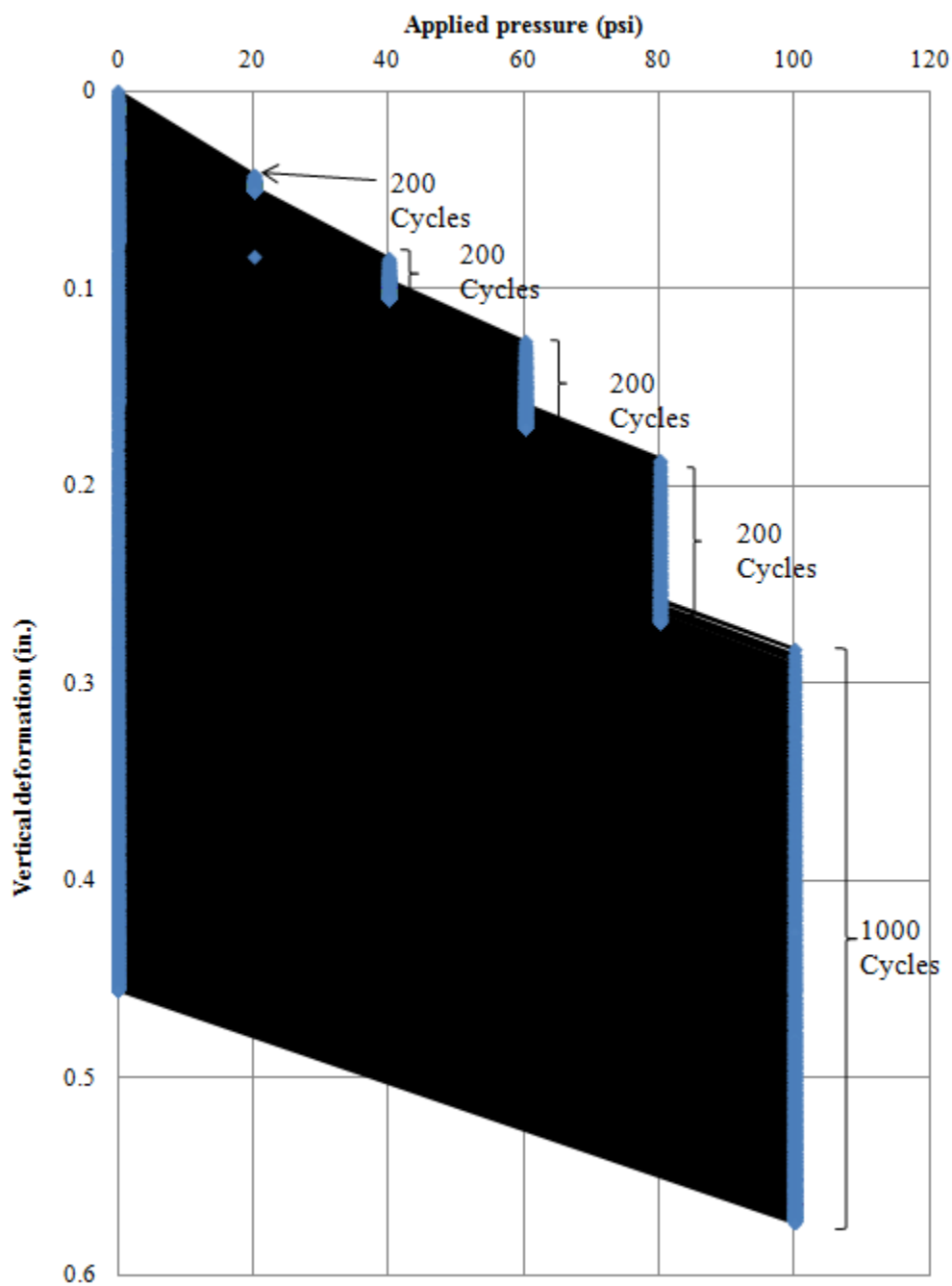


**FIGURE 5.56**  
Vertical Deformation of the Loading Plate under Cyclic Loading in Test 3

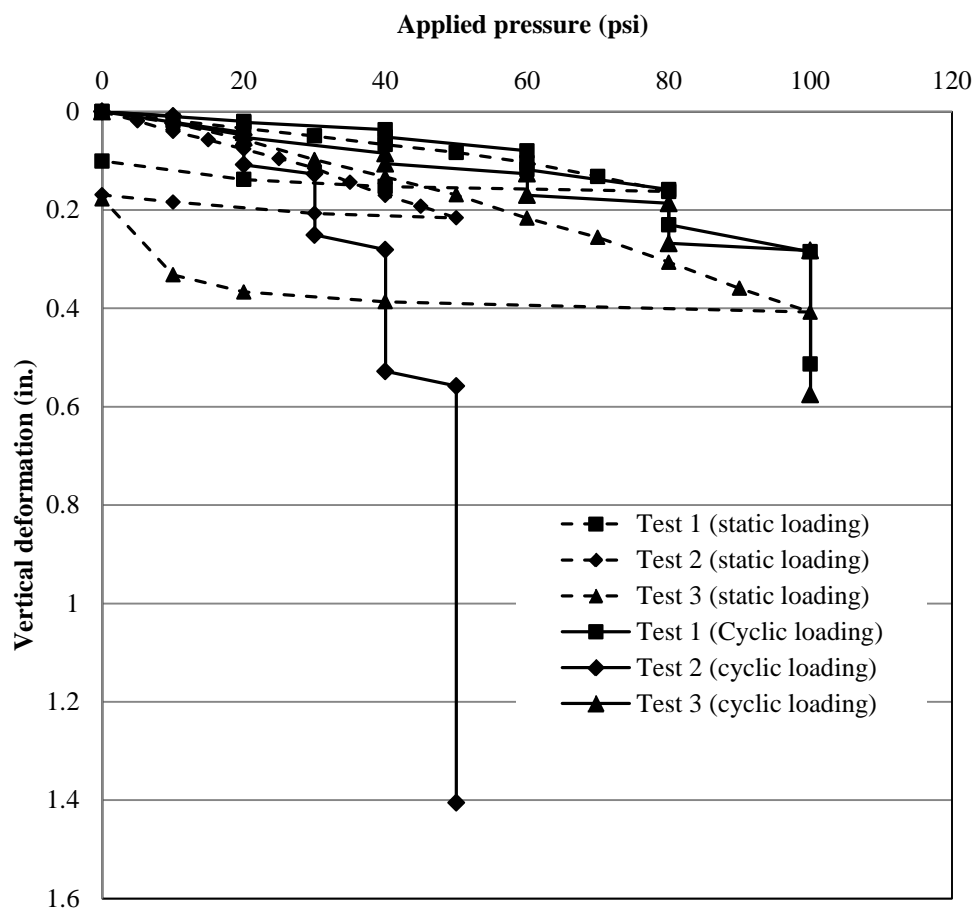


**FIGURE 5.57**  
Vertical Deformation of the Loading Plate under Static and Cyclic Loadings

**TABLE 5.1**  
Permanent Deformations

Loading Step	Applied pressure (psi)		Cycles		Permanent deformation (in.) (due to each load step)		
	Test 1 and 3	Test 2	Test 1 and 3	Test 2	Test 1	Test 2	Test 3
1	0-20	0-10	200	200	0.005	0.015	0.011
2	0-40	0-20	200	200	0.008	0.04	0.019
3	0-60	0-30	200	200	0.020	0.11	0.040
4	0-80	0-40	200	200	0.050	0.215	0.080
5	0-100	0-50	1000	260	0.227	0.818	0.296



### 5.3.2 Maximum Earth Pressure Results

The maximum earth pressures measured by the earth pressure cells during each loading step were induced by cyclic loading only. In other words, the earth pressures induced during installation and static loading were not included. These cyclic earth pressure results are discussed in this section.

#### 5.3.2.1 Test 1

Figure 5.58 shows the measured maximum earth pressures against the applied cyclic pressures in all the loading steps in Test 1. The earth pressure cell at the pipe crown ( $E_{C6}$ ) showed the highest earth pressure on the pipe. The maximum earth pressure measured at the crown ( $E_{C0}$ ) at the end of 1,000 cycles of the final load step (0 to 100 psi) was approximately 12 psi. The vertical earth pressure at 6 inches away from the center ( $E_{C6}$ ) was 0.55 to 0.67 times that at the pipe crown ( $E_{C0}$ ). The maximum horizontal pressure at the pipe springline ( $E'_{S0}$ ) was 0.3 to 0.4 times the maximum vertical earth pressure at the crown ( $E_{C0}$ ). The ratio of the maximum horizontal pressure at the springline ( $E'_{S0}$ ) to that at the shoulder ( $E'_{Sh0}$ ) was 1.25 to 1.5.

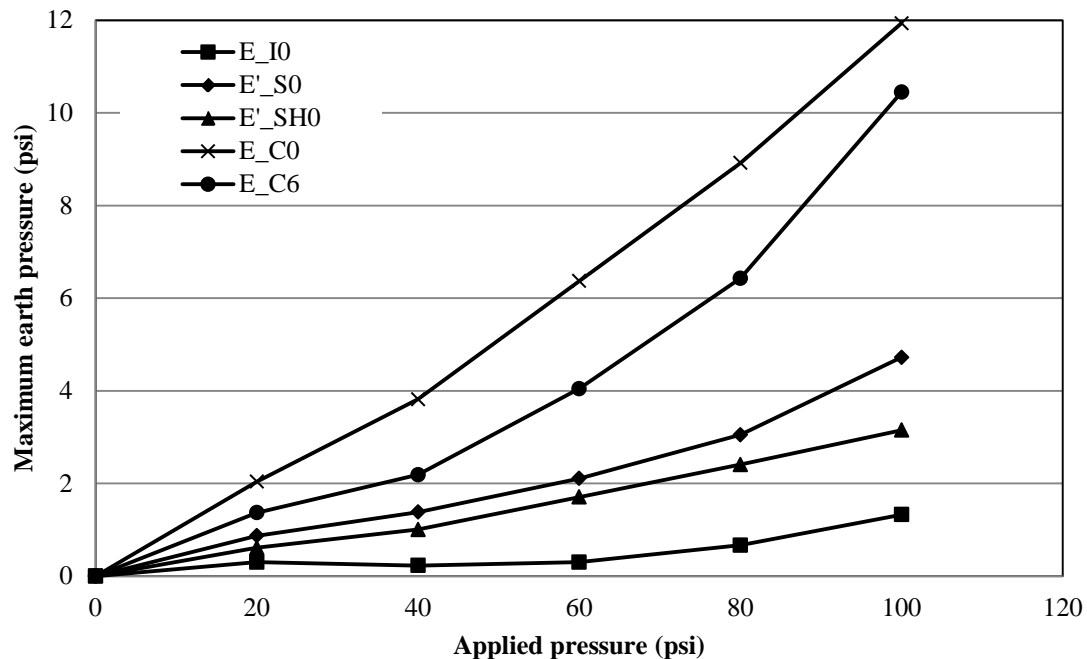


**FIGURE 5.58**  
**Measured Maximum Earth Pressures around the Pipe under Cyclic Loading in Test 1**

### 5.3.2.1 Test 2

Figure 5.59 shows the measured maximum earth pressures against the applied cyclic pressures in all the loading steps in Test 1. The earth pressure cell at the pipe crown ( $E_{C0}$ ) showed the highest earth pressure on the pipe. The maximum earth pressure measured at the crown ( $E_{C0}$ ) at the end of 260 cycles of the final load step (0 to 50 psi) was approximately 5.83 psi. The maximum vertical earth pressure at 6 inches away from the center ( $E_{C6}$ ) was 0.60 to 0.70 times that at the pipe crown ( $E_{C0}$ ). The maximum horizontal earth pressure at the pipe springline ( $E'_{S0}$ ) was 0.3 to 0.45 times the maximum vertical earth pressure at the crown ( $E_{C0}$ ). The ratio of the maximum horizontal earth pressure at the springline ( $E'_{S0}$ ) to that at the shoulder ( $E'_{Sh0}$ ) was 1.1 to 1.46.

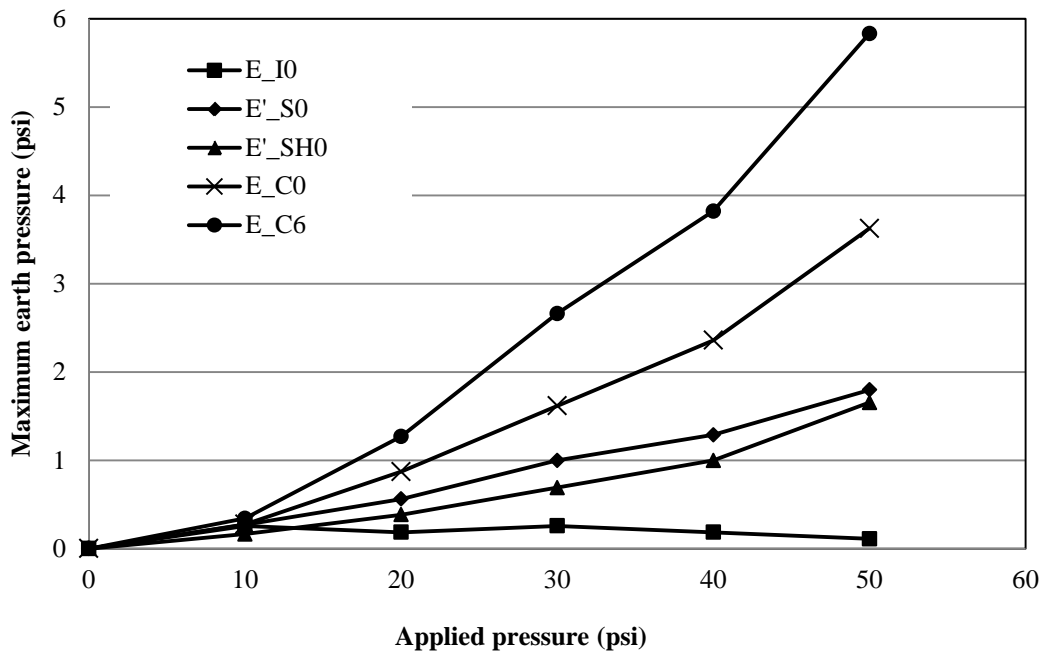


**FIGURE 5.59**  
Measured Maximum Earth Pressures around the Pipe under Cyclic Loading in Test 2

### 5.3.2.2 Test 3

Figures 5.60 and 5.61 show the maximum earth pressures recorded by the earth pressure cell ( $E_{IF}$ ) at the base course and backfill interface and nine other earth pressure cells around the pipe against the applied cyclic pressures in different loading steps. Figure 5.61 shows that the

maximum earth pressures recorded by the earth pressure cell ( $E_{C6}$ ) at 6 inches away from the pipe crown were the highest during loading. The maximum earth pressure measured at the crown ( $E_{C0}$ ) at the end of 1,000 cycles of the final load step (0 to 100 psi) was approximately 8 psi. The maximum vertical earth pressure at 6 inches away from the center ( $E_{C6}$ ) was mostly 1.5 to 2 times that at the pipe crown ( $E_{C0}$ ). The maximum horizontal earth pressures at the pipe springline ( $E_{S0}$  and  $E_{S8}$ ) were 0.04 to 0.10 times the maximum vertical earth pressure at the crown ( $E_{C0}$ ). The ratio of the maximum horizontal earth pressure at the springline ( $E_{S0}$ ) to that at the shoulder ( $E_{SH0}$ ) was 0.16 to 0.22.

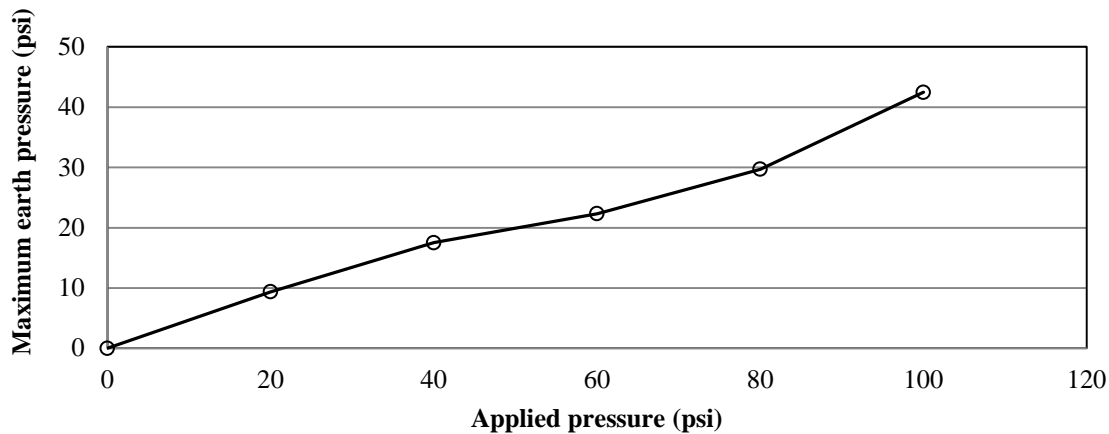


**FIGURE 5.60**  
**Measured Maximum Earth Pressure at the Backfill-Base Course Interface in**  
**Test 3**

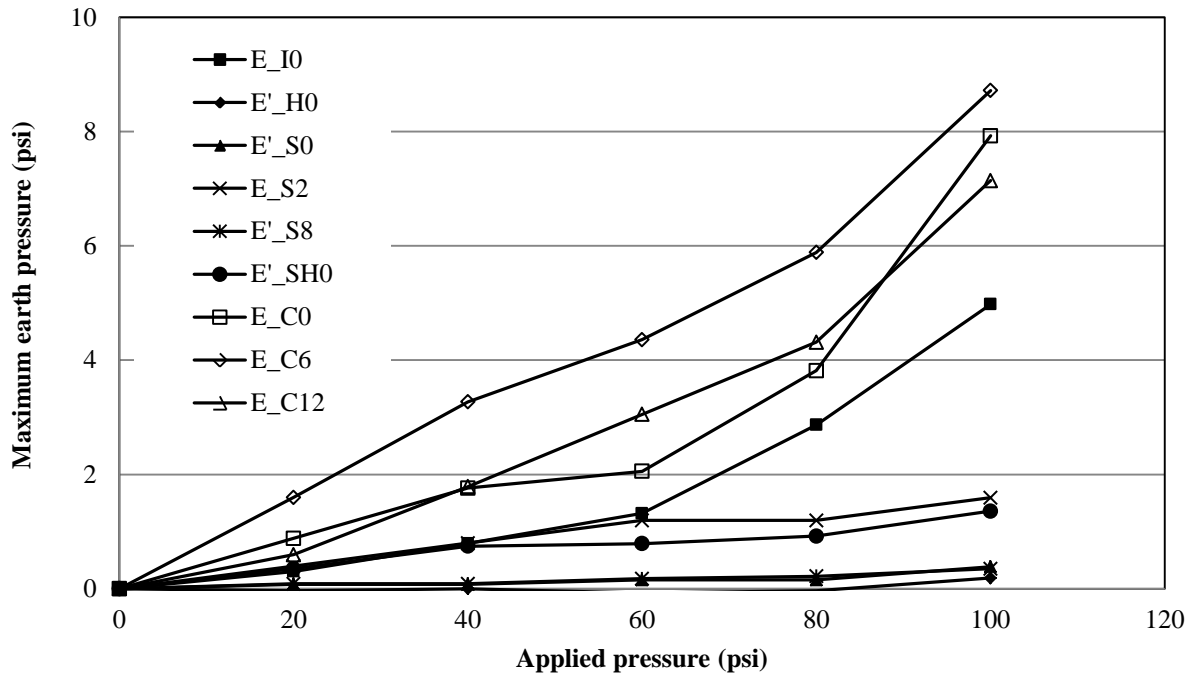


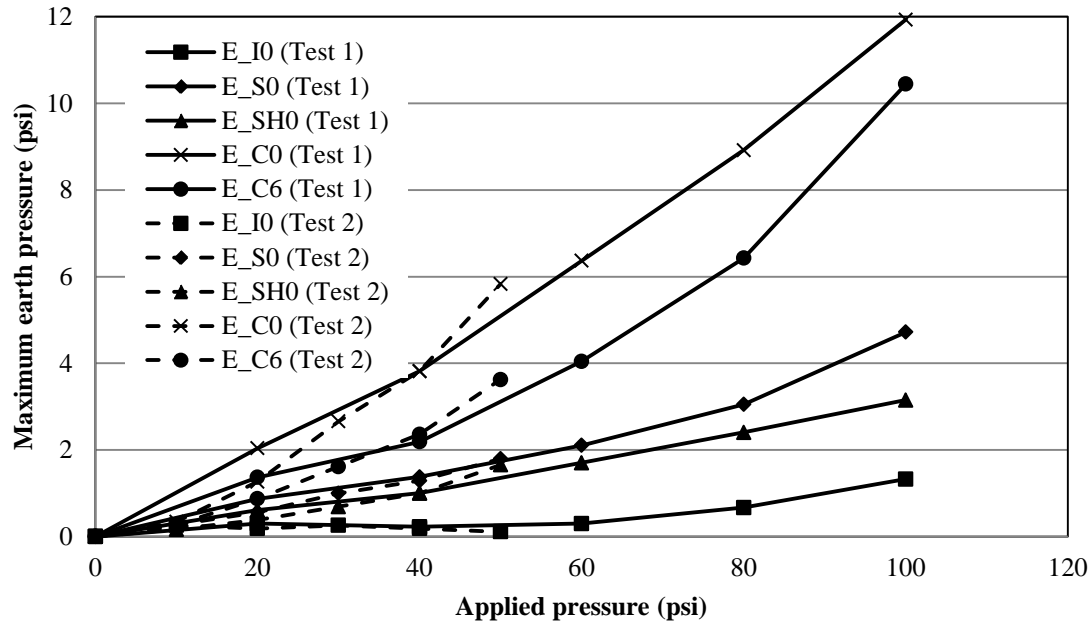
**FIGURE 5.61**  
Measured Maximum Earth Pressures around the Pipe under Cyclic Loading in Test 3

### 5.3.2.3 Comparison of Test Results

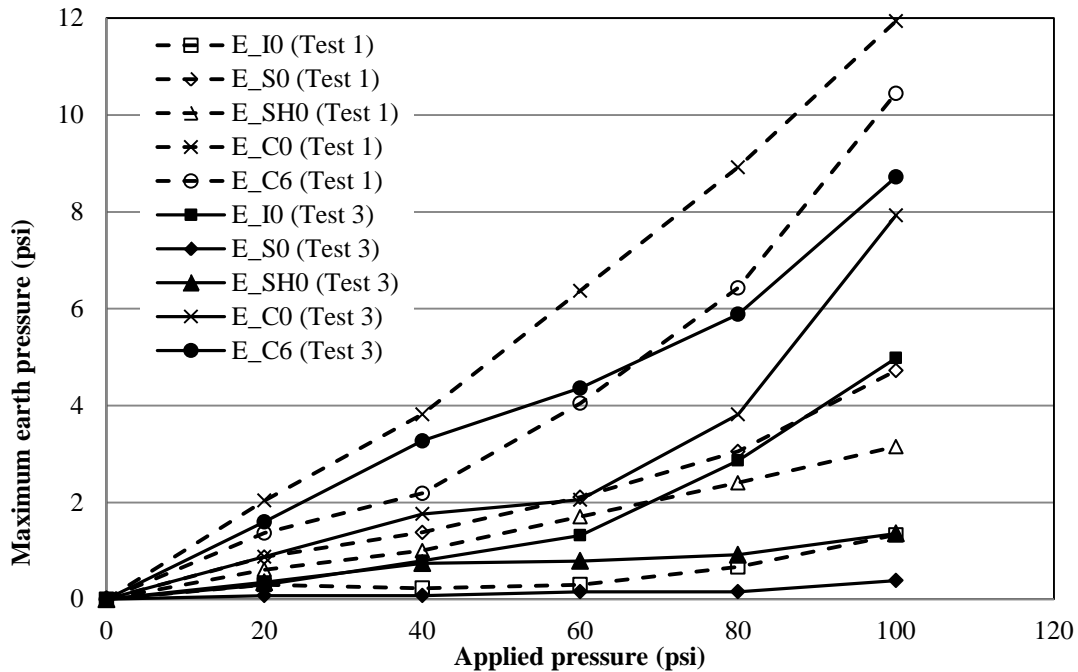
Figure 5.62 shows the comparison of the maximum earth pressure distributions around the pipe in Test 1 (with the AB-3 base course and the sand backfill) and Test 2 (with the sand as the backfill and the base course). The maximum earth pressures around the pipe were lower in Test 2 than in Test 1 at low applied pressures. As the applied pressure was increased, the differences became smaller. At the high applied pressures, the maximum earth pressures around the pipe were higher in Test 2 than in Test 1.

Figure 5.63 shows the comparison of the maximum earth pressure distributions around the pipe for two different backfills: the sand in Test 1 and the crushed stone in Test 3. The maximum earth pressures around the pipe were higher in Test 1 than in Test 3. The maximum vertical earth pressures at the crown ( $E_{C0}$ ) were higher than those vertical pressures at 6 inches away from the crown ( $E_{C6}$ ) in Test 1. However, the maximum earth pressures at the crown ( $E_{C0}$ ) were lower than those ( $E_{C6}$ ) in Test 3. Similarly, the maximum horizontal earth pressures at the

springline ( $E_{S0}$ ) were lower than those ( $E_{SH0}$ ) at the shoulder in Test 3. However, the maximum horizontal earth pressures at the springline ( $E_{S0}$ ) were higher than those earth pressures at the shoulder ( $E_{SH0}$ ) in Test 1. The earth pressure cell at the invert ( $E_{I0}$ ) showed the higher earth pressure in Test 3 than that in Test 1 because the pipe was lifted up in Test 1 as discussed in Section 5.1.1, but there was little or no lift-up of the pipe in Test 3 during backfilling.



**FIGURE 5.62**  
Comparison of the Maximum Earth Pressures around the Pipe under Cyclic Loading in Tests 1 and 2



**FIGURE 5.63**  
**Comparison of the Maximum Earth Pressures around the Pipe under Cyclic Loading in Tests 1 and Test 3**

### 5.3.3 Pipe Deflection Results

#### 5.3.3.1 Test 1

The maximum deflections of the pipe (or the changes in the inside diameters) against the applied cyclic pressures are shown in Figure 5.64. The maximum deflection of the test pipe illustrates that the vertical diameter of the pipe decreased while the horizontal diameter of the pipe increased as the load increased. The maximum vertical deflection at the center of the pipe was approximately 1.5 to 2 times the maximum horizontal deflection at the same pipe section and 2.5 to 3 times the maximum vertical deflection at 1 ft longitudinally from the center of the test pipe. The maximum decrease in the vertical diameter and the maximum increase in the horizontal diameter at the center of the pipe at the end of 1,000 cycles of the final load step (0 to 100 psi) was 0.055 inches (0.23% of the initial diameter) and 0.027 inches (0.11% of the initial diameter), respectively.

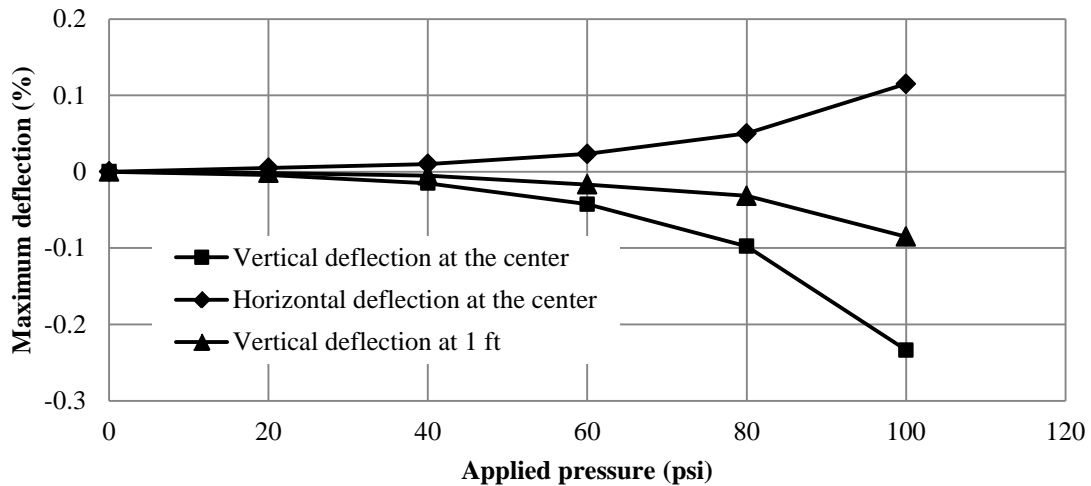


**FIGURE 5.64**  
**Maximum Deflections of the Pipe under Cyclic Loading in Test 1**

#### 5.3.3.2 Test 2

The maximum deflections of the pipe (or the changes in the inside diameters) against the applied cyclic pressures are shown in Figure 5.65. The maximum vertical deflection at the center of the pipe was approximately 1.26 to 1.8 times the maximum horizontal deflection at the same pipe section, and 1.75 to 3.1 times the maximum vertical deflection at 1 ft longitudinally from the center of the test pipe. The maximum decrease in the vertical diameter and the maximum increase in the horizontal diameter at the center of the pipe at the end of 260 cycles of the final load step (0 to 50 psi) were 0.0098 inches (0.042% of the initial diameter) and 0.0054 inches (0.023% of the initial diameter), respectively.

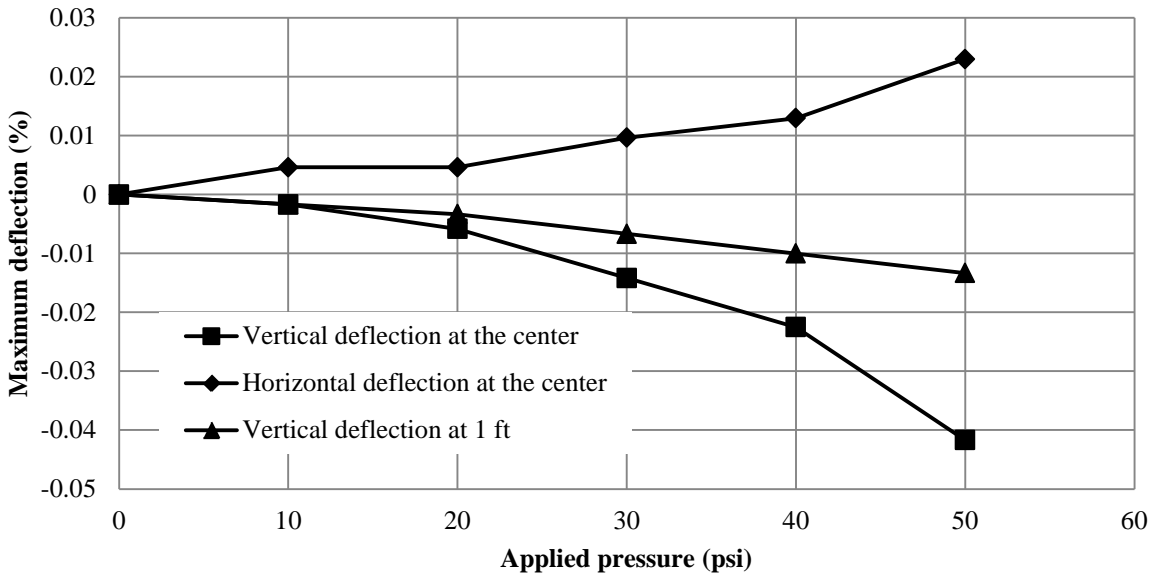
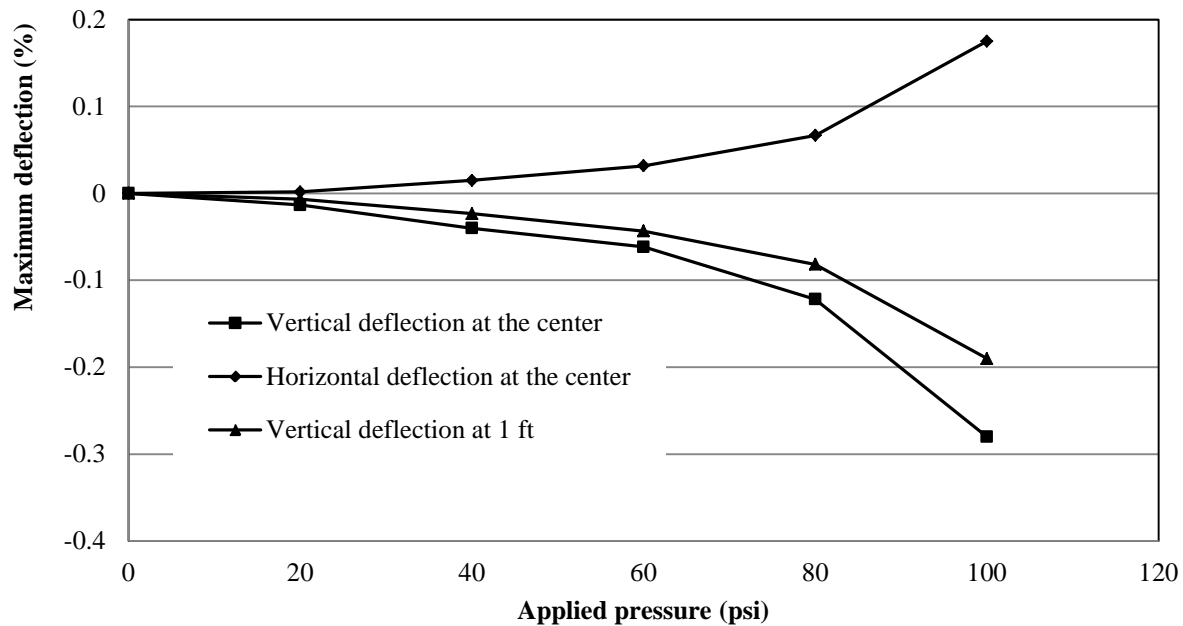


**FIGURE 5.65**  
**Maximum Deflections of the Pipe under Cyclic Loading in Test 2**

#### 5.3.3.3 Test 3

The maximum deflections of the pipe (or the changes in the inside diameters) against the applied cyclic pressures are shown in Figure 5.66. The maximum vertical deflection at the center of the pipe was approximately 1.5 to 2 times the maximum horizontal deflection at the same pipe section and 1.4 to 2.0 times the maximum vertical deflection at 1 ft longitudinally from the center of the test pipe. The maximum decrease in the vertical diameter and the maximum increase in the horizontal diameter at the center of the pipe at the end of 1,000 cycles of the final load step (0 to 100 psi) was 0.066 inches (0.28% of the initial diameter) and 0.040 inches (0.17% of the initial diameter), respectively.

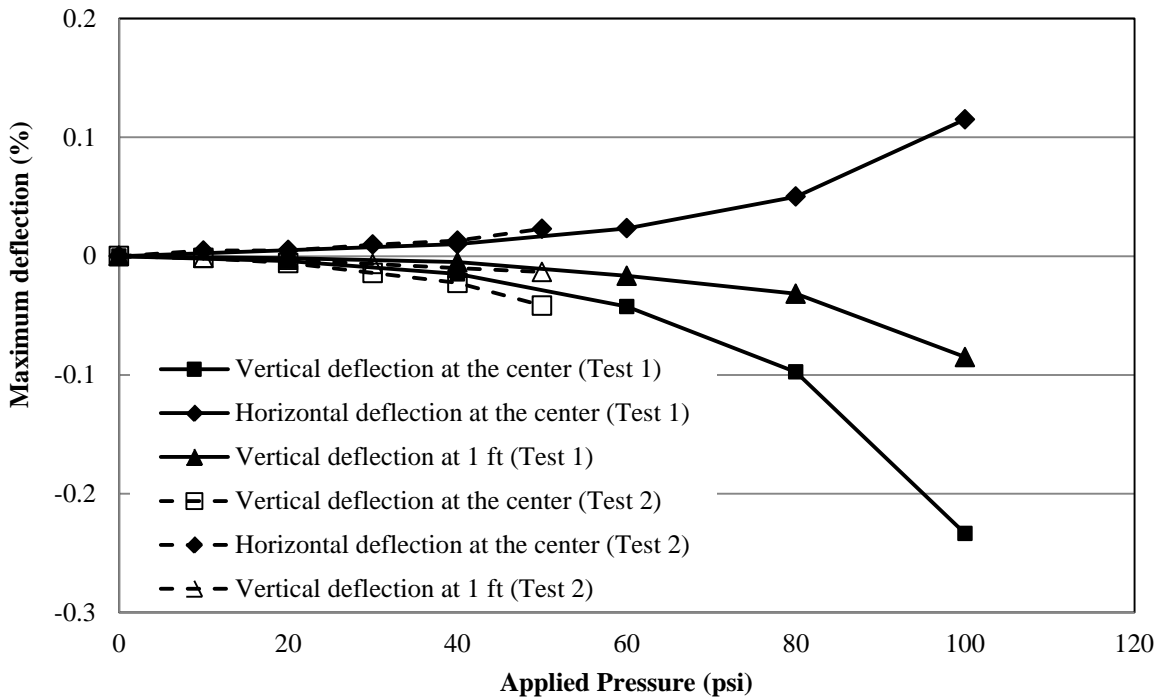




**FIGURE 5.66**  
**Maximum Deflections of the Pipe under Cyclic Loading in Test 3**

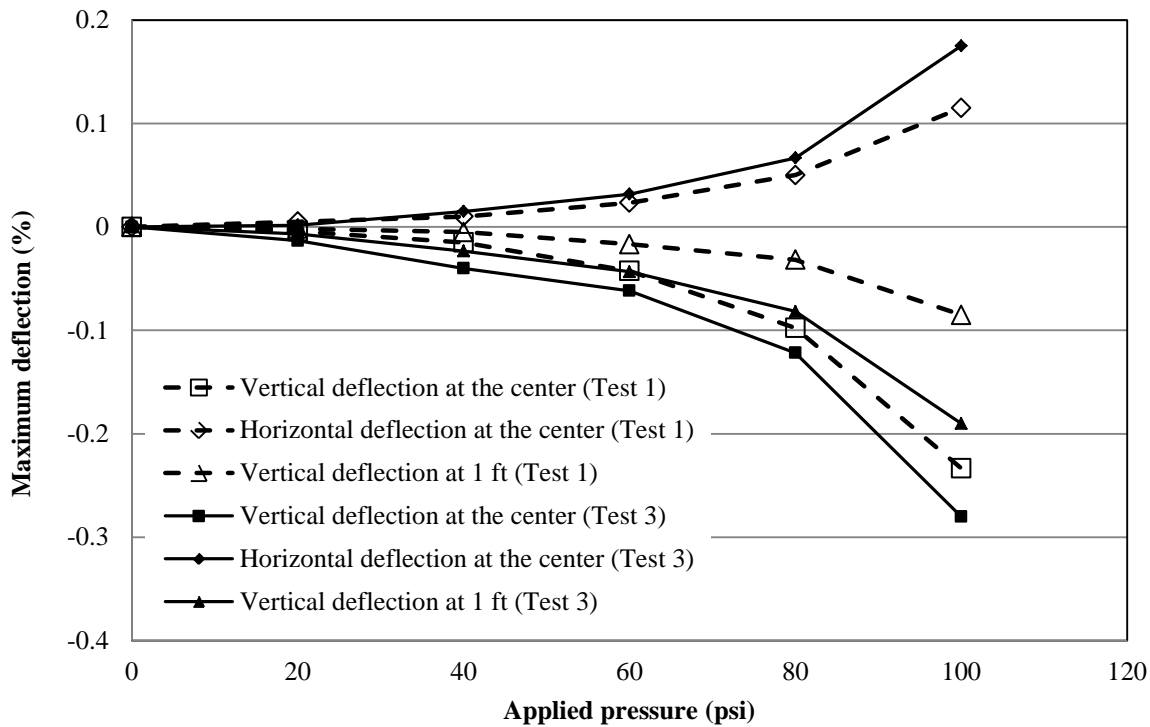
#### 5.3.3.4 Comparison of Test Results

Figure 5.67 shows the comparison of the maximum deflections of the pipe in Test 1 (with the AB-3 base course and the sand backfill) and Test 2 (with the sand as the base course and the backfill). The measured maximum deflections at the center of the pipe ( $\Delta D_{VC}$  and  $\Delta D_{HC}$ ) in Test 1 were less than those deflections in Test 2.



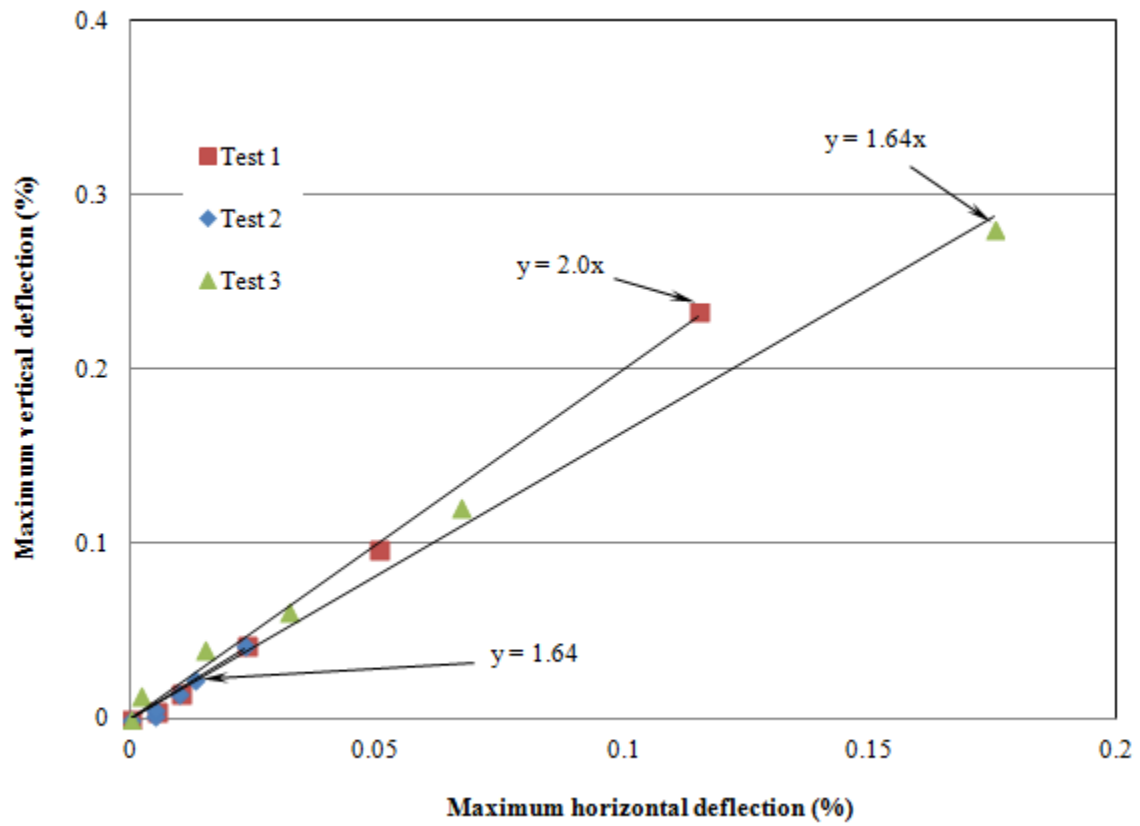
**FIGURE 5.67**  
**Comparison of the Maximum Deflections of the Pipe under Cyclic Loading in Tests 1 and 2**

Figure 5.68 shows the comparison of the maximum deflections of the pipe in Test 1 (with the sand backfill) and Test 3 (with the crushed stone backfill). The measured maximum deflections of the pipe in Test 1 were less than those in Test 3 because the crushed stone in Test 3 was dumped without any compaction.



**FIGURE 5.68**  
**Comparison of the Maximum Deflections of the Pipe under Cyclic Loading in Tests 1 and 3**

Figure 5.69 shows the relationship between the maximum vertical and maximum horizontal deflections at the center of the pipe during loading. The ratio of the vertical to horizontal deflection ( $\Delta D_{VC}/\Delta D_{HC}$ ) was approximately 1.64 in Tests 2 and 3 while the ratio was approximately 2.0 in Test 1. The ratios of the vertical to horizontal deflection ( $\Delta D_{VC}/\Delta D_{HC}$ ) at the center of the pipe under the buried conditions were higher than that of the pipe tested in air (i.e., 1.25). The higher ratios under the buried conditions were due to the resistance of the backfill against the horizontal deflections.



**FIGURE 5.69**  
Relationship between the Maximum Horizontal and Vertical Deflections at the Center of the Pipe under Cyclic Loading

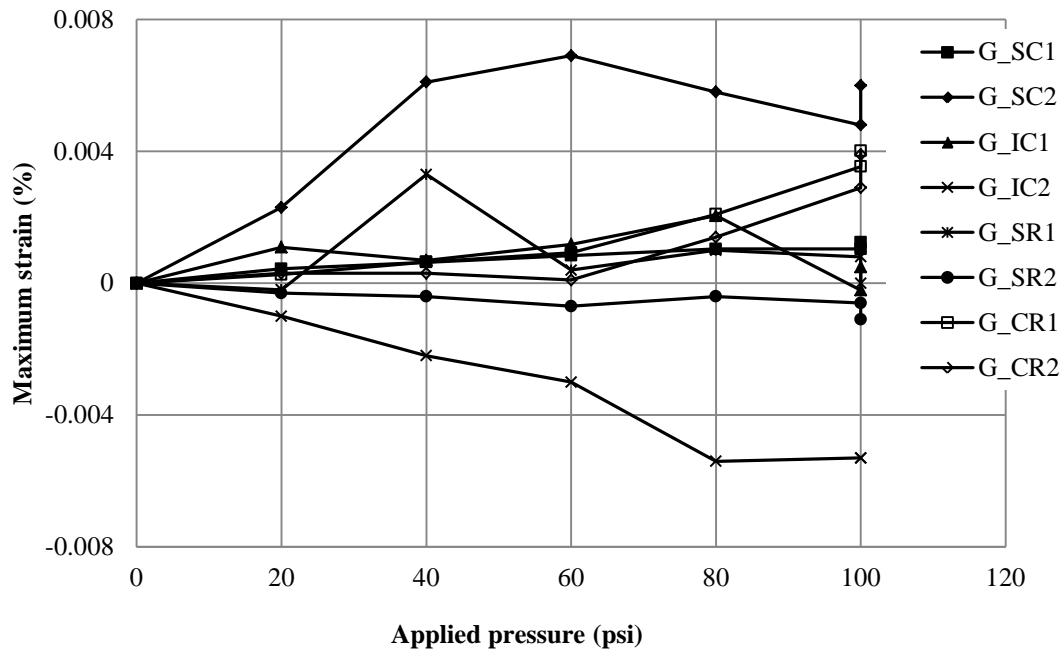
### 5.3.4 Strain Results

#### 5.3.4.1 Test 1

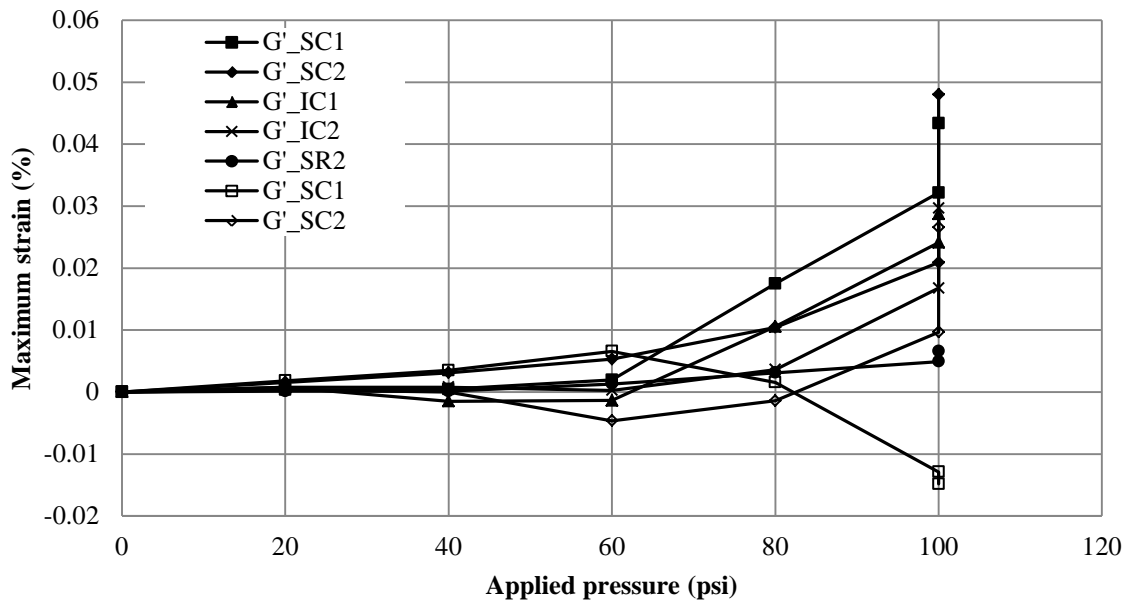
The maximum circumferential and radial strains on the steel of the pipe at different loading steps are shown in Figure 5.70. Strain gage  $G_{SC1}$  at the springline and  $G_{IC2}$  at the invert gave higher maximum strains in the circumferential direction than other strain gages on the steel. Strain gage  $G_{SC1}$  showed the maximum circumferential tensile strain of 0.0069% at the springline while strain gage  $G_{IC2}$  had a maximum circumferential compressive strain of 0.0053% at the invert.

Figure 5.71 shows the maximum circumferential and radial strains on the plastic cover at the ribs against the applied cyclic pressures. The maximum strains measured at most locations on the plastic cover were higher in magnitude than the maximum strains on the steel. Most of the strain gages showed an increase of tensile strains with an increase of the applied cyclic pressures except strain gage  $G'_{CR1}$ , which indicated an increase of compressive strains. Strain gage  $G'_{SC2}$  on the plastic cover at the rib at the springline in the circumferential direction showed a maximum tensile strain of 0.048% and strain gage  $G_{CR1}$  had a maximum compressive strain of 0.015%.

Figure 5.72 shows the maximum strains measured by strain gages  $G1''$  to  $G8''$  on the inside and outside plastic walls. Figures 5.70 to 5.72 indicate that the plastic walls between the steel ribs experienced the highest strains among other components of the pipe wall. The maximum tensile strain of 0.17% at strain gage  $G''_{CL1}$  and the maximum compressive strain of 0.025% at strain gage  $G''_{SL1}$  were measured on the outside plastic wall (valley) at the end of 1,000 cycles of the final load step (0 to 100 psi).



**FIGURE 5.70**  
Measured Maximum Strains on Steel under Cyclic Loading in Test 1



**FIGURE 5.71**  
Measured Maximum Strains on the Plastic Cover at Ribs under Cyclic Loading in Test 1

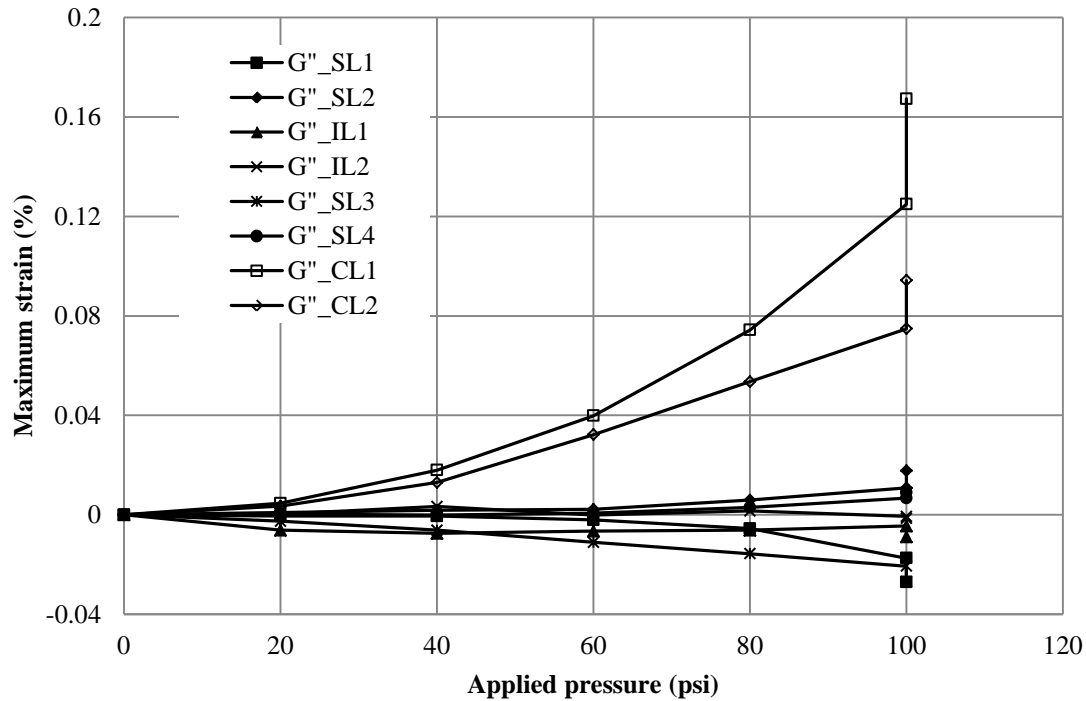


**FIGURE 5.72**  
**Measured Maximum Strains on the Inside and Outside Walls of the Pipe during**  
**Cyclic Loading in Test 1**

#### 5.3.4.2 Test 2

The maximum circumferential and radial strains on the steel of the pipe are shown in Figure 5.73. Most of the strain gauges showed an increase in tensile strains under the applied cyclic pressures. However, strain gauges,  $G_{SR1}$  and  $G_{SR2}$  at the springline and  $G_{CR1}$  and  $G_{CR2}$  at the crown in the radial direction, showed compressive strains at the lower cyclic loading step and tensile strains at the higher loading step. Strain gage  $G_{IC2}$  on the steel at the invert in the circumferential direction measured a maximum tensile strain of 0.0027% at the end of 260 cycles of the final loading step (0 to 50 psi).

Figure 5.74 shows the maximum circumferential and radial strains on the plastic cover at the ribs against the applied cyclic pressures. Most of the strain gauges showed an increase in tensile strains under the applied pressures. Strain gage  $G'_{SR2}$  showed a maximum tensile strain of 0.0083% at the end of 260 cycles of the final load step (0 to 50 psi).

The maximum strains measured by the strain gages on the inside and outside plastic walls are plotted in Figure 5.75, which indicates that the plastic walls between the steel ribs experienced the highest strains among all the components of the pipe wall. Strain gages  $G''_{SL1}$  to  $G''_{SL4}$  showed small strains as compared with those measured by strain gages  $G''_{CL1}$  and  $G''_{CL2}$  at the crown. The maximum tensile strain measured by strain gage  $G''_{CL1}$  was 0.041% and the maximum compressive strain measured by strain gage  $G''_{SL3}$  was 0.013% at the end of 1000 cycles of the final load step (0 to 100 psi).

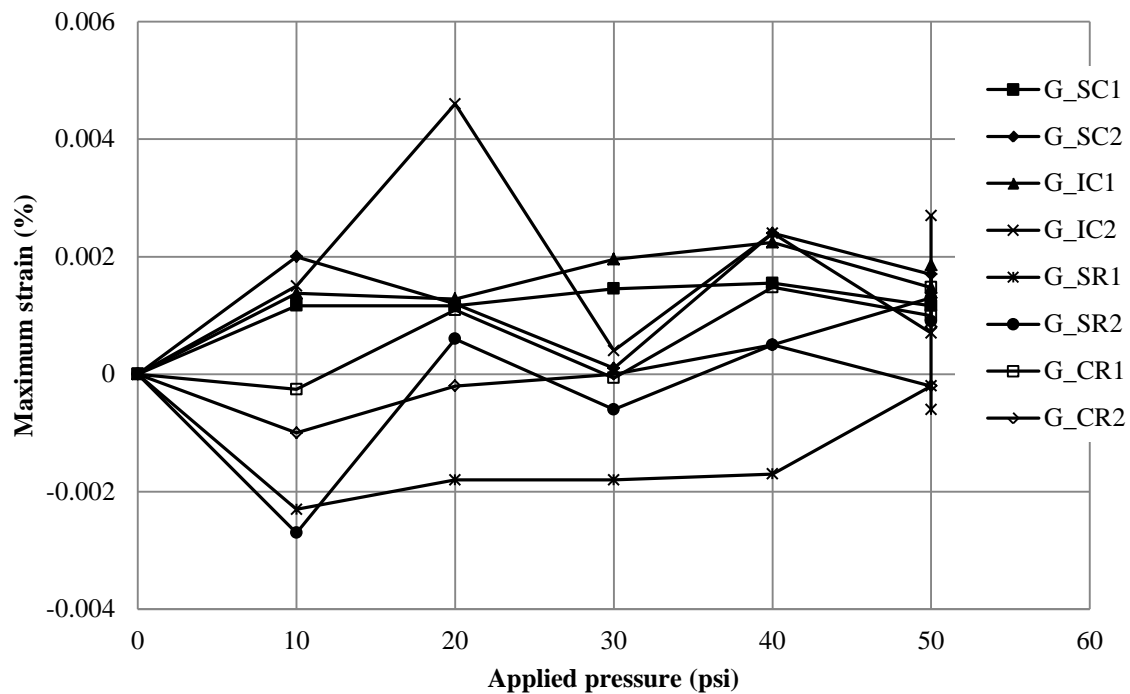


**FIGURE 5.73**  
Measured Maximum Strains on the Steel under Cyclic Loading in Test 2



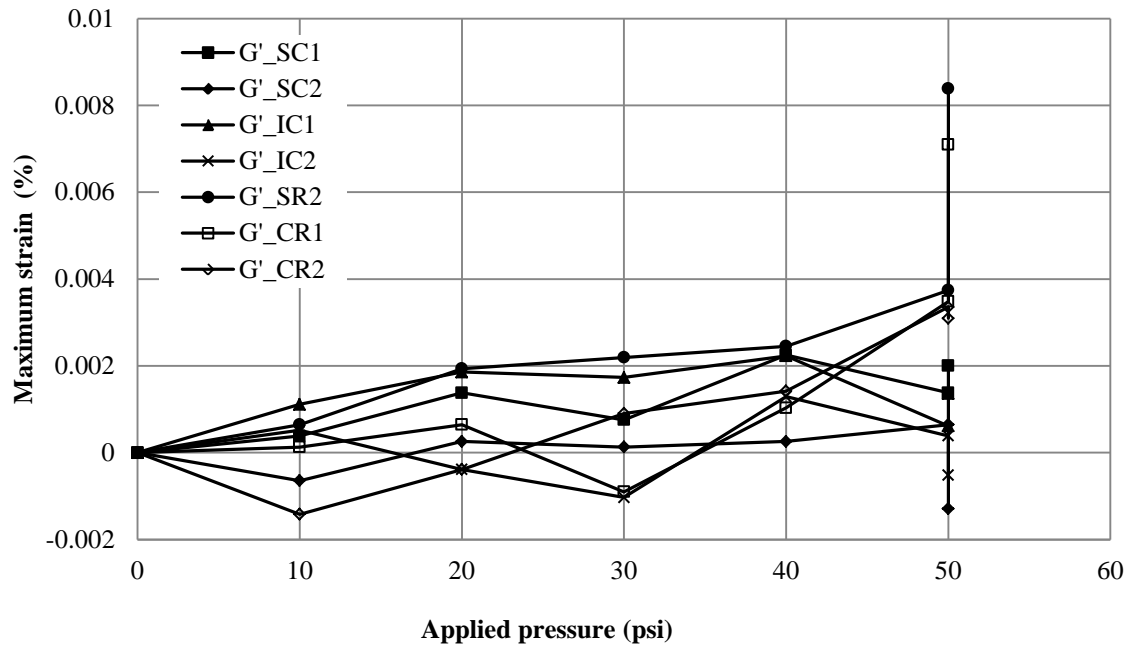


**FIGURE 5.74**  
Measured Maximum Strains on the Plastic Cover at the Ribs under Cyclic Loading in Test 2

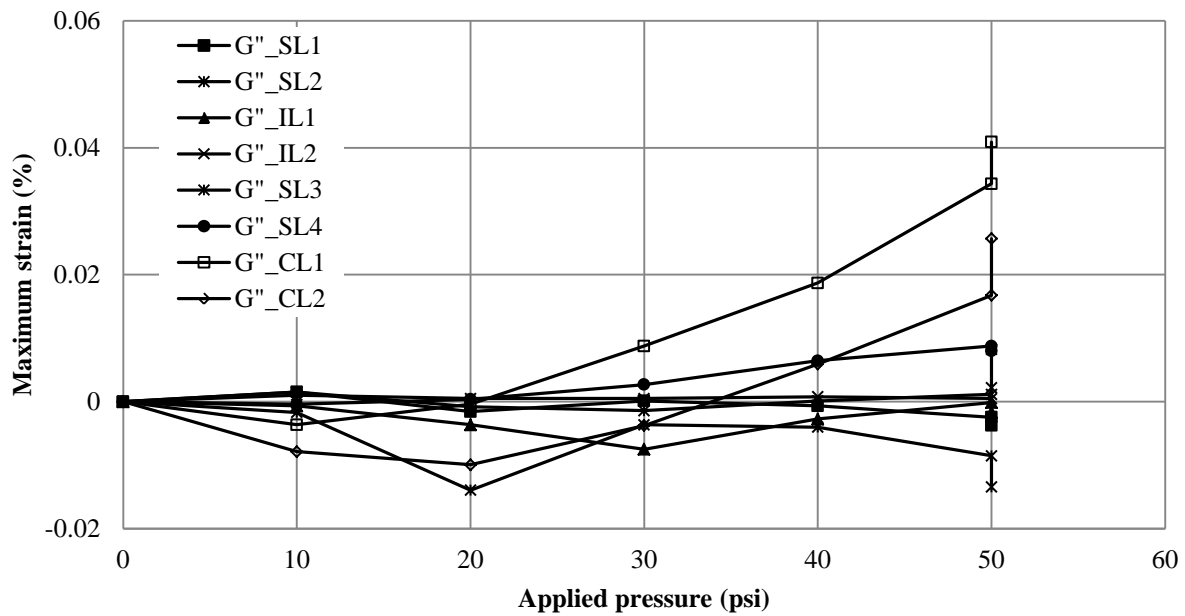


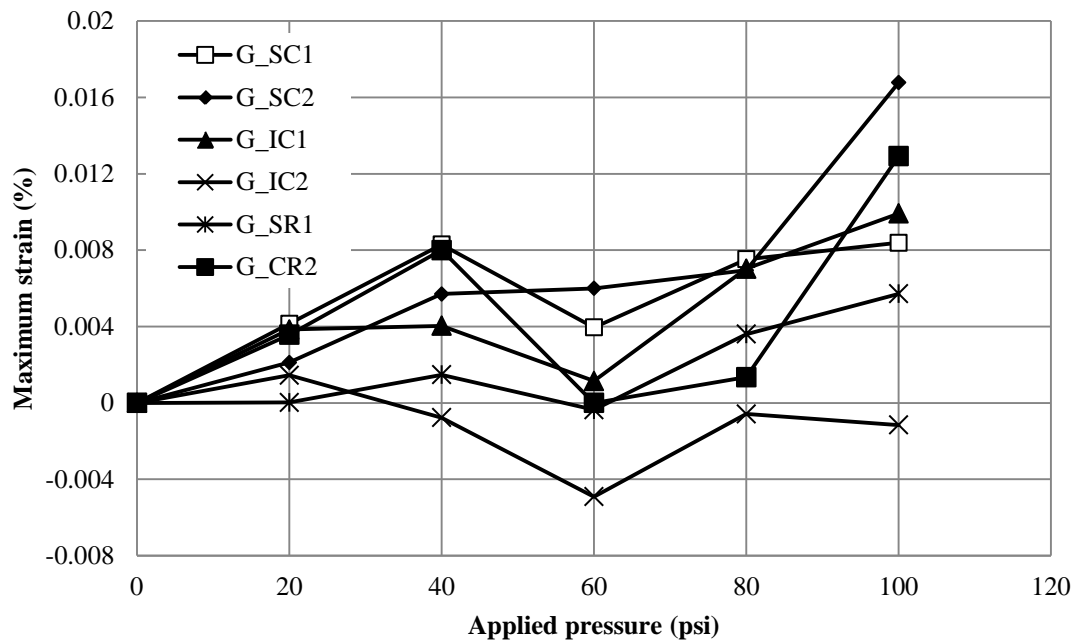
**FIGURE 5.75**  
Measured Maximum Strains on the Inside and Outside Plastic Walls of the Pipe during Cyclic Loading in Test 2

### 5.3.4.3 Test 3

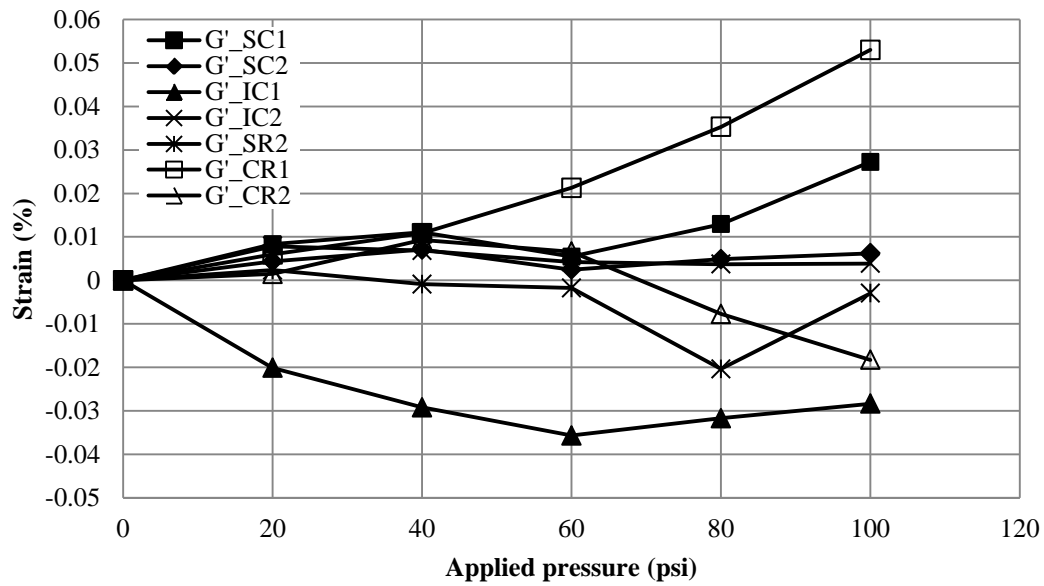
The maximum circumferential and radial strains on the steel of the pipe are shown in Figure 5.76. Most of the strain gages showed an increase in tensile strains under the applied cyclic pressures. Strain gage  $G_{SC2}$  on the steel at the invert in the circumferential direction showed a maximum tensile strain of 0.016% at the end of 1000 cycles of the final load step (0 to 100 psi).

Figure 5.77 shows the maximum circumferential and radial strains on the plastic cover at the rib against the applied cyclic pressures. Strain gage  $G'_{CR1}$  showed the maximum tensile strain of 0.053% at the end of 1,000 cycles of the final load step (0 to 100 psi).

The strains measured by strain gages on the inside and outside plastic walls are plotted in Figure 5.78, which indicates that the plastic walls between the steel ribs experienced the highest strains among all the components of the pipe wall. The maximum tensile strain measured by strain gage  $G''_{CL1}$  was 0.2% and the maximum compressive strain measured by strain gage  $G''_{SL1}$  was 0.0063% at the end of 1000 cycles of the final load step (0 to 100 psi).



**FIGURE 5.76**  
**Measured Maximum Strains on the Steel under Cyclic Loading in Test 3**



**FIGURE 5.77**  
**Measured Maximum Strains on the Plastic Cover at the Ribs under Cyclic Loading in Test 3**

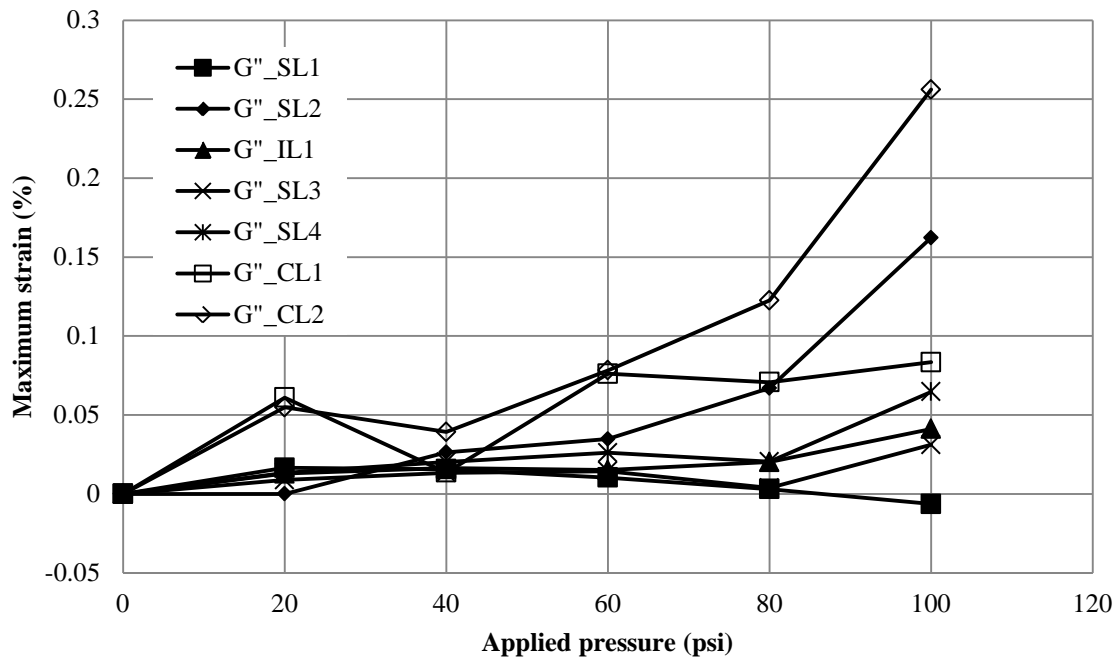


**FIGURE 5.78**  
**Measured Maximum Strains on the Inside and Outside Pipe Walls of the Pipe under Cyclic Loading in Test 3**

## 5.4 Comparison of Static and Cyclic Test Results

### 5.4.1 Earth Pressure Results

Figures 5.79, 5.80, and 5.81 indicate that the measured earth pressures around the pipe under static loading were higher than the maximum earth pressures under cyclic loading in Test 1, Test 2, and Test 3, respectively. The measured earth pressures around the pipe due to the applied static and cyclic loads for each test were normalized by the measured crown pressures for each loading step. The ratios of these normalized pressures around the pipe are presented in Table 5.2. The ratios of the measured earth pressures under static and cyclic loads in both Test 1 (with the AB-3 base course and the Kansas River sand backfill) and Test 2 (with the Kansas River sand as the base course and the backfill) were similar. However, the ratios of the measured earth pressures in Tests 1 and 2 (with the Kansas River sand backfill) were different from those in Test 3 (with the crushed stone backfill). In Tests 1 and 2, the highest earth pressures were recorded at the crown of the pipe ( $E_{C0}$ ) while in Test 3, the highest earth pressures were at 6 inches away from the crown of the pipe ( $E_{C6}$ ). The earth pressure at the invert ( $E_{I0}$ ) showed higher pressure in Test 3 than that in Tests 1 and 2 because the pipe was lifted up in Tests 1 and 2 as discussed in Section 5.1.1 during the compaction of the backfill, but there was little or no lift-up of the pipe in Test 3 during backfilling.

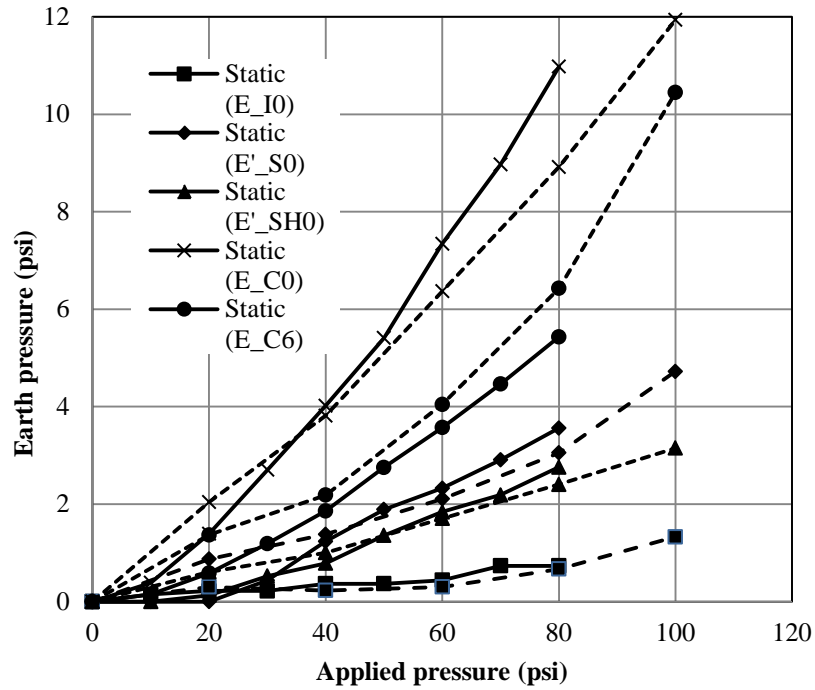


**FIGURE 5.79**  
Comparison of the Measured Earth Pressures around the Pipe under Static and Cyclic Loads in Test 1

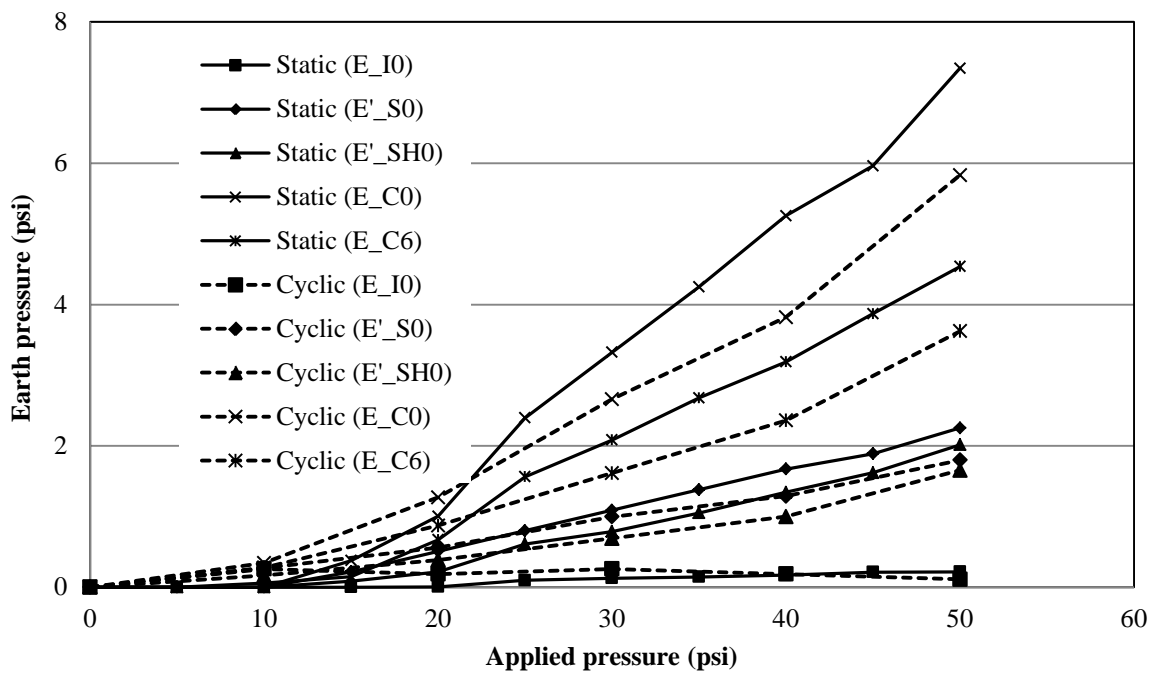


**FIGURE 5.80**  
Comparison of the Earth Pressures around the Pipe under Static and Cyclic Loads in Test 2

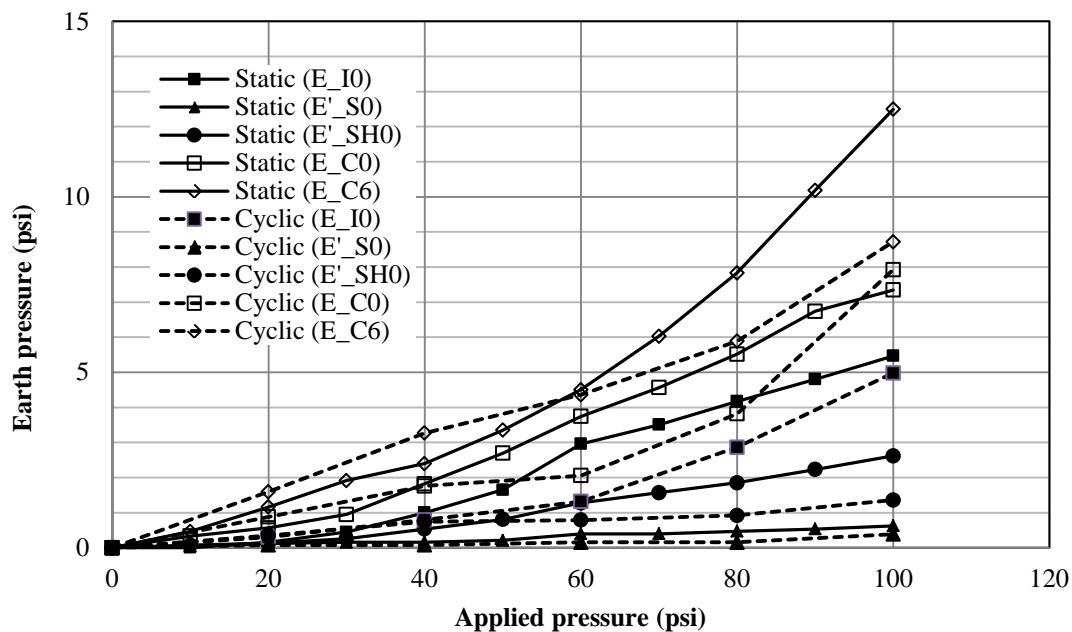


**FIGURE 5.81**  
Comparison of the Earth Pressures around the Pipe under Static and Cyclic Loads in Test 3

**TABLE 5.2**  
Comparisons of the Earth Pressures around the Pipe and the Deflections of the Pipe

		Vertical to horizontal deflection ratio	$E_{I0}:E_{S0}:E_{SH0}:E_{C0}:E_{C6}$
<b>In Air</b>		1.25	-
<b>Test 1</b>	Installation	0.95	-
	Static	1.64	0.075:0.32:0.24:1:0.50
	Cyclic	2	0.075:0.36:0.27:1:0.70
<b>Test 2</b>	Installation	-	-
	Static	2	0.035:0.32:0.25:1:0.63
	Cyclic	1.64	0.077:0.36:0.27:1:0.63
<b>Test 3</b>	Installation	0.85	-
	Static	1.64	0.70:0.08:0.30:1:1.38
	Cyclic	1.64	0.62:0.05:0.30:1:1.65

#### 5.4.2 Pipe Deflection Results

Figures 5.82, 5.83, and 5.84 indicate that the measured deflections of the pipe under static loading were higher than those deflections under cyclic loading in Test 1, Test 2, and Test 3, respectively. The ratio of the vertical to horizontal deflection at the center of the test pipe for each test is shown in Table 5.2. When the pipe was tested by the parallel plate test in air, the ratio was 1.25. However, the ratio was higher than 1.25 when the pipe was tested in a buried condition under a shallow depth under both static and cyclic loads. This is because the backfill soil minimized the outward movement of the pipe at the springline. The ratios of the vertical to horizontal deflection of the pipe under the buried condition were almost same for all tests under static and cyclic load tests, ranging from 1.64 to 2.0. During the installation of the test pipe, the ratios were 0.95 in Test 2 (with the Kansas River sand backfill) and 0.85 in Test 3 (with the crushed stone backfill).

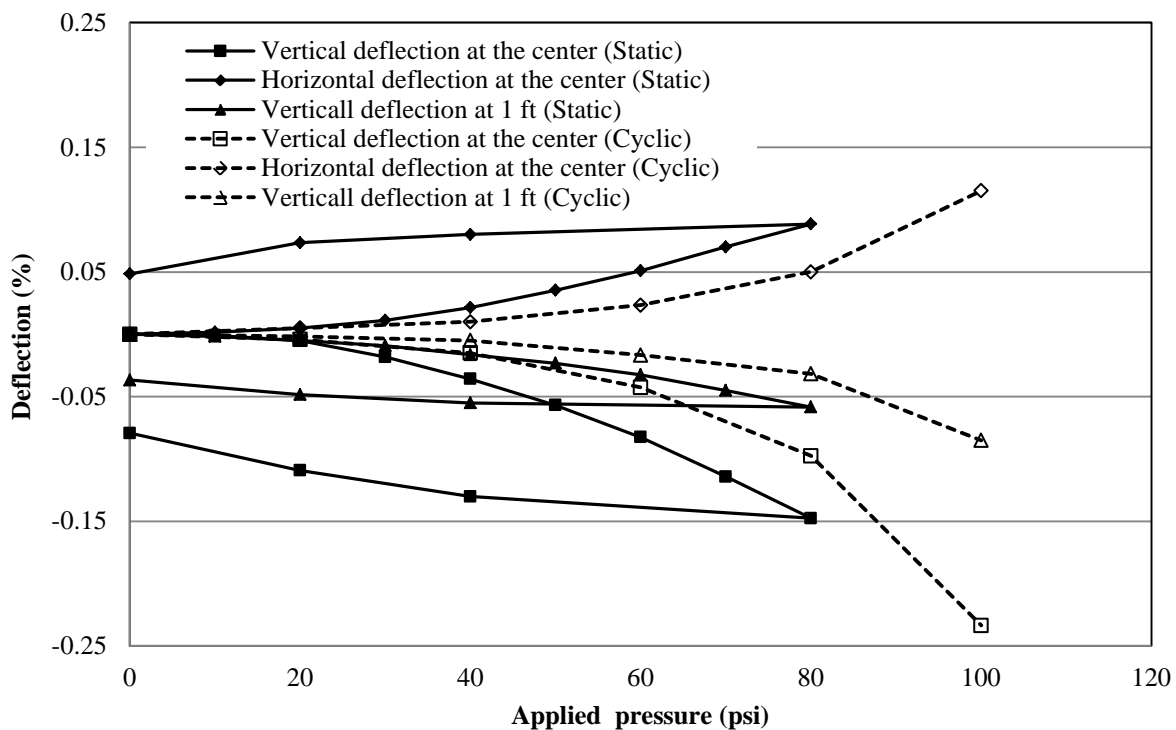


**FIGURE 5.82**  
**Comparison of the Deflections of the Pipe under Static and Cyclic Loads in Test 1**

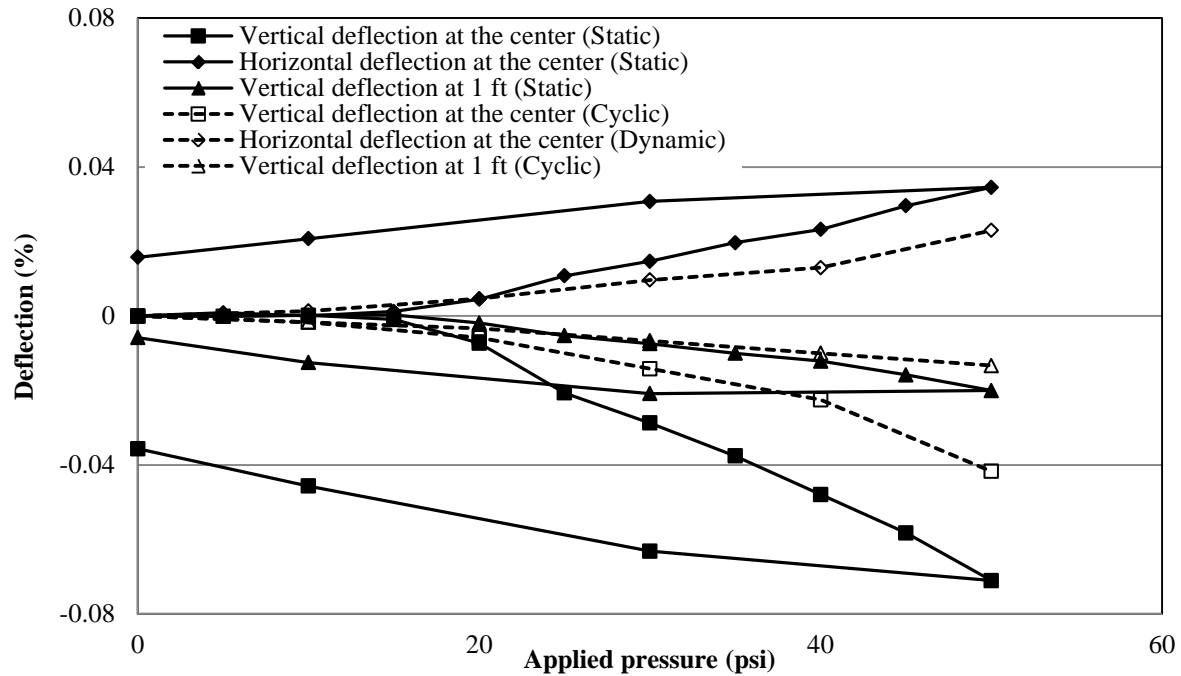


**FIGURE 5.83**  
Comparison of the Deflections of the Pipe under Static and Cyclic Loads in Test 2

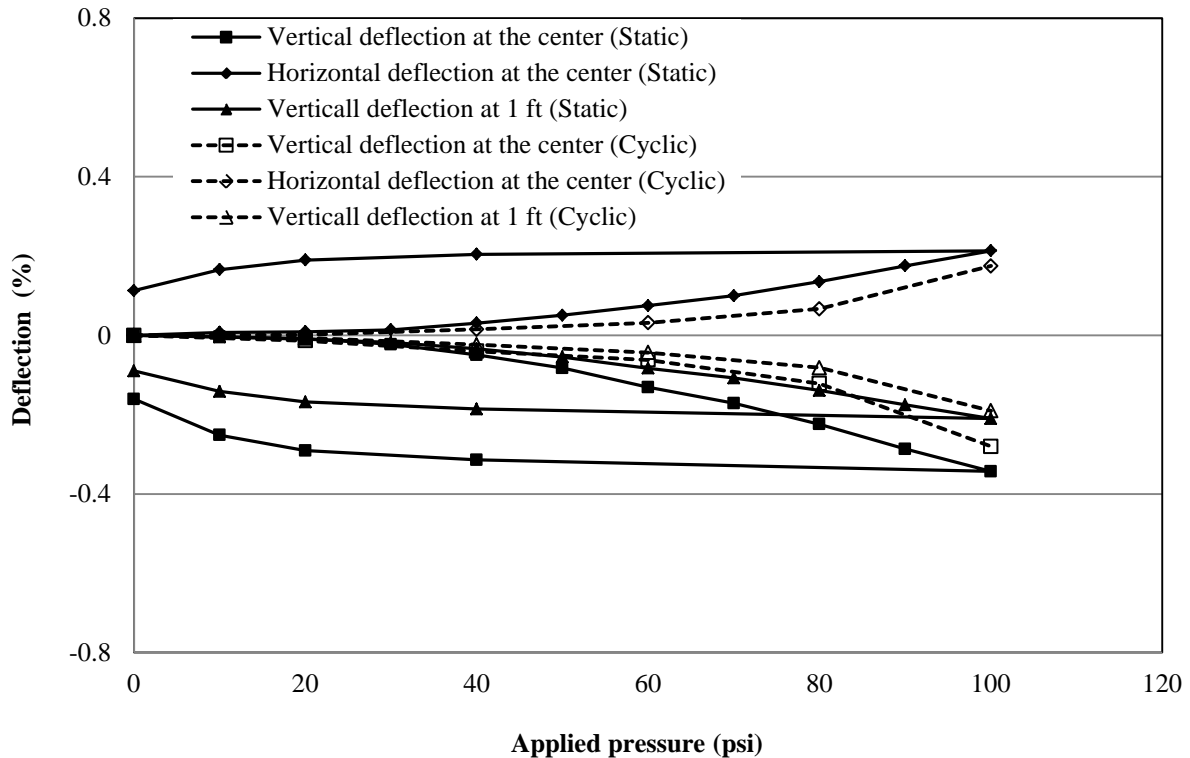


**FIGURE 5.84**  
Comparison of the Deflections of the Pipe under Static and Cyclic Loads in Test 3



### 5.4.3 Strain Results

The measured maximum strains on the steel and the plastic at various locations for each test during the installation and loading are shown in Table 5.3. The maximum strains on the plastic were higher than those in the steel. Most of the strains in the plastic were tensile. The strains measured on the inside and outside plastic walls were higher than those on the steel and the plastic covers at the ribs.

**TABLE 5.3**  
**Maximum Measured Strains on the Steel and the Plastic during the Installation and Loading**

Location		Test 1								
		Installation			Static			Cyclic		
		Steel rib	Plastic cover	Plastic wall	Steel rib	Plastic cover	Plastic wall	Steel rib	Plastic cover	Plastic wall
Springline	Circum.	-0.0265	0.114	-0.137	-0.0034	0.0061	0.0129	0.0069	0.0479	-0.0269
	Radial	0.0093	0.039	-0.180	0.0031	0.0147	0.0129	-0.0011	0.0065	0.0176
Invert	Circum.	0.0075	0.152	0.054	-0.0018	0.0033	-0.0002	-0.0053	0.0296	-0.0089
	Radial			0.066			0.0051			-0.0006
Crown	Circum.			0.158	-0.0066		0.1277			0.1673
	Radial	-0.0253	-0.083	0.158	0.0019	-0.0132	0.0670	0.004	0.0265	0.0942
		Test 2								
Springline	Circum.				-0.0032	-0.0061	0.0068	0.0014	0.0019	-0.0269
	Radial				-0.0038	0.0049	-0.0203	-0.0018	0.0083	0.0082
Invert	Circum.				0.00077	0.0010	0.0045	0.0027	0.0021	-0.0074
	Radial						0.0045			0.0021
Crown	Circum.				0.00096		0.0700			0.0408
	Radial				0.00096	0.0098	0.0512	0.0014	0.0070	0.0256
		Test 3								
Springline	Circum.	0.0464	0.091	0.060	-0.013	0.0219	0.1496	0.016	0.0270	0.0309
	Radial	0.034	0.048	0.142	0.008	-0.0258	0.1019	0.0057 1	-0.0203	0.1612
Invert	Circum.	0.0227	0.045	-0.054	-0.009	0.1806	0.0258	0.0099	-0.0258	0.0412
	Radial			0.141						
Crown	Circum.			0.072	-0.0061		0.1870			0.0825
	Radial	0.0253	0.058	0.191	0.0112	0.0696	0.3483	0.013	0.0528	0.2554

## 5.5 Safety against Structural Failure

The SRHDPE pipe was investigated at the strength limit state for: (1) wall area of the pipe, (2) global buckling, and (3) strain.

### 5.5.1 Wall Area of Pipe

The SRHDPE pipe was investigated at the strength limit state for the wall area of the pipe with and without considering local buckling. The total average measured pressures on the top of the pipe due to static/cyclic loading including the dead load (i.e., soil above the pipe and self-weight of the pipe) were calculated for all tests. The average measured pressure of 11 psi on the top of the pipe under the dead load and static load in Test 3 was the highest among all the tests. The pressure of 11 psi was then used to calculate the thrust ( $T_L$ ) on the pipe using Equation 2.31. The required wall area of the pipe was then calculated as  $A_{\text{reqd}} = T_L / (\phi F_y)$ , where  $\phi$  = resistance factor and  $F_y$  = the yield strength of steel. The calculated required area of the pipe-wall was found to be  $0.0016 \text{ in}^2/\text{in}$ , which was less than the wall area available ( $0.031 \text{ in}^2/\text{in}$ ).

To include the effect of the local buckling, the area of the pipe wall ( $0.031 \text{ inches}^2/\text{inch}$ ) was reduced to an effective area  $A_{\text{eff}}$ . The effective area of the pipe wall  $A_{\text{eff}}$  was determined using the stub compression test following AASHTO T341. The effective area of the pipe wall, which was calculated as  $A_{\text{eff}} = P_{\text{st}}/F_y$  where  $P_{\text{st}}$  = the stub compression capacity (see Section 3.1.2) and  $F_y$  = the yield strength of steel (80 ksi), was found to be  $0.025 \text{ in}^2/\text{in}$  if the stub compression capacity obtained by the independent test laboratory (TRI/Environmental, Inc. 2011) was used. The effective area of the pipe wall ( $0.025 \text{ in}^2/\text{in}$ ) was also higher than the required wall area of  $0.0016 \text{ inches}^2/\text{inch}$ . These results indicate that SRHDPE pipes maintain wall stability under expected traffic loads when the pipes are installed at the shallow depth as specified in the 2007 KDOT specification or the 2007 AASHTO LRFD Bridge Design Specifications. The gross pipe-wall area was reduced by approximately 20% if the local buckling was considered. The precise preparation of the specimen ends for the stub compression test may result in the effective area  $A_{\text{eff}}$  even closer to the gross area. This result concludes that the local buckling may not be an issue for an SRHDPE pipe under a shallowly buried condition (2 feet from the surface) subjected to traffic loading.

### *5.5.2 Global Buckling*

The wall area of the pipe was also investigated for global buckling using Equations 2.17 and 2.18 according to the 2007 AASHTO LRFD Bridge Design Specifications. The critical buckling stress was found to be 270 ksi, which was much higher than the yield strength of the steel ( $f_y = 80$  ksi). This result indicates that global buckling is not an issue for the SRHDPE pipe. In other word, the pipe may fail with the yielding of the material before the global buckling.

### *5.5.3 Strain Limit*

From Table 5.3, the highest measured strain on the steel among all the tests was 0.046%, which was less than the strain limit of 0.28% calculated at the yield point of the steel as  $\epsilon = F_y/E$  (where  $F_y$  = the yield strength of the steel and  $E$  = Young's modulus of elasticity of the steel). The highest measured strain on the plastic during the installation and loading among all the tests was 0.35%, which was within the permissible limit of 5% (the 2007 AASHTO LRFD Bridge Design Specifications).

## **5.6 Handling and Installation Requirement**

The AASHTO M294-07 specifications and KDOT use the parallel plate load test to verify that corrugated HDPE pipes have minimum pipe stiffness at 5% deflection to pipe diameter, and no buckling or loss of load before 20% deflection. The stiffness criterion at 5% deflection to pipe diameter is important for handling and installation of pipes, while the 20% deflection criterion provides necessary ultimate load capacity. From the parallel plate load test, the calculated pipe stiffness is more than the specified value (34 psi) per ASTM F2562/F2562M for Class 1 pipe of 24 inches in diameter at 5% vertical deflection to pipe diameter. Furthermore, the load at 20 % deflection is greater than 75 % of the peak load, although the peak load was reached before 20 % deflection. This result indicates that the SRHDPE pipes met the handling and installation requirement.

## Chapter 6: Conclusions and Recommendations

### 6.1 Conclusions

Steel-reinforced high-density polyethylene (SRHDPE) pipes were investigated in this study through compression tests of pipe specimens in air, installation of pipes in soil in a large geotechnical test box, and static and cyclic plate loading tests in the test box. The following conclusions were drawn from these three experimental studies.

#### *6.1.1 Compression Tests in Air*

1. Parallel plate loading test results showed that the tested SRHDPE pipes met both the minimum pipe stiffness and buckling limit criteria according to the ASTM F2562/F2562M. The SRHDPE pipes met the handling and installation requirement according to the ASTM F2562/F2562M.
2. The pipes started yielding at approximately 6% vertical deflection to pipe diameter and reached the ultimate load capacity at approximately 10% vertical deflection. These numbers are close to those obtained by Schluter and Shade (1999) for flexible metal pipes.
3. The photogrammetry method was an effective means of measuring the deflected shapes of the pipe under loading. The deflected shape of the SRHDPE pipe was found to be elliptical. The LiDAR scanner was able to obtain the deflected shapes of the pipe when the point of interest was not rapidly changing.
4. The strains measured on the steel showed that the pipe experienced out of plane buckling on the ribs of the pipe wall at a high level of load. The measured strains on the plastic covers at the ribs were higher than those strains of the steel during loading. This result indicates that the steel ribs and the plastic covers did not deform at the same strain rate during loading.
5. The profile wall of the pipe could resist a load up to 1,996 lbf/in based on the stub compression data from the independent testing laboratory, TRI. The gross pipe-wall area was reduced by approximately 20% when the local buckling was considered. The precise preparation of specimen ends for stub compression tests

may result in an effective area  $A_{\text{eff}}$  even closer to the gross area. In the three-point bending test, the equivalent bending stiffness of the pipe section was found to be  $2.6 \times 10^8 \text{ lb}\cdot\text{inch}^2$ .

6. The SRHDPE pipe deformed with time under a sustained load in air. As a result, the stiffness factor (EI) of the pipe decreased with time. The rate of stiffness factor (EI) reduction significantly decreased over the course of one month.

#### *6.1.2 Installation in Test Box*

1. Based on the measured earth pressures on the pipe crown, the calculated vertical arching factors (VAFs) varied from 1.0 to 1.44 with an average value of 1.26. Based on the criteria on the VAFs described by McGrath (1998), the SRHDPE pipe behaved as a corrugated steel pipe. The calculated VAFs were higher than the VAFs obtained using the Burns and Richard solutions based on the full-slip pipe-soil interface but less than the VAFs based on the fully-bonded pipe-soil interface. Therefore, the SRHDPE pipe-backfill soil interface should be considered fully-bonded in design to be conservative.
2. The calculated coefficients of lateral earth pressure (K) around the pipe were found to be between the coefficient of lateral earth pressure at rest ( $K_o$ ) and the coefficient of passive earth pressure ( $K_p$ ) for the compacted sand backfill and the dumped crushed stone. However, the K value for the dumped crushed stone was close to  $K_o$ .
3. The pipe exhibited peak deflections during backfilling. The measured peak deflections were larger than those deflections of the pipe under static and cyclic loadings when Kansas River sand or crushed stone was used. Due to the compaction effort applied, the peak deflections during the installation of the pipe in the sand backfill were larger than those deflections in the crushed stone backfill, which was placed by dumping without additional compaction.

4. The formula proposed by Masada and Sargand (2007) reasonably predicted the peak deflection of the pipe in the compacted sand backfill but under-predicted it in the dumped crushed stone backfill.
5. The modified Iowa formula reasonably predicted the deflection of the pipe installed in the dumped crushed backfill but under-predicted that in the compacted sand backfill. The larger measured deflection of the pipe installed in the compacted sand backfill may be due to the fact that the compaction-induced pressure on the top of the pipe was not considered.

#### *6.1.3 Static and Cyclic Plate Loading Tests*

1. The Giroud and Han (2004) method accurately predicted the vertical earth pressure on the top of the pipe induced by the applied load on the surface. The 2007 AASHTO LRFD Bridge Design Specifications slightly over-predicted the vertical earth pressure in the test sections with the AB-3 aggregate as a base course.
2. The average measured horizontal earth pressure from the side backfill to the pipe was approximately 0.30 and 0.20 times the vertical earth pressure on the top of the pipe in the compacted sand backfill and the dumped crushed stone backfill, respectively.
3. The calculated coefficients of lateral earth pressure ( $K$ ) for the dumped crushed stone backfill were found to be close to  $K_o$ .
4. The deflection of the pipe under the applied load was larger in the dumped crushed stone backfill than that in the compacted sand backfill. The modified Iowa formula overpredicted the deflection of the pipe under the applied load.
5. The measured earth pressures around the pipe and the deflections of the pipe under static loading were higher than those under cyclic loading.
6. The SRHDPE pipe material did not yield under the static and cyclic loads when the pipes were installed at the shallow depth.

7. The SRHDPE pipes maintained wall stability against the local buckling under the static and cyclic loads when the pipes were installed at the shallow depth.
8. The 2007 AASHTO LRFD Bridge Design Specifications design theory for corrugated metal pipes suggested that the SRHDPE pipe did not have a global buckling issue.
9. The highest measured strains recorded in steel and plastic during the installation and loading in all the tests were within the permissible values.
10. The out of plane buckling observed on the ribs of the pipe in the parallel plate test in air did not occur in the buried condition.

## **6.2 Recommendations**

This report focuses on the experimental work carried out on the SRHDPE pipes in air or buried at the shallow depth in a trench condition with sand or crushed stone as a backfill material. The SRHDPE pipes have helically wound steel strips, which are covered inside and outside with HDPE resin. The HDPE resin as the plastic cover on steel ribs and the plastic liner between steel ribs is a visco-elastic to visco-plastic and highly nonlinear material. Even though a creep test was conducted on the SRHDPE pipe in this study, the creep behavior of the pipe under a buried condition should be evaluated more fully. The laboratory tests done in the large geotechnical testing box had certain limitations. For example, the installation procedure of the pipe in the test box is different from the field installation due to the limited space and construction equipment in the lab. The moisture content of the soil in the test box is kept relatively constant. The effect of the moisture content or degree of saturation of the soil on the earth pressures and deformation of the pipe was not investigated in the laboratory study, but is likely to be important for the performance of SRHDPE pipes in the field. The laboratory test was short term (weeks), and was not designed to simulate the long-term behavior of the SRHDPE pipe in the field. As usual, box tests may have a boundary effect. Therefore, it is necessary to verify the lab test results and the design procedure developed based on the lab tests with a field study.

The following research is recommended for future studies to further understand the behavior of the SRHDPE pipes:

1. To evaluate the creep behavior of SRHDPE pipes under a buried condition;
2. To Investigate the performance of SRHDPE pipes in various backfill materials and with different soil cover thicknesses under static and cyclic loading; and
3. To evaluate field performance of SRHDPE pipes under shallowly and deeply buried conditions.



## References

- American Association of State Highway and Transportation Officials (AASHTO). 1992. *Standard Specifications for Bridge Design*, Washington, D.C.
- American Association of State Highway and Transportation Officials (AASHTO). 1996. *Standard Specification for Corrugated Polyethylene Pipe, 300 to 1500 mm (12 to 60 in.) Diameter*, Washington, D.C.
- American Association of State Highway and Transportation Officials (AASHTO). 2000. *Interim AASHTO LRFD Bridge Design Specifications*, Washington, D.C.
- American Association of State Highway and Transportation Officials (AASHTO). M36. 2003. *Standard Specifications for Corrugated Steel Pipe, Metallic-Coated, for Sewers and Drains*. Washington, D.C, 1–23.
- American Association of State Highway and Transportation Officials (AASHTO). 1998. *Standard Specifications for Bridge Construction*, Washington, D.C.
- American Association of State Highway and Transportation Officials (AASHTO). 2007. *Standard Specifications for Bridge Design*, Washington, D.C.
- American Association of State Highway and Transportation Officials (AASHTO) M294. 2009. *Standard Specifications for Highway Bridges*, Washington, D.C.
- American Association of State Highway and Transportation Officials (AASHTO). 2010. *Standard Specifications for Bridge Construction*, Washington, D.C.
- American Association of State Highway and Transportation Officials (AASHTO) T341. 2010. *Standard Method of Test for Determination of Compression Capacity for Profile Wall Plastic Pipe by Stub Compression Loading*, Washington, D.C.
- American Society for Testing and Materials (ASTM D2321). 2011. *Standard Practice for Underground Installation of Thermoplastic Pipe for Sewers and Other Gravity-Flow Applications*.
- American Society for Testing and Materials (ASTM D2412). 2002. *Standard Test Methods for Determination of External Loading Characteristics of Plastic Type by Parallel Plate Loading*.

- American Society for Testing and Materials (ASTM F2562/F2562M). 2010. *Specification for Steel Reinforced Thermoplastic Ribbed Pipe and Fittings for Non-Pressure Drainage and Sewerage*.
- American Water Works Association (AWWA M11). 2004. *Steel Pipe: A Guide for Design and Installation (M11)*.
- Arockiasamy, M., Chaallal, O., and Limpeteeparakarn, T. 2006. "Full-Scale Field Tests on Flexible Pipes under Live Load Application." *Journal of Performance of Constructed Facilities*, ASCE, 21–27.
- Bishop, R.R. and Lang, D.C. 1984. "Design and Performance of Buried Fiberglass Pipes – a New Perspective." *Pipeline Materials and Design*, B.J. Schrock (ed.), ASCE, 1–12.
- Brachman, R.W.I., Moore, I.D., and Munro, S.M. 2008. "Compaction Effects on Strains in Thermoplastic Culverts." *Geosynthetic International* 15 (2): 72–85.
- Bryan, G.H. 1891. "On the Stability of a Plane Plate under Thrusts in Its Own Plan with Applications to the Buckling of the Sides of a Ship." *Proceedings of the London Mathematical Society* 22: 55–67.
- Burns, J.Q. and Richard, R.M. 1964. "Attenuation of Stresses for Buried Cylinders." *Proceedings of the Symposium on Soil Structure Interaction*, the University of Arizona, Tucson, Arizona, 378–392.
- Burmister, D.M. 1958. "Evaluation of Pavement Systems of the WASHO Road Test by Layered System Method." *Bulletin 177*, Highway Research Board, 26–54.
- Cameron, D.A. 2006. *Analysis of Buried Pipes in Granular Backfill Subjected to Construction Traffic*. Ph.D. Dissertation, the University of Sydney.
- Carlstrom, B. and Molin, J. 1966. *Kunststoffe*, 56 (12): 895–898.
- Chambers, R.F., McGrath, T.J., and Heger, F.J. 1980. *Plastic Pipe for Subsurface Drainage of Transportation Facilities*. NCHRP Report 225, Transportation Research Board, 122–140.
- Dhar, A.S. and Moore, I.D. 2006. "Evaluation of Local Bending in Profile-Wall Polyethylene Pipes." *Journal of Transportation Engineering* 132 (11): 898–906.
- DiFrancesco, L.C. 1993. *Laboratory Testing of High Density Polyethylene Drainage Pipes*. MSc Thesis, Department of Civil Engineering, the University of Massachusetts.

- Faragher, E. 1997. *Structural Performance of Thermoplastic Drainage Pipes*. M. Phil Thesis, Loughborough University, Loughborough, Leicestershire, U.K.
- Faragher, E., Feleming, P.R, and Rogers, C.D.F. 2000. “Analysis of Repeated Load Field Testing of Embedded Plastic Pipes.” Transportation Research Record 1514, *Transportation Research Board*, Washington, D.C., 271–277.
- Folkman, S.L. 2011. *Monitoring of DuroMaxx Pipes Installed on Manhead Road in Rich County Utah (First Three Inspections)*. Final Report Submitted to Utah Department of Transportation Research Division by Utah State University.
- Goddard, J.B. 1992. “Plastic Pipe Design.” *Ohio Transportation Engineering Conference*.
- Goddard, J.B. 1994. “*Plastic Pipe Design*.” Technical Report 4.103, Advanced Drainage Systems Inc.
- Gumbel, J.E. and Wilson, J. 1981. “Interactive Design of Buried Flexible Pipes - a Fresh Approach from Basic Principles.” *Ground Engineering* 14 (4): 36–40.
- Hardert, M.T. 2011. *Shape Measurement of Existing 120" Diameter*. Report Submitted to Contech Construction Products, Inc.
- Hartley, J.D. and Duncan, J.M. 1987. “E' and Its Variation with Depth.” *Journal of Transportation Engineering*, ASCE, 113 (5): 538–553.
- Hashash, N.M.A. and Selig, E.T. 1990. *Analysis of the Performance of a Buried High Density Polyethylene Pipe*. Structural Performance of Flexible, Sergand, Mitchell, and Hurd (eds.), A.A. Balkema, Rotterdam, Netherlands.
- Howard, A.K. 1977. “Modulus of Soil Reaction Values for the Buried Flexible Pipe.” *Journal of the Geotechnical Engineering Division*, ASCE, 103 (1): 33–43.
- Howard, A.K. 1981. “The USBR Equation for Predicting Flexible Pipe Deflection.” *International Conference on Underground Plastic Pipe*, New Orleans, Louisiana, 37–55.
- Kansas Department of Transportation. 2007. *Standard Specification for Pipe and Culvert*. Kansas Department of Transportation (KDOT), Topeka, KS.
- Kansas Department of Transportation. 2012. *State Transportation Improvement Program Fiscal Year 2013–2016*. Kansas Department of Transportation (KDOT), Topeka, KS.

- Katona, M.G. (1988). “*Minimum Cover Heights for HDPE Corrugated Plastic Pipe under Vehicular Loading.*” Report to Corrugated Plastic Tubing Association.
- Kellogg, C.G. 1993. “Vertical Earth Loads on Buried Engineered Works.” *Journal of Geotechnical Engineering*, ASCE, 119 (3): 487–506.
- Krizek, R.J., Parmelee, R.A., Kay, J.N., and Elnaggar, H.A. 1971. *Structural Analysis and Design of Pipe Culverts*. National Cooperative Highway Research Program, Report 116, Highway Research Board, Washington, D.C.
- Leonhardt, G. 1978. “Belastungsannahmen bei erdverlegten GFK-Rohren.” AVK, Freudenstadt.
- Marston, A. and Anderson, A.O. 1913. *The Theory of Loads on Pipes in Ditches and Tests of Cement and Clay Drain Tile and Sewer Pipe*. Iowa Engineering Experiment Station, Ames, Iowa, Bull No. 31.
- Marston, A. 1930. *Theory of External Loads on Closed Conduits in Light of the Latest Experiments*. Iowa State College, Ames, Iowa, Bulletin 96.
- Masada, T. 2006. “Improved Solution for Pipe Stiffness as Measured by Parallel-Plate Load Test Method.” *Pipelines 2006*, Chicago, IL, American Society of Civil Engineers, 1–9.
- Masada, T. and Sargand, S.M. 2007. “Peaking Deflections of Flexible Pipe during Initial Backfilling Process.” *Journal of Transportation Engineering*, ASCE 133 (2): 105–111.
- McGrath, T.J. 1998. *Design Method for Flexible Pipes*. A Report to AASTHO Flexible Culvert Liaison Committee, Simpson Gumpertz and Heger Inc., Arlington, Mass.
- McGrath, T.J. and Sagan, V.E. 2001. “Design of Profile Wall Thermodynamic Pipe for Local Buckling.” Transportation Research Record 1170, *Transportation Research Board*, 209–219.
- McGrath, T.J., DelloRusso, S.J., and Boynton, J. 2002. “Performance of Thermoplastic Culvert Pipe under Highway Vehicle Loading.” *Pipelines 2002*, 1–14.
- Meyerhoff, G.G., and Baikie, L.D. 1963. “Strength of Steel Culvert Sheets Bearing against Compacted Sand Backfill.” *Highway Research Record* 30: 1–19.
- Mir Mohammad Hosseini S.M., and Moghaddas Tafreshi, S.N. 2002. “Soil-Structure Interaction of Buried Pipes under Cyclic Loading Conditions.” *International Journal of Engineering* 15 (2): 117–124.

- Moghaddas Tafreshi, S.N. and Khalaj, O. 2008. "Laboratory Test of Small Diameter HDPE Pipes Buried in Reinforced Sand under Repeated Load." *Geotextiles and Geomembranes* 26 (2): 145–163.
- Molin, J. 1981. "Flexible Pipe Buried in Clay." *Proceedings of International Conference on Underground Plastic Pipes*, ASCE, J. Schrock (ed.), New Orleans, 322–337.
- Moore, I.D. 2001. *Culverts and Buried Pipelines*. Geotechnical and Geoenvironment Handbook, R.K. Rowe (ed.), Kluwer Academic Publishers, 541–568.
- Moore, I.D. 2009. *DuroMaxx Pipe Assessment*. Final Report Submitted to Contech Construction Products Inc.
- Moore, I.D. and Hu, F. 1995. "Response of Profiled High-Density Polyethylene Pipe in Hoop Compression." *Transportation Research Board* 1914, Transportation Research Board, 29–36.
- Moser, A.P. 1998. "Structural Performance of Buried Profile-Wall High Density Polyethylene Pipe and Influence of Pipe Wall Geometry." *Transportation Research Record* 1624, Transportation Research Board, 206–213.
- Moser, A.P. 2008. *Buried Pipe Design*. New York: McGraw-Hill, Third Edition.
- Neilson, F.D. 1967. "Modulus of Soil Reaction as Determined from Triaxial Shear Test." *Highway Research Record* 185, Transportation Research Board, 80–90.
- Pokharel, S.K. 2010. *Experimental Study on Geocell-Reinforced Bases under Static and Dynamic Loading*. Ph.D, Dissertation, University of Kansas.
- Rogers, C.D.F., Fleming, P.R., Loeppky, M.W.J., and Faragher, E. 1995. "The Structural Performance of Profile-Wall Drainage Pipe-Stiffness Requirements Contrasted with the Results of Laboratory and Field Tests." *Transportation Research Record* 1514, Transportation Research Board, Washington, D.C., 83–92.
- Sargand, S., Masada, T.J., and Hurd, J.O. 1996. "Effect of Rib Spacing on Deformation of Profile Wall Plastic Pipes Buried in Coarse Granular Backfill." *ASTM, Geotechnical Testing Journal* 19 (2): 217–222.
- Sargand, S.M. and Masada, T.J. 2003. "Soil Arching over Deeply Buried Thermoplastic Pipe." *Transportation Research Record* 1849, *Journal of the Transportation Research Board*, 109–123.

- Schluter, J.C. and Shade, J.W. 1999. "Flexibility Factor or Pipe Stiffness: Significant Stiffness Consideration." *Transportation Research Board* 1656, 45–50.
- Schrock, B.J. 1993. "The Pipe/Soil Stiffness Ratio Variable." *Proceedings, Pipeline Infrastructure II*, M. Pickell (ed.), American Society of Civil Engineers, San Antonio, TX.
- Selig, E.T. 1990. "Soil Properties for Plastic Pipe Installation." *Buried Plastic Technology*, STP 1093, ASTM, Philadelphia, PA, 141–155.
- Spangler, M.G. 1941. *The Structural Design of Flexible Pipe Culverts*. Iowa Engineering Station Bulletin No. 153, Ames, Iowa.
- TRI/Environmental, Inc. 2011. *Stub Compression Test Results of Steel Reinforced HDPE Corrugated Pipe*.
- Trott, J.J. and Gaunt, J. 1976. *Experimental Pipelines under a Major Road: Performance during and after Road Construction*. Transportation and Road Research Laboratory Report 692, Crowthorne, Berkshire, 1–17.
- Turkopp, R.C., Torp, S., and Carlstrom, B. 1985. "Buried Fiberglass Pipe Performance and Installation Requirements and Design Calculations." *Advances in Underground Pipeline Engineering: Proceedings of the International Conference*, 383–395.
- Von Karman, T., Sechler, E.E., and Donnell, L.H. 1932. "The Strength of Thin Plates in Compression." *Transactions ASME* 54: 53–57.
- Watkins, R.K. 1960. "Failure Conditions of Flexible Culverts Embedded in Soil." *Highway Research Proceedings* 39: 361–371.
- Watkins, R.K. 1966. "Structural Design of Buried Circular Conduits." *Conduits and Behavior of Foundations*, Highway Research Record, Washington, 1–16.
- Watkins, R.K. 1971. "Response of Corrugated Steel Pipe to External Soil Pressures." *Highway Research Record* 37: 86–96.
- Watkins, R.J., Szpak, E., and Allman, W.B. 1973. *Structural Design of Polyethylene Pipes Subjected to External Loads*. Engineering Experiment Station, Utah State University, Logan, Utah.

- Watkins, R.K. and Spangler, M.G. 1958. "Some Characteristics of the Modulus of Passive Resistance of Soil: A study of Similitude." *Highway Research Board Proceedings*, Washington, D.C., 37: 576–583.
- Webb, M.C., McGrath, T.J., and Selig, E.T. 1996. "Field Tests of Buried Pipe Installation Procedures." *Transportation Research Record* 1541, 97–106.
- Whidden, W.R. 2009. *Buried Flexible Steel Pipe: Design and Structural Analysis*. American Society of Civil Engineers Manuals and Reports on Engineering Practice, No. 119.
- White, H.L., and Layer, J.P. 1960. "The Corrugated Metal Conduit as a Compression Ring." *Highway Research Proceedings* 39: 389–397.
- Winter, G. 1947. "Strength of Thin Compression Flanges." *Bulletin 35 part 3*, Cornell University Engineering Experiment Station, Ithaca, NY.



# K-TRAN

## KANSAS TRANSPORTATION RESEARCH AND NEW-DEVELOPMENT PROGRAM

